# Wideband and superdirective small antennas with embedded optimized loads using the characteristic modes theory

Hussein Jaafar

# THESE DE DOCTORAT DE

L'UNIVERSITE DE RENNES 1
COMMUE UNIVERSITE BRETAGNE LOIRE

ECOLE DOCTORALE N° 601
*Mathématiques et Sciences et Technologies de l'Information et de la Communication*
Spécialité : Télécommunication

Par

**Hussein Jaafar**

## Antennes Miniatures Large Bande et Superdirectives à Charges Optimisées par l'Analyse des Modes Caractéristiques

**Date de Soutenance : le 18, Septembre, 2018**
**Unité de recherche : IETR, UMR CNRS 6164, Institut d'Électronique et de Télécommunication de Rennes**
**Thèse N° :**

**Rapporteurs avant soutenance :**

| | |
|---|---|
| Hervé AUBERT | Professeur des Universités, INP / LAAS Toulouse |
| Christophe DELAVEAUD | Directeur du LAPCI, CEA Leti Grenoble |

**Composition du Jury :**

| | |
|---|---|
| Anja SKRIVERVIK | Professeure à l'Ecole Polytechnique de Lausanne / Présidente |
| Hervé AUBERT | Professeur des Universités, INP - LAAS Toulouse |
| Christophe DELAVEAUD | Directeur du LAPCI, CEA Leti Grenoble |
| Dominique LEMUR | Maitre de conférence à l'Université de Rennes 1 |
| Sylvain COLLARDEY | Maitre de conférence à l'Université de Rennes 1/ Co-encadrant de thèse |
| Ala SHARAIHA | Professeur à l'Université de Rennes 1 / Directeur de thèse |
| Philippe POULIGUEN | Responsable de Domaine Scientifique " Ondes acoustique et radioélectrique" - DGA / membre invité |

**Titre :** Antennes Miniatures Large Bande et Superdirectives à Charges Optimisées par l'Analyse des Modes Caractéristiques

**Mots clés :** Antennes Miniatures, Antennes à Large Bande, Antennes Superdirectives, Antennes à Multiport, Circuits non-Foster, Modes Caractéristique.

**Résumé :** L'évolution rapide dans les systèmes de communication sans fil nécessite plus de miniaturisation de divers composants électroniques en plus de l'élément majeur de la technologie sans fil: l'antenne. Dans ce cas, une antenne occupant un espace limité devrait être miniaturisée pour fonctionner aux bandes de communication souhaitées. Cependant, à mesure que la taille électrique de l'antenne diminue, ses performances se dégradent considérablement et sa bande passante, son efficacité et sa directivité sont limitées. Les techniques classiques de réduction de la taille avec chargement de matériau et mise en forme géométrique de l'antenne souffrent d'une bande passante étroite et d'une faible efficacité de rayonnement. D'autre part, les tentatives d'augmenter la directivité des petites antennes en utilisant des réseaux superdirectives sont également associées à une faible efficacité de rayonnement et une bande passante très étroite.

Pour pallier ces inconvénients, nous proposons de booster les performances des antennes compactes en utilisant des charges réactives embarquées. En plaçant correctement les charges (actives ou passives) à l'intérieur de l'antenne, il est possible de contrôler les courants pour améliorer de manière significative les performances de l'antenne en termes de bande passante et de directivité. Cependant, pour un succès des critères de chargement, il est obligatoire d'analyser les modes naturellement supportés par l'antenne étudiée. On les appelle les modes caractéristiques, qui fournissent des aperçus physiques profonds sur le comportement de l'antenne et ses modes de rayonnement. En combinant cette théorie avec l'algorithme d'optimisation, il devient possible de manipuler de manière optimale les courants à l'intérieur de l'antenne en utilisant des charges réactives pour obtenir des conceptions large bande, superdirectives et efficaces.

**Title :** Wideband and Superdirective Small Antennas with Embedded Optimized Loads Using the Characteristic Modes Theory.

**Keywords :** Miniature Antennas, Wideband Antennas, Superdirective Antennas, Multiport Antennas, non-Foster circuits, Characteristic Modes

**Abstract :** The rapid evolution in the wireless communication systems requires more miniaturization of various electronic components in addition to the major element of the wireless technology: the antenna. In this case, an antenna occupying a limited space should be miniaturized in order to operate at the desired communication bands. However, as the electrical size of the antenna decreases, its performance degrades dramatically and it becomes limited in bandwidth, efficiency, and directivity. Classical size reduction techniques with material loading and geometry shaping of the antenna suffer from narrow bandwidth and low radiation efficiency. On the other hand, attempts to increase the directivity of small antennas using superdirective arrays are also associated with low radiation efficiency and very narrow bandwidth.

To overcome these drawbacks, we propose boosting the performance of compact antennas using embedded reactive loads. By properly placing loads (active or passive) inside the antenna, it is possible to control the currents to significantly enhance the antenna performance in terms of bandwidth and directivity. Yet, for a successful loading criteria, it is mandatory to analyze the modes that are naturally supported by the antenna under study. These are called the characteristic modes, which provide deep physical insights about the behvaiour of the antenna and its radiating modes. By combining this theory with an optimization algorithm, it becomes possible to optimally manipulate the currents inside the antenna using reactive loads to achieve wideband, superdirective and efficient designs.

*To my parents*

*To Hadeel, Assil, and Ranim.*

# Acknowledgements

First, I would like to thank my supervisors Prof. Ala SHARAIHA and Dr. Sylvain COLLARDEY for offering me this wonderful opportunity to pursue my PhD. Their constant support and guidance have gave me the motivation and encouragement throughout the past three years. I deeply appreciate their willingness to share their knowledge, and for always being available to help me.

Thanks to Dr. Dominique LEMUR whose experience has been indispensable in achieving successful designs and fabrications of the active antennas. This part has been the most challenging throughout the PhD and I am very grateful for his help and for always being available for discussions.

I would also like to thank the jury members: Prof. Anja SKIVRVIC, Prof. Hervé AUBERT, Dr. Christophe DELAVEAUD, and Dr. Philipe POULIGUEN, for their insightful comments that favored in enhancing the quality of the manuscript.

Thanks to my fellow colleagues and friends at IETR, with whom I had interesting discussions and shared great moments.

I would also like to thank Christophe GUITTON from the technical staff who realized the prototypes and Jêrome SOL for his help in far-field measurements.

I am also thankful for the administrative team of IETR who were always available to deal with all my administrative procedures.

Finally, a special thanks to my parents and my sisters for their endless love, support and encouragement. I am so grateful to have you in my life.

# Contents

# List of Figures

# List of Tables

# Resumé des Travaux

## Contexte

Le développement rapide des systèmes de communication sans fil impose de concevoir des antennes fonctionnant dans une ou plusieurs bandes de communication (GSM, UMTS, BLUETOOTH, WLAN, ...). En général, les antennes fonctionnant dans ces bandes de fréquence doivent occuper un espace restreint pour optimiser l'intégration du dispositif sans fil. Dans ce cas, il est nécessaire de miniaturiser la taille électrique de l'antenne pour occuper le volume requis. Cependant, à mesure que les dimensions de l'antenne diminuent la bande passante et l'efficacité diminuent également, et le rayonnement tend à devenir quasi omnidirectionnel. Une antenne est alors qualifiée d'électriquement petite, et donc par conséquent miniature, si elle occupe un volume sphérique dont le rayon $a$ est inférieur ou égale à $\frac{\lambda}{2\pi}$ c'est-à-dire $ka$ inférieur ou égal à 1 [2]. Chu a établi que le facteur de qualité Q pour une antenne est inversement proportionnel à l'espace occupé. En d'autres termes, la bande passante diminue rapidement au fur et à mesure que $ka$ diminue. Pour les antennes miniatures, la limite minimale atteignable par le facteur de qualité Q en fonction de $ka$ proposée par Chu [1] est définie comme suit :

$$Q = \frac{1}{(ka)^3} + \frac{1}{(ka)} \tag{1}$$

Harrington [3] a étendu cette limite pour la directivité de l'antenne en fonction de sa taille électrique :

$$D = (ka)^2 + 2(ka) \tag{2}$$

Dans ce contexte, l'objectif de ces travaux de thèse sont de développer à partir de la théorie des modes caractéristiques des méthodes pour concevoir des antennes miniatures larges bandes avec ou sans rayonnement directif. Grâce à l'analyse modale, ces méthodes permettent de contrôler les modes en intégrant une ou plusieurs charges réactives sur la structure de l'antenne.

## Théorie des Modes Caractéristiques

La Théorie des Modes Caractéristiques (TMC) a été introduite par Grabacz en 1965 [14] et ensuite développée par Grabacz et Turpin [15] puis généralisée par Harrington [11]. Les modes caractéristiques d'une antenne représentatifs de sa géométrie sont obtenus à partir de la matrice impédance associant les courants de surface à la

composante tangentielle du champ électrique à la surface de l'antenne et ce indépendamment de toute excitation. La formulation du problème conduit à la résolution de valeurs propres :

$$[X]J_n = \lambda_n[R]J_n \tag{3}$$

Où $R$ et $X$ sont symétriques et représentent respectivement la partie réelle et imaginaire de la matrice d'impédance obtenue à partir de la méthode des moments (MoM). $J_n$ est un vecteur propre réel qui représente les courants caractéristiques alors que $\lambda_n$ est liée directement à l'énergie totale du champ électrique stocké. Lorsque $\lambda_n = 0$ à une fréquence donnée, le mode correspondant est dit résonant.

Puisque les courants caractéristiques sont orthogonaux, le courant global sur une structure parfaitement conductrice peut être écrit comme la somme pondérée des courants modaux :

$$J = \sum_n a_n J_n \tag{4}$$

Chaque courant caractéristique $J_n$ rayonne un champ caractéristique $E_n$. Par conséquent, le champ rayonné total est défini comme une somme pondérée des champs caractéristiques :

$$E = \sum_n a_n E_n \tag{5}$$

De plus, si l'élément rayonnant est alimenté à partir d'un ou plusieurs ports spécifiés, son admittance d'entrée peut être exprimée en termes d'admittance de modes caractéristiques à la fréquence angulaire $\omega$ :

$$Y_{in}[input] = \sum_{n=1}^{N} \frac{J_n[input]^2(1 - j\lambda_n)}{(1 + \lambda_n^2)((\tilde{J}_n^*[R]J_n)} = \sum_{n=1}^{N} Y_n \tag{6}$$

Où $\tilde{J}_n^*$ est le conjugué transposé du $n^{ième}$mode caractéristique.

Lorsqu'il s'agit de structures antennaires à plusieurs accès ou ports, il est plus pratique de calculer les modes caractéristiques de réseau au lieu des MC classiques. Les modes caractéristiques de réseau sont calculés à partir de la matrice d'impédance multiport en utilisant la même équation que la TMC. Dans ce cas, l'antenne multiport peut être modélisé sous forme de circuit comprenant un ensemble d'admittances parallèles correspondant chacune à un mode caractéristique donné (Fig. i).

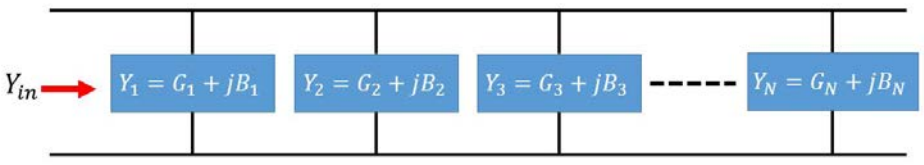


Figure i: Circuit équivalent de l'antenne à N port en termes d'admittances modales $Y_N$ représentant le $n^{ième}$ mode caractéristique

## Conception d'Antennes Miniatures à Large Bande à Charges Optimisées à partir des Modes Caractéristiques de Réseau

Les systèmes d'antennes multiports peuvent être considérés comme des réseaux à N port et ainsi être analysés par la théorie des modes caractéristiques de réseau (NCM). En raison des informations sur le comportement physique fournies par la NCM, les performances de l'antenne peuvent être améliorées en manipulant les modes à partir de charges réactives connectées sur un ou plusieurs accès localisés sur la structure de l'élément rayonnant.

Quand une antenne à N port est chargée par des charges réactives, (3) devient :

$$[X_a(\omega) + X_L(\omega)]\bar{I}_n(\omega) = \mu_n(\omega)[R_a(\omega)]\bar{I}_n(\omega) \tag{7}$$

Par conséquent, (6) devient :

$$Y'_{in}(\omega)[input] = \sum_{n=1}^{N} \frac{\bar{I}_n[input]^2(1 - j\mu_n(\omega))}{(1 + \mu_n^2(\omega))((\tilde{I}_n^*(\omega)[R_a(\omega)]\bar{I}_n(\omega))} = \sum_{n=1}^{N} Y'_n(\omega) \tag{8}$$

Où $X_L(\omega)$ est la matrice diagonale N × N représentant la réactance du réseau (figure 1). $I_n(\omega)$ et $\mu_n$ $(\omega)$ sont respectivement le $n^{ième}$ courant caractéristique et sa valeur propre correspondante du mode modifié par la charge réactive à la pulsation $\omega$, et $Y'_{in}[input]$ est l'admittance d'entrée de l'antenne chargée obtenue par la sommation des admittances modales modifiées $Y'_n$.

Par conséquent, afin de trouver les charges pouvant contrôler de manière optimale les modes de l'antenne, il est nécessaire de combiner les MC avec un algorithme d'optimisation. Dans notre cas, nous utilisons un algorithme à évolution différentielle. Après avoir défini la géométrie de l'antenne et la topologie de chargement (localisation des charges sur l'antenne), l'algorithme recherche la valeur de charge optimale pour modifier les admittances d'entrée des modes de sorte que l'antenne soit adaptée dans une large bande.

Cette approche est ensuite appliquée pour concevoir une antenne monopôle large bande intégrée sur un plan de masse. En plus du port d'alimentation, une capacité négative connectée sur un autre port interne à l'antenne de dimension $(130\times45mm^2)$ afin de miniaturiser et d'adapter l'antenne dans une bande passante de 30% [0.855-1.16 GHz]. Avec plus de ports internes et des topologies de chargement plus complexes, il est possible d'obtenir des bandes passantes plus larges. Avec une topologie de chargement en série de type LC, l'antenne monopôle peut être adaptée dans une bande passante beaucoup plus large [0.5-4 GHz] soit 61%. Cependant, les charges requises ne sont toujours pas des charges à comportement Foster.

Pour éliminer le besoin de charges non-Foster, une élément parasite méandre a été ajoutée au dos de l'antenne sur l'autre face du substrat. Ce parasite interagit avec le champ proche capacitif du monopôle et l'adapte dans une bande passante étroite à $860MHz$. Cela permet de faciliter l'adaptation de l'antenne en utilisant des charges passives plutôt que des charges actives à comportement non-Foster. Avec deux charges inductives, il est possible d'adapter l'antenne dans une bande passante de 20%. L'antenne a été fabriquée et mesurée comme montré dans Fig.ii. La bande passante peut encore être augmentée jsuqu'à 32% en ajoutant une troisième charge inductive.

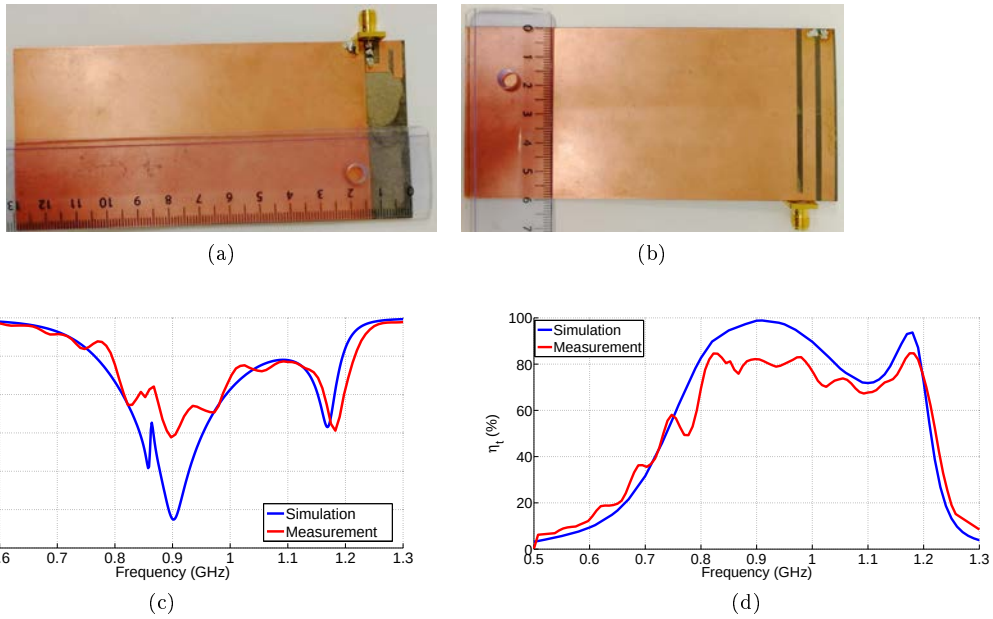


Figure ii: Prototype. (a) Couche supérieure, (b) couche inférieure, (d) simulation et mesure du S11 (a) et de l'efficacité.

La méthodologie est également appliquée sur la même antenne pour obtenir un comportement multibande. En choisissant correctement la position des charges, il a été possible de concevoir une antenne multibande fonctionnant sur les bandes GSM 850/950 et Bluetooth.

## Antenne électriquement Petite Chargée Avec des Circuits non-Foster

Dans la plupart des cas, les charges qui adaptent de façon optimale une antenne miniature dans une large bande nécessitent l'utilisation de circuits non-Foster. Le travail présenté dans ce chapitre montre une antenne miniature large bande à capacité négative. Afin d'optimiser les performances du circuit et de réduire les pertes résistives, le modèle électromagnétique du circuit est pris en compte dans la simulation électromagnétique de l'antenne. Avec cette approche, il est possible d'identifier les paramètres clés qui affectent l'efficacité de l'antenne. Une étude paramétrique est ensuite appliquée sur ces éléments afin d'identifier les valeurs optimales permettant d'offrir les meilleurs compromis en termes de bande passante et d'efficacité de l'antenne.

D'autre part, l'effet de la position du circuit à l'intérieur de l'antenne est également étudié. Il a donc été montré que lorsque la distance entre le port d'entrée et le circuit actif augmente, le rendement augmente car l'effet résistif du circuit diminue.

Deux cas ont été étudiés pour différentes positions du circuit NIC vis-à-vis de l'antenne. Considérant le premier cas où le point d'accès du circuit NIC est éloigné l'un de l'autre, l'antenne est adaptée dans une bande passante 43% avec une efficacité maximale $\eta_{max}$ = 18%. Cependant, lorsque les points d'accès sont rapprochés les uns des autres, il est possible d'obtenir de meilleures performances avec une bande passante de 50% et une efficacité de 23% (Fig.iii). Par conséquent, lors de la conception d'une antenne adaptée par un circuit actif, il est nécessaire d'utiliser la topologie

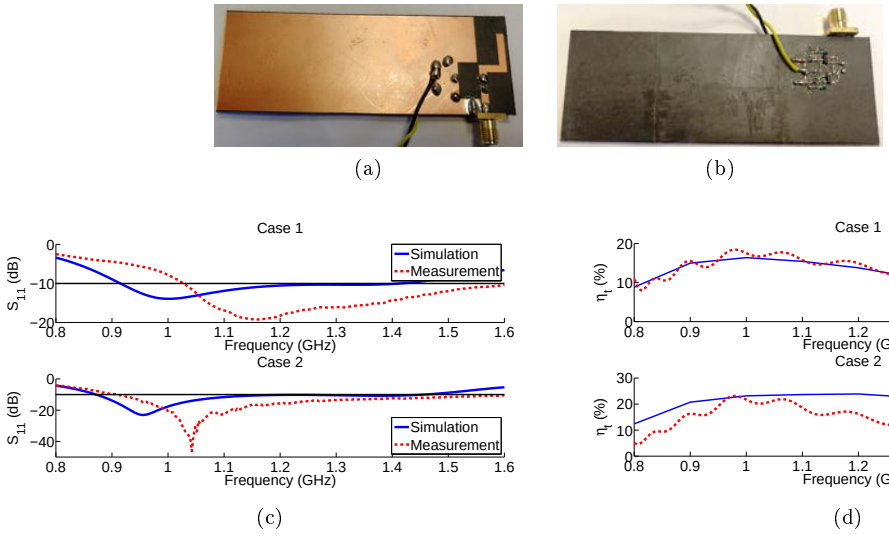


Figure iii: (a) Vue de dessus du prototype, (b) vue de dessous, (c)$S_{11}$, (d) efficacité.

du circuit dans la simulation EM pour étudier son effet sur la performance globale de l'antenne, puis essayer d'améliorer cette performance en optimisant sa position et les valeurs des composants du circuit.

## Conception de Réseaux Superdirectifs Compacts Utilisant les Modes Caractéristiques

Les antennes superdirectives est une technologie intéressante pour obtenir un rayonnement directif tout en conservant des dimensions compactes. En formant un réseau étroitement espacés ($d < 0.25\lambda$), il est possible d'obtenir une directivité qualifiée de "Superdirectivité". Cependant, augmenter la directivité de l'antenne compacte se fait au prix d'une largeur de bande de fonctionnement extrêmement étroite et d'une efficacité de rayonnement très faible lorsque la distance entre éléments diminue

Dans ce contexte, nous avons conçu un réseau large bande et superdirectif. Afin d'atteindre ce comportement, le point critique a été de choisir l'antenne élémentaire appropriée. Le choix s'est porté sur un monopôle miniature préalablement chargé pour atteindre un comportement large bande et donc présentant un faible facteur de qualité. En formant un réseau d'antenne superdirectif à partir de cet élément rayonnant, il devient possible d'obtenir une bande passante plus large avec une conception plus compacte. Cependant, lors de la conception d'un réseau superdirectif, il est important de trouver les excitations de courant optimales sur les ports du réseau qui peuvent orienter la puissance rayonnée dans la direction souhaitée. Ces excitations sont identifiées à l'aide de l'optimisation des modes caractéristiques de réseau. Puisque chaque courant caractéristique rayonne un champ caractéristique correspondant, le champ global peut être présenté comme une sommation pondérée des champs caractéristiques comme indiqué dans (5). Par conséquent, les coefficients de pondération sont optimisés pour maximiser la directivité dans la direction souhaitée. Cependant, ces excitations sont optimisées en fonction du mode de fonctionnement du réseau : parasite ou alimenté. Pour chaque mode de fonctionnement, une fonction du coût différente est proposée :

$$F(a) = -D(\theta_0, \phi_0) \tag{9}$$

$$F(a) = -D(\theta_0, \phi_0) + 0.5 \times real(Z_{Ln}) \tag{10}$$

Où (9) correspond au cas alimenté et (10) correspond au cas parasite, dans lequel un second composant est utilisé pour éliminer ou réduire la partie résistive de la charge parasite.

Tout d'abord, un réseau empilé à deux éléments est formé à partir de l'élément unitaire mentionné précédemment. Pour examiner l'avantage d'utiliser cet élément large bande au lieu d'un élément à bande étroite, nous avons considéré un réseau de même dimensions mais avec une antenne demi-boucle à bande étroite. La performance des deux réseaux a été étudiée en fonction de la distance de séparation. Avec le réseau à élément bande étroite, l'efficacité diminue considérablement en fonction de la distance jusqu'à ce qu'il atteigne 0% avec une distance de séparation de $d = 0.01\lambda$. D'autre part, le réseau ayant une antenne élémentaire à large bande présente une performance bien meilleure. Une efficacité et une directivité élevées ont été maintenues en fonction de la distance. Même à une distance de séparation très faible, le réseau conserve une efficacité relativement élevée de 40% à $d = 0,01\lambda$ avec une directivité maximale de $7,5dBi$. Un prototype du réseau a été réalisé et mesuré par une distance inter-élément de $d = 0,5\lambda$ (Fig.iv). Cependant, avec cette configuration, le réseau présente un fonctionnement à bande étroite en directivité et en $S_{11}$ .

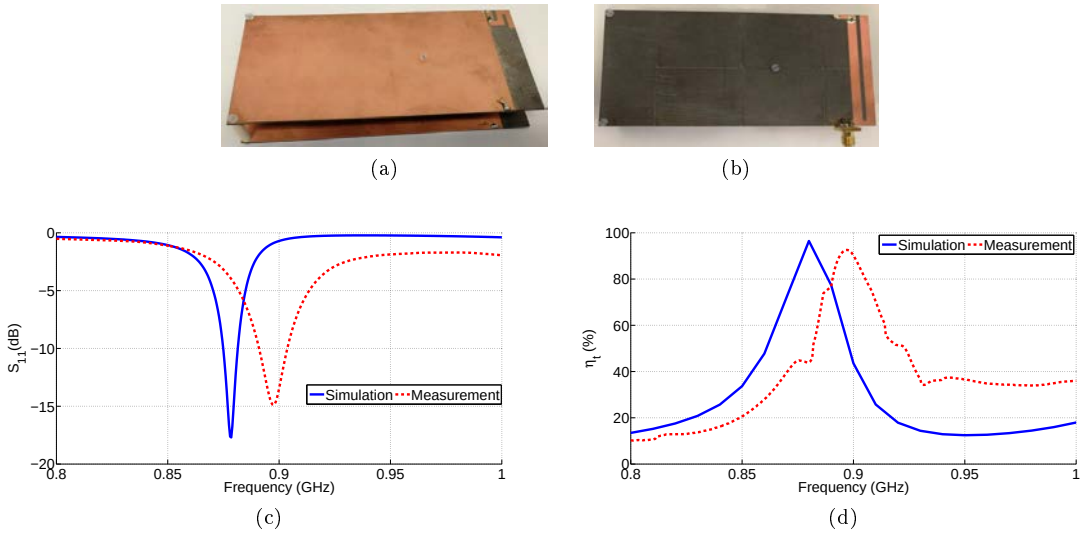


Figure iv: Prototype du réseau parasite empilé. (a) Vue de dessus, (b) vue de dessous, (c) $S_{11}$, (d) efficacité.

Pour améliorer la bande passante de l'antenne en termes de directivité et d'impédance, le réseau est reconfiguré sous forme linéaire (Fig.va). La configuration linéaire du réseau impose une distance de séparation plus élevée et, par conséquent, les dimensions globales augmentent. En étudiant l'ensemble des excitations optimales à divers points de fréquence à l'intérieur de la bande d'intérêt, il a été possible d'en déduire une valeur d'excitation pour maintenir la directivité constante en fonction de la fréquence. Un réseau d'alimentation réalisé à partir d'un diviseur de Wilkinson

a ensuite été intégré sur la structure de l'antenne pour fournir l'excitation désirée. Avec cette configuration, le réseau présente une large bande passante en directivité de 23% avec une valeur maximale $D_{max} = 6dBi$ (Fig.v).

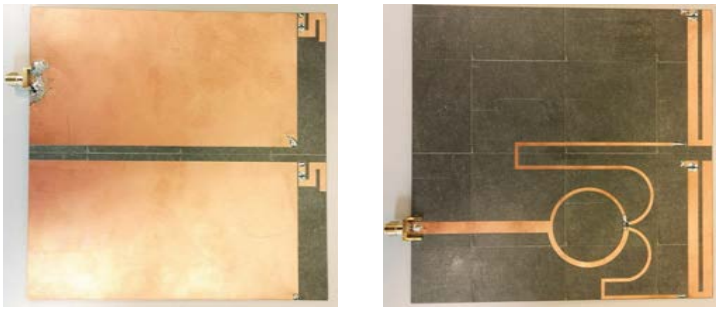

(a) (b)

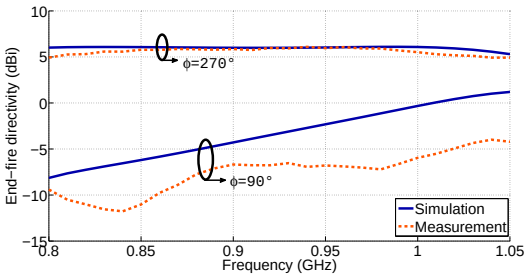


(c)

Figure v: Prototype du réseau en configuration linéaire avec circuit d'alimentation. (a) Vue de dessus, (b) vue de dessous, (c) directivité en fonction de la fréquence.

## Conception d'une Antenne Large Bande à Polarisation Circulaire

Après avoir appliqué la théorie des modes caractéristiques de réseau pour analyser et concevoir des antennes large bande et superdirectives, la conception d'une antenne à polarisation circulaire (CP) large bande a ensuite été examinée. L'objectif était d'analyser une structure non-conventionnelle d'antenne à fente et d'étudier la possibilité de générer une polarisation circulaire en étudiant puis en manipulant les modes en utilisant des modifications de géométrie. Une antenne à fente en forme de triskèle de dimensions $70mm(0,39\lambda) \times 70mm(0,39\lambda)$ a été choisie comme géométrie initiale. L'analyse modale de la structure a montré qu'il y a deux modes dominants dans la bande passante d'intérêt (GPS L1). Cependant, ces modes ne présentent pas de propriétés autorisant une polarisation circulaire ($MS_1 = MS_2$, $\alpha_1 - \alpha_2 = \pm 90°$). La structure a donc été ensuite modifiée en éliminant une partie de la structure pour permettre aux modes d'avoir les propriétés désirées et de la rendre plus compacte ($70mm(0,39\lambda) \times 45mm(0,23\lambda)$). Après diverses modifications de géométrie, un monopôle a été conçu pour exciter les modes désirés permettant d'obtenir la polarisation circulaire. L'antenne présente au final une bande passante en rapport axial (AR) de 8% et une bande passante en adaptation représenté par $S_{11}$ de 36%. Cependant, afin de supprimer le rayonnement bidirectionnel et d'obtenir un LHCP dans l'axe +z, un réflecteur a été positionné parallèlement à l'antenne à une distance de $\lambda/4$ (Figvi). Avec cette configuration, le rayonnement en polarisa-

tion circulaire droite (RHCP) a été supprimé avec une discrimination de polarisation croisée supérieure à $10dB$, une bande passante AR de 9,5% et une bande passante d'impédance de 34% (Fig.vii). Bien que ces résultats préliminaires soient en deçà de résultats observés dans la littérature, cette étude utilisant les modes caractéristiques présente un caractère didactique et ouvre de nombreuses possibilités pour accroitre non seulement la réduction de la taille de l'antenne mais également les performances tant du point du rapport axial que de l'adaptation.


(a) (c)

Figure vi: Prototype. (a) Vue de dessus, (b) vue de dessous (c) Antenne sur réflecteur métallique.

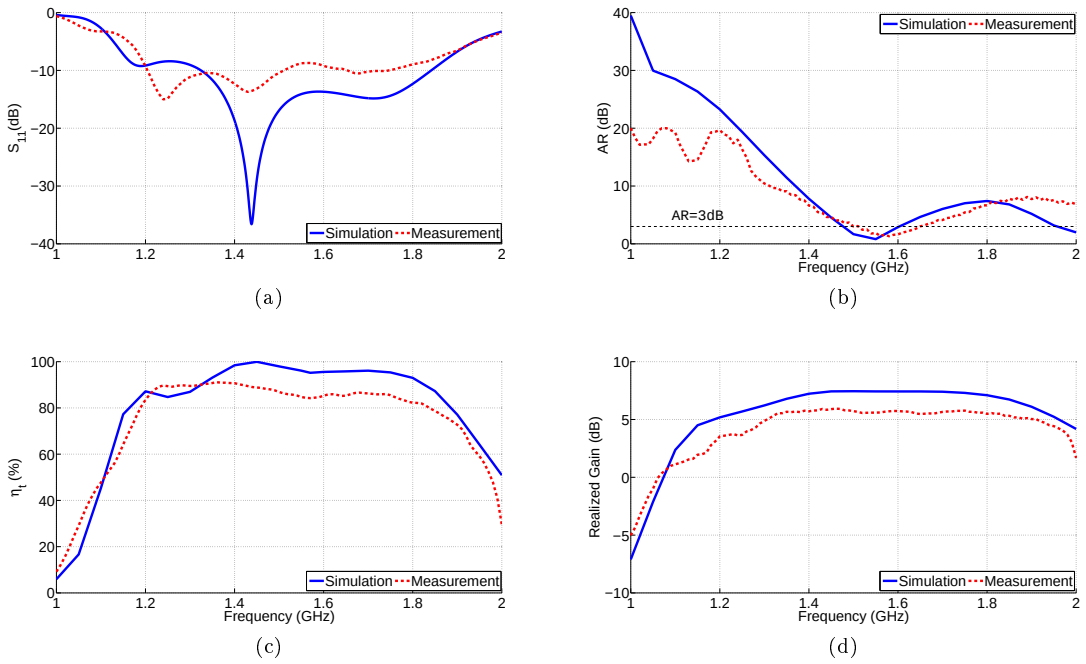


(a) (b) (c) (d)

Figure vii: Performance de l'antenne. (a) $S_{11}$, (b) rapport axial, (c) efficacité total, (d) gain réalisé maximal.

# Introduction

Electrically small antennas (ESAs) are limited in bandwidth, efficiency and directivity [1, 2, 3, 4]. As the electrical size of the antenna becomes smaller with respect to the wavelength, its radiation resistance decreases significantly to the point that the resistive losses in the structure become important. Therefore the radiation efficiency decreases dramatically. On the other hand, the reactance of the antenna increases. Consequently, in 1947, Wheeler [2] considered that an ESA exhibits a behaviour similar to a lumped circuit element (C or L) (Fig.viiia,b), showing that the radiated power $P$ is limited by the volume occupied by the small antenna:

$$P \approx \frac{Abk^3}{6\pi} \tag{11}$$

where $k = \frac{2\pi}{\lambda}$ is the wave number, $A$, and $b$ are the dimensions of the cylindrical volume occupied by the antenna.

Furthermore, by considering an antenna enclosed in a radian sphere (Fig.viiib), Chu derived the well known relation between the electrical size of the antenna and its Q factor [1]:

$$Q = \frac{1}{(ka)^3} + \frac{1}{(ka)} \tag{12}$$

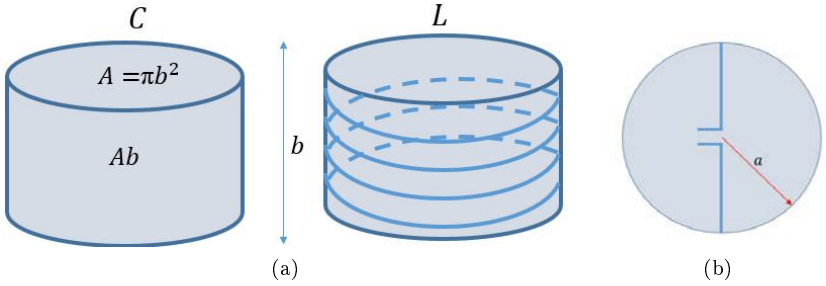


Figure viii: (a) A presentation of ESA of type L and C occupying the same volume [2]. (b) ESA antenna enclosed in a radian sphere [1]

This relation shows that $Q$ is inversely propotional to the electrical size of the antenna, which imposes a physical limitation on its performance as it becomes electrically smaller. Later on, following this work, extensive researches have been carried to study the fundamental limitations of small antennas, as the formula presented by Chu is considered optimistic and becomes imprecise as the electrical size of the antenna ($ka$) approaches 1 [5, 6, 7, 8]. Nevertheless, all these developed formulas on the Q limits of ESAs have validated the initial proposition of Chu and Wheeler,

showing that the antenna Q factor increases as the electrical size decreases. However, this limitation in Q, imposes a limitation in the impedance bandwidth which is inversely related to the Q factor by the following equation [9]:

$$BW = \frac{1}{Q}\frac{S-1}{\sqrt{S}} \tag{13}$$

In addition to the bandwidth limitaion, Harrington [3] defined a limit on the maximum attainable directivity in a specific direction $(\theta_0, \phi_0)$ with respect to the order $N$ of the spherical modes associated to the antenna's radiation:

$$D = N^2 + 2N \tag{14}$$

He later established a relationship between the size of an antenna enclosed in a sphere of radius $a$ and the spherical wave order $N$:

$$N = ka \tag{15}$$

Consequently (14) becomes:

$$D = (ka)^2 + 2(ka) \tag{16}$$

which proves that as the electrical size of the antenna decreases, its radiation pattern becomes less directive. However, By forming an array of closely spaced electrically small unit elements with optimized phase and magnitude at the different elements, an extraordinary directivity "superdirectivity" can be achieved [10]. This directivity was proven to overcome the Harrington limit.Yet, such arrays suffer from a very narrow bandwidth.

In this context, the major goal of this thesis, is to develop techniques to design ESAs with wideband behaviour and directive patterns. The work is based on the Theory of Characteristic Modes (TCM) and its corresponding theory of the Network Characteristic Modes (NCM) [11, 12, 13]. Due to the profound physical insights provided by the modal analysis, a desired antenna performance can be achieved by properly manipulating the modes through internal reactive loading at specified ports. The aim is to change the impedance of the modes (reduce their Q factor) so that the antenna becomes matched in a wideband without the need of an input matching network. In order to optimize the performance, NCM is combined with the Differential evolution algorithm (DE) to find the optimal reactive load values that can match the antenna in a wideband. The required loads vary as a function of the antenna geometry where in some cases active loads (non-Foster loads) are required to match the antenna in a wideband. On the other hand, to enhance the superdirectivity bandwidth, a closely spaced end-fire array based on the wideband reactively loaded unit element is formed. The excitation coefficients of the radiated characteristic fields are then optimized at multiple frequency points in a wide bandwidth, in order to conclude the optimal excitation that can provide the wideband "superdirectivity" of the array. A feeding network is then integrated on the antenna structure in order to provide the desired excitation.

This dissertation is organized as follows:

Chapter 1 presents an overview on the formulation of the TCM and the NCM, in addition to a state of the art for both theories. The chapter starts with the basic equations that govern the characteristic modes and the physical interpretation of

each expression. Then an example of a dipole antenna is given in order to emphasize on the physical interpretations of the characteristic modes after which another example is designated to distinguish between the TCM and NCM. In chapter 2, we present the methodology we propose to design wideband electrically small antennas using NCM optimization. The process is explained in details, then various examples with different number of internal loads is presented to verify the effectiveness of the method. Moreover, by forcing the modes to resonate at multiple bands, we also study in this chapter the possibility to design multiband antennas. However, in this chapter, it is shown that in some cases, loads with negative impedance values (non Foster loads) are needed to match the antenna in a wideband. The design of a wideband ESA embedded with a non-Foster load is presented in chapter 3. In this chapter, the modeling of the circuit in the presence of the antenna is explained and various parametric studies are carried out to optimize the overall performance. Chapter 4 presents the design of a compact wideband superdirective array taking the antenna designed in chapter 2 as a unit element. The optimization of the excitation coefficients of the characteristic fields at multiple frequency points, helps us deduce the best excitation that can maintain a wideband directivity. A feeding network is then designed to provide the desired excitation. In this chapter, we also investigate the array superdirectivity at very close separation distances in a stacked configuration. In this case we show that a superdirective array of wideband unit element is less sensitive than conventional arrays presented in literature. This array exhibits a high directivity and efficiency at the same time. A further elaboration on the usage of Characteristic Modes Analysis (CMA) is presented in chapter 5, in this part, the CMA is used to systematically design a compact broadband circularly polarized antenna. By analyzing the modes on the defined structure, it is possible to apply the appropriate geometry modifications in order to permit specific modes to be effectively exciting to produce circular polarization. Finally, the work is concluded and a perspective is drawn towards the future progress that could be done.

# Chapter 1

# Theory of Characteristic Modes

In this chapter we present a brief review on the Theory of Characteristic Modes (TCM) and its corresponding theory of characteristic modes for multiport networks (NCM). The basic formulation of these theory is given. Moreover, we present a literature review on the different applications of TCM and NCM in the antenna design. Finally, we present a case study of a dipole to compare between the NCMs and TCM. Although the methodology presented in the next chapters is mainly based on the NCMs, it is important to understand the formulation of TCM and the advantage of using the NCM.

## 1.1 Review of the theory of characteristic modes

The TCM was first introduced by Grabacz in 1965 [14] and was then developed by Grabacz and Turpin [15]. They defined the Characteristic Modes (CM's) as a set of surface currents and corresponding radiated fields which are characteristic of the shape of a conducting obstacle and independant of any specific excitation. Later Harrington and Mautz [11, 12] reformulated the TCM for PEC bodies based on a weighted eigenvalue equation in which explicit formulas were produced to calculate the CM's. The generalized eigenvalue equation for CM's at each angular frequency ($\omega$) is given by [12]:

$$[X]J_n = \lambda_n[R]J_n \tag{1.1}$$

where $R$ and $X$ are symmetric and they represent respectively the real and imaginary part of the impedance matrix:

$$[Z] = [R] + j[X] \tag{1.2}$$

$J_n$ is a real eigenvector which represents the characteristic currents while $\lambda_n$ is a real eigenvalue which directly indicates the total stored field energy. When $\lambda_n = 0$ at a specific frequency the corresponding mode is resonant. However, in the case where $\lambda_n > 0$ the stored magnetic fields dominates over the stored electric fields and the modes are known as inductive. On the other hand, when $\lambda_n < 0$ the associated modes are capacitive. These characteristic modes are orthogonal with respect to each other. The orthogonality property of the modal currents is given by:

$$\langle J_m, R.J_n \rangle = \langle J_m^*, R.J_n \rangle = \delta_{mn} \tag{1.3}$$

$$\langle J_m, X.J_n \rangle = \langle J_m^*, X.J_n \rangle = \delta_{mn} \tag{1.4}$$

$$\langle J_m, Z.J_n \rangle = \langle J_m^*, Z.J_n \rangle = (1 + j\lambda_n)\delta_{mn} \tag{1.5}$$

where:

$$\delta_{mn} = \begin{cases} 1 & m = n \\ 0 & m \neq n \end{cases} \tag{1.6}$$

With these orthogonality property, the overall current on a PEC body can be written as a weighted summation of the modal currents:

$$J = \sum_n a_n J_n \tag{1.7}$$

Each characteristic current $J_n$ radiates a characteristic field $E_n$. Consequently, the total radiated field can also be given as a weighted summation of the characteristic fields:

$$E = \sum_n a_n E_n \tag{1.8}$$

where $a_n$ is the complex modal weighting coefficient which shows the contribution of each mode in the overall radiation and is given by the following equation:

$$a_n = \frac{V_n^i, J_n}{1 + j\lambda_n} \tag{1.9}$$

$V_n^i$ is the modal excitation coefficients which signifies how the $n^{th}$ mode is coupled with the excitation, i.e; if the mode is well excited by the feed network or the incident field. The modal excitation coefficient is given by:

$$V_n^i = \left\langle J_n, E^i \right\rangle = \oint_n J_n.E^i ds \tag{1.10}$$

it should be noted that the eigen currents of equation 1.1 should be normalized to have a unit radiation power such that:

$$\langle R.J, J^* \rangle = 1 \tag{1.11}$$

Hence, if the antenna is fed at specified position(s), its input admittance can be expressed in terms of the admittance of the characteristic modes at angular frequency $\omega$ [16]

$$Y_{in}[input] = \sum_{n=1}^{N} \frac{J_n[input]^2(1 - j\lambda_n)}{(1 + \lambda_n^2)((\tilde{J}_n^*[R]J_n)} = \sum_{n=1}^{N} Y_n \tag{1.12}$$

where $\tilde{J}_n^*$ is the transpose conjugate of the $n^{th}$ characteristic modes.

As it was explained earlier, the analysis of the eigenvalues of the modes provides accurate information about the resonance and radiating properties of each mode. However, some alternative representations can be also used to clarify the properties of these modes. Since the characteristic fields on the surface $S$ of the PEC are real, the tangential component of the charateristic field on the surface S ($E_n^{tan}(S)$ is equiphase. Therefore, $E_n^{tan}(S)$ exhibits a constant phase lag with its associated

real current $J_n$. This lag is denoted by characteristic angle and is expressed as a function of $\lambda_n$ [17]

$$\alpha_n = 180° - tan^{-}1(\lambda_n) \tag{1.13}$$

if the modal current and its corresponding tangential electric field are 180° out of phase, the mode is said to be resonant (good radiator), while if they are in 90° or 270° out of phase the mode is said to be in internal (cavity) resonance. Therefore, the characteristic angle provides information about the radiation capabilities of the modes. If $\alpha_n = 180°$ the mode is resonant, while if $90° < \alpha_n < 180°$ and $180° < \alpha_n < 270°$ the modes are inductive or capactive. Furthermore, an alternative representation of the eigenvalues is given by the Modal Significance (MS) which transforms the $[-\infty, +\infty]$ range of the eigenvalue into [0,1]. The modal significance is independent of any external source.

$$MS = \left| \frac{1}{1 + j\lambda_n} \right| \tag{1.14}$$

The modal weighting coefficient from (1.9) can then be expressed as a function of MS:

$$a_n = (V_n^i, J_n) \times MS e^{j(\psi_n)} \tag{1.15}$$

where $\psi_n$ is the phase of the complex value $\frac{1}{1+j\lambda_n}$.

Hence, a high modal significance is a necessary condition to insure the ability of the mode to be excited and participate in the radiation.

Therefore, the TCM provides physical insights about the behaviour of the modes that are supported by the conducting body regardless of the excitation. Consequently, TCM has become a frequent approach in the analysis and design of various types of antennas especially electrically small antennas for bandwidth enhancement, improved radiation and efficiency, reduced size factor and optimized feeds.

### Characteristic Modes Analysis of Dipole Antenna

In order to demonstrate the physical insights provided by the TCM, a classical example for a dipole antenna is given. Fig.1.1 shows the geometry of the dipole antenna ($12cm \times 0.16cm$) printed on a substrate of $\epsilon_r = 4$ and the MS of the first 5 modes associated with this structure. The 5 modes resonate at various frequency

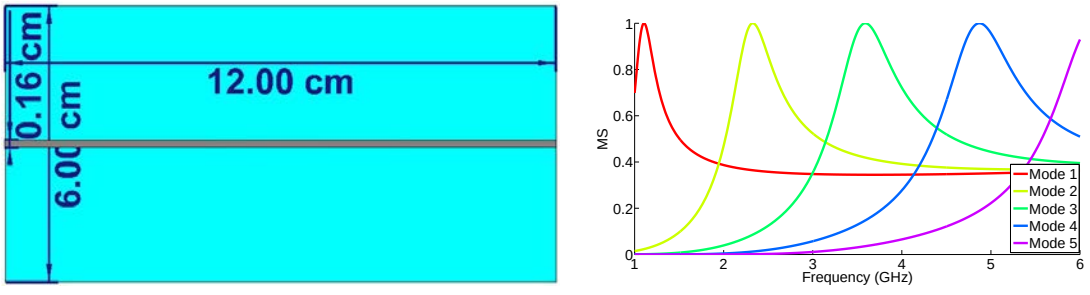


(a) (b)

Figure 1.1: Characteristic modes analysis of the planar dipole. (a) Geometry of the dipole, (b) Modal significance of the first 5 modes.

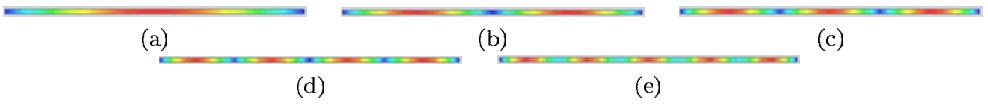


Figure 1.2: Surface current distribution of the first five modes of the dipole at their resonance frequencies. (a) Mode 1, (b) Mode 2, (c) Mode 3, (d) Mode 4, (e) Mode 5.

points in the frequency range between $[1-6GHz]$. The resonance is illustrated by a $MS$ of value 1 which corresponds to an eigenvalue $\lambda_n = 0$. Mode 1 resonates at $1.12GHz$, Mode 2 at $2.3GHz$, Mode 3 at $3.6GHz$, Mode 4 at $4.9GHz$ while Mode 5 approaches resonance at $6GHz$. These are the modes that are naturally supported by the given structure and independent of the excitation. Therefore, in order to excite a specific mode, an important consideration should be taken into account for the feeding position. In this case, to excite a certain mode, the feed should be placed at the point where the latter mode exhibits a high current distribution. Fig.1.2 shows the current distributions of the first 5 modes at their resonance frequency. A feed placed at the middle of the dipole, will couple with the odd modes (Modes 1,3, and 5) since they have a high surface current distribution at this position, while the even modes (Modes 2 and 4) will not be excited since they have a null surface current distribution at the middle position. The Input reflection coefficient of the dipole excited in the middle exhibits three resonances at the resonance frequencies of Modes 1,3, and 5 respectively Fig.1.3a. On the other hand, if two offset excitations are placed at the positions where the even modes exhibit a high surface current distribution, the even modes will be effectively excited while the odd modes will not be excited. This is evident in the input reflection coefficient of the dipole with offset excitations, where it resonance frequencies correspond to those of modes 2 and 4 (Fig.1.3b).

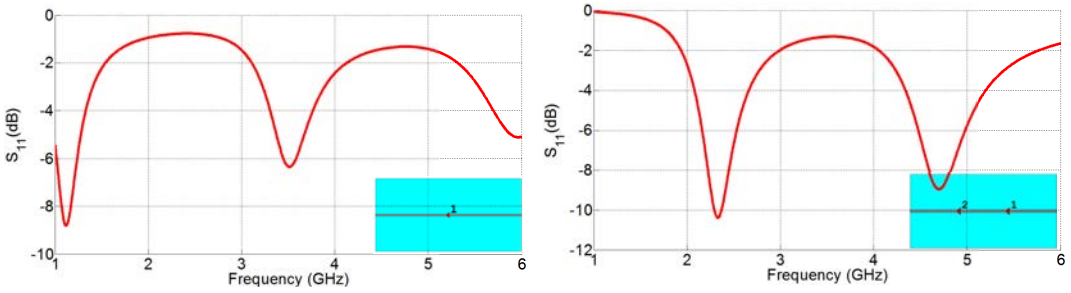


Figure 1.3: Input reflection coefficient of the dipole with different excitation setups. (a) Center excitation, (b) offset excitations.

Therefore, TCM provides physical insights on the modes that are naturally supported by the structure under studies by giving information about the resonance frequencies of these modes, their surface current distributions and their radiation patterns, which offers guidelines to achieve a desired performance by exciting specific modes and suppressing others.

In the next section we present a literature review on the various utilities of TCM in the design of antennas for various applications.

## 1.2 TCM: Literature Review

Since its formulation in the 1970's, TCM have been found to be an effective design approach in antenna engineering. However, the breaking point in the application of TCM in antenna design was'nt reached until it was re-introduced by Fabrés in 2007 [18] after which extensive researches on antenna design using TCM have been investigated [19]-[49]. TCM have been applied in various antenna designs such as pattern synthesis, Electrically small antennas, antennas mounted on platforms (Unmanned Air Vehicles,...), decoupling, circularly polarized antenna and antennas on Artificial Magnetic Conductors (AMCs).

**Radiation Pattern Synthesis** One of the first applications of TCM was found in the control of the radar scattering pattern. The approach was based on reactively loading a conducting body in order to force the resonance of a desired real current $I_d$ ($\lambda_d = 0$) at a specific frequency point [19]. The overall current on the scatterer will then be approximately equal to $I_d$ ($I_{total} \simeq I_d$) and hence the scattered pattern will be the pattern corresponding to $I_d$ ($E_{total} \simeq E_d$). In other words, the desired pattern is synthesized by mapping its corresponding current distribution $I_d$ on the conducting body and then forcing $I_d$ to be a resonant mode by adding reactive loads to the conducting body, such that $\lambda_d$ becomes 0, and hence mode $d$ becomes the dominant mode:

$$[X_a + X_L]I_d = \lambda_d[R_a]I_d \tag{1.16}$$

**Electrically Small Antennas** The most common example found in literature for ESA design using TCM was presented by Adamas *et al.* in [20]. In this publication, the TCM was used to enhance the bandwidth performance of an ESA ($ka = 0.49$) whose geometry is presented in Fig.1.4a. Since the antenna is electrically small, only two significant modes can be found. The current distribution of these modes are given in Fig.1.4b showing that the current of mode 1 is concentrated in the helical wires while that of mode 2 is mainly concentrated in the feed trace (solid arrows represent currents on the helical arms, unfilled arrows represent the currents on the planar feed lines, and solid circles represent current nulls). By tuning the resonances of both modes, it was possible to achieve multiple resonance behaviour in the antenna and combine them in order to achieve a wider bandwidth. The tuned antenna exhibited a $120MHz$ impedance bandwidth which corresponds to 11.4% relative bandwidth (Fig.1.4c).

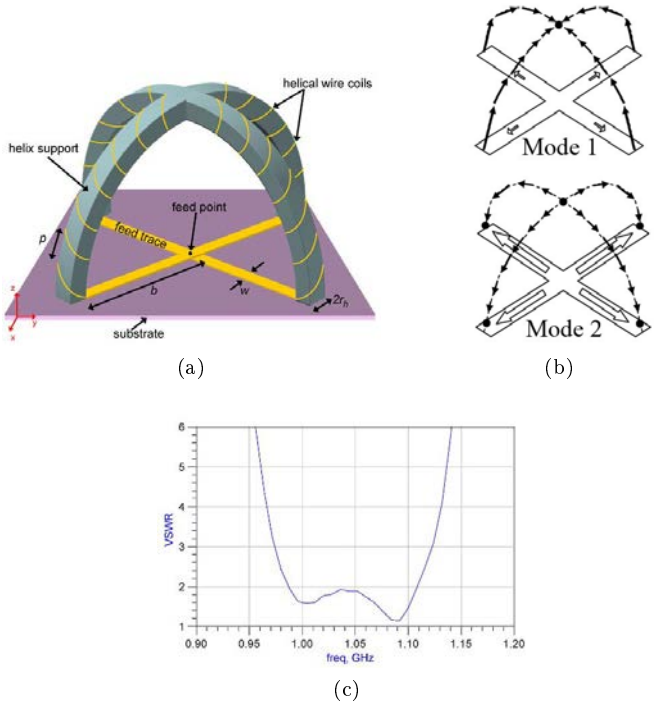


Figure 1.4: Bandwidth enhancement of electrically small $TM_{01}$ antenna. (a) Geometry, (b)current distributions of Mode 1 and Mode 2, (c) VSWR of the multiresonant antenna [20]

**Antennas on Platforms** TCM have found extensive application in the design of electrically small low profile antennas mounted on platforms for HF,VHF and UHF bands. In literature, most of the designs related to this subject are studied using the guidance of TCM[21, 22, 23, 24, 25]. In [23], the CM's of an Unmanned Air Vehicle (UAV) body were used to determine the optimal positions of the antenna and the feed structure to excite the desired modes. By applying modal analysis, it was possible to increase the impedance and the far-field pattern bandwidth in addition to improve the gain. The authors in [21] used the TCM to design a reconfigurable radiation pattern antenna by exciting CM's on an electrically small UAV body which is used as the radiation aperture. The characteristic currents of the UAV and their corresponding radiated fields are given in (Fig. 1.5). Since the total radiated field is the weighted summation of the radiated characteristic field, a desired pattern can be achieved by exciting each mode with its proper modal weighting coefficient $a_n$. By combining the TCM with a multibobjective algorithm, it was possible to identify the required coefficients $a_n$ for each desired excitation. Finally, a feeding network was integrated on the UAV structure in order to provide these desired excitations. The reconfigurable radiation patterns of the UAV is given in Fig1.6. In a recent article [22], the authors use the TCM to design a dual-band platform mounted HF/VHF antenna. Two half-loops are mounted on the platform Fig.1.7. At HF band, the loops act as coupling elements to excite the dominant mode of the platform. At VHF band, these loops are stand-alone radiators operating over an ultra-wide frequency bandwidth.

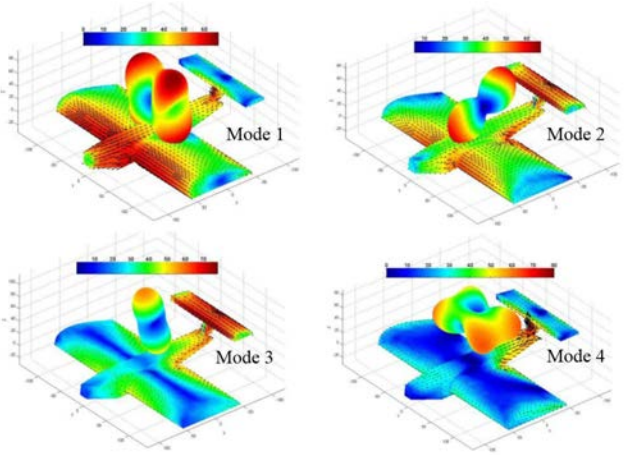


Figure 1.5: Radiation pattern of the first four modes of UAV platform [21]

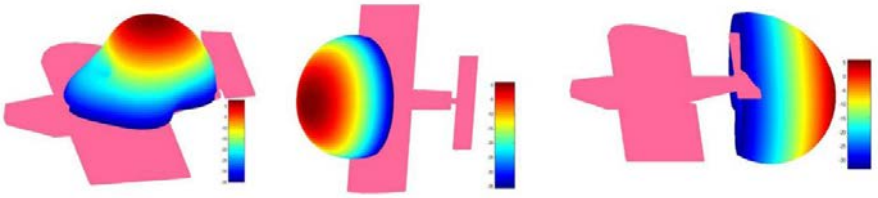

Figure 1.6: Reconfigurable radiation pattern by exciting currents on the UAV [21]

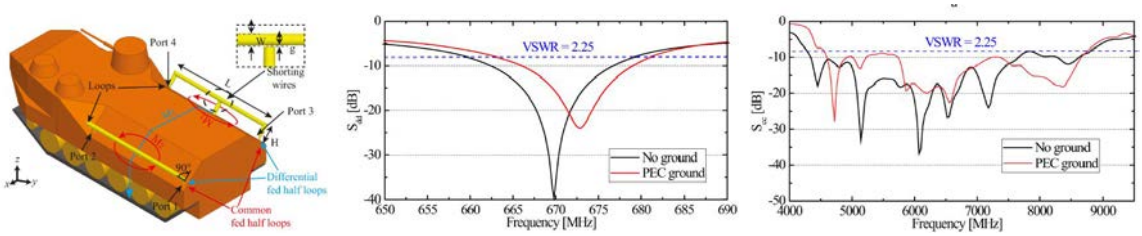


(a) (b) (c)

Figure 1.7: UAV platform with half-loop elements. (a) input reflection coefficient in the lower band, (b) input reflection coefficient in the higher band [22]

**Mobile Antenna Handset Design** TCM analysis has also become a necessary approach in the design of mobile antenna handsets [26]-[38]. In [26], Martens *et al* introduced the concept of selective excitations of the charateristic modes that are supported by a mobile handset chassis using coupling elements. Fig.1.8a shows the current distribution contours of the first three modes on a small rectangular chassis. Mode 1, exhibits a maximum at the center of main edge, while mode 2 exhibits two maxima along the main edge, and mode 3 has a maximum at the secondary edge. In order to excite these modes, coupling elements should be placed on the maxima of each current mode as shown in Fig.1.8b. With these excitation, the three orthogonal characteristic modes which radiate orthogonal characteristic

currents are excited resulting in a relatively perfect de-correlated MIMO system. This proposition, paved the way to the contribution of TCM analysis in the design of MIMO terminals. The orthogonality properties of the CMs presents an ideal candidate to de-correlate the excited ports. At each port, a specific mode is excited, and hence a low cross-correlation is achieved. Further study was developed for massive MIMO antenna systems using the CM approach [33]. Another approach was based on adding a bezel or strip to the chassis. Adding such structures can aid in the manipulation of the chassis modes and allows to independantly excite multiple modes at multiple bands with a low antenna correlation and sufficient bandwidth and efficiency [34, 35, 36, 37].

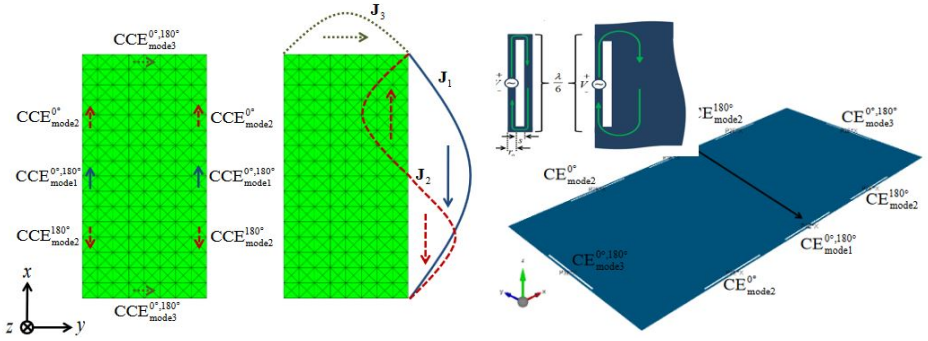


Figure 1.8: Selective excitation of the characteristic modes on a small chassis by coupling elements. (a) Chasis geometry, (b) coupling elements implimentation [26]

**Circularly Polarized Antennas** : The analysis of the CM have also been helpful in determining the optimal position to excite a patch antenna in order to produce circular polarization. In [39], Chen and Wang studied the characteristic modes on a U slot and E shaped patches. By analyzing the modal significances and the characteristic angles, they determined the two modes who present the best candidates to radiate circularly polarized fields. From the CM point of view, the ideal case for circular polarization is that the two modes should have equal modal signifcance ($MS_1 = MS_2 = 0.7$) and a characteristic angle difference of 90° ($\alpha_1 - \alpha_2 = \pm 90°$) (Fig. 1.9a,b ). The patches are fed at the point where both mode exhibit a high current distribution (difference between the modes is minimum)(Fig.1.10) giving rise to an excellent AR performance while however having a narrow $3 - dB$ axial ratio bandwidth of about 3%. Another design approaches for circularly polaized antennas can be found in literature [40, 41].

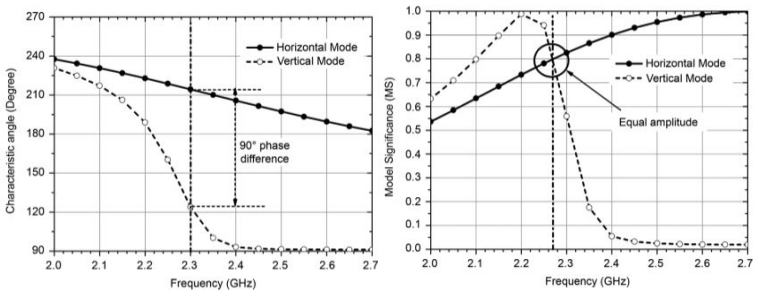


(a) (b)

Figure 1.9: Characteristic modes analysis of a U slot patch antenna. (a) Characteristic angle, (b) modal significance. [39]

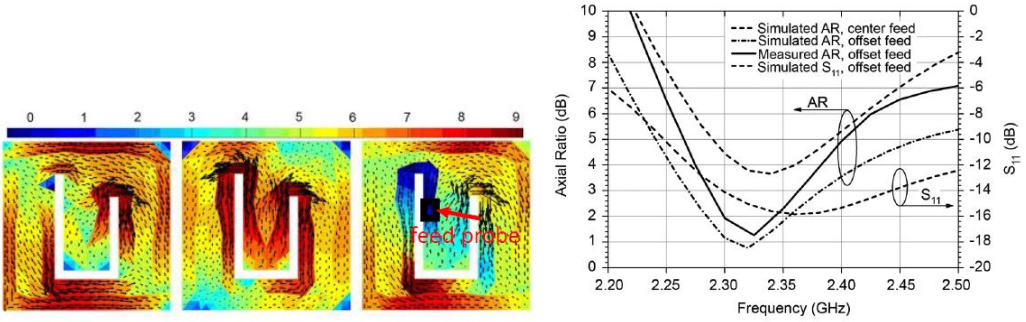


(a) (b)

Figure 1.10: (a) Current distribution of first mode $J_1$, second mode $J_2$ and $J_1 - J_2$, (b) axial ratio of the patch with offset feed compared to center feed [39]

**Computation of the Quality Factor** Computation of the antenna quality factor using characteristic modes have also been studied. In [43], Elghannai proposed the expansion of the total input admittance of the antenna in terms of the individual admittance of each CM. The total quality factor was then calculated based on the summation of the quality factor of each mode. Another approach to compute the Q factor of metamaterial-based electrically small antennas based on characteristic modes was proposed in [44]. Capek *et al.* calculated the radiation Q from eigen energies and powers [45]. This approach allows the study of the effect of radiating shape separately to feeding. The total Q was then calculated as a superposition of the modal Q factor ($Q_n$). He then derived an optimzation procedure to excite the optimal currents on an arbitrarly shaped small radiator that insures a minimal Q. This optimal current is represented as a basis of modal currents [46].

**Other Contributions** Other contributions of the CM analysis can be found in literature. Reduction of out-of-band coupling in antenna array was studied using CM's [42]. The mutual coupling between two antennas is studied and the contribution of each mode in this coupling is evaluated. It was found that higher order modes are the ones that contribute much to the out-of-band coupling. These modes are then suppressed using inductive loading.

Another interest in Characteristic Modes Analysis (CMA) have been found in the domain of metasurface (MTS) antennas which is pioneered by a research group in

Singapore [47, 48, 49]. In [47], the authors presented the design of a low profile MTS antenna with wideband operation. CMA was used in the analysis and optimization of the antenna. The modal behaviour of the MTS was studied to provide guidelines for best excitation positions. Following this work, the authors proposed a technique to eleminate the pattern distortion in MTS [48]. CMA showed that this distortion was caused by higher order modes. Consequently, slots and vias were added at specified positions in the unit cell of the MTS as a way to suppress the higher order modes.

To study radiating structures with multiports , Harrington and Mautz extended the classical TCM to analyze N-port systems. The modes in such systems are called the Network Characteristic Modes (NCMs). In the next section we present the formulation of the NCMs, in addition to a state of the art literature review concerning the contribution of NCMs in antenna designs.

## 1.3 The Network Characteristic Modes

Characteristic modes can also be defined for multiport antenna systems. In this case, the antenna is regarded as an N-port network (Fig. 1.11). However, for an N-port network, the characteristic modes are extracted from the N-port Z-matrix rather than the Z-matrix as in the classical CMs. These extracted modes are called NCMs [13]. In this case the number of extracted modes is the same as the number of ports. This kind of modal analysis, provides simplicity in understanding the modal behaviour as the number of modes becomes limited. In other words, all the existing modes in the antenna, will be combined in $N$ Network characteristic modes in an N-port antenna system. The Generalized Eigenvalue Problem (GEP), modal currents and modal admittances at specific frequency point are given in the equations below :

$$[X_a]\bar{J}_n = \lambda_n [R_a]\bar{J}_n \tag{1.17}$$

$$\bar{J} = \sum_{n=1}^{N} \frac{\tilde{J}_n^* \bar{V}_{oc} \bar{J}_n}{(1+j\lambda_n)(\tilde{J}_n^*[R_a]\bar{J}_n)} = \sum_{n=1}^{N} \alpha_n \bar{J}_n \tag{1.18}$$

$$Y_{in}[input] = \sum_{n=1}^{N} \frac{\bar{J}_n[input]^2(1-j\lambda_n)}{(1+\lambda_n^2)(J_n^*[R_a]\bar{J}_n)} = \sum_{n=1}^{N} Y_n \tag{1.19}$$

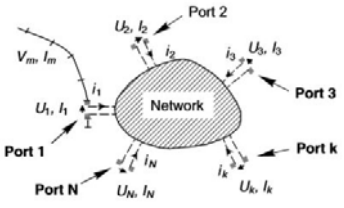


Figure 1.11: N-port network

where $R_a$ and $X_a$ are respectively the real and imaginary parts of the impedance matrix of an N-port antenna. $\bar{J}_n$ is the characteristic current vector at the defined

ports. Therefore, all the equations presented for CM in the previous section are applicable to NCM. From (1.19), an N-port antenna system can be represented in the form of an equivalent circuit as shown in Fig.1.12 which is formed of the set of modal admittances connected in parallel. It should also be noted that the NCMs also hold the orthogonality property just like CMs.

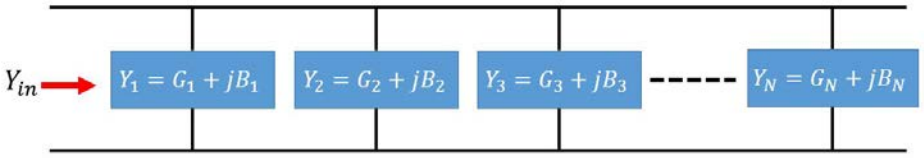


Figure 1.12: Equivalent circuit of N-port antenna in terms of modal admittances

Although NCM didn't gain popularity as much as CM. Some contributions of NCM in antenna design have been stated in literature. In the next section, a literature review on the NCM applications is elaborated.

### 1.3.1 Literature Review

Similar to TCM, NCM have found to be helpful in various antenna designs.

**Radiation Pattern Synthesis:** After Harrington and Muatz introduced the theory of characteristic modes for an N-port scatterer in 1974, Harrington was the first to use this theory in the design of reactively controlled directive arrays[50, 51]. In this work, a seven-element circularly polarized array of reactively loaded dipoles was studied (Fig.1.13). His aim was to determine the current $I_d$ required on the ports for maximum gain in a specific direction and then resonate this current using reactive loads. In other word, with reactive loading, $I_d$ was forced to be a characteristic mode with eigen value $\lambda_d = 0$. The formulation is given in the equations below:

$$[X_a + X_L]I_d = \lambda_d[R_a]I_d \tag{1.20}$$

for $\lambda_d = 0$ (1.3.1) becomes:

$$[X_a + X_L]I_d = 0 \implies X_{Li} = \frac{-1}{I_i}([X_a]I_d)_i \tag{1.21}$$

where $i = 1, 2, \ldots N$.

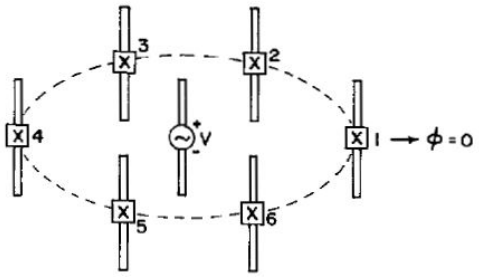


Figure 1.13: A seven-element circular array of reactively loaded dipoles [50]

Using the same array, Chen and Wang combined the NCM with a (Differential Evolution) DE algorithm in order to maximize the array gain in a specific direction[52]. The DE was used to optimize the modal expansion coefficients $a_n$ of the radiated characteristic fields. The optimized expansion coefficients are then used to calculate the total current from (1.18).

$$Z_{Li} = \frac{(-[Z_A][I_{port}])_i}{[I_{port}]i}, i = 1, 2, \cdots, N \tag{1.22}$$

Finally the reactive loads is determined from (1.22). A steerable pattern with maximal directivity was obtained by changing the values of the reactive loads (Fig.1.14). Following the same principle, they used the NCM theory to optimize the radiation pattern of a Yagi-Uda antenna by reactively loading the parasitic elements to maximize the gain and to reduce the Side Lobe Level (SLL)[53].

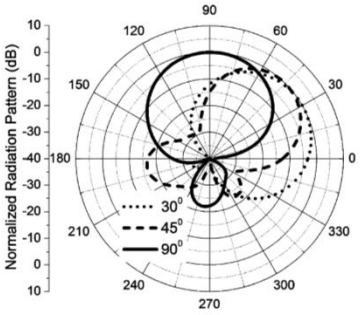


Figure 1.14: Normalized radiation pattern of reactively loaded antenna for different maximal radiation angle [52]

**MIMO Systems:** Ethier and McNamara proposed an interesting NCM approach to design a de-correlated 3-antenna MIMO system on a small mobile terminal [54](Fig.1.15). The NCM eigenvectors of the three port network are calculated. Taking advantage of the orthogonality property of the eigen modes, a decoupling network is connected to the MIMO radiating elements (Fig.1.15b). The decoupling network provides the proper excitation to generate the network characteristic modes at the radiating elements. In other words, each signal at each MIMO antenna port, excites a separated NCM resulting in a low correlation at the desired frequency (Fig.1.15c).

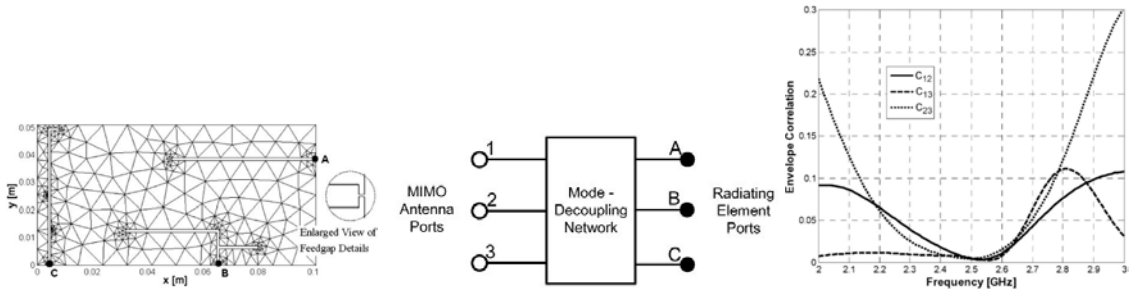


(a) (b) (c)

Figure 1.15: Mode decoupled MIMO antenna system. (a) Antenna geometry, (b) mode decoupling network, (c) correlation coefficient of the antennas. [54]

**Tightly Coupled Antenna Array:** A novel technique to calculate an optimized aperture excitation for a finite size tightly coupled antenna array using the NCM was introduced in [55]. An 8×8 array of overlapping dipoles was studied (Fig.1.16)a. By examining the modal significance (denoted by $\alpha$) of the modes in the proposed structure, it was noticed that mode 1 exhibits the widest bandwidth considering ($\alpha$ = 0.6) (Fig.1.16)b. Hence the eigen current vector $I_1$ of this mode presents a good choice in guiding the aperture excitation. Based on this selected current, the active impedance of the array elements is calculated as follows:

$$[Z_{active}]_i = \frac{([R_A][I_1]_i)}{[I_1]_i}, i = 1, \cdots, 64. \tag{1.23}$$

Then a feeding network is designed to feed the array elements with feeding lines having impedances identical to the calculated active impedance. In other words, the feeding network is used to excite the first mode in the given array. With this configuration, the array exhibited a high aperture efficiency, an improved realized gain and a reasonable matching of all the array elements (Fig.1.16c).

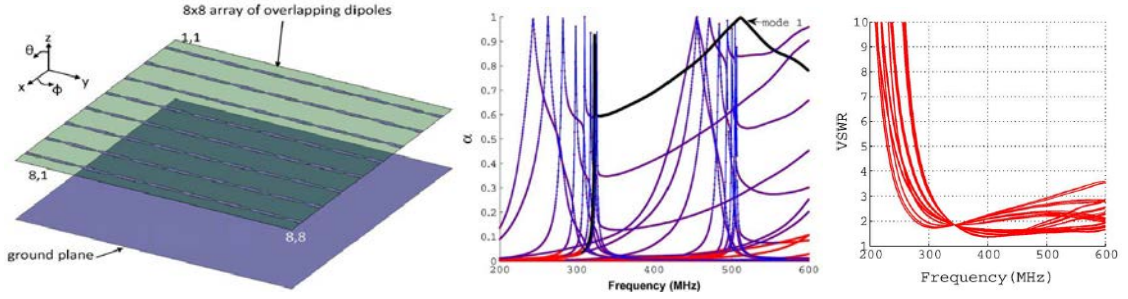


(a) (b) (c)

Figure 1.16: Tightly coupled dipole array. (a) Geometry, (b) modal significance, (c) VSWR of the array elements [55]

**Electrically Small Antennas:** In addition to the contribution of the NCM in the design of antenna arrays and MIMO structures, this theory have found application in the design of small antennas. In [56], the authors used the NCM to investigate the effect of the antenna impedance loading on the characteristic modes. This study showed that the behaviour of the modes can be modified by impedance loading at

specific positions in the antenna. Depending on the type of the loading (inductive or capacitive), it is possible to shift the resonance frequency of a desired mode upwards or downwards.

An example of a dipole reactively loaded at its center was considered, showing that with an inductive loading it is possible to shift down the resonance frequency of the first mode while with capacitive loading it is possible to shift up this resonance frequency (Fig.1.17a) . In this context a modified reactively loaded dipole is considered where a capacitive load at its center shifts the resonance frequency of mode 1 upwards, while inductive loads at the modified nearby edges shifts the resonance frequency of mode 2 downwards (Fig.1.17b).

With this loading configuration, the resonances of both modes are combined in order to increase the operating bandwidth of the dipole (Fig.1.17c). Here, it should be noted that the loads were placed in positions where the modes exhibit a high surface current distribution (Fig.1.17d). At these position, maximal manipulation of the desired modes can be achieved.

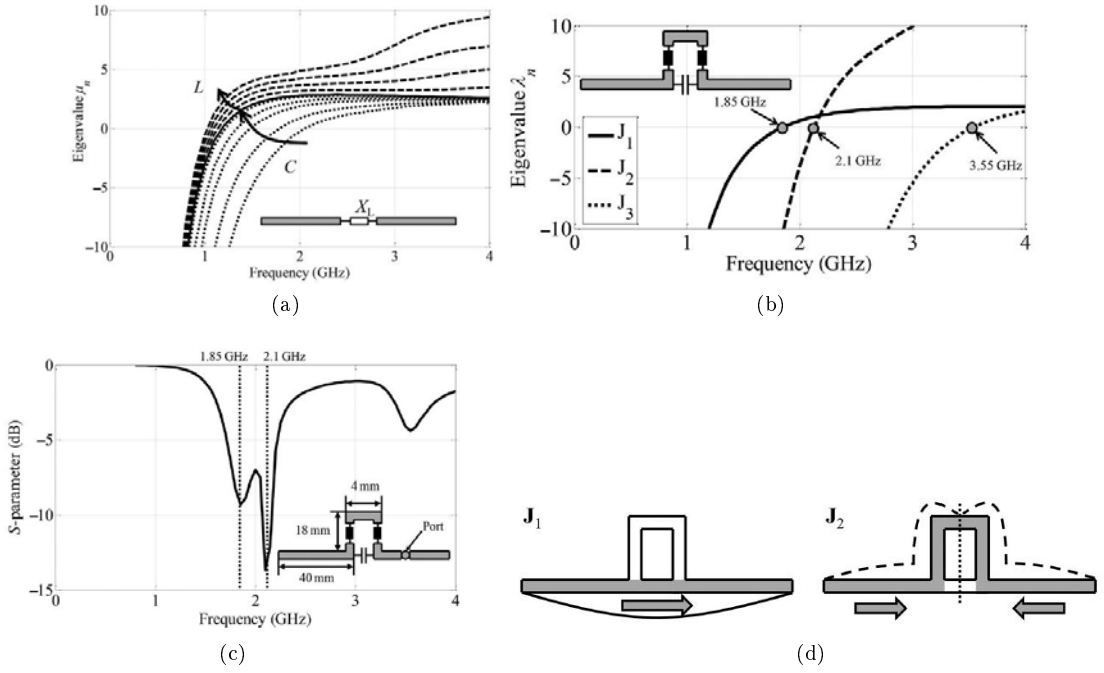


Figure 1.17: Mode manipulation using reactive loading. (a) Eigenvalue behaviour $\mu_1$ of the mode 1 under the influence of inductive and capacitive loading , (b) mode manipulation of the first two modes using inductive and capacitive loading, (c) input reflection coefficient of the modified dipole with the combined resonances, (d) Surface current distribution of the first two modes.[56]

In this context, Obeidat *et al.* examined the effect of internal reactive loading on the resonance of a given antenna [57]. In analogy with the approach used by Harrington for reactively loaded arrays [50], the NCM was utilized to compute the reactive load values required to resonate a desired current $I_d$ in a wideband. At each frequency point in the desired bandwidth, the load reactance at each port is calculated from (1.3.1), and then loads are synthesized to satisfy the frequency behaviour of the computed reactance as a function of frequency. To demonstrate this approach, a $1.2m$ dipole with 5 ports was considered (Fig.1.18a).

With a desired current vector $I_d$ = [0.66 0.98 1 0.98 0.66] the caclulated reactance of the loads at each port is given in Fig.1.18b. The negative slope of the reactance as a function of frequency indicated that in order to have a wideband resonance of the desired current $I_d$, the ports need to be loaded by non-Foster circuits (Fig.1.18c). A wideband resonant mode insures a low antenna Q factor. However, in order to match this mode, a matching network was connected at the input port of the dipole (Fig.1.18c). Furthermore, since the internal loads impose a control on the current inside the antenna where $I_d$ is dominant in the whole bandwidth, the loaded dipole maintained a stable raduiation pattern as a function of frequency. A similar approach was used to design a frequency reconfigurable antenna [58].

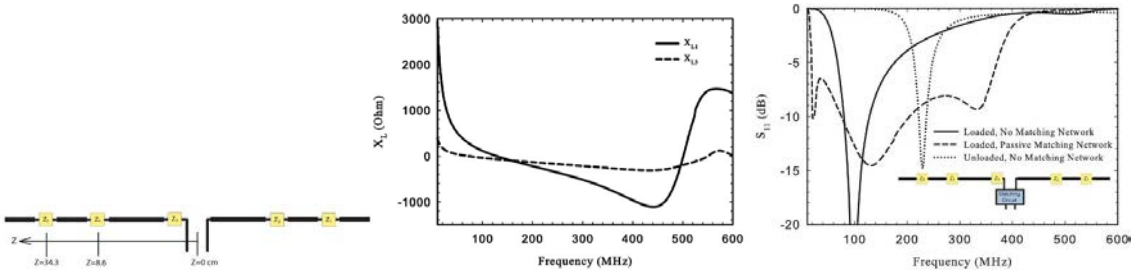


(a) (b) (c)

Figure 1.18: Five port dipole antenna. (a) Geometry, (b) Reactance of the desired loads as a function of frequency, (c) input reflection coefficient of the loaded and unloaded antenna [57]

Nevertheless, in order to eleminate the need for a matching circuit at the input port, the authors in [59] followed the work of Obeidat, by developing a technique to determine the set of loads distributed along the antenna structure that can resonate and simultaneously match a desired characteristic mode in a wideband without the need of an external matching network. This was simply achieved by calculating the value of the desired resonant current at the input port $I_d[input]$ such that its input admittance $Y_d[input]$ is ideally matched to the source ($Y_d[input] = \frac{1}{R_0}$). For this condition $I_d[input]$ can be calculated from (1.19):

$$Y_d[input] = \frac{\bar{I}_d[input]^2}{(I_d^*[R_a]\bar{I}_d)} = \frac{1}{R_0} \tag{1.24}$$

It should be noted that since the mode is considered as a resonant mode, then $\lambda_d = 0$. The other values of the current vector are then manually set depending on the desired radiation pattern and the reactances of the loads are finally calculated following the approach of obeidat. This techinque was also applied on a $1.2m$ dipole antennas with three ports (Fig.1.19a). The current at the input port was computed and plotted as shown in Fig.1.19b. The reactance load values were then synthesized resulting in a wideband small antenna . However, similar to the results given by obeidat, the resulting loads were a complex topology of non-Foster elements (Fig.1.19c). This technique was then applied in the design of a multiband USB antenna and RFID tag antenna [60].

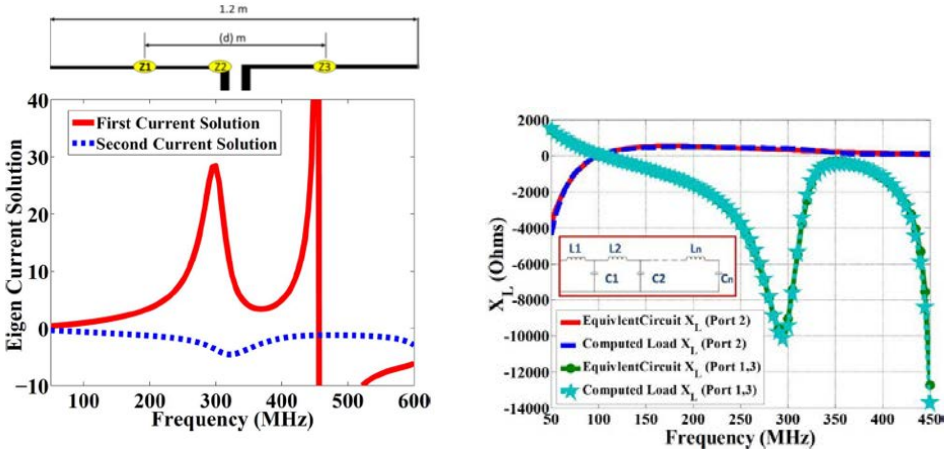


(a) (b)

Figure 1.19: Wideband dipole with distributed matching network. (a) Geometry, (b) computed desired current at the input port, (c) computed reactance loads and their corresponding equivalent circuits at the antenna ports. [59]

NCM analysis has not been yet widely used in antenna design as much as CM. However, it is found that this theory might also be interesting in the future design of antennas as it provides the possibility to perfectly control the currents on the antennas through loading or multiple excitations. To highlight the difference between the CMs and the NCMs, the next section presents an example to examine the modal behaviour of a dipole for classical characteristic modes as well as network characteristic modes by introducing ports inside the antenna structure.

### 1.3.2 Distinguishing between CMs and NCMs

Initially the Network Characteristic Modes theory was developed for N-port loaded scatterer. The aim was to find the set of reactive loads required to resonate any given real current and make it a dominant mode of the loaded scatterer. However, the NCM is analogous with its original theory the CMs as both modes are extracted from the generalized eigenvalue problem. However, the original TCMs represent the numerical calculation of the set of infinite orthogonal currents that are supported by a conducting body. On the other hand, the NCMs are the numerical calculations of the finite orthogonal currents that are supported by conducting body. The number of the modes given by NCM are directly related to the number of ports defined in the structure as it is extracted from the muliport Z-matrix, contrary to CMs which are extracted from the overall Z-matrix. It should be noted that the overall Z-matrix for CMs is the MOM impedance matrix where the number of extracted modes is infinite. While for NCM the number of modes are limiter to the number of ports since The NCM is mainly used with multiport antenna to calculate the reactive loads that must be connected to these ports in order to achieve a desired performance (Fig.1.20), or to excite specific eigen current vectors along the defined ports. This was already shown in the previous section with the different antenna designs based on NCM. Therefore, in a multiport antenna, it is more convenient to use the NCMs as all the CMs are coupled into a finite number of NCMs which provides a clearer understanding of the structure and how to manipulate the modes (through reactive loading) or excite specific modes and suppress others.

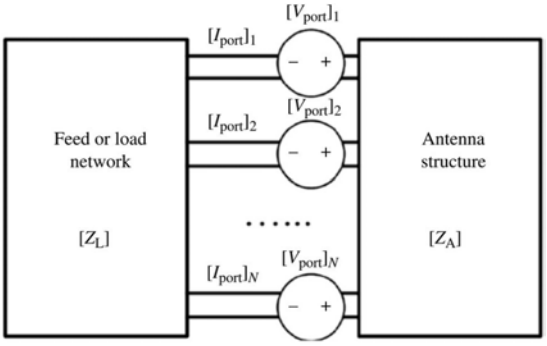


Figure 1.20: Thevenin equivalent of an N-port loaded antenna.

Basically, NCM is just another way to represent the characteristic modes supported by a conducting body. To show how the NCMs change we consider the dipole of dimensions $12cm \times 0.16cm$ presented in Section 1.1.1. The modal significance of the first five modes of the dipole are shown in Fig.1.22a. Mode 1 resonates at $1.12GHz$, Mode 2 at $2.3GHz$, Mode 3 at $3.6GHz$, Mode 4 at $4.9GHz$ while Mode 5 approaches resonance at $6GHz$. The surface current distribution of the modes at their resonance frequencies was already given in Fig.1.2. Modes 1,3 and 5 exhibit maximum current at the center while modes 2 and 4 have a null current at this position.

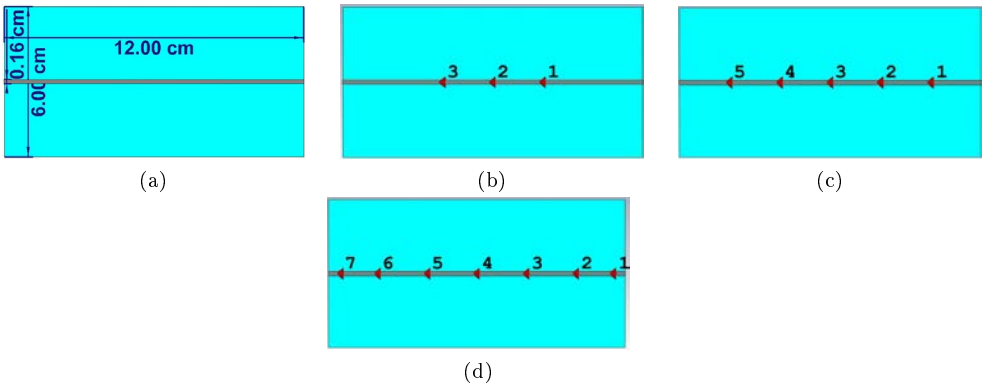


Figure 1.21: Geometry of the planar dipole. (a) Original dipole for CM analysis, (b) 3-port dipole, (c) 5-port dipole, (d) 7-port dipole.

To compare the CMs with NCMs we consider 3 cases for the N-port dipole. First case, three ports are defined in the antenna. Port 2 is at the center while ports 1 and 3 are symmetric and separated 2 cm from port 2 (Fig.1.21). The NCM analysis of the 3-port antenna is given in Fig.1.22b in terms of the Modal Significances. Due to the presence of just three modes which are extracted from the 3-port Z-matrix, the modes existing in the original dipole are coupled into 3 modes. Mode 3 of the original dipole is now a combination of Modes 1 and 2 of the 3-port dipole. Similarly, Mode 5 of the original dipole is now a combination of all three modes in the 3-port dipole, while the resonance of the $4^{rth}$ mode in the original dipole is represented by a third resonance of Mode 2 in the 3-port dipole. Just like the CMs Modes 1 and 3 of the 3-port antennas exhibit maximal currents at the center (port 2) while Mode 2 has a null at this port (Fig.1.23a).

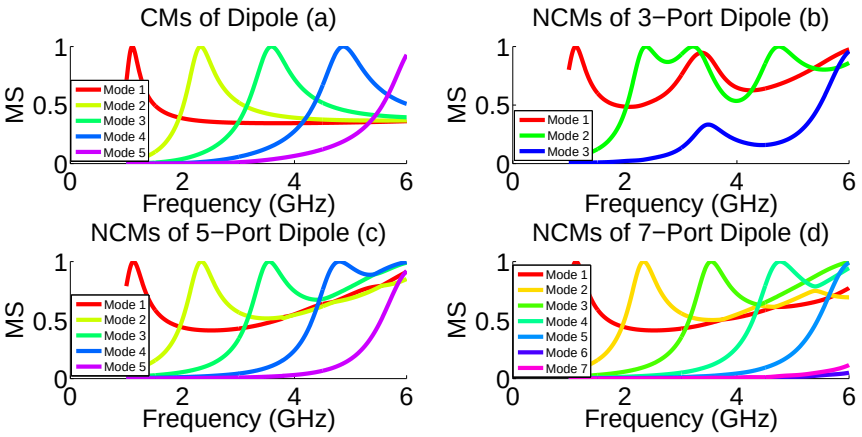


Figure 1.22: CMs and NCMs of the dipole for different number of ports

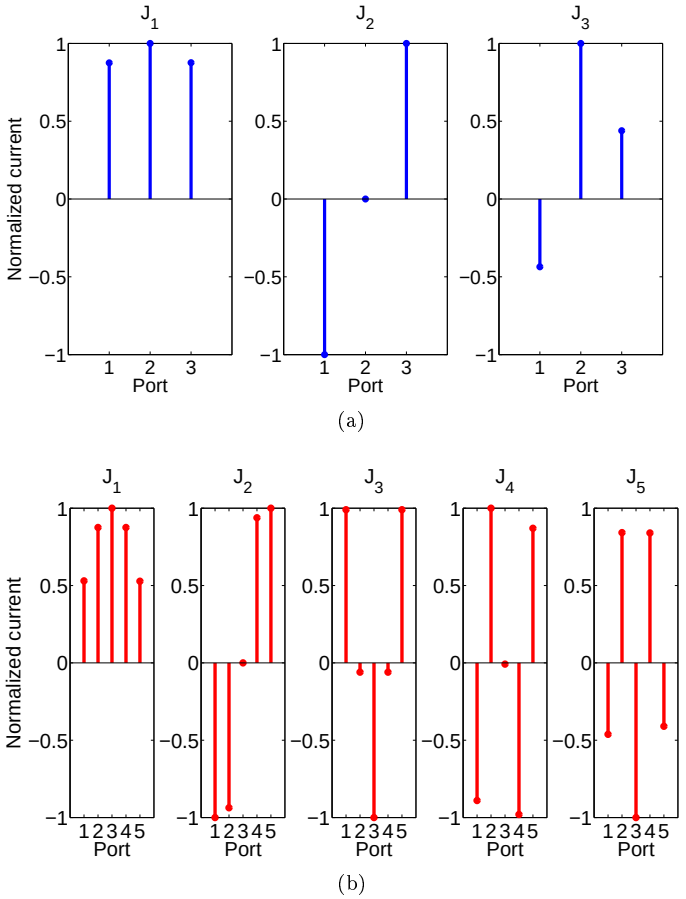


Figure 1.23: Normalized eigen currents on the multiport dipoles. (a) 3 ports, (b) 5 ports.

Similar study have been done for a 5-port dipole (Fig.1.21c). In this case the modes exhibit almost the same behaviour as the original antenna, except for the $5^{th}$ mode where all the 5 modes are combined together (Fig.1.22c). The port currents of the modes for this case are given in Fig.1.23b. The modes are in analogy with the original case in which modes 1,3, and 5 exhibit maxima at the center while mode 2

and 4 exhibit minima at this position. The last study was done on a 7-port dipole. The behaviour of the modes is similar to a 5 port dipole where they are all coupled as the frequency approaches 6 $GHz$ (Fig.1.22c).

In a multiport structure, the infinite CMs could be represented by a finite number of NCMs. As the number of ports in the multiport antenna increases, the NCMs will decouple to their original CMs offering a higher degree of freedom in changing the behaviour of the antenna and alter its electromagnetic characteristics. This property can be used to study the possibility to manipulate the impedance characteristics of the modes through reactive loading in order to match the antenna in a desired frequency band.

## 1.4 Conclusion

In this chapter the theory of the characteristic modes and its associated network characteristic modes were introduced. The CMs which are extracted from the impedance matrix using a generalized eigenvalue problem provide deep physical insights on behind the orthogonal currents that are supported by a given structure and their resonance behaviour. A literature review on the application of TCM in the domain of antenna design was then presented, showing that TCM have become a very useful approach in many design problems. However, in the analysis of multiport structures, the NCMs are mainly used. The NCMs have found application in multiport antennas such as maximizing the gain in antenna arrays or designing wideband electrically small antennas using distributed reactive loads. Finally, a comparison between the TCMs and NCMs was given to examine how the CMs are coupled into NCMs showing that as the number of ports increase, the NCMs will be decoupled and this might offer the possibility to have better control on the structure currents to achieve a desired performance.

The next chapter presents a new approach to maximize the bandwidth of small antennas using the NCMs. By defining ports inside the antenna, it is possible to control its currents by properly loading its ports. With reactive loads, the admittances of the NCMs can be optimized in order to achieve a desired bandwidth. Various examples are presented showing that with increased number of ports a better performance can be achieved.

# Chapter 2

# Optimized Manipulation of the Network Characteristic Modes for Wideband and Multiband Small Antennas

## 2.1 Introduction

Multiport antenna systems can be regarded as N-port networks, which can be analyzed using the theory of Network Characteristic Modes (NCMs). Due to the profound physical insights provided by NCMs, a desired antenna performance can be achieved by properly manipulating the modes through reactive loading at specified ports. This chapter presents a new matching technique for N-port internally loaded small antenna. By combining the NCM with the Differential Evolution (DE) algorithm, optimal reactive load values can be calculated. These loads can manipulate the NCMs to match the antenna in a desired bandwidth. Unlike other matching techniques based on NCM, the desired bandwidth is achieved through internal reactive loading without the need for an input matching network.

This chapter is organized as follows: first a state of the art on various design approaches of electrically small antennas is presented, then the aspect of modal manipulation through reactive loading is illustrated with an example in order to later introduce and explain the design methodology. Several examples are then presented to verify the approach, and finally some measurement results are presented.

## 2.2 State of the Art

Electrically small antennas are limited in bandwidth as demonstrated by Chu and Wheeler [1, 2]. Wheeler stated that the $Q$ factor of an antenna can be decreases by utilizing the maximal volume of a sphere whose diameter is equal to the dimensions of the antenna [2]. Since then, extensive studies were conducted to miniaturize and enhance the performance of small antennas, by designing complex three dimensional spherical structures [61, 62]. In [62], the quality factor of a resonant electrically small elctric dipole is minimized by folding the antenna in order to utilize the occupied spherical volume as much as possible (Fig.2.1). However, the massive development in the wireless technology limited the volume of the antenna and forced the use of

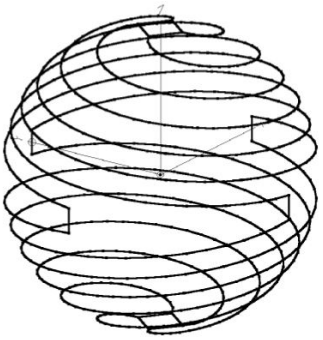

Figure 2.1: Electrically small 4-arm folded spherical helix dipole [62]

low profile planar structures. In this context, input matching networks were adopted to match the antenna in a specified bandwidth. Nevertheless, these networks are passive and are limited by the gain and bandwidth theory of Bode-Fano [63], [64]. The Bode-Fano criterion provides theoretical limits on the maximum bandwidth that can be achieved for a specified matching level, when a loss-less matching network is connected to a load of a given quality factor $Q$. The Bode-Fano limit is given by:

$$BW \leq \frac{\pi}{Q \times ln(\frac{1}{\Gamma_m})} \tag{2.1}$$

where $BW = \frac{\Delta f}{f_0}$ is the fractional bandwidth, $\Gamma_m$ is the maximal reflection coefficient in the matched band.

To overcome such limitation, active matching networks based on non-Foster circuits were connected to the antenna's feed [65, 66]. In this case, even if the reactive part of the antenna's input impedance is compensated, the frequency variation of the input resistance limits the operational bandwidth [67]. A detailed review on the non-Foster matched antenna will be presented in the next chapter.

A powerful technique for antenna miniaturization is adding a near field parasitic resonant parasitic. In literature this kind of antennas is called metamaterial inspired antennas [68, 69, 70, 71]. A conjugate reactive inclusion is placed in the highly reactive near field of the antenna which creates a narrowband resonance at lower frequencies (Fig.2.2).

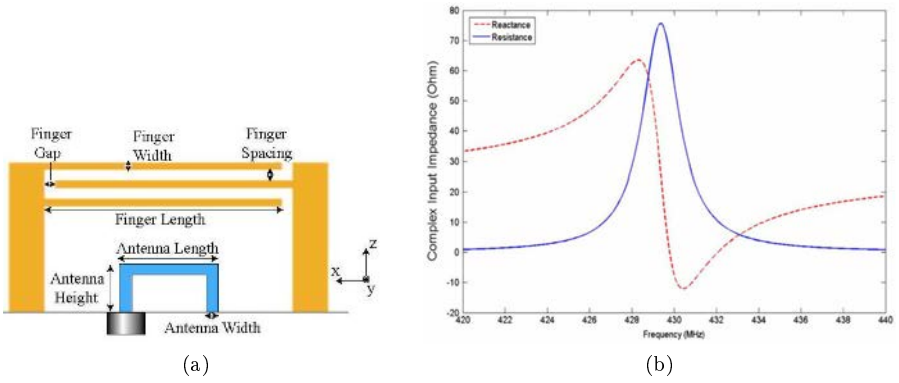


(a) (b)

Figure 2.2: (a)Geormetry of the metamaterial inspired antenna, (b) complex impedance values.[68]

Consequently, a non-Foster load value is calculated and embedded inside the antenna in order to match it in a wider bandwidth [72, 73]. Despite the broadband achieved, this technique is limited to one internal load. To address this issue, a new approach to match an ESA in a wideband using multiple distributed internal loads was proposed in [74]. In this study, the authors proposed a model to calculate the inductive loads required to match a printed dipole in a wideband to cover the UHF band. However, this technique is powerfull for up to two internal loads, after which the calculations becomes complicated. Similar approach was used in [75] to design wideband electrically small USB antenna for UMTS and WLAN applications. The antenna is internally loaded with meander line inductor in order to combine multiple resonance to produce a wideband behaviour (Fig.2.3).

Apart from antenna loading and matching network, it is worth mentioning the matching approach presented by Kabiri in [76]. In this study, the authors investigate wideband electrically small antenna matching using current injection. This technique is composed of defining two ports inside the antenna, in which a current is injected in the secondary port in order to match the primary port to the source. The secondary port is injected with a current having specified amplitude and phase relative to the primary port. The approach was applied on a patch antenna which achieved a relative bandwidth higher than 100% (Fig.2.4).

In this chapter, we present a fast and efficient distributed wideband matching technique based on the theory of the Network Characteristic Mode combined with the Differential Evolution algorithm (DE) [77]. By embedding loads inside any given antenna structure, a better control on its current distribution can be achieved. This control offers more flexibility in manipulating the radiating modes to match the in-

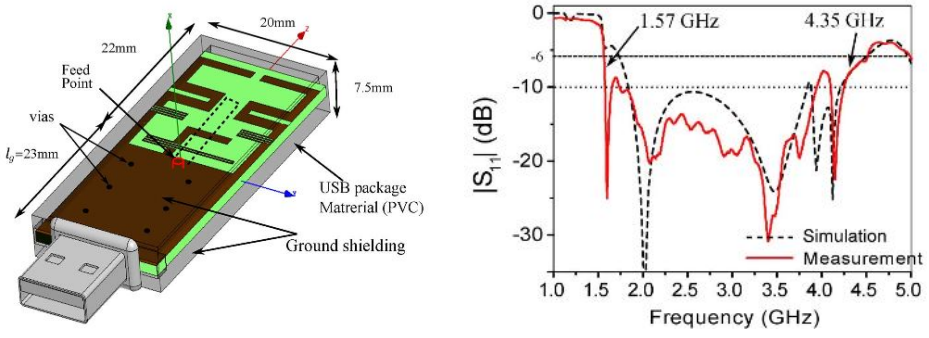


(a) (b)

Figure 2.3: (a)USB antenna model, (b) simulated and measured input reflection coefficients of the antenna.[75]

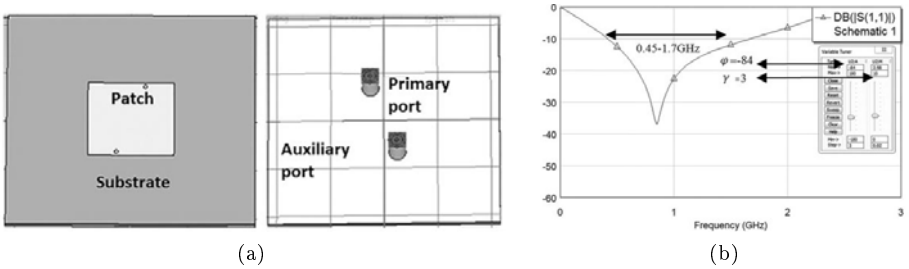


(a) (b)

Figure 2.4: Injection matched patch antenna. (a) Geometry and feed configuration, (b) input reflection coefficient.

put impedance of the antenna to the source over a wide bandwidth. The physical insights given by the NCM analysis, provides guidelines for choosing the simplest loading topology possible to match the antenna in a desired bandwidth. Nevertheless, to obtain optimized results, the DE optimization algorithm is combined with NCM. This combination yields the best load values at specified ports that fulfill the desired antenna performance. It is worth mentioning that the idea of wideband loaded antenna have been originally applied to design Ultra Wideband Antennas (UWB) using the popular Wu-King theory in which resistive loading are used to control and maintain a traveling wave current distribution on the antenna [78]. Although this technique has been proven effective in UWB antennas [78, 79, 80, 81], its application becomes limited when the antenna size becomes smaller as the resistive effects become more important and the efficiency degrades rapidly.

The NCM have been considerably applied in the analysis of multiport antenna systems and arrays as discussed in chapter 1. Matching techniques based on the NCM have been presented in [57], and [59]. In [57], Obeidat proposed matching scheme by loading the antennas with complex non-Foster topologies at specified positions. This loading forces a predefined current distribution to be a resonant characteristic mode over a desired bandwidth, which significantly reduces the quality factor of the antenna, making it more suitable for wideband matching. A passive matching network is added to match the antenna in this bandwidth. Following the work in [57], the authors in [59] determined the set of loads distributed along the antenna structure that can directly match the input impedance of the antenna to the source over a wide bandwidth. Although it was possible with this methodology to eliminate the need for the passive input matching network, yet active (non-Foster) matching was still needed at the input. In addition, the loads were calculated to achieve perfect matching (i.e. pure $50Ohm$ resistance ), which results in a complex loading topology, making it impractical to realize such wideband antennas.

In this proposed scheme, we totally eliminate the need for passive or active loads at the input port. Wideband antenna matching is achieved exclusively using the internal loads. By analyzing the behaviour of the modes, the loading topology is chosen to be as simple as possible. Based on this topology, the algorithm will optimize the input admittance of the modes such that the antenna becomes matched to the source in a predefined bandwidth. Although the combination of NCM and DE have been used in [52, 53] for controlling the array radiation pattern at a single frequency point (which was mentioned and explained in chapter 1). Applying optimization with NCM to internally match a small antenna in a wide bandwidth is believed to be novel.

To explain our design methodology, the chapter is organized as follows. In the first section we present the numerical expression of the mode manipulation through reactive loading in addition to a brief review on DE and its integration with NCMs. Next, the design methodology is explained and examples are provided to verify the method. Two examples of a monopole antenna integrated on a PCB are presented, we demonstrate that internal distributed wideband matching is possible using active non-Foster loads as well as passive loads. In addition, NCM analysis is carried out to explain the effect of loading on the interaction between the radiating modes, that resulted in a wideband matching. Prototype and measurements are then shown to verify the simulation results. Multiband behaviour of the antenna is then examined. Adding loads at specific positions in the antenna imposes the resonance of the set

of modes in the desired bands leading to multiband behaviour.

## 2.3 NCM Manipulation by Reactive Loading

When an N-port antenna is loaded by reactive loads (1) becomes:

$$[X_a(\omega) + X_L(\omega)]\bar{I}_n(\omega) = \mu_n(\omega)[R_a(\omega)]\bar{I}_n(\omega) \tag{2.2}$$

Consequently, (1.19) becomes:

$$Y'_{in}(\omega)[input] = \sum_{n=1}^{N} \frac{\bar{I}_n[input]^2(1 - j\mu_n(\omega))}{(1 + \mu_n^2(\omega))((\tilde{I}_n^*(\omega)[R_a(\omega)]\bar{I}_n(\omega))} = \sum_{n=1}^{N} Y'_n(\omega) \tag{2.3}$$

Where $X_L(\omega)$ is the N×N diagonal reactance matrix of the loading network. $I_n(\omega)$ and $\mu_n(\omega)$ are respectively the $n^{th}$ characteristic current and its corresponding eigenvalue of the reactively manipulated mode at the angular frequency $\omega$, and $Y'_{in}[input]$ is the input admittance of the loaded antenna which is a summation of the manipulated modal admittances $Y'_n$.

Hence manipulation of the characteristic modes is possible through multiport reactive loading. With the correct loading topologies and values, it is possible to control the overall current distribution on the antenna. Consequently the input admittance can be controlled, in order to achieve a desired antenna bandwidth.

An example of loading the 5-port dipole is given to demonstrate the effect of reactive loading on the NCMs. The geometry of the 5-port dipole is re-shown in Fig.2.5a. Port 3 is placed at the center and the other 4 ports are placed symmetrically to the center with $2cm$ separation distance. The effect of the reactive loading on the first three modes is depicted in the MS of the modes given in Fig.2.5b. For all loading cases, Mode 1 is represented by a solid line, Mode 2 by a dashed line and Mode 3 by a dotted line. For simplicity, in this study all ports are loaded with the same value of reactive loads. The modal manipulation is studied for both

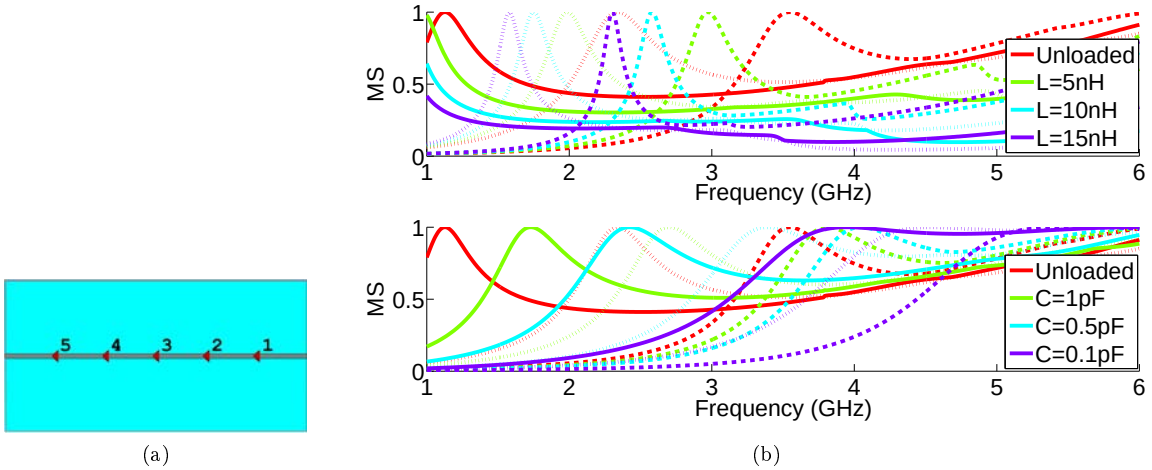


(a) (b)

Figure 2.5: (a) Geometry of the 5-port dipole, (b) Variation of the modal significance of the first three modes as a function of inductive and capacitive loading. Mode 1 is represented by the solid lines, Mode 2 is represented by the dashed lines and Mode 3 is represented by the dotted lines.

inductive and capacitive loading. In the case of inductive loading, the resonance frequency of the modes is shifted to lower values. Moreover, as the value of the inductance increases, the shift in the frequency increases and is associated with a decrease in the bandwidth of the modes. On the other hand, the capacitive loads increase the resonance frequency of the modes. Contrary to inductive loads, as the value of the capacitance decreases, the resonance of the modes shifts higher and their bandwidths increase. These results are predictable as the inductance increases the effective length of the dipole while the capacitance shrinks it.

With this example, it was demonstrated that reactive loading can significantly change the resonance behaviour of the modes. Therefore, with the proper loading, it is possible to manipulate the resonances and impedances of the modes in order to match an antenna in a desired bandwidth. Consequently, this poses the question: *What is the best and most simple reactive load value /topology that is sufficient to match an antenna in a desired band?.*

To answer this question, the insights given by NCM are combined with an optimization algorithm as an effective way to optimally manipulate the modes in the antenna in order to achieve a desired behaviour. In the next section, we present a novel matching technique based on the combination of the NCM with the DE optimization algorithm. The concept of the DE is explained along with its integration with the modal equations to finally form the required scheme.

## 2.4 Design Methodology

### 2.4.1 Differential Evolution Algorithm (DE)

Differential Evolution (DE) is a stochastic population based optimization algorithm which was first introduced by Storn and Price [77]. Due to its simplicity and performance, DE have been recently introduced to solve electromagnetic problems [21, 25, 82, 83]. Similar to Genetic Algorithm, DE is an evolutionary algorithm which is used to optimize an objective function with multiple parameters. Suppose that we want to optimize a function with N parameters. Then each parameter vector of the population can be represented as:

$$X_{i,G} = \left[x_{1,i,G}, x_{2,i,G}, \cdots, x_{N,i,G}\right], i = 1, 2, \cdots, N_{pop} \tag{2.4}$$

Where $G$ is the generation number, and $N_{pop}$ is the size of the population, so for each generation, the population can be written as $N \times N_{pop}$matrix:

$$X_G = \begin{bmatrix} x_{1,1,G} & \cdots & x_{N,1,G} \\ \vdots & \ddots & \vdots \\ x_{1,N_{pop},G} & \cdots & x_{N,N_{pop},G} \end{bmatrix} \tag{2.5}$$

To start the optimization, the first population is initialized randomly and is uniformly distributed in the parameter interval defined by two parameter vectors $A = [a_1, a_2, \cdots, a_n]$ and $B = [b_1, b_2, \cdots, b_n]$. These two vector represent the interval in which the first population is initialized. However, the search domain in the next generations is not restricted to the values specified in $A$ and $B$. In order to expand the search space at each iteration, each parameter vector of (2.4), undergoes mutation, in which a weighted differential vector between two parameter vectors is added to a

third one, to produce the mutant vector:

$$V_{i,G} = X_{opt,G} + F(X_{i1,G} - X_{i2,G}) \tag{2.6}$$

Where $F \in (0,2)$ is the mutation factor. $opt, i2, i3 \in [1, N_{pop}]$, $i2$ and $i3$ are chosen randomly, while $opt$ is the index of the best parameter vector in the current population. In order to increase the diversity of the parameter vector, a child vector $U_{i,G}$ is generated based on the following crossover operation:

$$u_{k,i,G} = \begin{cases} v_{k,i,G} & if \quad \gamma(k) < CR \\ x_{k,i,G} & if \quad \gamma(k) \geq CR \end{cases} \tag{2.7}$$

Where $\gamma$ is a $1 \times N$ vector with real random numbers in the range $[0,1]$, and $CR$ is a preset crossover probability. Finally the new parameter vector $X_{i,G+1}$ of the generation $(G+1)$, is derived based on the following criteria:

$$X_{i,G+1} = \begin{cases} U_{i,G} & if \quad f(U_{i,G}) < f(X_{i,G}) \\ X_{i,G} & if \quad f(U_{i,G}) > f(X_{i,G}) \end{cases} \tag{2.8}$$

Where $f$ is the objective function. The algorithm converges when the fitness of the best parameter vector at a current generation is less than or equal to a desired value $\epsilon$. The flow chart of DE is presented in Fig. 2.6.

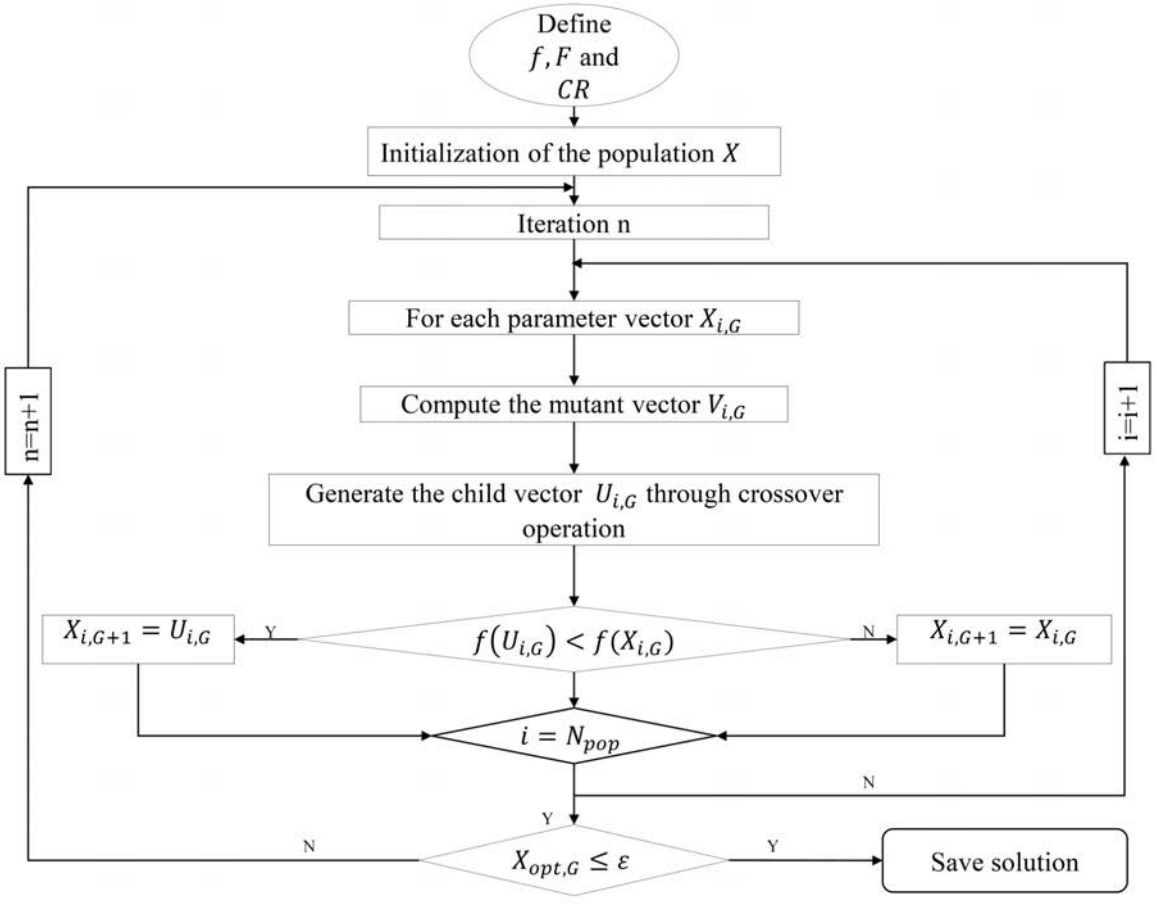


Figure 2.6: Flow chart of the differential evolution algorithm.

### 2.4.2 Matching Technique:NCM Optimization

The change in the performance of the antenna caused by internal loads can be numerically predicted using the NCM analysis. Any load connected to an antenna port will manipulate the eigenvalues and eigenvectors of the modes. Therefore, by combining the NCM with the DE algorithm, optimal load values that can achieve a desired antenna behavior can be calculated.

Before starting the optimization process, several parameters should be defined first. The number of the ports N is a critical parameter in maintaining the simplicity of the design. Although as the number of the ports increases, it would be possible to have a better control on the antenna's current (since the number of NCMs increase), a high number of ports can result in a complex antenna system. Therefore, in our design procedure we start with the minimal number of ports (two ports minimum, one input port and a second loaded port). Setting a good port is also important to insure it effectivenes in controlling the modes. It is believed that placing the ports at positions where the antenna exhibits a high surface current distribution can have the maximal effect in manipulating the modes [56]. After specifying the port positions, the N-port impedance matrix over the desired operating bandwidth is generated using CST software [84]. We then solve the generalized eigenvalue problem of (1) and track the modes in the bandwidth of interest using an in-house MATLAB code. Based on the behavior of the input admittance of the modes, we can predict the loading topology that can match the antenna in the bandwidth of interest. To maintain a simple design, it is important to specify the loading topology to be as simple as possible. Therefore, the optimization of the load values is restricted to the preset loading topology. After specifying these parameters, the extracted Z-matrix is then imported in the optimization code.

In the optimization process, setting a good objective function is very important to ensure that the DE converges to the desired return loss characteristics. The general form of the objective function can be given as:

$$f(Xl) = W_1 \times \sum_{\omega=\omega_{L1}}^{\omega_{H1}} Compare\_S_{11}(Xl(\omega)) + W_2 \times \sum_{\omega=\omega_{L2}}^{\omega_{H2}} Compare\_S_{11}(Xl(\omega)) + \cdots W_i \times \sum_{\omega=\omega_{Li}}^{\omega_{Hi}} Compare\_S_{11}(Xl(\omega)) \quad (2.9)$$

Where $f(Xl)$ is the objective function, $Xl$ is a $1 \times p$ vector containing the load values to be optimized, and $p = (N-1) \times N_e$ considering that the input port will not be loaded and $N_e$ represents the number of components in the loading topology. $Xl(\omega)$ is a $1 \times p$ vector containing the reactances of $Xl$ at the angular frequency $\omega$, where $\omega$ belongs to the desired frequency bands $[\omega_{L_1}, \omega_{H_1}], [\omega_{L_2}, \omega_{H_2}], \cdots [\omega_{L_i}, \omega_{H_i}]$, these bands can be partitions of a wideband or several multiple bands. $W_{1,2,3,\cdots,i}$ are the weighting coefficients to stabilize the contribution of each term in the objective function. In the presented examples, the weighting coefficients are set to 1, and the

optimization is focused on one band, so the objective function is given as:

$$f(Xl) = \sum_{\omega=\omega_{L1}}^{\omega_{H1}} Compare\_S_{11}(Xl(\omega)) \tag{2.10}$$

$Compare\_S_{11}$ is a predefined function given in (2.4.2), that compares at each angular frequency $\omega$, the input reflection coefficient ($S_{11}(Xl(\omega))$ of the antenna loaded by $Xl$ to the desired input reflection coefficient $S_{11\_desired}$.

$$Compare\_S_{11}(Xl(\omega)) = \begin{cases} 1 & if \quad S_{11}(Xl(\omega)) > S_{11\_desired} \\ 0 & if \quad S_{11}(Xl(\omega)) < S_{11\_desired} \end{cases} \tag{2.11}$$

where $S_{11}(Xl(\omega))$ is easily calculated from (2.2) and (2.3):

$$\begin{aligned} S_{11}(Xl(\omega)) &= 20log_{10}\left|\frac{Y_0 - Y'_{input}(\omega)}{Y_0 + Y'_{input}(\omega)}\right| \\ &= 20log_{10}\left|\frac{Y_0 - \sum_{n=1}^{n=N} Y'_n(\omega)}{Y_0 + \sum_{n=1}^{n=N} Y'_n(\omega)}\right| \end{aligned} \tag{2.12}$$

$Y_0$ is the admittance of the source. $S_{11\_desired}$ represents the value under which the antenna is said to be matched, in our case $S_{11\_desired} = -10\ dB$. Therefore, the algorithm directly optimizes the input admittance of each mode, by searching for the best load value that can effectively manipulate $Y'_n$, such that the overall input admittance of the antenna is matched to the source in the desired bandwidth. So, the algorithm will optimize the modes based on the pre-selcted bandwidth and loading topology.

In the DE optimization, the population is formed of a set of parameter vectors $Xl_{i,G}$ which represent the set of internal load candidates. The algorithm converges when $S_{11}(Xl_{opt,G}(\omega))$ is less than -10 $dB$ over the desired bandwidth. Fig. 2.7 presents the key steps of the proposed design methodology. It should be noted that in the overall procedure, just one full wave simulation is required. After extracting the N-port Z matrix of the antenna, the optimization and the post processing is done numerically using MATLAB. It is also important to mention that the elements of the initialization vectors $A$ and $B$, are set to $a_k = 10pF$ and $b_k = 1pF$ for a capacitive component, while for an inductive component $a_k = 10nH$ and $b_k = 1nH$, $k \in [1, p]$.

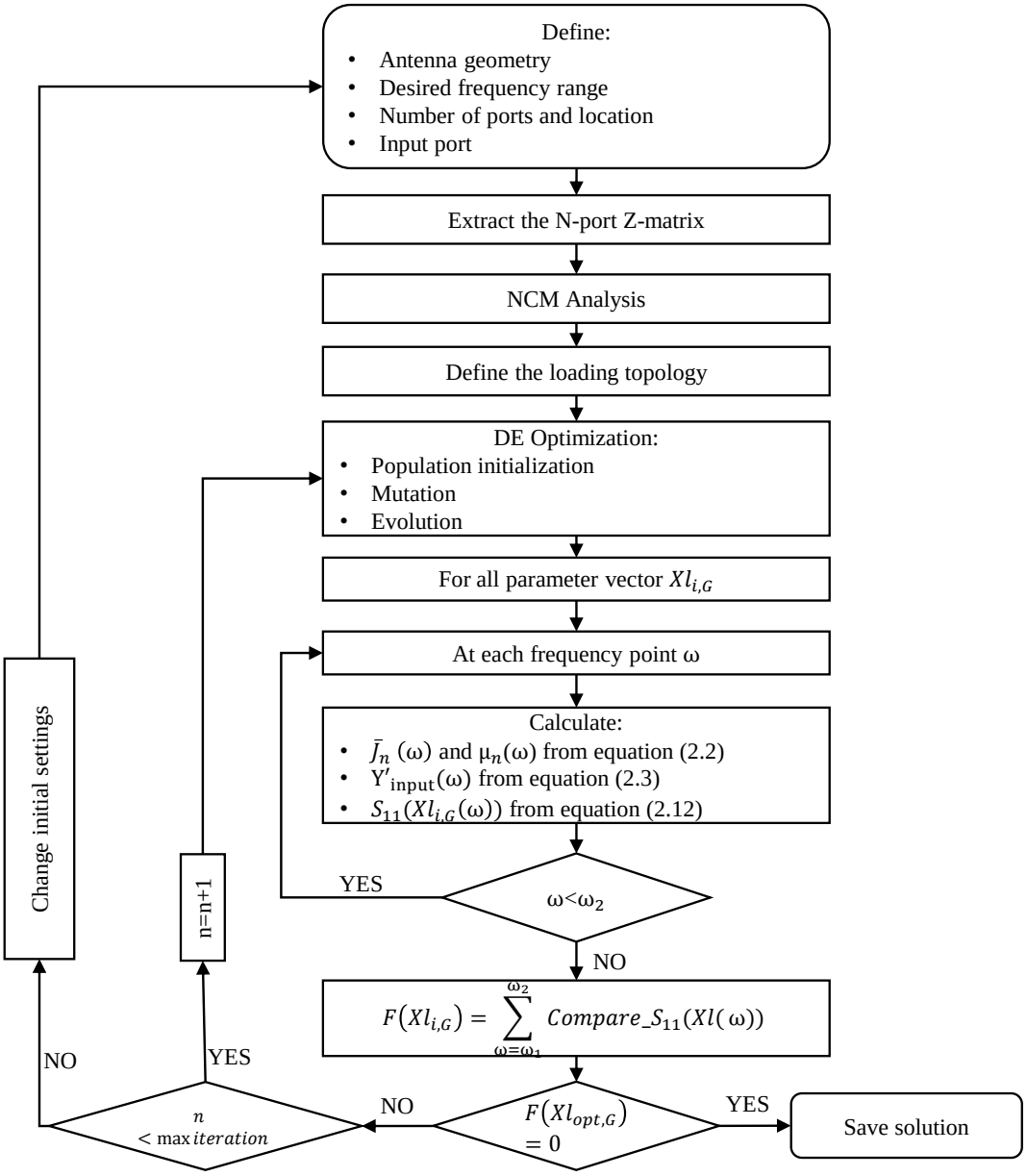


Figure 2.7: Flow chart of the design methodology.

## 2.5 Example I: S-Monopole Antenna

This technique can be applied to any geometry, however, for a more practical design we consider in this example a mobile handset antenna, composed of an S-shaped monopole integrated on a copper ground plane on its top layer, while the bottom layer is not metalized. The antenna is mounted on a Rogers Duroid RT5880 substrate of thickness 0.8 mm and excited at the input port 1 (Fig. 2.8a). The yellow color represents the copper layer which is mounted on a the Rogers Duroid layer represented in red. The overall dimensions of the antenna system is 130 mm × 45 mm, while the monopole is confined to 13 mm × 45 mm. This antenna has a natural

resonance at 2.55 GHz, and a bandwidth of 1.5 GHz which represents 50% of the central frequency (Fig. 2.8b). Three different examples are presented in this section in which we study the effect of the loading topology and the number of ports on the achieved bandwidth.

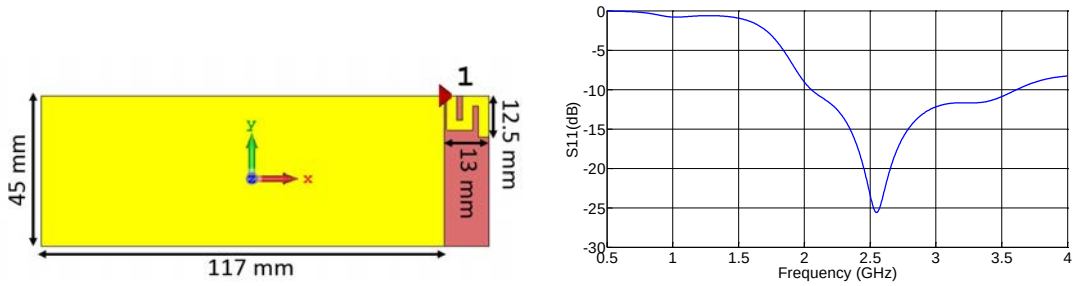


(a) (b)

Figure 2.8: Original unloaded antenna. (a) Geometry, (b) input reflection coefficient.

### 2.5.1 One Internal Port

The aim is to miniaturize the antenna using the proposed technique so that it operates at a lower frequency band. As a primary approach the GSM-900 [880 MHz-960 MHz] band is considered as the desired frequency range. At the central frequency of this band $f_0 = 920MHz$ the radiating element has an electrical size $ka = 0.17$ while that of the overall structure is $ka = 1.325$. Following the methodology presented, the design steps are given below:

#### 2.5.1.1 Setting Ports

Defining the positions of the ports is a critical step for the convergence of the optimization. By studying the current distribution of the antenna at 900 MHz, it is evident that the antenna exhibits a high surface current distribution in its first section (Fig.2.9a ). Therefore, and starting with the minimal number of ports, the second port was set 5 mm from the input port (Fig.2.9b). Hence, with this configuration, the antenna will be excited at port 1 while port 2 will be loaded based on the load value given by the optimization.

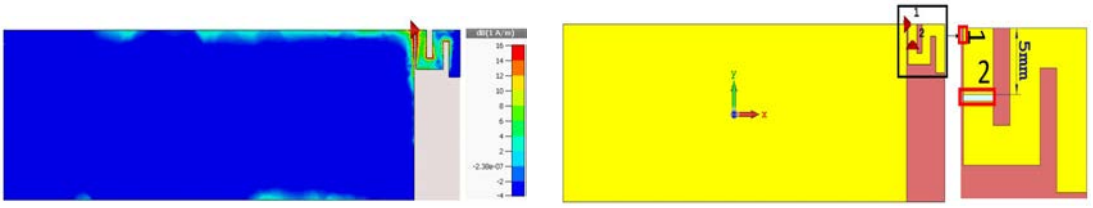


(a) (b)

Figure 2.9: Port setup based on current distribution. (a) surface current distribution of the original antenna at 900MHz. (b) positions of the ports.

#### 2.5.1.2 Loading Topology

After specifying the location of the internal port, the 2-port impedance matrix is extracted. By studying the behavior of the modes, it is obvious that mode 1 is the dominant mode which is contributing in the overall antenna radiation, while the high

eigenvalue magnitude of mode 2 indicates that it is a non-radiating mode (Fig.2.10a). mode 1 resonates at 2.45 GHz which is the natural resonance of the antenna. In the GSM 900 band, mode 1 exhibits a capacitive behavior (Fig. 2.10c) with a low input conductance ($G_{in}$) (Fig. 2.10b). A negative capacitance connected at port 2 can properly manipulate the current distribution of the antenna to compensate the input susceptance ($B_{in}$) of mode 1 and match its input conductance to the source. Therefore, the loading topology chosen is a simple capacitance.

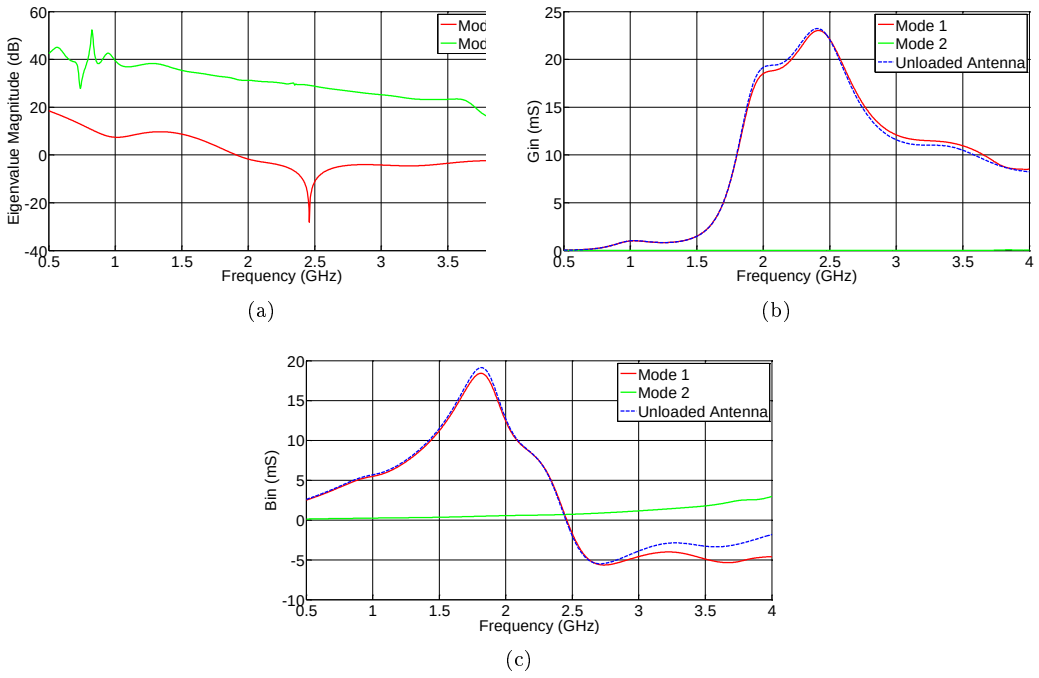


(a) (b) (c)

Figure 2.10: Network characteristic modes analysis of the unloaded antenna. (a) eigenvalue spectrum. (b) input conductance of the modes of the antenna. (c) input susceptance of the modes of the antenna.

#### 2.5.1.3 Optimization Results

After specifying all the required parameters, the 2-port impedance matrix is imported in the optimization code. The algorithm converges to a capacitance value of -0.86 pF after 34 iterations and a CPU run time of 15.8 seconds. Hence, an internal negative capacitance is needed to miniaturize the antenna to be matched in the desired bandwidth. However with such loading, the antenna is matched over a wider bandwidth [0.855 GHz-1.16 GHz] which represents 30% of the central frequency (Fig. 2.11). Such miniaturization represents 60% size factor reduction relative to the original antenna.

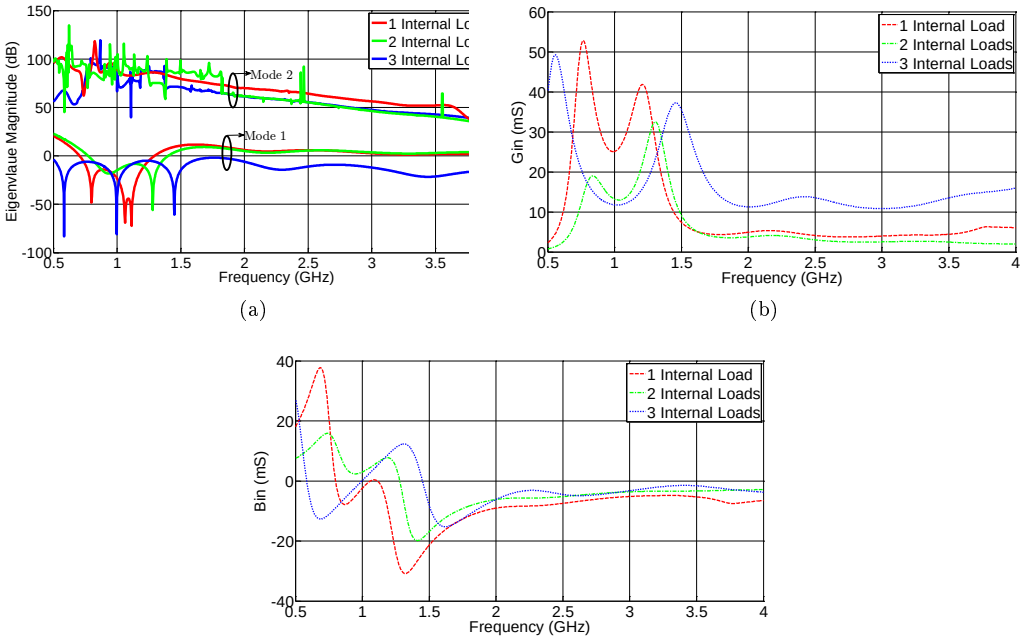


Figure 2.12: Network characteristic modes analysis of the loaded antennas. (a) eigenvalue spectrum. (b) input conductance of the modes. (c) input susceptance of the modes.

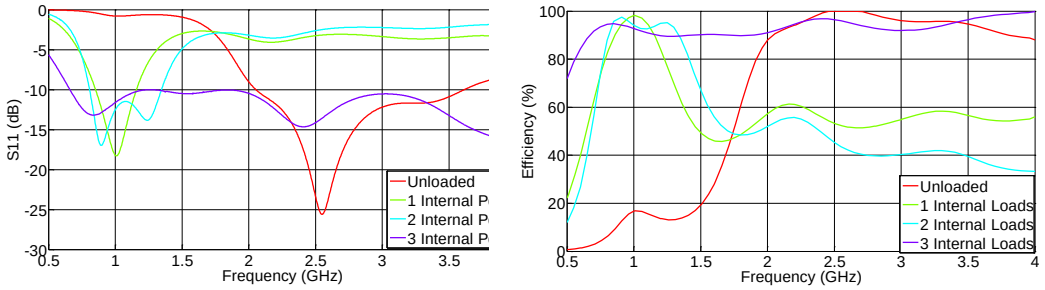


Figure 2.11: Performance of the loaded and Unloaded antennas. (a) Input reflection coefficient, (b) total efficiency.

#### 2.5.1.4 Network Characteristic Mode Analysis

The negative capacitance significantly compensates the susceptance of mode 1 (Fig. 2.12c), on the other hand mode 2 is still a non significant mode and is not contributing in the overall current (Fig. 2.12a). The resonance frequency of mode 1 is shifted towards the desired bandwidth and it resonates at three frequency point [0.8 GHz, 1.04 GHz, 1.12 GHz] (Fig. 2.12a). In addition, the non-Foster loading also served in increasing the input conductance of mode 1 so that it becomes matched to the source. Therefore, with the internally loaded negative capacitor a better control on the antenna's input admittance was achieved.

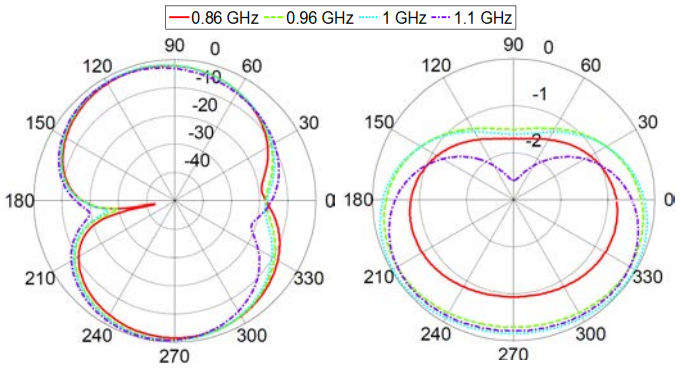


(a)

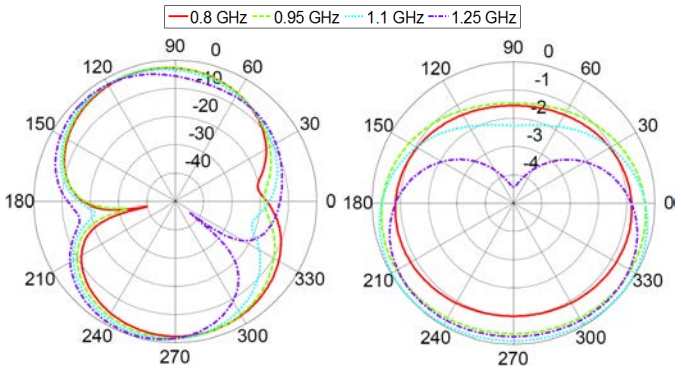


(b)

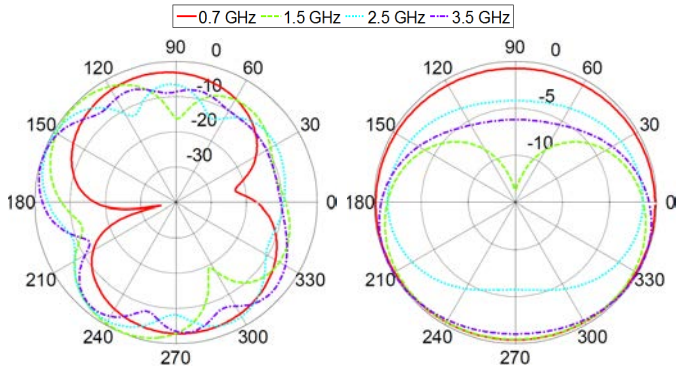


(c)

Figure 2.13: Normalized radiation pattern of the loaded antennas in E-plane (left) and H-plane (right). (a) antenna with one internal loads. (b) antenna with two internal loads. (c) antenna with three internal loads.

#### 2.5.1.5 Efficiency and Radiation Pattern

With the ideal negative capacitor, the efficiency of the loaded antenna is significantly enhanced in the desired bandwidth with respect to the original one (Fig.2.11b). The efficiency of the loaded antenna attains 93% at 860 MHz rather than 18% for the original antenna at the same frequency. However, it is insufficient to discuss the antenna's bandwidth based on the input impedance and efficiency. It is also important to maintain the pattern shape in the desired frequency range. Fig. 2.13a illustrates the normalized radiation pattern of the loaded antenna at different fre-

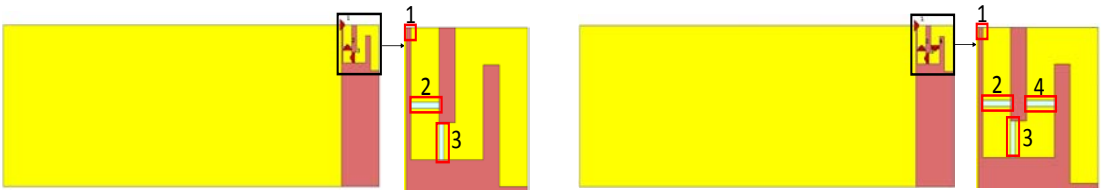


(a) (b)

Figure 2.14: Port setup. (a) two internal ports. (b) three internal ports.

quency points in the operating frequency range. Since mode 1 is the only resonant mode contributing in the current of the loaded antenna between 0.85 GHz and 1.16 GHz, the antenna maintains a relatively constant pattern shape.

### 2.5.2 Two Internal Ports

After achieving a wideband matching using one internal negative capacitance, we study the possibility to match the antenna in a wider bandwidth. Based on the previous results, the negative capacitive load transforms the capacitive behaviour of mode 1 into an inductive behaviour beyond 1.15 GHz (Fig. 2.12c). Hence, an additional capacitive load will be sufficient to compensate this reactance and match the antenna in a wider bandwidth. A second port is considered as shown in Fig. 2.14a. The desired frequency band is set to [0.85 GHz-1.3 GHz], and the loading topology is set as capacitance. The 3 port Z-matrix is extracted over the bandwidth. A positive capacitance $C_2 = 3.11pF$ and a negative capacitance $C_3 = -0.62pF$ are the optimal values yielded by the algorithm at port 2 and port 3 respectively. With this load configuration, the antenna is matched in a wider bandwidth [0.8 GHz - 1.34 GHz], which represents 50% of the central frequency (Fig. 2.11). The behaviour of the first two modes in the loaded antenna is shown in Fig. 2.12. The dominant mode (mode 1) is resonant at 1.25 GHz, its input conductance is matched to the source with a compensated input admittance over the desired bandwidth. The antenna is efficient in the bandwidth of operation (Fig. 2.11b) and has a stable radiation pattern Fig. 2.13b. Compared to the one internal port matching given in the previous section, the second internal port plays a significant role in controlling the impedance of the dominant modes. In the bandwidth of interest, the conductance decreases to become closer to the source conductance ($20mS$) while maintaining a compensated susceptance in all the band.

It should be noted that since mode 1 is the dominant mode, while the higher order modes are not significant, just the admittance of mode 1 is drawn for the loaded antenna which essentially reflects the input admittance of the antenna.

### 2.5.3 Three Internal Ports

In this section we study the possibility to match the antenna over the entire bandwidth [0.5 GHz-4 GHz]. In this case three ports are considered (Fig. 2.14b). For the unloaded antenna, mode 1 exhibits a capacitive behaviour at the lower band and an inductive behaviour at the upper band. Therefore, an LC series load topology might be the proper load candidate. However, for this large bandwidth, the convergence conditions are relaxed, where $S_{11-desired}$ is set to $-6dB$.

In this case the algorithm converges after 40 iterations with a 47 seconds of CPU

run time. The optimized load values yielded by the algorithm are given in Table. 2.1. These loads are a combination of Foster and non-Foster loads. With these loads, the antenna is matched and efficient over the whole bandwidth and beyond 4 GHz (Fig. 2.11). This result is reflected by the low eigenvalue of first mode over the entire bandwidth (Fig. 2.12a). The higher order modes remain insignificant in the loaded antenna. At higher frequencies, the radiation pattern is modified due to the contribution of the ground plane in the radiation (Fig. 2.13d).

In this section, the design of ESA loaded with non-Foster and Foster loads was presented. Yet, the design of non-Foster circuit at high frequencies adds complexity, losses, and stability issues. Detailed design of wideband small antenna internally loaded with a negative capacitance will be explained in the next chapter. On the other hand, in the next section, we elaborate with more examples on the proposed matching technique to design wideband ESA. However, this time we propose some geometry modification in order to eliminate the need of non-Foster loads for antenna matching.

Table 2.1: Optimized load values on the internal ports

| | port 2 | port 3 | port 4 |
|---|---|---|---|
| L(nH) | -3.94 | -0.53 | -3.49 |
| C(pF) | 1.55 | -0.5 | 302 |

### 2.5.4 Inadequate Port Position

The principle key in successfully controlling the NCMs to achieve a desired bandwidth is the appropriate choice of the internal ports. A poor choice of the position of the ports will definitely affect the convergence of the algorithm and might result in undesired antenna behaviour. Considering a worst case scenario where an internal port is defined in the section of the S-monopole where the surface current distribution is low (Fig.2.15a,b).

With this port configuration, it is not possible to match the antenna in the desired GSM band. Despite the defined loading topology, the algorithm did not converged to an acceptable solution. The load solutions yielded by the optimizer, had a negligible effect on the antenna performance where it was still resonant at frequencies in the neighborhood of $2.2GHz$ while totally unmatched in the desired frequency band. To examine the sensitivity of the antenna to the defined port position, we considered various values of inductive and capacitive loads connected to $port2$. By analyzing the results given in Fig.2.15c, it is noticed that the eigenvalue magnitude of mode 1 remains almost unchanged for the capacitive or inductive loads, and it maintains a fixed resonance frequency. Therefore, at this loading position, the antenna is insensitive to any kind of loads.

Hence, in addition to chosing a convenient loading topology, the port position represents also a critical point in the convergence of the algorithm in order to achieve the desired impedance behaviour.

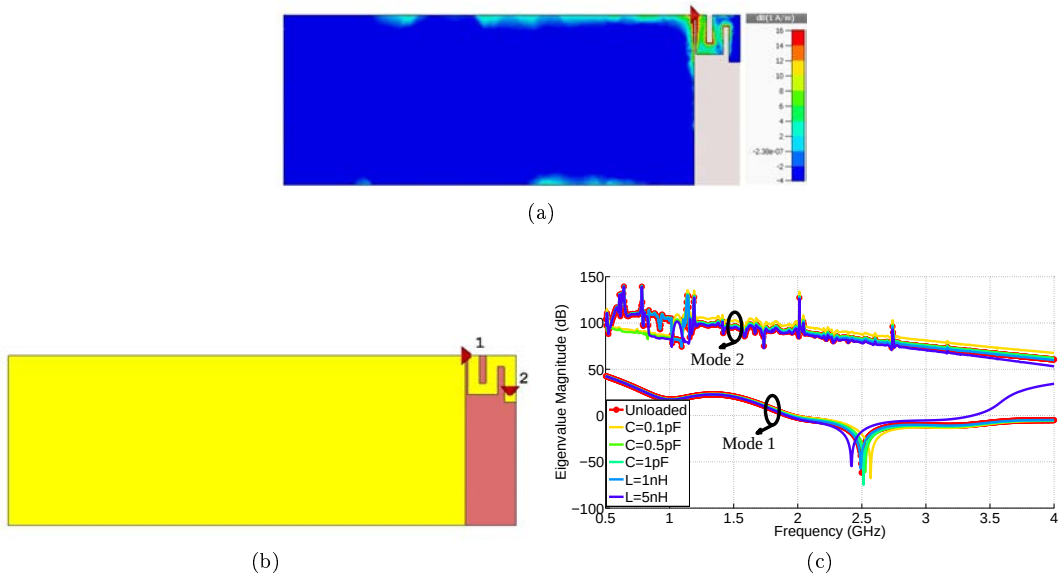


Figure 2.15: Port setup of the antenna. (a) Surface current distribution at $900MHz$, (b) two-port antenna geometry, (c) sensitivity of the eigenvalue magnitude as a function of reactive loading.

## 2.6 Example II: S-Monopole Antenna with Near Field Parasitic Element

Although wideband matching is possible using internal active circuits, the design of such circuits is usually associated with stability issues in addition to resistive losses which may degrade the overall performance. Therefore passive matching remains an interesting alternative in terms of complexity and performance. In this section we apply some modifications on the previous S-monopole antenna to achieve wideband passive matching. In the capacitive near field of the radiating antenna, we introduce a parasitic meander line. The overall structure dimensions are $130mm \times 60mm$ ($ka = 1.37$ at $f_0 = 920MHz$), while the radiating element is confined to $13mm \times 60mm$ ($ka = 0.59$ at $f_0 = 920MHz$).

Fig. 2.16 shows the geometry of the structure. The radiating antenna is printed on the top side of the substrate, while the parasitic meander line is printed on the bottom side. This planar meander line provides an inductance which effectively interacts with the capacitive near field of the antenna to obtain a matching in space, which is visible by the narrow band resonance at 860 MHz (Fig. 2.17). In the band of interest, the resistance of the antenna with meander line is almost the same as that of the antenna without meander line. However, although both antenna are capacitive, the reactance of the parasitic antenna is much less than that of non-parasitic antenna. This enhancement can be translated into a decrease in the $Q$ of the antenna, which makes it more suitable for wideband matching.

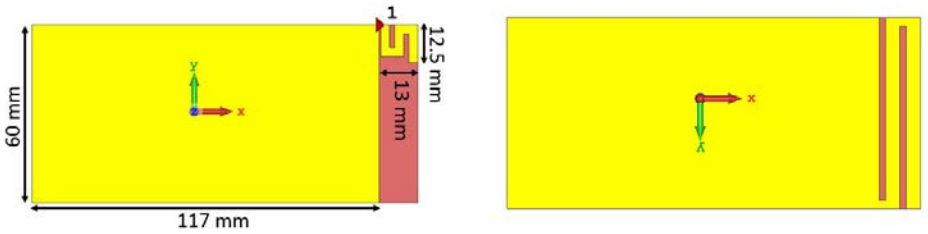


(a) (b)

Figure 2.16: Geometry of the s-monopole antenna with near field parasitic. (a) top view. (b) bottom view.

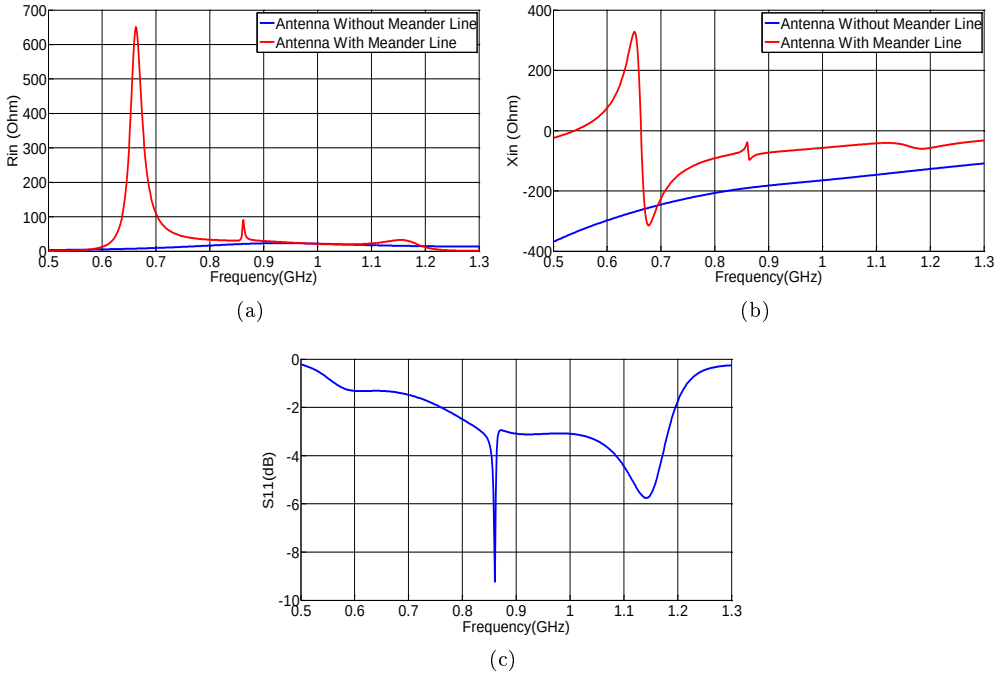


(a) (b)

(c)

Figure 2.17: Effect of the parasitic meander line on the input impedance of the antenna. (a) input resistance. (b) input reactance. (c) input reflection coefficient of the unloaded antenna.

### 2.6.1 Two Internal Ports

The parasitic meander line effectively compensates the reactive part of the antenna and makes it more suitable for wideband passive matching rather than using non-Foster circuits. Considering GSM-900 band as the desired bandwidth, we define two internal ports to be loaded. Based on the current distribution of the antenna at 900 MHz (Fig. 2.18), port 2 was set in the first section of the s-monopole with a $5mm$ distance from the input port (port 1), while port 3 was set in the second vertical section of the meander line (Fig. 2.19)

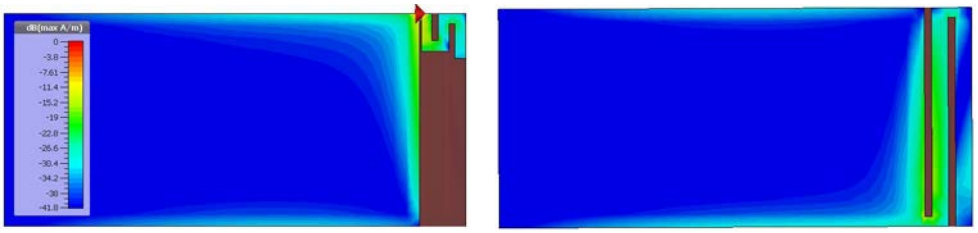

(a) (b)

Figure 2.18: surface current distribution of the antenna at 900 MHz.(a) Top view, (b) bottom view.

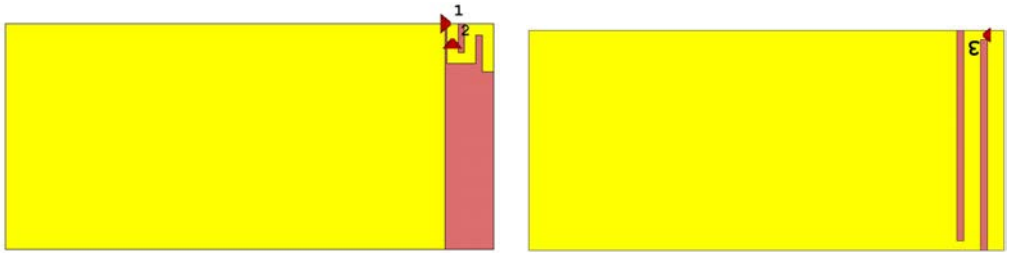


(a) (b)

Figure 2.19: Port setup of the antenna.(a) port 2 in the antenna. (b) port 3 in the meander line.

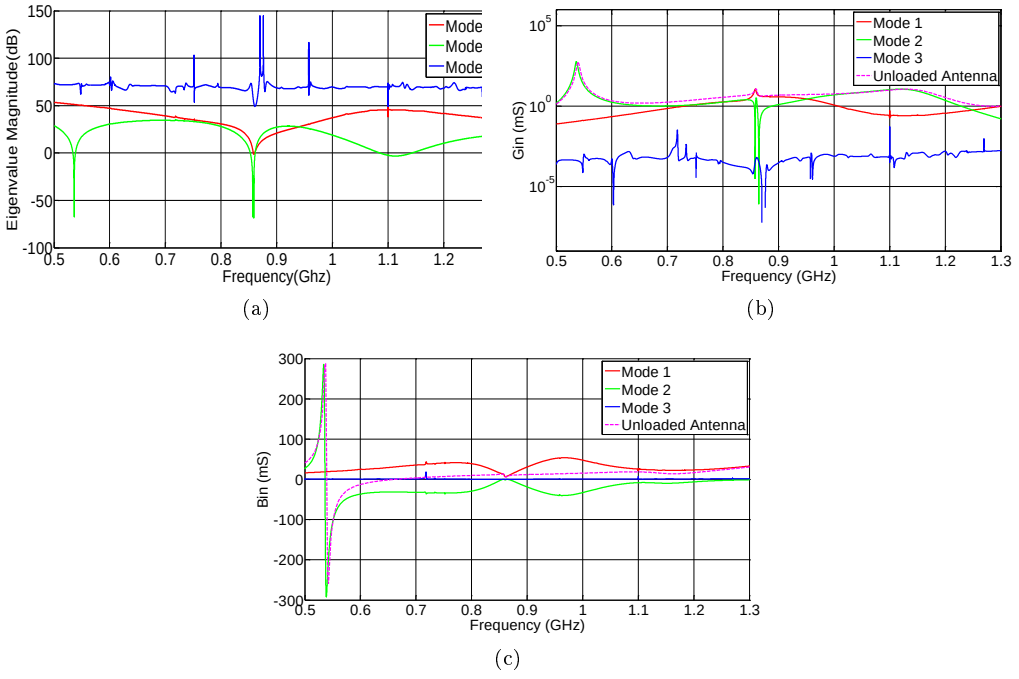


(a) (b) (c)

Figure 2.20: Network characteristic modes analysis of the unloaded antenna. (a) eigenvalue spectrum. (b) input conductance of the three modes. (c) input susceptance of the three modes.

To identify the loading topology, NCM analysis was applied on the 3-port antenna system. The first two modes are contributing in the antenna radiation, while mode 3 is a non-radiating mode (Fig. 2.20a). In the bandwidth of interest, the inductive mode 2, is compensating the capacitance of mode 1 and hence reducing the overall

susceptance of the antenna (Fig. 2.20c). Nevertheless, the capacitance of the antenna can be further reduced by adding inductive loads at the defined ports. These inductive loads will aid mode 2 in compensating more of the capacitance of mode 1. Based on this given the admittances of the NCMs is optimized with inductive loads. After 20 iterations and a CPU run-time of 25.65 seconds the optimal inductive load values were found to be $L_2 = 16\ nH$ at port 2 and $L_3 = 1.5\ nH$ at port 3. With this load configuration, the antenna is matched in the bandwidth [0.81 GHz - 1 GHz] (Fig. 2.21), which represents 20% of the central frequency.

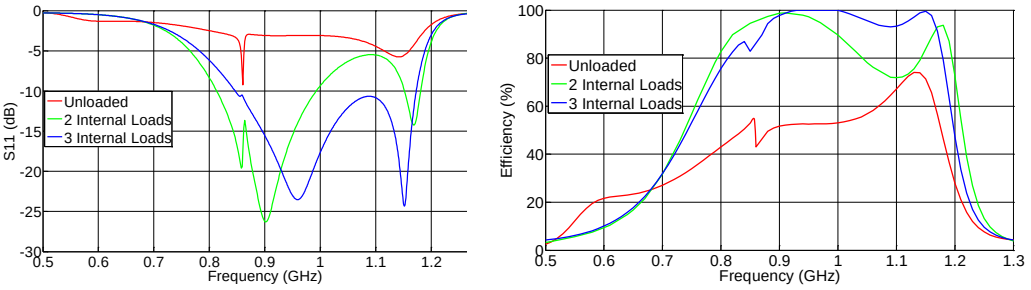


(a) (b)

Figure 2.21: Performance of the loaded and unloaded antenna with meander line parasitic. (a) Input reflection coefficient, (b) total efficiency versus frequency.

A better understanding of the results can be given by analyzing the effect of the inductive loading on the modes. As expected, the capacitance of mode 1 was efficiently reduced, which resonates this mode at 4 frequency points 0.87 GHz, 0.96 GHz, 1.16 GHz, and 1.27 GHz (Fig. 2.22a, c).Therefore, the inductive loading successfully manipulated the current distribution such that the input conductance of mode 1 becomes matched to the source in the bandwidth of interest (Fig. 2.22b). The modal resonance at $1.16GHz$ is visible in the input reflection coefficient of the 2-internally loaded antenna of Fig. 2.21. Yet, the antenna is not matched at this frequency since the conductance of the first mode is not low enough to maintaining an $S_{11} < -10dB$ beyond $1GHz$.

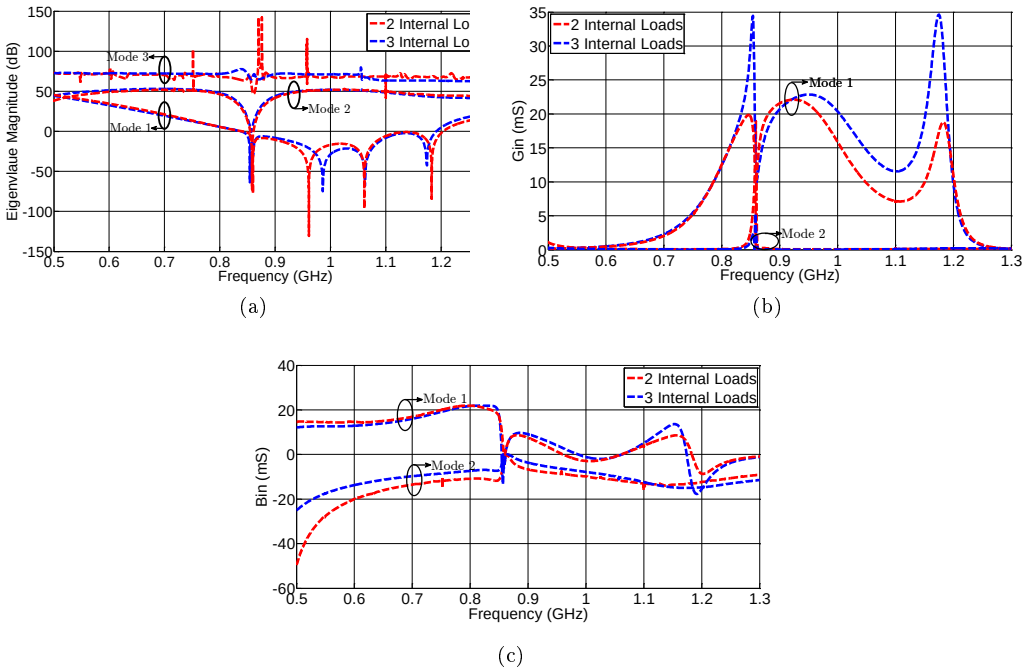


Figure 2.22: Network characteristic modes analysis of the loaded antennas. (a) Eigenvalue spectrum, (b) input conductance, (c) input susceptance of the three modes.

Nevertheless, we notice an anomalous drop in the input conductance of mode 1 at 0.87 GHz. This null input conductance was compensated by the increased input conductance of mode 2 at the same frequency point. This anomalous drop can be explained by examining the equation of the input conductance of mode 1:

$$Y'_{in1}(\omega)[input] = \frac{\bar{I}_1[input]^2(1 - j\mu_1(\omega))}{(1 + \mu_1^2(\omega))((\tilde{I}_1^*(\omega)[R_a(\omega)]\bar{I}_1(\omega))} \tag{2.13}$$

Since $\mu_1$ is very low at $0.87GHz$ due to its resonance, the only reason that $Y_{in1}$ becomes null is that the eigen current $\bar{I}_1$ has a null value at the input port $\bar{I}_1[input] = 0$.

The simulated total efficiency of the antenna is shown in Fig. 2.21b. With the passive internal loads, the antenna is highly efficient in the bandwidth of interest. Its efficiency attains 98% at $900MHz$. Besides, as shown in Fig. 2.23a, the antenna maintains a relatively constant radiation pattern in its operating bandwidth.

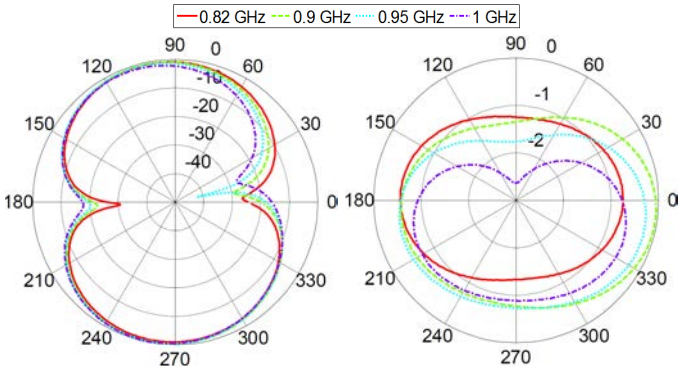


(a)

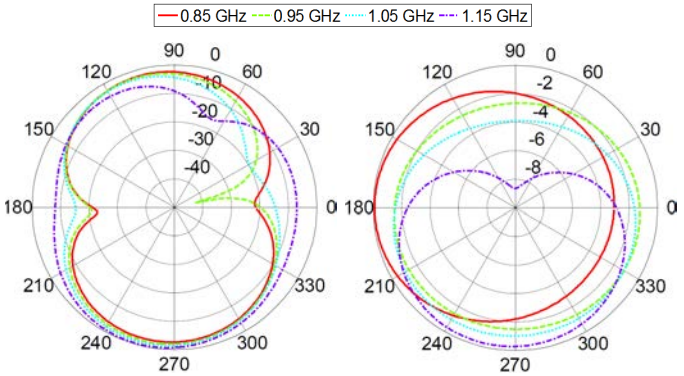


(b)

Figure 2.23: Normalized radiation pattern of the loaded antennas in E-plane (left) and H-plane (right). (a)antenna with two internal loads. (b) antenna with three internal loads.

### 2.6.2 Three Internal Loads

With two-internal load configuration, mode 1 is resonant at 1.17 GHz, however its input impedance is not matched to the source. An additional inductive load will provide a better control on the admittance of the mode and would be sufficient to match the antenna beyond 1 GHz. A third port is selected as shown in Fig. 2.24. With $L_2 = 6.8nH$, $L_3 = 13nH$, and $L_4 = 6.8nH$ the conductance of mode 1 increased in the higher band Fig. 2.22b, while the resonance is maintained. Therefore the bandwidth of the antenna reached 32% $[0.84 - 1.17GHz]$which is 12% higher than the previous configuration. The antenna is also efficient in the operating bandwidth (Fig.2.21b) with a stable radiation pattern (Fig.2.23b).

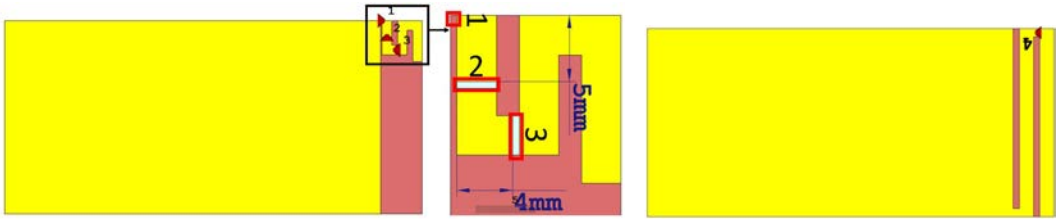


(a) (b)

Figure 2.24: Antenna with three internal ports. (a) top view. (b) bottom view.

### 2.6.3 More Internal Loads

In the given examples, it was shown that as the number of internal ports increases, it becomes easier to control the eigen currents inside the antenna resulting in wider impedance bandwidth. In order to examine the possibility of enhancing more the bandwidth of the given antenna, a $4^{th}$ internal port is added in the parasitic meander line as shown in Fig.2.25. Aiming to achieve higher miniaturization and wider bandwidth, the desired frequency band is set to $[0.7 - 1.2GHz]$ and the loading topology is set to inductive. Contrary to the previous case, the algorithm does not converge to the desired goal. After 100 iterations and 2 minutes CPU run time, the best values of the internal loads are: $L_2 = 9.4nH$, $L_3 = 9.2nH$, $L_4 = 2.7nH$ and $L_5 = -0.5nH$. With this configuration, the antenna is matched in a 34% relative bandwidth $[0.84 - 1.19GHz]$ which is just 2% higher than the previous case (Fig.2.26). This slight increase in the bandwidth, is visible in the higher part of the band which increased by about $20MHz$, while no miniaturization or shift in the lower part of the bandwidth is noticed. In addition, a negative inductance is connected to the fifth port. The optimization was carried for more complex loading topologies, such as LC series loading and no enhancement was noticed either.

Therefore, even with increased number of ports, it was not possible to increase the miniaturization factor of the antenna neither increase its bandwidth. In this case, it becomes mandatory to perform some geometry modifications on the antenna structure, in order to reduce its Q-factor and make it more suitable for a reactive distributed matching.

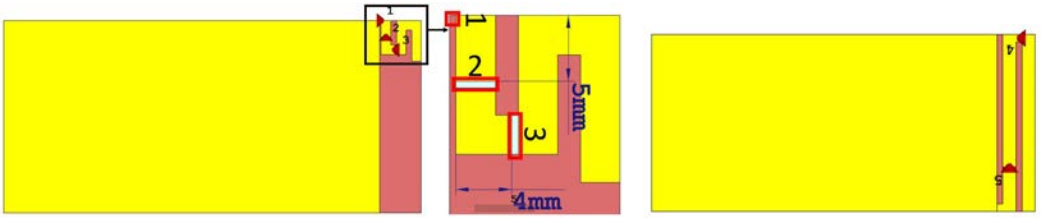


(a) (b)

Figure 2.25: Antenna with four internal ports. (a) top view. (b) bottom view.

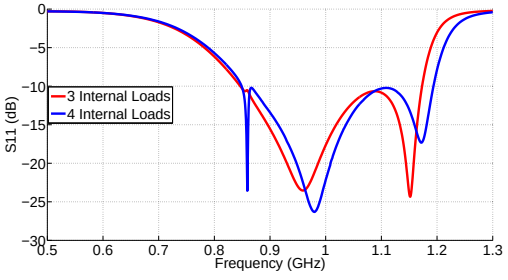


Figure 2.26: Input reflection coefficient of the antennas with three and four internal loads.

## 2.7 Experimental Validation

To validate the simulation results, a prototype of the s-monopole with near field meander line parasitic and loaded with two internal loads was fabircated (Fig. 2.27).

Commercial 0603Murata RF inductors [85] with the optimized values are connected to the ports. The measured input reflection coefficient is in good agreement with the simulation results where the antenna is matched in a 19.3% bandwidth with a slight mismatch at $0.86GHz$ (Fig. 2.28a). The measured antenna is also efficient with an average efficiency of about 80% in the bandwidth of operation (Fig. 2.28b). Therefore, with the proposed technique, a wideband efficient compact antenna was designed using simple inductive loads and without an input matching network.

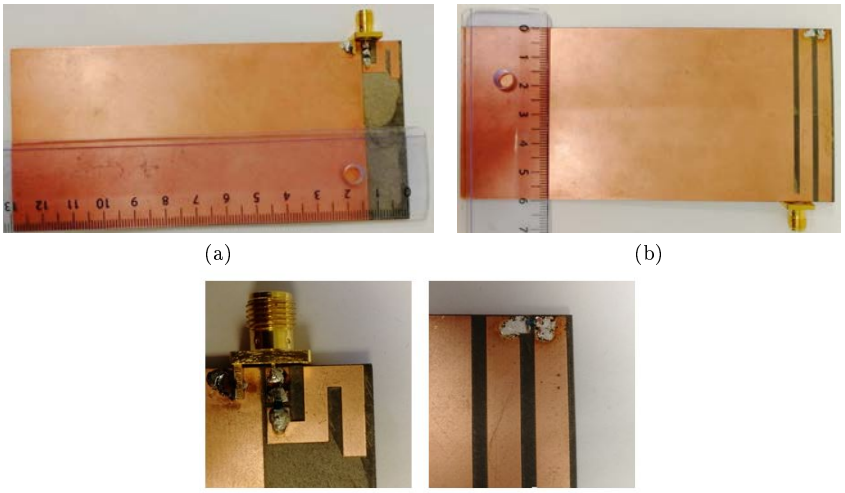

(a) (b)

(c)

Figure 2.27: Prototype. (a) Top layer, (b) bottom layer, (c) zoomed screen shot of the load locations.

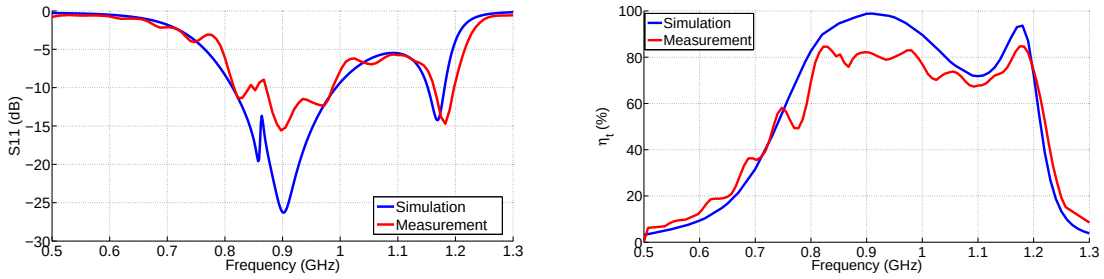


(a) (b)

Figure 2.28: Simulation and measurement of the loaded s-monopole with near field parasitic element. (a) input reflection coefficient. (b) efficiency.

The simulation results for the case of three internal ports was also validated in measurements. The fabricated prototype given in Fig. 2.29. Similar to the previous case, the measured impedance and efficiency of the reactively loaded antenna are in good agreement with the simulations. The measured antenna attains a wideband impedance behaviour of 32% with a total efficiency higher than 80% inside this bandwidth, while achieving a maximal efficiency of 92% at $920MHz$ (Fig. 2.30).


(a) (b)

Figure 2.29: Prototype. (a) Top view, (b) bottom view.

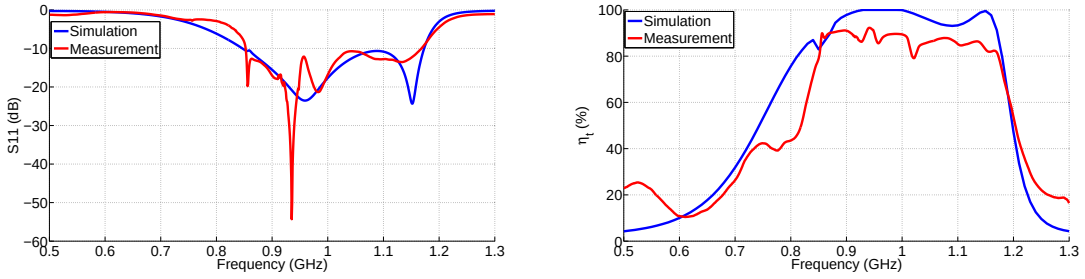


(a) (b)

Figure 2.30: Simulation and measurement of the loaded antenna. (a) Input reflection coefficient, (b) total efficiency.

After studying and validating the possibility to match an ESA in a wideband, in the next section, we investigate the possibility to manipulate the modes in the antenna in order to match it in multiple bands.

## 2.8 Multiband Antenna

The limited size available to design mobile handset antennas that can cover multiple bands imposes various challenges[86, 87]. At low frequency bands, the electrical size of the antenna becomes smaller, which restricts its operational bandwidth and efficiency. However it is also important to take into account the input impedance matching at the higher frequency bands. Therefore, multiple objectives should be achieved simultaneously in order to achieve a successful design.

In this section, we present the design of a multiband antenna using the proposed matching technique. By studying the surface current distribution of the proposed antenna at the desired frequency bands, the locations of the ports are specified. Then, the value of the load that can optimally control the network characteristic currents to provide the best performance are calculated. The designed antenna covers the GSM 850/900 band ([824 MHz - 890 MHz],[880 - 960 MHz]) and the Bluetooth band ([2.4 GHz - 2.48 GHz]).

Since the optimization is desired at three bands, the objective function of (2.4.2) becomes:

$$f(Xl) = \sum_{\omega=\omega_1}^{\omega_2} U\,|S_{11}(Xl(\omega)) - S_{11desired}| + \sum_{\omega=\omega_3}^{\omega_4} U\,|S_{11}(Xl(\omega)) - S_{11desired}| + \sum_{\omega=\omega_5}^{\omega_6} U\,|S_{11}(Xl(\omega)) - S_{11desired}| \quad (2.14)$$

where $\omega_{1-6}$ correspond to the upper and lower angular frequencies of the previously defined bands. In order to relax the convergence constraints,$S_{11desired}$ is set to $-6dB$.

For this design we consider the previously studied S-shaped monopole antenna with a near field meander line parasitic. The current distribution of the antenna at $900MHz$ and $2.44GHz$ is given in Fig. 2.31. It should be noted that in this design, loading is also considered for the input port (port 1). Similar to the previous design, a port (port 2) is defined in the first section of the radiating antenna (Fig.2.32a). At this position, it was shown that the loads can effectively manipulate the NCMs in low frequency bands. Taking into account that the antenna is already resonant at $2.4GHz$ a slight modification in the modes can be sufficient to match the antenna in the upper band. Consequently, port 3 is defined at the extremity of the parasitic meander line (Fig.2.32b). Although at this position, the surface current distribution at both frequencies is almost of the same order of magnitude. The main effect on the low band is controlled by the loads at port2, while those at ports 1 and 3 control the modes at the upper band. Following the same approach presented in the previous section,the loading topology is chosen to be inductive loading. After 12 iterations and a CPU run time of 14 seconds, the optimization yields the following load values:$L_1 = 6.6nH$,$L_2 = 13nH$,$L_3 = 5.4nH$ at ports 1, 2 and 3 respectively.

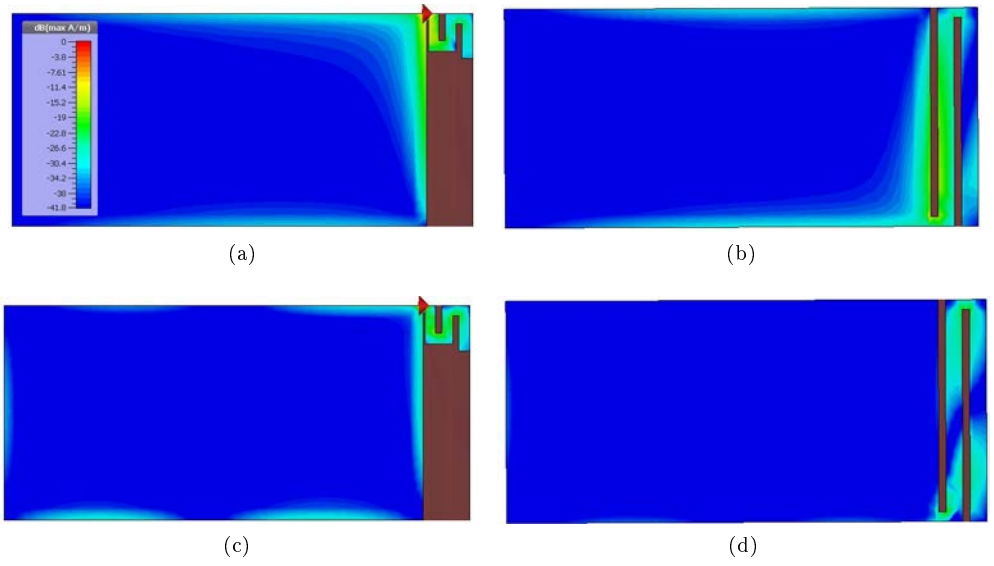


Figure 2.31: Surface current distribution of the antenna. (a) top 900 MHz, (b) bottom 900 MHz, (c) top 2.44GHz, (d) bottom 2.44 GHz

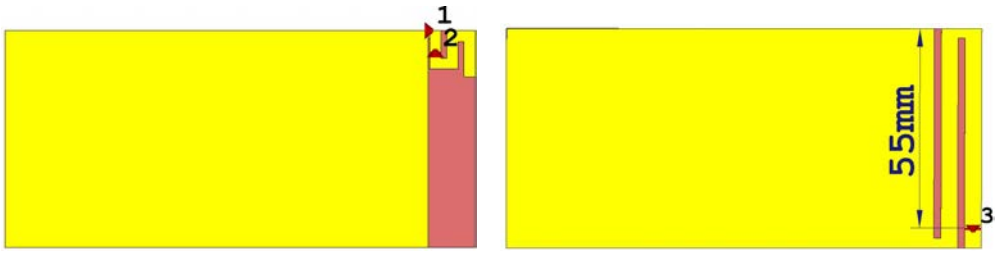


(a) (b)

Figure 2.32: Geometry of the 3-port antenna. (a) Top, (b) bottom.

To analyze the result, we consider the modal significance for this example to study the behaviour of modes in the desired bands. As explained in the previous chapter, the modal significance is an alternative representation of the eigen modes. When $MS$ approaches 1 it means that the mode is resonant. The modal significance of for the unloaded and loaded antennas are given in Fig.2.33. In the first two bands (GSM 850/900) Fig.2.33a, mode 1 in the unloaded is the dominant mode with a narrow band resonance at $0.86GHz$ however mode 2 and mode 3 are non-significant modes. With the inductive loading, a clear enhancement is noticed in terms of the modal significance which is similar to the improvement seen in the previous section for the wideband antenna. The resonance frequency of mode 1 is shifted to a lower frequency band ($0.82GHz$), while it remains significant up till $0.87GHz$. In other words, with inductive loading, the bandwidth of mode 1 is increased to cover the lower part of the band $[0.82GHz - 0.87GHz]$. On the other hand, beyond $0.86GHz$, mode 2 becomes a significant mode, along with mode 1. Therefore the interaction of the first two modes contributes in matching the antenna to the source in the GSM bands. In the third band, mode 1 was already resonant in the unloaded antenna as shown by the full red line in Fig.2.33b.

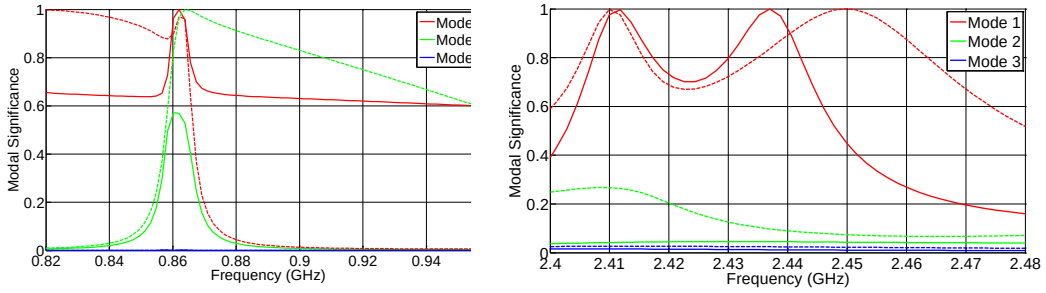


(a) (b)

Figure 2.33: Modal significance of the unloaded (full lines) and loaded (dotted lines) antenna. (a) Low bands, (b) high band.

In this band, mode 1 was the dominant mode with a very slight contribution from mode 2. After adding the inductive loads, the dominance of mode 1 is enforced to cover the desired bandwidth. Moreover, the effect of the inductive loads is demonstrated in Fig2.34. At 900 MHz, the current distribution becomes stronger at the position of the second load and weaker at the position of the third load. On the other hand, in the upper band, the surface current distribution was unforced by the third load. At this position we notice an increase in the current distribution with respect

to the unloaded antenna. Therefore, the inductive loads, served in manipulating the current on the antenna structure in order to match it in the desired frequency bands.

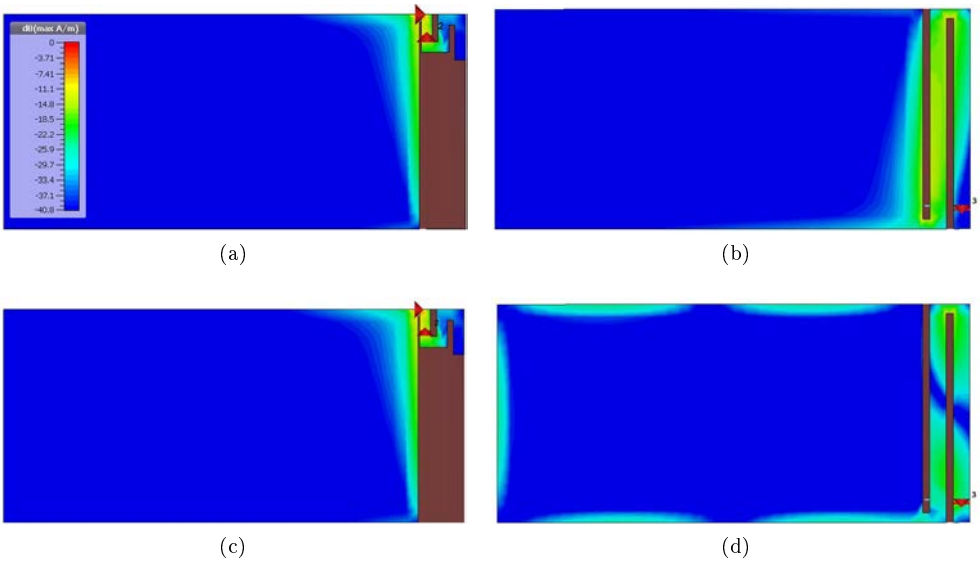


Figure 2.34: Surface current distribution of the loaded antenna. (a) top 900 MHz, (b) bottom 900 MHz, (c) top 2.44GHz, (d) bottom 2.44 GHz

The input reflection coefficient of the loaded antenna is shown in Fig.2.35. As desired, the antenna is matched at the three bands. Therefore, by applying optimal inductive loading at the ports of the antenna, it was possible to control the characteristic modes and take advantage of the interaction between them in order to match the antenna in the desired bands. The total efficiency of the loaded antenna is also shown in Fig.2.35. In the desired bands the antenna exhibits a high efficiency.

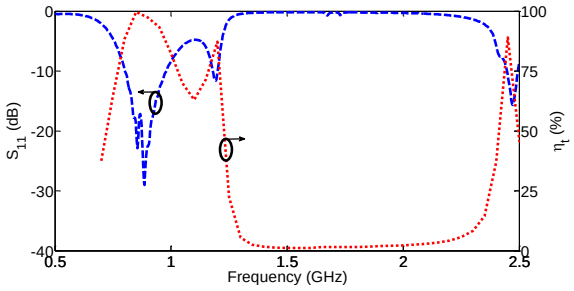


Figure 2.35: Input reflection coefficient and total efficiency of the loaded antenna.

A prototype of the presented antenna have been fabricated and measured (Fig.2.36). The antenna is loaded at the defined positions using commercial Murata RF inductors. The measurement results are in good agreement with the simulations (Fig. 2.37). However, in the upper band, we notice a shift in the resonance frequency of the antenna. This is due to the dispersion of the inductor values that becomes more apparent as the frequency increases. The efficiency of the antenna was measured using the Wheeler Cap. The antenna is also efficient having a peak total efficiency of 95% at $0.85GHz$.

(a) (b)

Figure 2.36: Prototype. (a) Top, (b) bottom.

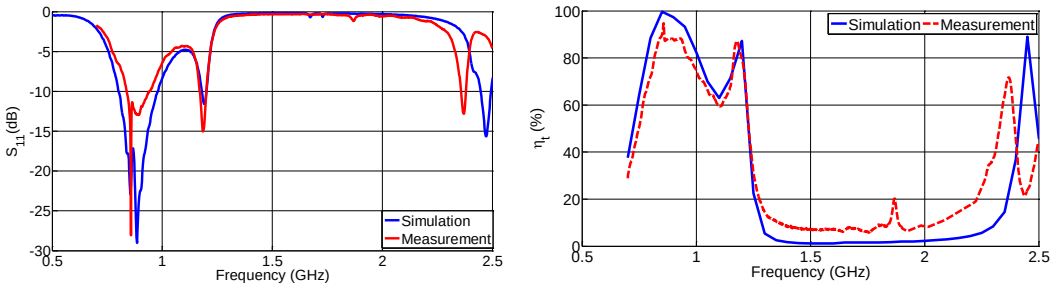


(a) (b)

Figure 2.37: Performance of the measured prototype. (a) Input reflection coefficient, (b) total efficiency.

## 2.9 Conclusion

In this chapter, a systematic approach to design wideband and multiband compact antennas was presented. The technique is based on the combination of the NCM theory with the DE optimization algorithm. The physical insights provided by the modal analysis provides guidelines to determine the suitable loading mechanism that can manipulate the modes and match the antenna in a defined band. In the first section, a literature review about the limitations and the state of the art designs of ESAs was presented. After that, the inductive and capacitive loading of a 5-port dipole was examined to demonstrate the capability to manipulate the modes using reactive loading. Later, the matching method was introduced in details. Various examples have then been presented to validate the approach and two prototypes with optimized internal inductance have been measured with good agreement with respect to the simulations. Furthermore, it was shown that it is possible to achieve very wideband impedance behaviour, while however increasing the complexity of the system in terms of the number of ports and the loading topology.

Fig. 2.38 shows the $B\eta$ (Bandwidth-efficiency) product as function of the electrical size $ka$ of various design presented in literature compared to the wideband antenna with three internal ports which was designed using our methodology. The electrical size of the antennas was calculated by considering its overall size including the ground or its image depending on the size of the ground plane. The blue plot illustrates the $B\eta$ limit that is imposed by the electrical size of the antenna. This limit is given by [100]:

$$BW \times \eta = \frac{1}{\sqrt{2}} \left( \frac{1}{ka} + \frac{1}{(ka)^3} \right)^{-1} \tag{2.15}$$

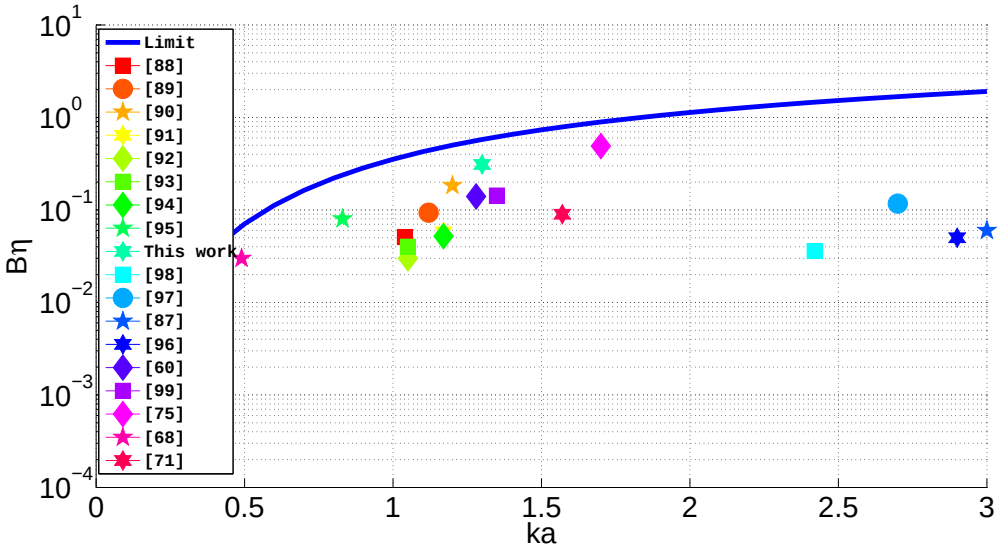


Figure 2.38: Bandwidth-efficiency product comparison of our design to various designs presented in literature

Among the presented designs, our measured antenna with three internal ports (denoted by this work) exhibits an enhanced compromise between bandwidth and efficiency. The $B\eta$ product of this antenna is higher than the other designs presented in literature and approached the designated limit. Therefore, the method developed in this chapter presents a robust approach in designing wideband small antenna while maintaining a good compromise with efficiency and compactness.

On the other hand, we highlighted some limitations that could be encountered during the design procedure. Placing a port in a bad position (where the surface current distribution is low) will not be an effective choice as the modes will be insensitive to any kind of load connected through the bad port. However, a "bad position" is relative to a specific mode, where it might be a good position for a higher order mode, which can be beneficial in designing multiband antennas. This was demonstrated in an example where the design of a multiband antenna using internal loads was investigated. By properly chosing the positions of the loading ports, it was possible to efficiently manipulate the modes and match the antenna in the desired bands. Moreover, it was also shown that in certain case, the method attains a limitation where adding more ports will not have an impact on the overall performance compared to the case where there is less ports. In this case, it becomes mandatory to examine the antenna geometry and apply some modifications in order a desired performance. Therefore, the initial choice of the antenna geometry is very important in facilitating the overall design procedure.

It was also demonstrated that for a simple monopole antenna without a near field parasitic element, an internal negative capacitance is needed to achieve a wideband performance. In the next chapter, we present in details the design of a wideband

electrically small antenna loaded with a negative capacitance. Since the design of a negative capacitor required active components and is associated with losses. The topology of the circuit is considered in the EM simulations and various parametric studies are carried to optimize the overall performance.

# Chapter 3

# Electrically Small Antenna Loaded with Internal non-Foster Circuit for Wideband Matching

## 3.1 Introduction

Foster stated in his reactance theorem [101], that the reactance (or susceptance) of any losseless passive two-terminal device, should have a strictly monotonically increasing slope as a function of frequency:

$$\frac{\delta X(\omega)}{\delta \omega} > 0 \ and \ \frac{\delta B(\omega)}{\delta \omega} > 0 \tag{3.1}$$

If a component does not obey this theorem, it is said to be a "non-Foster" element. In this case, it has a negative slope as a function of frequency. Consequently the reactance of a non-Foster capacitance is represented as $X = \frac{j}{\omega C}$ whereas the reactance of a non-Foster inductor is given by $X = -j\omega L$. This behaviour can be visualized on a smith chart. Contrary to the reactance of a Foster element, the reactance of a non-Foster element moves in anti-clock wise as a function of frequency (Fig.3.1)

With this remarkable property, non-Foster circuits have found an important application for wideband matching of electrically small antennas. Contrary to classical matching networks which normally cancel the reactance at one frequency point. The

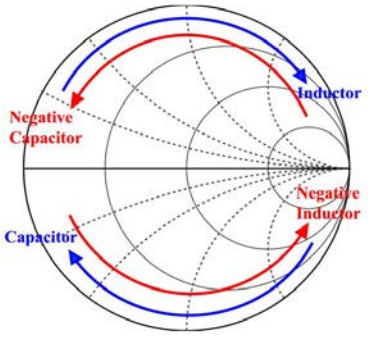


Figure 3.1: Smith chart behaviour of foster and non-foster capacitance and inductance

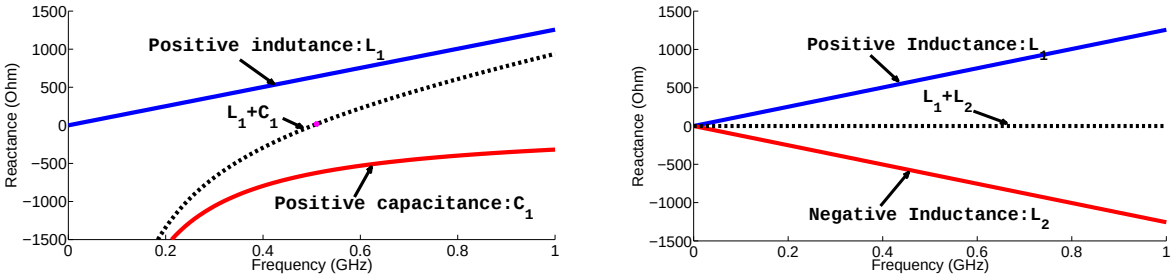


Figure 3.2: Difference between classical matching and non-Foster matching. (a) Inductance connected in series with a capacitance, (b) inductance connected in series to a negative inductance.

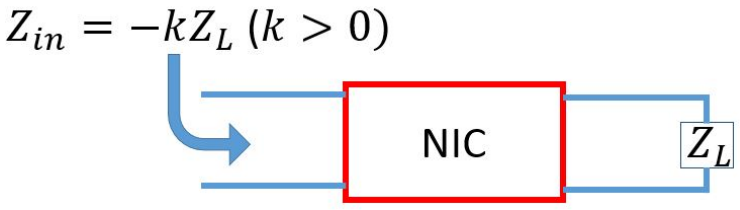


Figure 3.3: Representation of an ideal NIC.

negative slope of the reactance of a non-Foster load as a function of frequency provides the possibility to cancel the high reactance of an electrically small antenna over a wideband (Fig.3.2). This results in a significant reduction in the quality factor of the antenna which makes it more suitable for a wideband matching.

Since all natural passive components exhibit a Foster behaviour. Non-Foster elements are normally implemented through transistor based Negative Impedance Converters (NICs). NIC is defined as an active two port network in which the impedance at one port is the negative of the impedance connected to the other port as shown in Fig.3.3. The main concept of the functionality of a NIC is that it reverses the polarity or the direction of the input voltage (VNIC) or current (INIC) respectively which results in a 180° shift between them. Consequently the impedance seen at the input is negative.

Transistor based NICs were first introduced by Linvill in 1954 which is based on voltage inversion (VNIC) [102]. Fig.3.4a depicts the topology which was used. The two port balanced circuit has its inputs connected to the emitters of the cross-coupled transistors. The entire current $I_1$ flows into the loads ($510Ohm$) which creates a voltage across them. This voltage is then cross-coupled back to the bases of the transistors. The resulting voltage at the input terminal is the negative of that at the loads. A conceptual representation of the voltage inversion inside a NIC is given in Fig.3.4b. Other topologies of VNICs can be found in literature [103, 104]. INICs were also reported in literature [105, 106, 107].

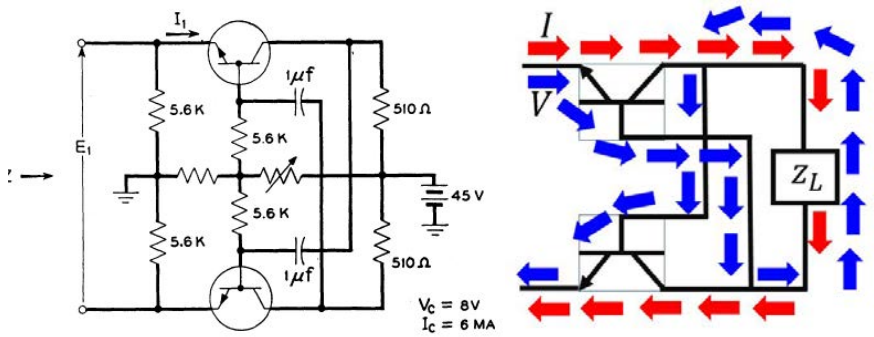


(a) (b)

Figure 3.4: NIC circuits. (a) Linvill's topology, (b) conceptual representation of the voltage inversion of NIC.

Another perspective in realizing non-Foster circuits was introduced by Mirzaei and Eleftheriades in [108]. In this study, the authors established an analogy between non-Foster elements and loss compensated negative group delay (NGD) circuits which are mainly realized using RLC resonators. Such circuits exhibit an increasing phase $\phi$ variation of the scattering parameters as a function of frequency. The group delay $\tau_D$ is defined as:

$$\tau_D = -\frac{\delta\phi}{\delta\omega} \tag{3.2}$$

Similarly, the counter clockwise behaviour of the non-Foster reactance on the Smith chart, indicates that its reflection phase is increasing as well with frequency. Therefore, a loss compensated NGD network was used to realize a T-network of non-Foster elements (Fig.3.5).

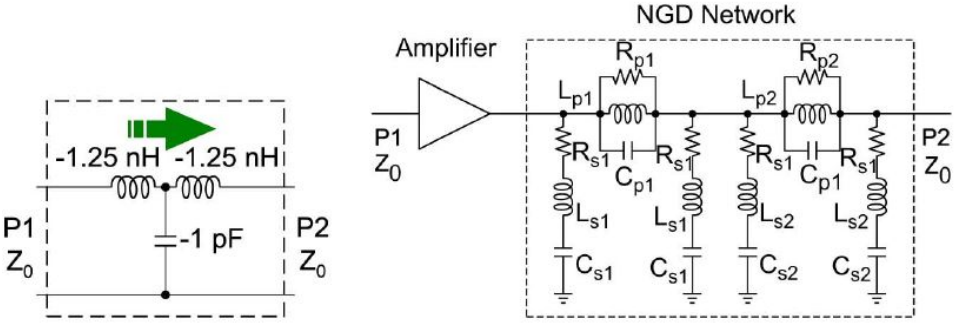


Figure 3.5: Non-Foster T-network realized using an NGD circuit [108].

Recently, Nagargoti *et al.* [109] proposed a new topology for implementing a non-Foster device using Resonant Tunneling Diode (RTD). At certain biasing voltages, RTD behaves as a negative differential resistor (NDR) which maybe transformed to exhibit a negative impedance. This topology serves as a negative impedance inverter (NII), where the impedance of the load is inverted. An inductive load will lead to a negative capacitance and vice-versa. The basic topologies of non-Foster circuits using RTDs is given in Fig.3.6

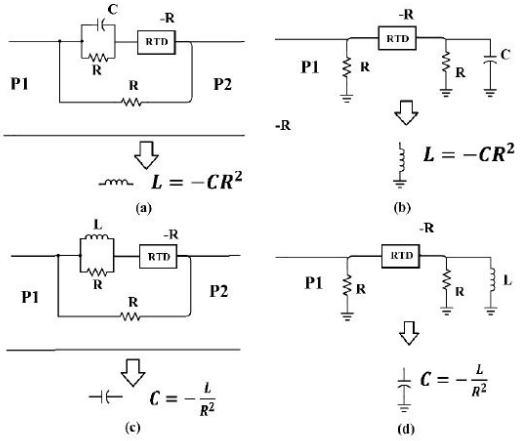


Figure 3.6: Non-Foster circuit topologies using RTD. [109]

After briefly introducing the basic functionality and different remarkable topologies of non-Foster circuits, we present in the next section the various applications of non-Foster circuits which was reported in literature, especially for matching of ESAs.

## 3.2 Application of non-Foster circuits

After introducing and testing the transistorized NIC by Linvill which produced a non-Foster element, extensive researches have been dedicated since then to design various non-Foster circuits for different RF applications. The most common application of non-Foster circuits in antenna engineering is the wideband active matching of ESAs. Wideband matching using non-Foster elements can be separated into two categories: input matching and embedded matching.

### 3.2.1 Input Matching

Early work on non-Foster circuits to match ESAs was reported by Harris and Myers in 1968 [104]. Their study began by extracting the RC equivalent circuit of an electrically small monopole antenna in the HF band. The equivalent circuit was then converted into RC parallel circuit. A shunt negative capacitor is then added at the input of the antenna in order to cancel its high capacitive reactance over a wide frequency range. However, this did not insure matching the antenna since its resistance is proportional to $Q^2$, which makes it frequency dependent and significantly larger. The schematic description of the work done by Harris and Myers is given in Fig.3.7. Although the wideband matching was not achieved, a significant enhancement in terms of gain was noticed for the ESA monopole loaded with a negative capacitor.

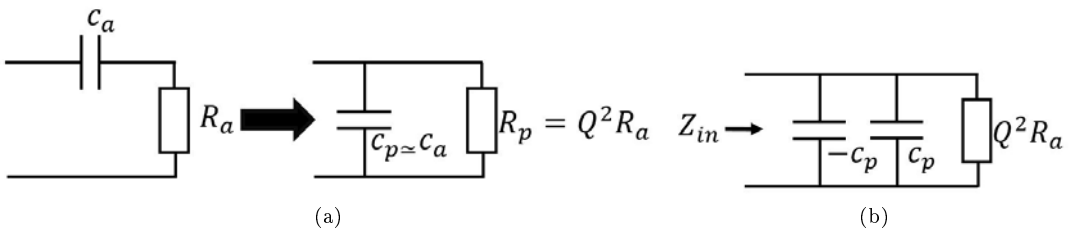


Figure 3.7: Schematic of eliminating the reactance of the antenna using non-Foster input reactance. (a) Series to parallel circuit conversion, (b) negative shunt capacitance at the input of terminal to eliminate the reactance of the antenna.

To eleminate the frequency squared dependence of the resistance of the electrically small dipole antenna, Skahill [111] proposed the matching scheme given in Fig.3.8. The negative capacitance will effectively compensate the reactance of the antenna. However, as stated in the previous paragraph, this does not ensure the matching of the antenna. Consequently, a T-network with a negative shunt inductance is connected in series with the negative capacitance. This network serves in as an impedance transformer where it eliminates the frequency dependence of the real part of the antenna impedance. With the right choice of the inductance value, a wideband matching can be achieved. Nevertheless, this scheme seemed to be complicated and difficult to implement.

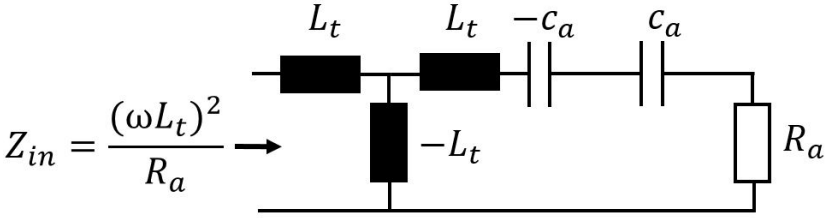


Figure 3.8: Skahill matching scheme using negative capacitance and non-Foster T transformer.

Aberle [112] proposed a similar matching approach while however considering a two-port representation of an antenna. With this representation it was possible to use circuit simulators to optimize the components of the non-Foster circuit in order to achieve a wideband matching while also considering the radiation efficiency.

Using the RTD non-Foster circuit, Nagargoti *et al.* achieved a wideband matching of an antenna in the VHF/UHF bands [109]. Two stages of non-Foster circuits were used for this purpose Fig.3.9a. The circuit directly connected to the antenna cancels the capacitive reactance leaving an approximately real impedance. The second stage is then used to transform the frequency-dependent resistance to match it to the source impedance. By changing the key parameters in the circuits it was possible to match the antenna in different bands Fig.3.9b.

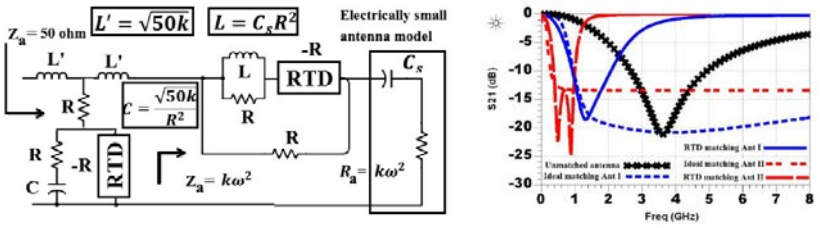


(a) (b)

Figure 3.9: Input matching network of ESA based on RTD non-Foster circuits. (a) Schematic representaion of the matching network with the antenna, (b) input matching network of matched and unmatched antennas.[109]

Without using two stage non-Foster matching network, the authors in [113] succeeded to show in simulation that it was to possible match an electrically small half loop antenna in a wideband, using a negative parallel LC load at the input of the antenna. With the help of the full wave simulation, the equivalent circuit model of the antenna was extracted, and then it was shown that a parallel negative LC element connected at the input can cancel a large part of the reactance and match the input resistance to the source in a wideband.

It is also worth mentioning the work done by Fort and Rudish in [114]. Although the authors did not address specifically the input matching of ESAs using non-Foster loads. They have demonstrated that loading the input of the antenna with a non-Foster circuit can have a significant effect on enhancing its signal-to-noise ratio (SNR) and its power efficiency as compared to passive matching.

In this section, a literature review on input non-Foster matching have been presented. Placing a non-Foster load at the input of an ESA can significantly compensate its reactance. However, in most cases, the frequency-dependence of the resistive part presents an issue in limiting the practical operational bandwidth of the antenna. In consequence, another non-Foster circuit is connected to eliminate this dependence and match the resistance to the source which results in a wideband antenna. However, introducing multiple non-Foster circuits in a system will add more complexity to the design in addition to deteriorating the overall efficiency due to the resistive losses dissipated by the active circuit. Embedded non-Foster matching can be a better alternative compared to the traditional input matching. As demonstrated in the previous chapter, embedding load inside the antenna can effectively manipulate the currents to match it in a wideband. Therefore, a proper internal non-Foster load can significantly compensate the reactance of the ESA while simultaneously matching its resistance to the source. In the next section we present as state of the art review on some of the remarked researches that focused on wideband ESAs using embedded non-Foster loads.

### 3.2.2 Embedded Matching

Embedded non-Foster matching was first proposed by Di Nallo *et al.* in 2007 [115]. The approach was applied on a PIFA antenna mounted on a finite ground plane which can be considered as a hand-held device (Fig.3.10a). Two ports are considered inside the antenna, one port is coupled with the signal and the other is chosen to be reactively loaded. By tuning the reactance needed at each Frequency to match the antenna, it was concluded that a negative inductance connected at the second port

can achieve a wideband matching over the desired band (Fig.3.10b).

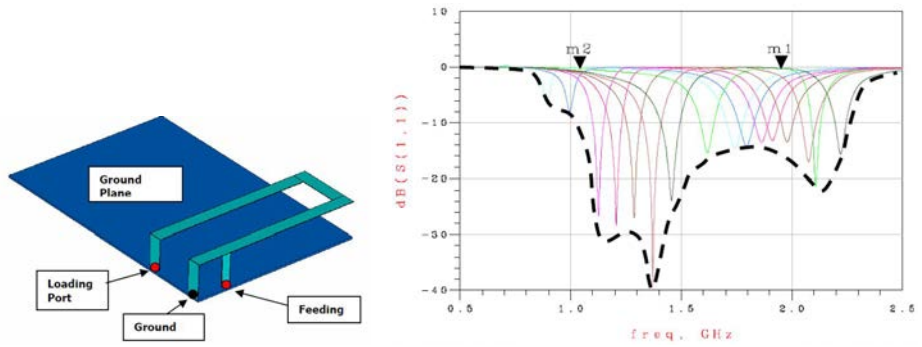


(a) (b)

Figure 3.10: Embedded non-Foster matching of PIFA. (a) Antenna configuration, (b) input reflection coefficient of the antenna loaded with non-Foster circuit.[115]

Later Jin and Ziolkowski derived an internal matching approach for wideband ESA matching [72]. The scheme focused mainly on matching meta-material-inspired antennas which have an extremely small electrical size and a very narrow bandwidth. By modeling the antenna and the internal matching network in terms of their ABCD matrix, it was possible to calculate the reactance values that can perfectly match the antenna in a wideband. The decreasing variation of the internal load reactance as a function of frequency indicated the need of a negative inductor as internal load to achieve the desired wideband.

The first practical implementation of wideband ESA with internal non-Foster element was reported by Zhu and Ziolkowski in [73]. The design was also applied on a metamaterial inspired antenna where near field parasitic element was loaded with a series negative LC (Fig.3.11a). The loaded antenna of size $ka = 0.49$ successfully achieved a 10% fractional wideband around $300MHz$ as shown in Fig.3.11b. Various metamaterial inspired antenna embedded with non-Foster circuits were later reported by Ziolkowski and his research group [116, 117]. Another practical implementation of embedded non-Foster matching was later reported in [118]. With an internal non-Foster circuit a resonant printed monopole antenna of size $ka = 0.58$ was matched in a broadband achieving a maximal fractional bandwidth of 8.3% in the UHF band around $400MHz$. Although the efficiency of the realized system was not mentioned, a comparison between the active antenna and a corresponding passive antenna was done. It was then shown that an active antenna had a better received signal compared to the passive one. However, these aforementioned designs dealt with a particular case where the antennas are already resonant in their electrically small domain and the embedded non-Foster circuit is used solely to increase the bandwidth in the resonance domain without miniaturizing the antenna.


(a) (b)

Figure 3.11: Practical implementation of wideband ESA internally loaded with non-Foster circuit. (a) Loaded antenna, (b) input reflection coefficient.[73]

Recently Vargas *et al.* proposed a global methodology for the design of actively matched antenna regardless its geometry[119]. In this study the antenna and the non-Foster network are considered as a whole system (Fig.3.12), and the impedance $Z_{NIC}$ is calculated such that the input reflection coefficienct $\Gamma_{in} = 0$ to insure perfect matching, in addition the sensitivity of the impedance matching with respect to the variations in $Z_{NIC}$ is studied. The position of the NIC is then chosen in the location where the antenna exhibits the lowest sensitivity to the changes in $Z_{NIC}$. With this method a half loop antenna was miniaturized and matched in over 100% bandwidth. However the resistive loss added by the NIC have contributed in expanding this bandwidth in addition to degrading the total efficiency which attained 9.6%. Here it is important to mention that the lowest NIC sensitivity was found on the other side of the loop i.e. the farthest position from the input port. This also verifies the sensitivity results presented in [120] where it was shown that slight changes in the values of a negative load connected at the input of a half-loop antenna can have dramatic changes on its impedance matching, however this sensitivity decreases with the negative load embedded inside the antenna.

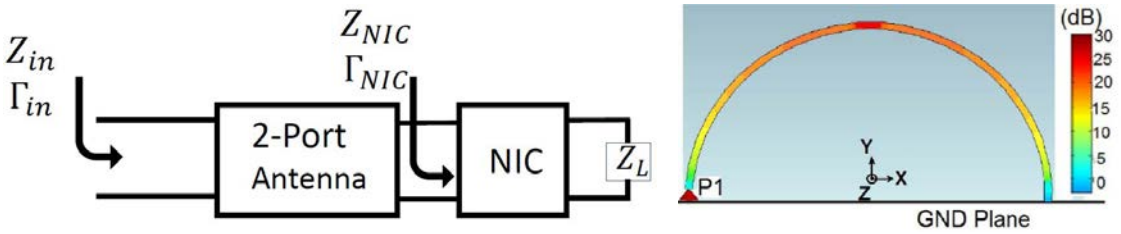


(a) (b)

Figure 3.12: (a) Active matching for a two port antenna. (b) Sensitivity of $Z_{NIC}$ over the antenna structure [119]

The Characteristic modes theory was also used to determine the best non-Foster load values that can match the antenna in a desired band [57, 59]. This was mentioned and explained in the previous chapter.

Embedding non-Foster circuits inside the antenna for the purpose of matching have proven to be an effective alternative compared to the traditional input active matching. Placing the load inside the antenna, can provide a better control on the radiating currents and hence wider bandwidth can be achieved if the proper load is introduced. On the other hand, input active matching introduces the need for a transformation network in addition to the non-Foster load. The non-Foster load serves in compensating the reactance of the antenna whereas the transformer net-

work eliminates the frequency dependence of the resistance and matches it to the source. Furthermore, it was also shown that the sensitivity of the bandwidth of the antenna with respect to the variations in the NIC impedance reduces when the active circuit is integrated inside the antenna. Therefore, Embedded non-Foster matching presents an advantageous approach compared to input non-Foster matching. Nevertheless, in both matching cases, it is noticed that the practical implementation of actively matched antenna are limited to targeting frequency bands below $500MHz$. The lack of practical study of non-Foster matching at higher bands is due to the fact that the design of such circuits becomes more constrained by stability, the non-linearity of the active components and the effect of their parasitic elements, which might eventually limit the possibility to optimize the performance of the circuit. In the next section, we present a non-Foster matching circuit that have been developed in IETR. This circuit was used as an input matching network for an electrically small ILA antenna to achieve a wideband matching at frequencies above $800MHz$. However, the active antenna did not present an optimal performance due to the resistive loss dissipated by the circuit.

## 3.3 previous work in IETR

Previous work in IETR focused on a challenging task which was the design of a NIC to obtain a small negative capacitance $C = -0.87pF$ for a frequency higher than $900MHz$ [121]. This was the lowest reported negative capacitance value produced by a NIC circuit. This small capacitance was realized by using the parasitic capacitors of the transistors. The topology of the circuit is an optimized Linvill floating type NIC presented in Fig.3.13. As can be seen there is no capacitance connected in the feedback path. Only a resistance $R_L = 62Ohm$ is placed in order to compensate the input resistance of the circuit and reduces its losses. To ensure the stability of the circuit the stability factor $\mu$ given in (3.3) and (3.4) was studied. It was shown that the circuit is unconditionally stable starting from $1.61GHz$ (Fig.3.14a). The stabilization possibilities of the circuit were then studied using stability circles showing that a capacitive load is required to stabilize it (Fig.3.14b).

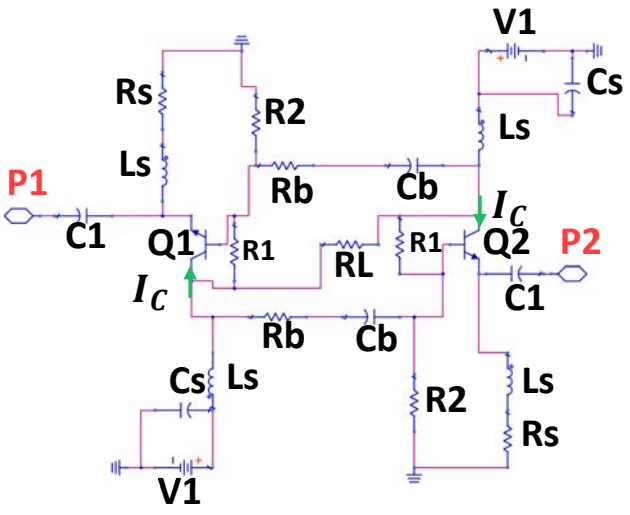


Figure 3.13: Schematic of the proposed NIC

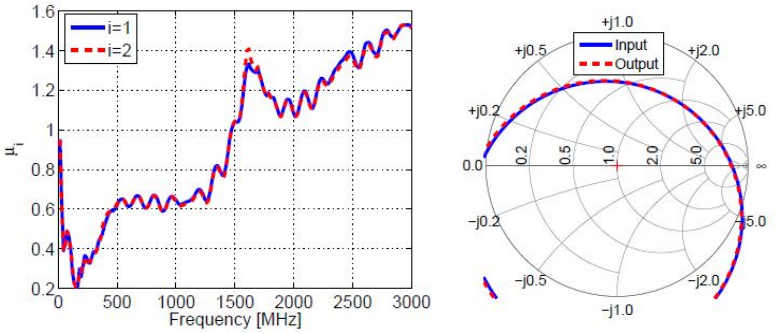


(a) (b)

Figure 3.14: NIC characteristics. (a) Stability $\mu$ factor, (b) stability circle at 510 MHz. [121]

The circuit was connected at the input of an ILA antenna Fig.(3.15a). The negative capacitance successfully compensated the capacitive reactance of the ILA antenna which was therefore miniaturized and matched in a 92% bandwidth [0.86 – 2.33$GHz$] compared to a 12% bandwidth of the original unloaded antenna (Fig.3.15b,c) which was matched around 2.4$GHz$. Nevertheless, the losses which were still dissipated in the circuit affected the overall efficiency especially in the low frequency band where it attained 12% (Fig.3.15d). It should also be noted that the resistive losses have also played a role in significantly enlarging the matching bandwidth.

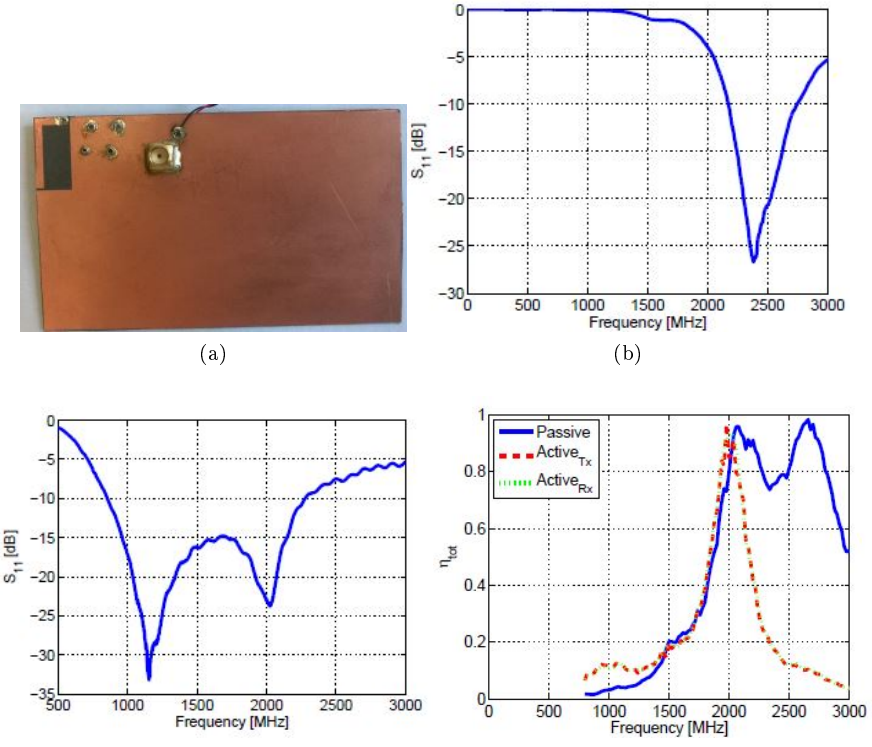


(a) (b)

(c) (d)

Figure 3.15: Inverted L antenna with input non-Foster circuit.(a) Prototype, (b) input reflection coefficienct of the original ILA, (c) input reflection coefficient of the matched ILA,(d) efficiency of the active and passive ILA.[121]

$$\mu_1 = \frac{1 - |S_{11}|^2}{|S_{22} - (S_{11}S_{22} - S_{21}S_{12})S_{11}^*| + |S_{12}S_{21}|} \tag{3.3}$$

$$\mu_2 = \frac{1 - |S_{22}|^2}{|S_{11} - (S_{11}S_{22} - S_{21}S_{12})S_{22}^*| + |S_{12}S_{21}|} \tag{3.4}$$

Therefore a wideband electrically small ILA was designed using an input non-Foster matching. The stable non-Foster circuit produced a sufficiently low negative capacitance which was capable to compensate the reactance of the antenna and miniaturize it. The negative capacitance along with the resistive losses dissipated by the NIC insured the matching of the antenna in a wideband. However, in the previous section it was shown that internal non-Foster matching is a better alternative since along with compensating the reactance, it provides better control on the real part of the antenna to insure a wideband impedance matching. Moreover, embedding the NIC circuit inside the antenna away from the feeding point can also reduce the effect of the resistive loss which is inevitable in this kinds of circuits and hence a better overall efficiency can be achieved.

In the next section, we present the design and fabrication of an electrically small antenna internally loaded with a NIC producing a negative capacitance. The NIC topology is similar to the one used in this section (Fig.3.13a). Yet we propose considering the EM model of the NIC while simulating the antenna. This approach offers the possibility to identify the key elements in the active circuit that affect the overall performance of the system. These elements are then changed accordingly in order to optimize the efficiency of the antenna while maintaining a wideband impedance matching.

## 3.4 Internally loaded antenna

It has been clearly noted the advantage of internal active matching instead of input active matching. A systematic design of a wideband electrically small monopole antenna embedded with a non-Foster circuit will be presented in this section. The monopole has a natural resonance frequency at $2.2GHz$. The non-Foster circuit is then embedded to miniaturize the antenna and match it in a wideband. Unlike most of the practical design for embedded non-Foster matching, the antenna is just a simple monopole with no parasitic elements in its near field. In this case, achieving a wideband matching in the electrically small domain of the antenna becomes more challenging since it is required first to miniaturise the antenna, then match its resistance to the source. To accurately model the effect of the non-Foster circuit inside the antenna, the EM model of the circuit is taken into account. Given that the behaviour of the NIC is sensitive to its layout configuration [122], the EM model of the NIC in the full wave simulation of the antenna is introduced to accurately predict the measured results. This consequently provides the possibility to optimize the location of the NIC inside the circuit in addition to its critical parameters in order to reduce the resistive loss of the active circuit while maintaining a stable behaviour and a wideband matching.

### 3.4.1 Antenna with Ideal Negative Capacitance

The geometry of the unloaded antenna is shown in Fig.3.16. The antenna is a bent monopole integrated on a PCB and mounted on a Rogers RO5880 substrate ($\epsilon_r$ = 2.2, $tan\delta$ = 0.0009). The overall dimensions of the structure is ($90mm \times 35mm$) while the radiating part is confined to ($10mm \times 23mm$). The input reflection coefficient and impedance behaviour of the antenna are shown in Fig.3.17. The antenna resonates at $2.2GHz$, while having a significant capacitive reactance below this frequency.

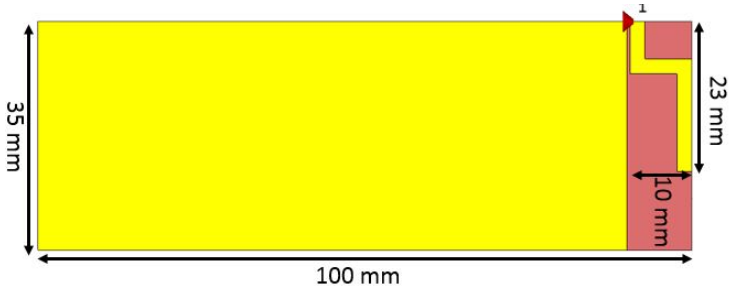


Figure 3.16: Geometry of the unloaded antenna

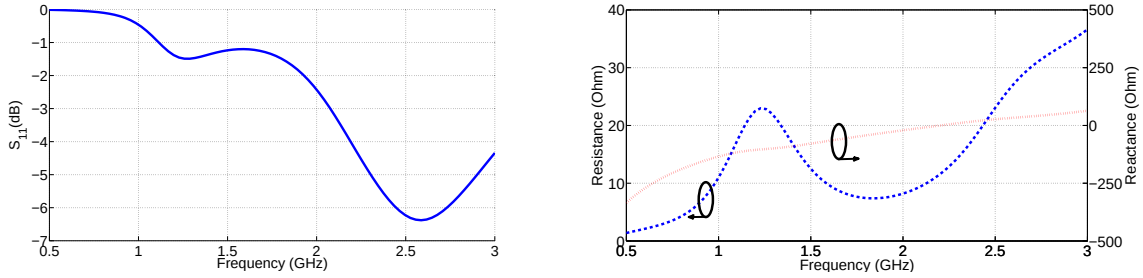


Figure 3.17: Simulated antenna parameters (a) Input reflection coefficient, (b) input impedance.

In order to miniaturize the antenna, its capacitive reactance should be compensated. The surface current distribution of the antenna at $1GHz$ is given in Fig.3.18a. Following the distributed matching methodology presented in the previous chapter, an internal port (port 2) is defined at $3.8mm$ from the feeding point Fig.3.18b. At this position, the antenna exhibits a relatively high surface current distribution. Therefore a load placed at this position can efficiently control the impedance of the NCMs in order to match the antenna in a wideband. Using this method, the optimal capacitive value needed to miniaturize the antenna and match it in a lower frequency band is found to be $C = -0.87pF$, which resembles the optimal capacitive value obtained in the previous chapter for the S-shaped monopole. With this negative capacitance connected at the second port, the antenna is matched in a wide bandwidth $[1.06 - 1.44GHz]$ which represents 30% of the central frequency. The antenna's resonance frequency shifts to $1.25GHz$ at which its electric size is $ka = 0.31$ ($ka = 1.2$ considering the dimensions of the ground plane). Hence the negative capacitive load miniaturizes the antenna by a factor of 2.2. A comparison between the input reflection coefficient of the loaded and unloaded antennas is shown in Fig.3.19.

(a)


(b)

Figure 3.18: (a) Current distribution of the antenna at $1GHz$, (b) geometry of the two port antenna

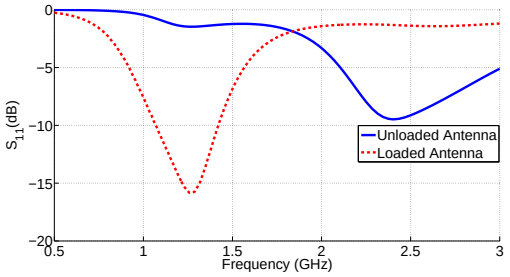


Figure 3.19: Input reflection coefficient of the unloaded and loaded antennas

After showing the possibility of miniaturizing and matching the antenna using and ideal negative capacitor, the next section presents the integration of the realistic model of the non-Foster circuit at the second port of the antenna. The effect of this integration is studied and appropriate modifications are performed to optimize the performance.

### 3.4.2 NIC Circuit Topology

After determining the ideal non-Foster load value that is capable to miniaturize and match the antenna in a wideband, in this section we present the NIC circuit design. To obtain a negative capacitance, a linvill floating type NIC circuit is considered. The schematic of the circuit was shown in the previous section in Fig.3.13a. Two BJT transistors connected through a feedback path with a resistance $R_L$. The transistors used are BFR93A. Rather than including a capacitance in the feedback path, the parasitic capacitance of the transistors is used to generated the desired negative capacitance. Fig.3.20 shows the capacitive behaviour of the circuit. It is evident that the circuit generates a negative capacitance over the whole band. In the band of interest, the value of the capacitance is almost equal to $-0.87pF$ which corresponds to the optimized value required to match the antenna in a wideband. The initial parameters of the circuit components is given in Table. 3.1. As mentioned

in the previous section, the stability of the circuit have been studied showing that it can be stable if it is connected to a capacitive load which is compatible with the case of a monopole antenna that acts as a capacitance.

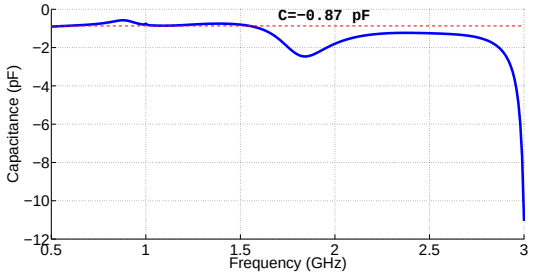


Figure 3.20: De-embedded capacitance of the NIC circuit.

Table 3.1: Initial circuit parameters

| | | | |
|---|---|---|---|
| C1 | 100 pF | Ls | 470 nH |
| Cs | 33 nF | Rs | 100 Ohm |
| Cb | 100 pF | Rb | 100 Ohm |

### 3.4.3 Antenna With Integrated NIC Circuit

After designing the schematic NIC circuit, the next step is to integrate the circuit inside the antenna. However in order to obtain accurate results, the EM model of the NIC circuit is taken into account in the full wave simulation of the antenna. In this section, we study the effect of the circuit position on the antenna's matching and efficiency. Moreover, a parametric study of the key circuit components that can enhance the overall system performance. Two cases are taken into account, in which we show that a slight change in the NIC topology while maintaining the same component values can have an impact on the impedance bandwidth and efficiency of the antenna.

#### 3.4.3.1 Case 1

The initial geometry of the antenna with the NIC circuit is given in Fig. 3.21. Due to the dimensions of the NIC circuit, the first arm of the monopole is increased by $5mm$ in order to properly fit the NIC inside the given dimensions (Fig. 3.21a). This increase will just result in shifting the resonance frequency of the antenna. A $0.5mm$ gap is cut in the antenna. At each end of the gap, a via is connected to a terminal of the NIC which is located on the bottom side of the antenna (Fig. 3.21b). To predict the behaviour of the antenna in the presence of NIC, each component in the circuit is defined as a discrete port, which yields to an overall network of 27 ports. After running the full wave simulation in CST [84], each port in the network is connected to its corresponding circuit element in post processing. The association of the ports to the components is given in Fig. 3.21. $C, B, E$ corresponds respectively to the collector,base, and emitter of the BJT. The input reflection coefficient and the total efficiency of the antenna is given in Fig. 3.22a. With $I_c$ = $2.95mA$ the antenna is matched in a wide band $[1-2.04GHz]$ (66%) which is larger than the one with ideal

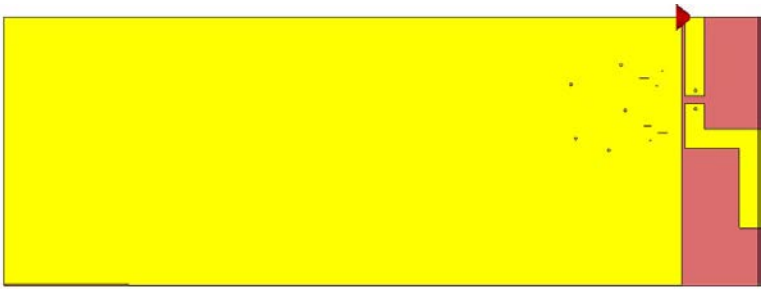

(a)

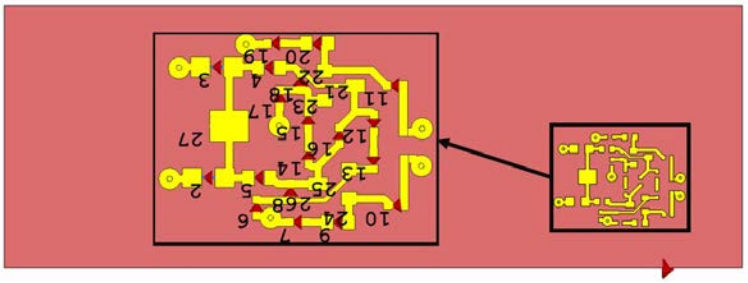

(b)

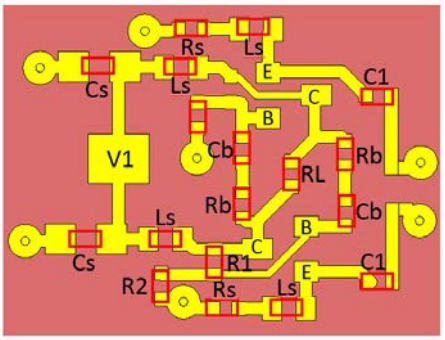


(c)

Figure 3.21: Geometry of the antenna with internal NIC(a) Top view, (b) bottom view, (c) EM NIC model with associated elements

capacitance. However, the overall system efficiency is very low in the whole band ($\eta_{max}$ = 2.7%). To investigate the effect of the NIC in producing this low efficiency, two external ports are placed at the vias connecting the terminals of the NIC to the antenna. With this configuration, we are able to calculate the transmission coefficient of the NIC circuit. Fig.3.22b shows the transmission coefficient of the NIC in the given configuration. In the operating bandwidth, more than $11dB$ of the power is lost inside the active circuit, which explains the degradation in the efficiency.

A more physical explanation of the very low efficiency can be given regarding the electromagnetic interaction between the antenna and the circuit. Since the NIC is embedded inside of the antenna, the current of the antenna should pass inside this circuit. Moreover, this current is supposed to radiate. However, the ground plane which is placed directly above the circuit will prevent the current traversing its transmission lines to radiate, resulting in a significant degradation in efficiency. Therefore, placing a gap above the transmission lines of the NIC (where the useful

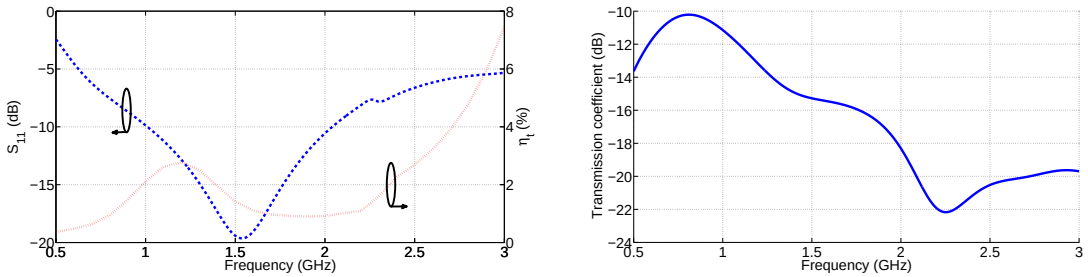


(a) (b)

Figure 3.22: Parameters of the proposed antenna with active circuit. (a) Input reflection coefficient and efficiency, (b) transmission coefficient of the NIC circuit.

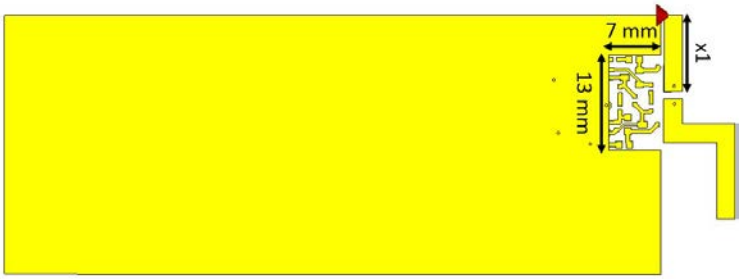


(a)

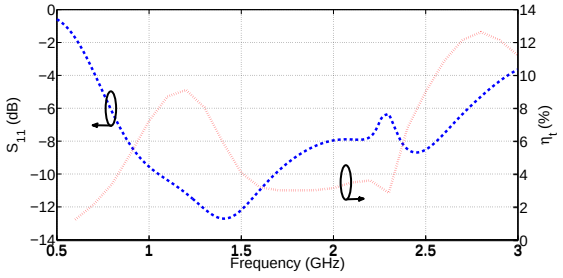


(b)

Figure 3.23: Antenna with slot in the ground plane. (a) Geometry of the antenna, (b) input reflection coefficient and efficiency.

current of the antenna passes) will allow the current to radiate, hence resulting in an increase in the efficiency. A gap of size $13mm \times 7mm$ is etched in the ground plane of the antenna, exactly above the circuit. Fig. 3.23a shows the geometry of the antenna with the gap. The substrate is made transparent to visualize the NIC circuit on the bottom side. With this configuration the antenna is matched in a wide bandwidth $[1.05 - 1.68GHz]$ (46%) for a DC feed $I_c = 4.7mA$, in addition to an increase in the overall efficiency in the operating bandwidth ($\eta_{max} = 9\%$) at $1.2GHz$ which represents an enhancement by a factor of 3 with respect to the initial configuration.

Fig. 3.24 shows the difference in the surface current distribution inside the NIC with and without a gap in the ground plane. As explained previously, the gap in the ground plane will allow the current traversing the NIC transmission lines to radiate radiate which is clear by comparing the two cases where in Fig. 3.24a the current in the NIC is almost null while in the second case, the current inside the NIC

exhibits a high surface current distribution indicating that this part of the system is participating in the radiation (Fig. 3.24b).

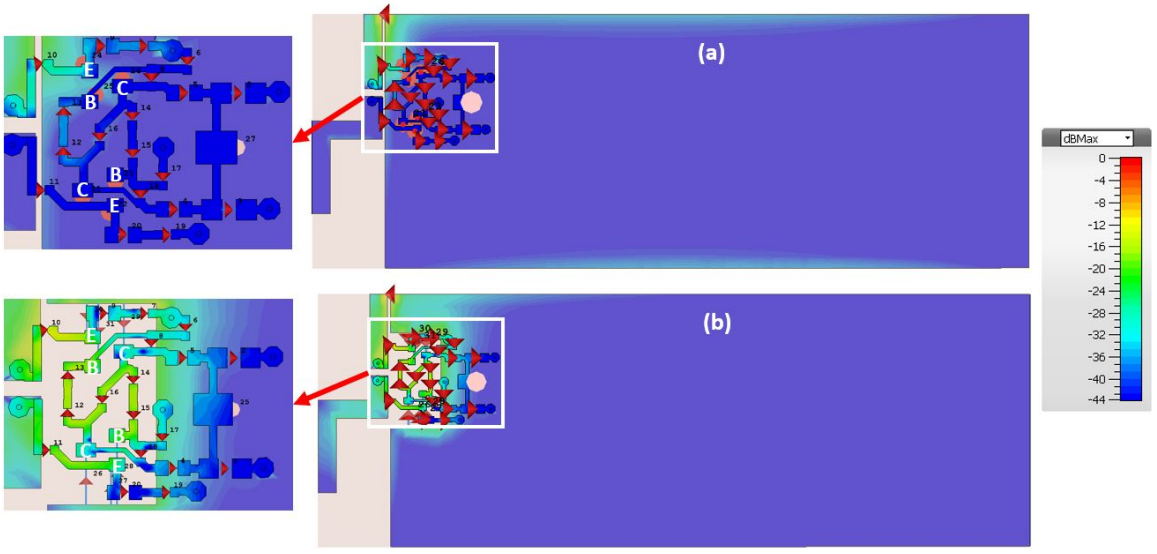


Figure 3.24: Surface current distribution of the antenna with embedded NIC at 1GHz. (a) With full ground plane, (b) with slotted ground plane.

On the other hand, using the suggested modeling, it is possible to launch a parametric study to show the effect of the different components in the NIC circuit on the performance of the antenna using the post processing in CST. Therefore, we are then more capable of optimizing the performance of the active antenna to find the best compromise between the bandwidth and efficiency. After running various parametric studies, we notice that there are two components that affect the efficiency of the circuit. These components are the choke inductance $Ls$ and the base resistance $Rb$. The parametric study is carried out in the band of interest between $0.8GHz$ and $1.6GHz$.

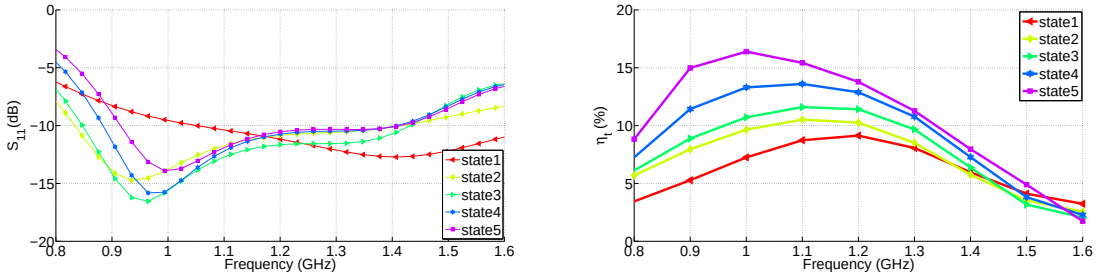


Figure 3.25: Variation of the antenna performance as a function of $R_b$ and $L_s$. (a) Input reflection coefficient, (b) total efficiency.

Fig.3.25 shows the variation of the antenna performance as a function of $R_b$ and $L_s$. Each parametric change of these components is represented by a state, whose values are given in Table 3.2. In the first three states, the value of $L_s$ was fixed

Table 3.2: Parametric values of $R_b$, $L_s$, and $I_c$ for different states

| state | $R_b$ ($\Omega$) | $L_s$ (nH) | $I_c$ (mA) | $BW$ (%) | $\eta_t$(%) |
|---|---|---|---|---|---|
| 1 | 100 | 470 | 4.7 | 46 | 9 |
| 2 | 60 | 470 | 5.7 | 52 | 10.5 |
| 3 | 20 | 470 | 4.1 | 51.2 | 12 |
| 4 | 20 | 270 | 2.95 | 45 | 13.5 |
| 5 | 20 | 220 | 2.5 | 43.7 | 17 |

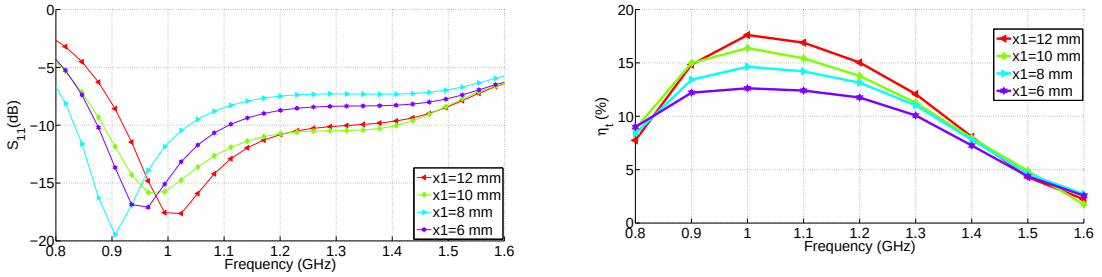


(a) (b)

Figure 3.26: Variation of the antenna performance as a function of the NIC position. (a) Input reflection coefficient, (b) total efficiency

to $470nH$ while the value of $R_b$ was decreased from $100Ohm$ to $20Ohm$. At each state, the DC feed $V1$ is also varied to ensure the correct excitation of the transistor so that the NIC circuit functions properly. We notice that as the value of the base resistance $R_b$ decreases the total efficiency of the circuit increases up to 12% with a corresponding relative bandwidth of 51.2%. Moreover, while fixing the value of $R_b$ to $20Ohm$ and decreasing the value of $L_s$ to $220nH$, the total efficiency increases up to 17% with a corresponding relative bandwidth of 43.7%. Therefore, by performing a parametric study on the values of $R_b$ and $L_s$ it was possible to increase the total efficiency of the active antenna from 9% up to 17% while maintaining a wideband impedance matching. As the values of $R_b$ and $L_s$ decrease, the resistive effect of the NIC circuit decreases and hence the total efficiency increases. It should be noted that at high frequencies, the parasitic components of the inductance start to play an important role in the overall circuit behaviour, therefore it is important to correctly model the inductors in order to accurately predict the overall system performance. In the simulations, the s2p touchstone files of the Murata LQW18AN library are used to model $L_s$ [85]. By using those realistic touchstone files, the parasitic elements of the inductors are taken into account, and hence accurate results can be obtained.

On the other hand, it is also important to study the effect of the circuit position on the overall system performance. Fig. 3.26 shows the variation of the antenna performance as a function of the circuit position ($x1$) with respect to the feeding point with the optimized components values $R_b$ = $20Ohm$ and $L_s$ = $220nH$. As expected the overall efficiency of the antenna drops as the circuit approaches the feeding point. Therefore, as the NIC circuit approaches the feed point, its resistive effect becomes more important, resulting in a decrease in the efficiency. For a distance of $x1$ = $10mm$ the antenna exhibits the best trade off between bandwidth (43.7%) and efficiency (17%).

#### 3.4.3.2 Case 2

In this section we study the effect of changing the topology of the NIC circuit on the overall system performance. By looking at the surface current distribution of the antenna and the NIC, it can be shown that the current traversing the transmission lines of the NIC (the ones directly connected to the antenna) is circulating in opposition with respect to the antenna currents located just above these transmission lines (Fig. 3.27). Therefore part of the radiated power will be canceled due to this opposition.

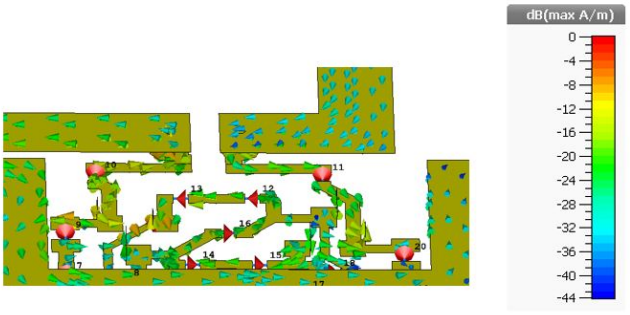


Figure 3.27: Vector surface current distribution of the NIC with the antenna

To avoid this drawback, the transmission lines of NIC causing this current opposition should be eliminated. Therefore, a new NIC topology is considered where the terminals of the NIC are separated by $8mm$ rather than $2mm$ (Fig.3.28b). In order to integrate the active circuit, the gap of the internal port is increased to $7.5mm$. To compensate the introduced gap, the terminal section of the antenna is enlarged by $7mm$ (Fig. 3.28a). With this new configuration, the current opposition caused by the NIC transmission lines is eliminate Fig. 3.29

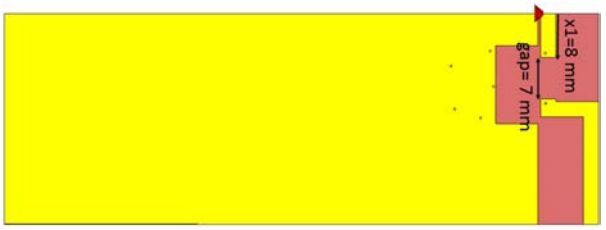


(a)

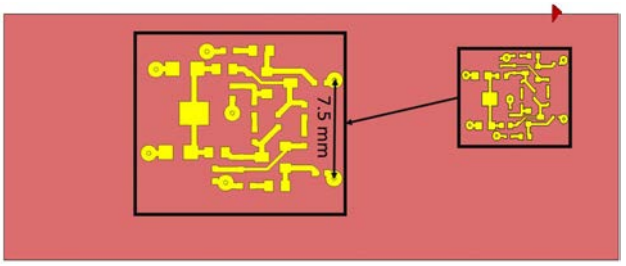


(b)

Figure 3.28: Geometry of the antenna with modified NIC topology. (a) Top view, (b) bottom view.

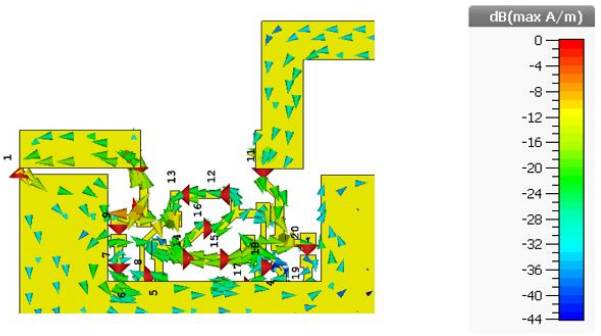


Figure 3.29: Vector surface current distribution of the antenna with modified NIC

Following the same procedure presented in the previous example, it was found that the antenna exhibits the best performance for $R_b = 20Ohm$, $L_s = 220nH$, and with a separation distance $x1 = 8mm$. This is the maximal separation distance in this case, since the increased gap approaches the terminal of the NIC towards the feed point. With this configuration, the antenna is matched in a wideband $[0.87 - 1.45GHz]$ which corresponds to 50% relative bandwidth. Moreover, a maximal efficiency of 24% is achieved at $1.2GHz$ while the efficiency remains higher than 20% in most of the band . Compared to the previous case, the modified NIC topology shows a better performance for both bandwidth and efficiency Fig.3.30. So, even a slight change in the NIC topology in terms of the terminal positions and configuration results in a change in performance. Hence, in an actively matched antenna, it is important to take the NIC model in the full wave simulation, in order to determine the best position, topology and component values that can improve the overall performance.

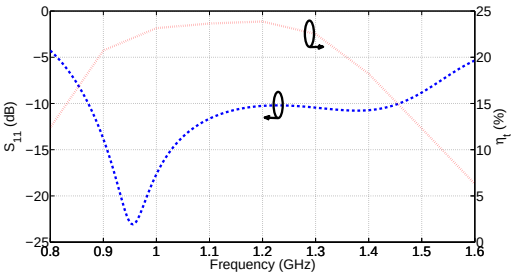


Figure 3.30: Input reflection coefficient and total efficiency of the antenna with modified NIC topology.

### 3.4.4 Experimental Validation

Two prototypes of the previous cases have been fabricated. The prototype of case 1 is shown in Fig. 3.31 with the antenna printed on the top side and the NIC circuit on the bottom connected through vias. As stated in section II, the antenna is printed on a Rogers RO5880 substrate ($\epsilon_r = 2.5, tan\delta = 0.0009$). The measured input reflection coefficient of both cases is shown in Fig. 3.32. For case 1, the measured active antenna is driven by $I_c = 2.95mA$ and is matched in a wideband $[1.02 - 1.63GHz]$ which represents 45.6% relative bandwidth. This result agrees with the simulated

antenna driven by the same DC voltage and having a relative bandwidth of 43.7%. However, the measured antenna exhibits a shift in the resonance frequency with respect to the simulation. Moreover, the measured results of the case 2 are also in good agreement with the simulation. The measured antenna driven by $I_c = 2.5mA$ is wideband and matched in 58.7% relative bandwidth ($[0.9-1.66GHz]$). It should be noted that using the NIC circuit, the antenna achieves a wider bandwidth compared to the ideal capacitance case presented in section II. This is due to the existing resistive loss in the circuit that causes this increase in the bandwidth.

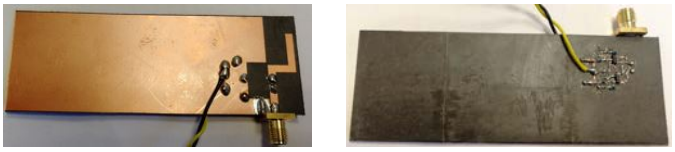

(a) (b)

Figure 3.31: Prototype of case 1. (a) Top view, (b) bottom view.

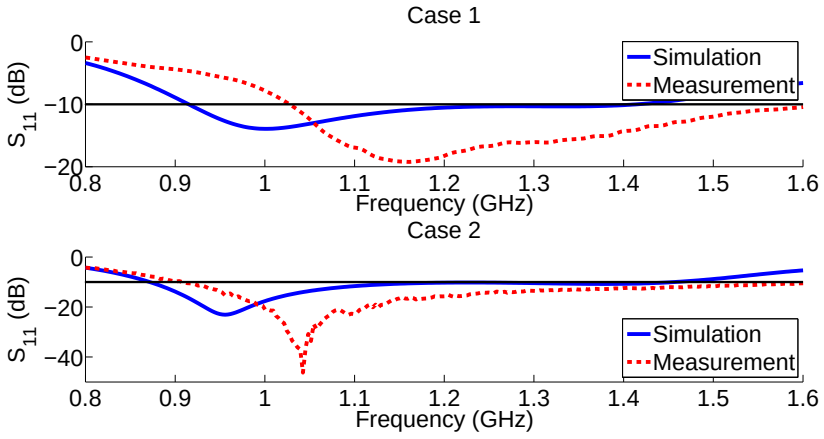


Figure 3.32: Input reflection coefficients of the measured active antennas.

On the other hand, the measured efficiency of both cases is presented in Fig. 3.33. As predicted in simulation, the antenna of case 1 attains a maximal efficiency of 18% and a 23% for case 2. Fig. 3.34a shows the comparison between the realized gain of the passive antennas and the active antennas. In its bandwidth of operation, the antenna of case 1 achieves a peak gain of $-4.6dB$ at $1.05GHz$ while that of case 2 achieves a peak gain of $-3.5dB$ at $0.93GHz$. In both cases, the realized gain is significantly better than the passive antenna which has a gain less than $-10dB$ at the previously mentioned frequencies. Furthermore, the gain of the active antennas is also higher than the actively matched antenna designed in [121] and having the same size, which proves the advantage of internal active matching rather than input matching in this frequency band.

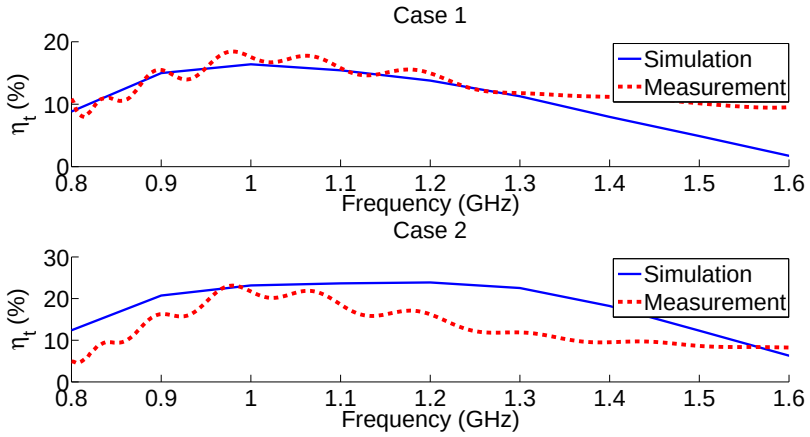


Figure 3.33: Total efficiency of the active antennas.

The quality factor of the measured passive and active antennas given by (3.5)[9] is shown in Fig.3.34b. A dramatic decrease is noticed in the Q factor of the antenna when the non-Foster circuit is connected. As expected, the antenna of case 2 presents a slightly lower Q with respect to the antenna of case 1 especially in the lower part of the band. This decay in the Q factor between the passive and active antennas, proves that the negative capacitance effectively compensated the reactance of the electrically small monopole making it more suitable to be matched in a wideband.

$$Q = \frac{\omega_0}{2R(\omega_0)} \left| Z'(\omega_0) \right| \tag{3.5}$$

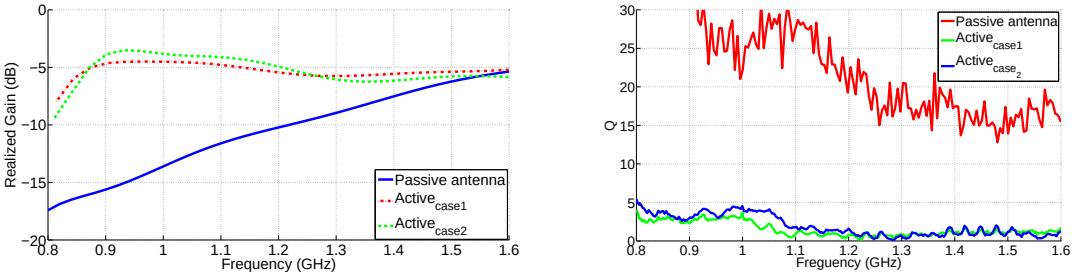


(a) (b)

Figure 3.34: Comparison between the internally loaded antennas and the original antenna.(a) Realized gain, (b) Q factor.

## 3.5 Conclusion

In this section we presented the design of an active internally matched electrically small antenna. The original passive antenna resonates at $2.2GHz$. Using an ideal non-Foster capacitance embedded inside the antenna, it was shown that it is possible to miniaturize it by a factor 2.2 where $ka = 0.31$ and match it in a wideband (30%). However, the realization of a negative capacitance is associated with INC circuits which are sensitive and introduce resistible losses. Therefore, we propose modeling

the INC circuit with the antenna in the full wave simulation in order to have more accurate results. Each component of the INC is defined as a discrete port and finally connected to its corresponding element in the post processing. It was noticed that by introducing a gap exactly above the INC circuit, the total efficiency was increased by approximately a factor of 3 (from 2.7% up till 9%). Moreover, using the post processing in CST, a parametric study have been carried to identify the key components in the INC that can affect the total efficiency of the system. It was then shown that for an $R_b$ = 20$Ohm$ and $L_s$ = 220$nH$, a maximal efficiency of 18% was achieved with an impedance bandwidth of 43.7%. Furthermore, the position of the circuit inside the antenna was varied to show its effect on the overall performance. It was shown that as the INC approaches the feed point, the overall efficiency drops. This is due to the Nix's resistible loss which becomes more important as it gets closer to the antenna's feed. Following the same procedure, another case have been considered in which the distance between Nix's terminals is increased. In this case, the antenna shows a better performance than the previous one with a 24% efficiency and 50% bandwidth. Measurement results are in good agreement with the simulation in both cases. The realized gain and the Q factor of the active antenna shows a significant enhancement with respect to the passive antenna.

Therefore, using the EM modeling of the NIC in the presence of the antenna it is possible to predict the overall behaviour of the system and to carry out parametric studies in order to optimize the performance. In addition, internal active matching is advantageous compared to input active matching where the resistive effect of the NIC becomes more important.

Compared to the design presented in literature [121], which matches an ESA occupying the same volume as our designed antenna. The matching is achieved by connecting the given topology at the input of the antenna. Despite the wideband achieved, the antenna suffered from a poor efficiency at low frequencies > 12%. However, in our case, it was shown that by placing the embedding the non-Foster circuit inside the antenna and optimizing its components it was possible to enhance the bandwidth up to 24% which is two times higher than the aforementioned study. Despite the enhanced performance, the achieved results are still non satisfying if we look at the design complexity that is imposed by the use of a non-Foster circuit.

In theory, it is possible to enhance more the bandwidth of the antenna up to higher than 100%. However, this might require multiple non-Foster loads distributed along its geometry. This has already been verified analytically in literature [57, 59]. While in an ideal scenario, this can provide a very efficient and wideband antenna, practically this adds a huge complexity to the system in addition to the limited space available especially for a physically small antenna. Therefore, the initial antenna geometry remains an important point in obtaining a desired behaviour.

In this chapter and the previous one, the NCM approach was used to address the issue of bandwidth limitation of small antennas and optimize the impedance of the modes to find the best loading configuration, that can match the antenna in a wideband. The methodology was verified for passive and active loads. In the next chapter, the issue of the limited bandwidth in superdirective small antennas is examined. The NCM is used to optimize the port excitation for optimal directivity, while taking advantage of the distributed matching technique to internally load the array elements in order to insure a wideband performance.

# Chapter 4

# Design of Compact Superdirective Arrays Using Network Characteristic Modes

## 4.1 Introduction

Compact antennas are physically limited in bandwidth, efficiency and directivity. As the size of the antenna reduces with respect to the wavelength, its efficiency and bandwidth will degrade dramatically and its radiation pattern approaches a quasi-omnidirectional form, leading to radiation in undesired directions. Nevertheless, the massive development in wireless communication systems, imposes the need for compact and directive antennas to be integrated in limited spaces of the wireless devices. Superdirective array antennas can be an attractive technique in overcoming the omnidirectional radiation pattern of small antennas. By forming an array of closely spaced elements ($d < 0.25\lambda$) an extraordinary directivity namely "superdirectivity" can be achieved. However, boosting the directivity of the compact antenna comes at the price of an extremely narrow operating bandwidth and a very low radiation efficiency when the inter-element separation distance becomes smaller.

In this chapter we present the design of a two-element superdirective array using NCM. To address the issue of narrow bandwidth in superdirective arrays, the design of a wideband superdirective array based on internally loaded wideband small unit element is presented. The internal loads inside the unit element serve in enlarging its impedance bandwidth as shown in the previous chapter. Furthermore, the NCM is later used to find the optimal excitation that can ensure a stable directivity over a desired bandwidth. Finally a feeding network is integrated to provide the required relative phase and magnitudes on the array ports. In the next part of this chapter, the array elements are placed in a stacked configuration to allow closer separation distances. We demonstrate that a very compact array based on a wideband unit element can achieve a significantly higher radiation efficiency compared to an array of narrow-band unit elements occupying the same size.

## 4.2 Directivity Limits

Superdirective array antennas can be an attractive technique in overcoming the omnidirectional radiation pattern of small antennas. By forming an array of closely spaced elements ($d < 0.25\lambda$) an extraordinary directivity called "superdirectivity" can be achieved. Several works on superdirectivity focused on the upper directivity limits with respect to the antenna size. Uzkov [123] showed that the directivity of $N$ closely spaced isotropic radiators can achieve $N^2$ if each element is properly excited in phase and magnitude.

On the other hand, Harrington showed that the maximum directivity of an antenna enclosed in a sphere of radius $a$ and allowing spherical modes of order $N$ can achieve $N^2 + 2N$. He later established a relatione between $N$ and the size of the antenna where $N = ka$ and $k$ is the wave number [3]. Nevertheless, this approximation does not stand true as the electrical size of the antenna decreases where the upper directivity bound becomes negative when $ka$ decreases. The upper directivity bound proposed by harrington is shown in Fig.4.1, where $D < 0$ when $ka < 0.5$. However, this does not respect the maximal directivity achieved by a huygens source in which the two first order spherical modes ($TE_{01}$,$TM_{01}$ $\implies$ $N = 1$)are excited where the directivity achieves 4.77 $dBi$. In this context, a renormalized Harrington limit was proposed in [124] where $N = ka + 1$ (Fig. 4.1). This new limit respects the condition of a Huygens source where $D = 4.77$ $dBi$ when $ka = 0$.

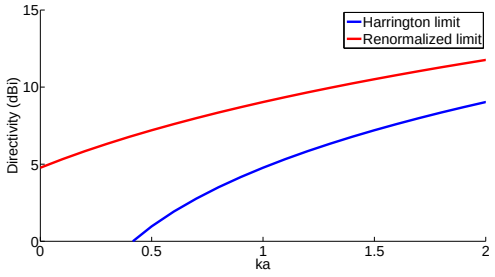


Figure 4.1: Harrington directivity limit and the normalized limit.

### 4.2.1 Limitations of Superdirective Arrays

The limitation of superdirective arrays can be noticed in the efficiency drop and the high sensitivity especially as the number of the elements increases. In [137], the authors carried out a study on the limits of superdirective arrays by considering $N$ isotropic radiators with an inter-element separation distance $d$. It was noticed that despite the increased directivity as $N$ increases, the normalized radiated power decreases more rapidly as the elements are brought closer together (Fig. 4.2).

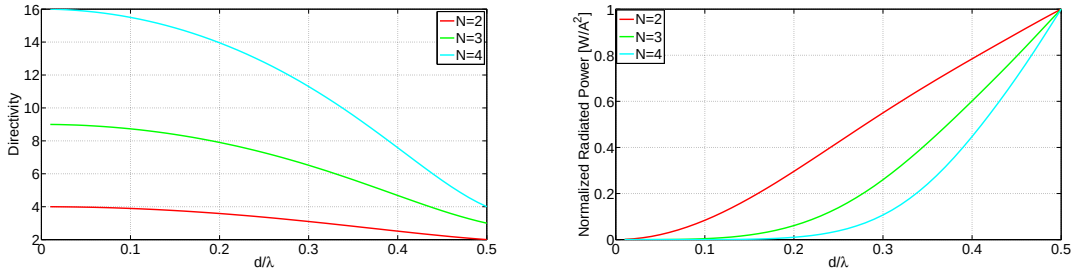


(a) (b)

Figure 4.2: Effect of interelement separation and number of elements of the array performance. (a) Peak end-fire directivity, (b) normalized radiated power. [137]

On the other hand, it was also shown that the sensitivity of the array to relative excitation increases as $N$ increases and $d$ decreases. So for higher $N$ the array becomes more sensitive and less efficient as $d$ decreases. For example, a two-element array becomes sensitive to 5% changes in the relative excitation magnitude and phase starting from a separation distance of $d = 0.1\lambda$, while in the case of a 4-element array, the sensitivity to excitation becomes significant starting from $d = 0.25\lambda$ (Fig.4.3).

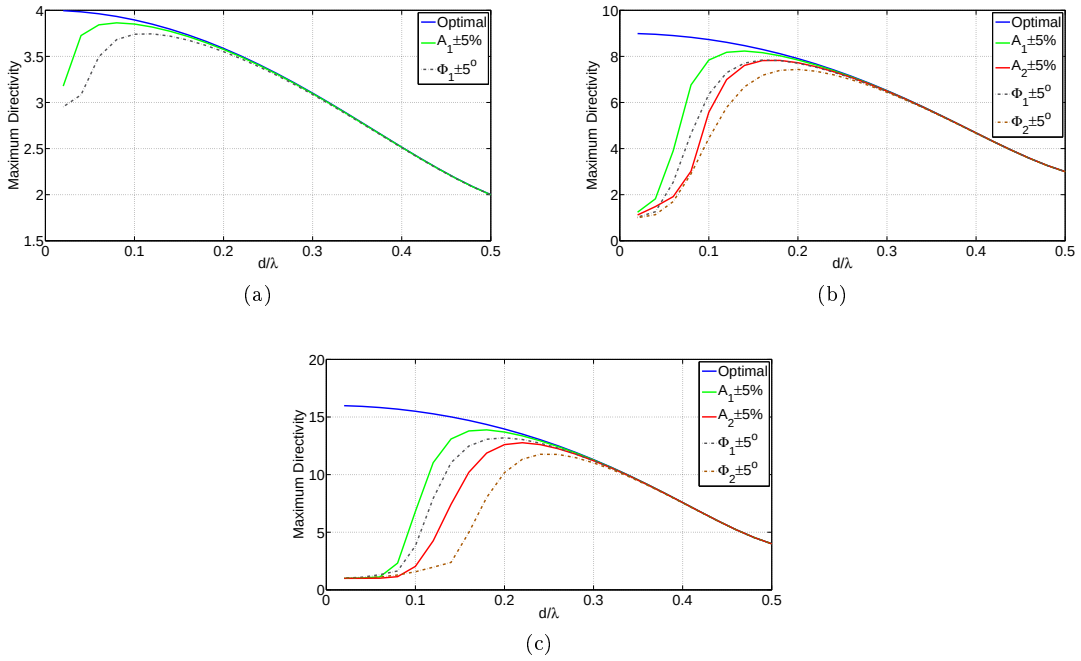


(a) (b)

(c)

Figure 4.3: Sensitivity of the superdirective arrays as a function of the number of elements. (a) Two elements, (b) three elements, (c) four elements.[137]

Therefore, the design of a practical superdirective array requires a certain level of accuracy to guarantee a successful design. However, in a realistic scenario, there is an important degree of freedom in the choice of the unit element to design the array. Choosing a proper unit element with certain specifications can be a key element in overcoming the previously mentioned limitations or at least approaching them.

## 4.3 Superdirective Arrays: Literature Review

After Harrington defined the upper bound on the directivity for electrically small antennas, several attempts have then been carried out to overcome this limit by forming arrays of closely spaced element aiming to achieve superdirectivity. Two classes of superdirective arrays can be found in literature: the fully driven superdirective array in which all elements are fed using a feeding network, and the parasitic loaded arrays in which only one element is driven and the other are loaded or short circuited.

### 4.3.1 Fully Driven Superdirective Arrays

The first successfull realization of a superdirective array was reported by Bloch *et al.* in 1953 [125]. In this study, the authors derived an experimental end-fire array of four parallel half-wave dipoles with an inter-element distance of $0.2\lambda$. Due to the losses of the elements and the feeding system, the array achieved a peak end-fire gain of 8.7 $dBi$ which is 1.4 $dBi$ less than the theoretical maximal gain with a limited directivity bandwidth of 0.01%. However, some of the works that examined superdirective arrays succeeded in obtaining interesting theoretical results but concluded that such arrays seem to be impractical due to the small bandwidth, low efficiency and impactical tolerances [126].

Following the theoretical works on superdirective arrays, Newman *et al.* concluded that high sensitivity of the system is the main reason that lies behind the impractibility of superdirective array [127]. In this context the authors proposed a superdirective array for maximum directivity associated with the constraint that the system not be overly sensitive to slight errors which was defined by a sensitivity factor $K$. The study showed that as the sensitivity factor increases, the maximal achievable directivity increases up to $D_{max}$ after which the directivity starts to decay (Fig. 4.4). This relation was experimentally validated for a four-element array of $\frac{\lambda}{4}$ monopoles separated by $d = 0.1\lambda$. Two designs were considered for a low sensitivity ($K$ = 3) and high sensitivity factor ($K$ = 23.3). The experimental results of the radiation pattern for a low sensitivity were in good agreement with the numerical calculations while that of high sensitivity was considerably different from theoretical results especially in the side lobes. This work concluded that in order to design a superdirective array, a compromise between the system sensitivity and the maximal desired directivity should be taken into consideration.

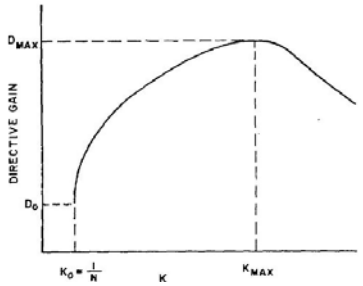


Figure 4.4: Maximal directive gain versus the sensitivity factor. [127]

On the other hand, Dawoud and Anderson proposed a different approach to design

a realizable superdirective arrays [128]. Starting form a Chebyshev polynomial for arrays, they generated a polynomial which optimizes the radiation efficiency and reduces the half-power beam-width in a given array. This technique produces array functions which are insensitive to changes in element values. A theoretical study was carried on an 11-element array having a total length of $2\lambda$ to demonstrate the effectiveness of the approach. Using the proposed polynomial the array achieved a radiation efficiency higher than 30% and 18° half-power beam-width showing a significant improvement with respect to other array design techniques.

In [129], Altshuler *et al.* proposed an interesting technique to optimize the directivity of $N$ arbitrary placed radiators. Assuming that each element of the array radiates a scalar complex far-field pattern given by $f_n(\theta, \phi)$ phased to $r_n$, the complex far-field pattern of the arbitrarily excited elements can be given by:

$$f(\theta, \phi) = \sum_{n=1}^{N} a_n f_n(\theta, \phi) e^{jk\hat{r}.r_n} \tag{4.1}$$

where $a_n$ is an arbitrary complex excitation coefficient. For a maximal directivity in a desired direction $(\theta_0, \phi_0)$ the optimal excitation coefficients $a_{0n}$ is given by:

$$a_{0n} = [H^*_{mn}]^{-1} e^{-jk\hat{r}_0 r_m} f^*_m(\theta_0, \phi_0) f_n(\theta_0, \phi_0) \tag{4.2}$$

and $H^*_{mn}$ is expressed as:

$$H^*_{mn} = \frac{1}{4\pi} \sum_{\theta=0}^{2\pi} \sum_{\phi=0}^{\pi} f_m(\theta, \phi) f^*_n(\theta, \phi) e^{-jk\hat{r}(r_m - r_n)} sin(\theta) \Delta(\theta) \Delta(\phi) \tag{4.3}$$

This method was then dedicated to examine the optimal excitation coefficients in a two-element monopole array for maximal end-fire directivity. It was shown that as the inter-element distance decreases the directivity increases up to $10.5dBi$ for very close distance (Fig.4.5a). Yet, this increase in directivity is associated with a decrease in the input resistance of the elements which approaches zero at separation distance $0.05\lambda$ (Fig.4.5a). Consequently, since the resistance of the monopoles becomes more significant which results in a low radiation efficiency in addition to a mismatch caused by the high coupling between the elements. Therefore, despite the high directivity, a low measured realized gain was noted due to the aforementioned low efficiency and mismatch (Fig.4.5c).

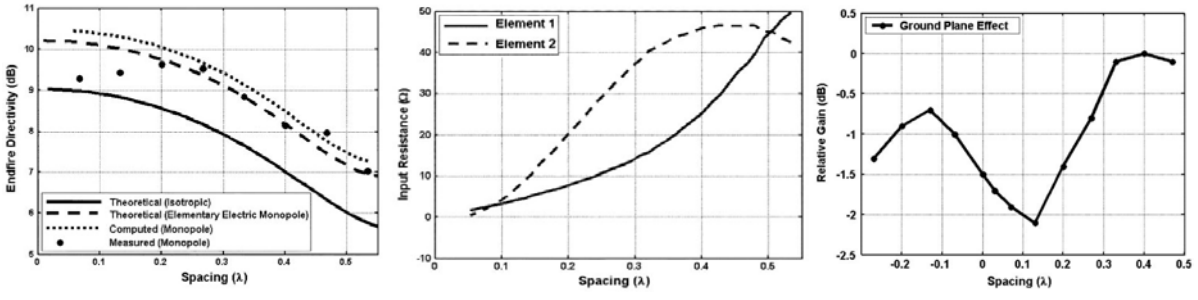


(a) (b) (c)

Figure 4.5: Effect of inter-element spacing on gain and input resistance [10](a)Maximum end-fire theoretical and computational directivities and measured gain as a function of spacing (b) Computed input resistance for the two monopoles as a function of spacing for maximal end-fire directivity, (c) measured gain.

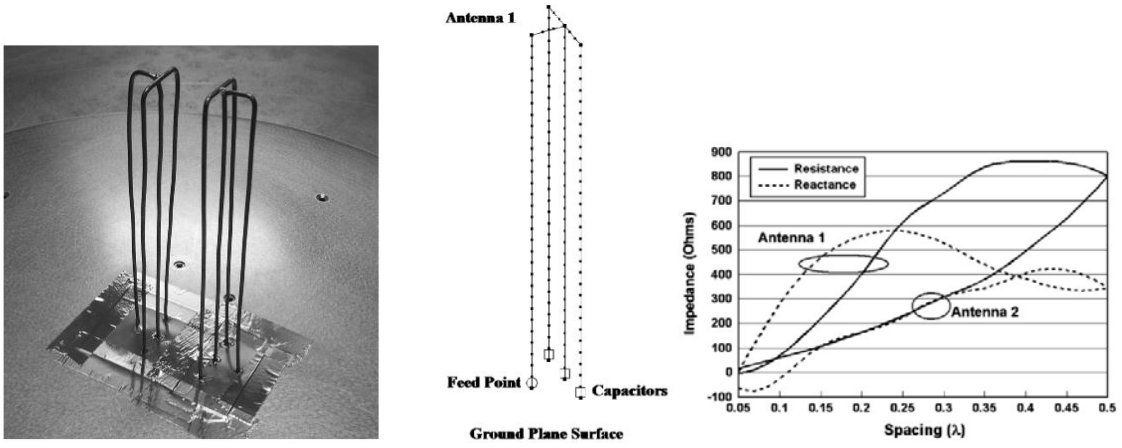


(a) (b) (c)

Figure 4.6: Two-element end-fire array of folded arm monopole [130].(a) Impedance of the two elements as a function of spacing, (b) impedance matching using capacitors, (c) prototype of the two-element array

Taking into account that the significant decrease in the radiation resistance of the array elements is inevitable as the inter-element distance decreases, Best *el al.* proposed the design of a two-element superdirective array based on a unit element having a high input resistance [130]. A multiple arm folded monopole having a feed point impedance of $637 + j153Ohm$ was found to be an appropriate candidate for the desired design. Despite the decrease in the input resistance of the element as the separation distance decreases, the monopoles exhibit a resistance of about $50Ohm$ at a separation distance of $0.1\lambda$ (Fig.4.6a). The reactance of the array elements is then compensated using capacitors connected between the non-fed folded arms (Fig.4.6b). With such configuration, the array achieved a peak directivity of $10.18dB$ at $443.8MHz$ with a high radiation efficiency but however a limited bandwidth (4.9%). To simplify the measurement process, only one element was fed and the other was short circuited making it a parasitic element (Fig.4.6c). The parasitic exhibited a $9.8dB$ directivity which is $0.5dB$ less than the driven one.

The design of superdirective parasitic arrays will be elaborated more in the next section. This approach presents an advantage with respect to the fully driven configuration in that it provides more simplicity of the design where just one element is fed while the other parasitic elements are either short circuited, open circuited or reactively loaded.

### 4.3.2 Parasitic Superdirective Arrays

After studying superdirective arrays in a fully driven configuration, O'Donnel and Yaghjian introduced the analysis and design of small superdirective arrays using parasitic elements [131]. The study was performed on various monopoles having different quality factor (Fig.4.7a). It was shown that the parasitic array achieves a superdirectivity which is almost equivalent to the fully driven configuration at the unit element resonance frequency $f_0$. However, this is limited to a specific separation distance after which the parasitic array directivity drops significantly contrary to the fully driven array which has an increasing directivity as a function of frequency (Fig.4.7b). It was also shown that using unit element with lower $Q$ factors allowed

closer separation distances and higher directivity values and bandwidths (Table.4.1).

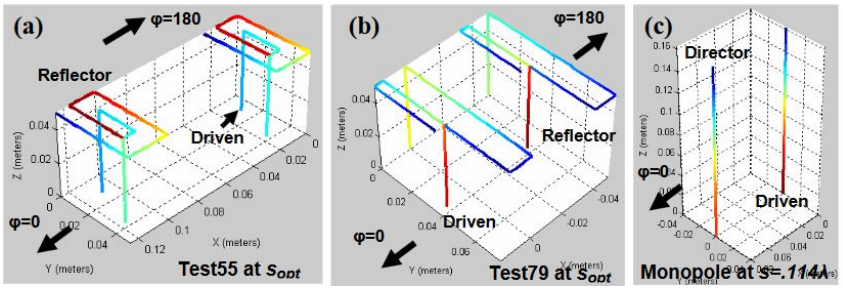


(a)

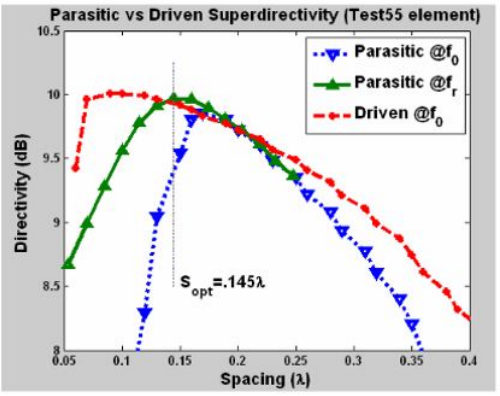


(b)

Figure 4.7: Superdirectivity as a funtion of spacing [131]

Table 4.1: Radiation characteristic of superdirective array with different unit elements.

| $Test$ | $f_0(MHz)$ | $f_r(MHz)$ | $Q$ | $s_{opt}(\lambda)$ | $D_{max}(dB)$ | $BW_{1dB}(\%)$ | $size(\lambda^3)$ |
|---|---|---|---|---|---|---|---|
| 55 | 436.8 | 434.9 | 179 | 0.145 | 9.97 | 1.3 | 0.00096 |
| 79 | 703 | 690.3 | 41.6 | 0.115 | 10.1 | 8.9 | 0.00308 |
| monopole | 436.8 | 426 | 44.3 | 0.114 | 10.48 | 5.1 | 0.00005 |

Following this work, the authors examined the directivity of the parasitic array at frequency points in the neighborhood of $f_0$ [132]. It was noticed that there are two optimal frequencies $f_r$ and $f_d$ at which the relative phase between the parasitic and the driven element approaches the optimized relative currents for a fully driven case. At these frequencies the peak directivity of the parasitic array resembles that of the fully driven array (Fig.4.8).

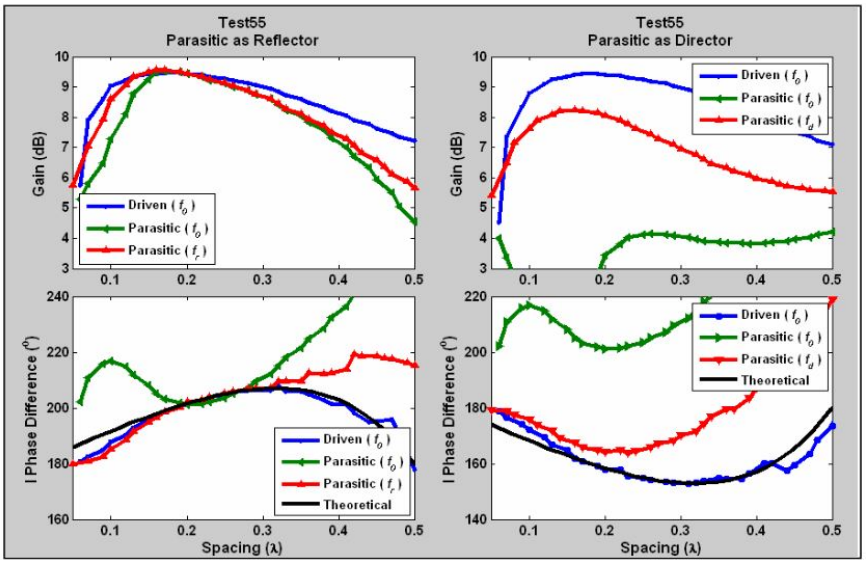


Figure 4.8: Comparison of the directivity and phase difference of the parasitic and driven array[132]

Rather than optimizing the frequency or change the separation distance in order to achieve superdirectivity in a parasitic array, Clemente *et al.* proposed the design of superdirective parasitic arrays where the parasitic elements are loaded with specific impedances rather than being short circuited [134]. The loads at the parasitic elements provide the desired relative magnitude and phase between the different elements of the array to enforce a superdirectivity at a specified frequency. The methodology is based on optimizing the excitation coefficients of the compact array using spherical wave expansion approach. The corresponding loads that can ensure these excitations are then concluded using the s-parameter flow diagram. A 4-element end-fire parasitic array of $0.4\lambda_0$ for $f_0$ = $868MHz$ dipoles and a $0.1\lambda_0$ inter-element separation was then designed and fabricated (Fig.4.9a). The measured array exhibited an $11.7dBi$ directivity at $871MHz$ with a low realized gain $-12dBi$ due to the high coupling between the elements, the resistive loads that existed in the parasitic loads, and mainly due to the surface mounted balun which contributed in a gain loss around $8dB$ (Fig.4.9b). Furthermore, the directivity bandwidth was very narrow 0.34%.

To effectively reduce the high feeding losses, a similar four-element array of meandered dipole unit elements was designed [135] (Fig.4.9c). The meandered geometry offered a more compact design where the unit element had a dimension of $0.26\lambda_0$ for $f_0$ = $868MHz$, and the inter-element separation distance was set to $0.15\lambda$. The same design procedure was followed to calculate the loads at the parasitic elements. Nevertheless, the active element was fed with an integrated balun rather than a surface mounted one. This provided a significant increase in the gain which reached a peak value$0.82dBi$ at $861MHz$ with a maximal directivity of $10dBi$ and a 1-dB directivity bandwidth of 1.1% (Fig.4.9d).

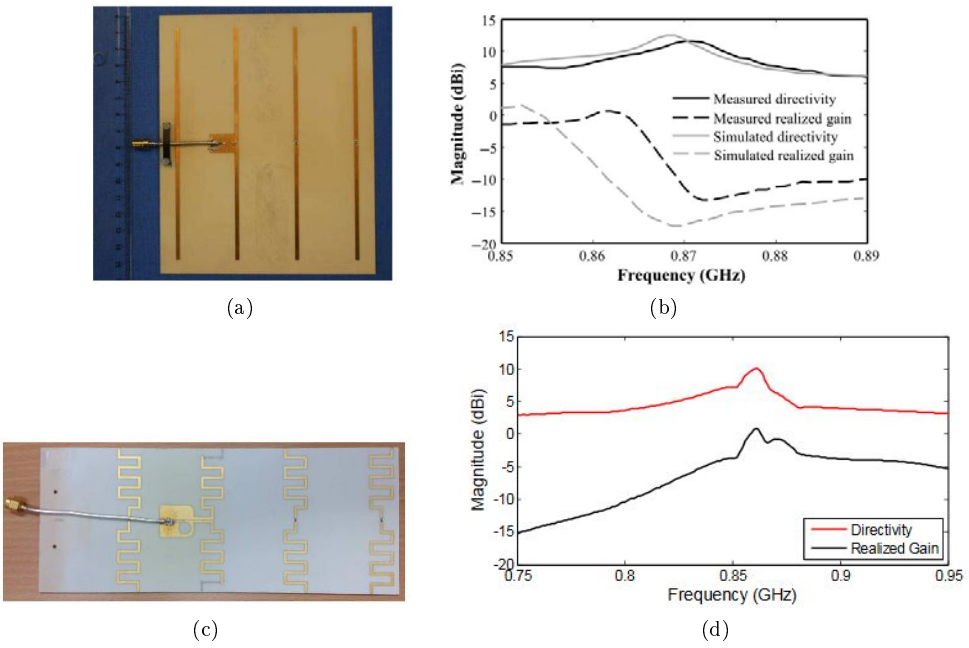


Figure 4.9: Four element parasitic superdirective array. (a) Realized array with surface mounted balun, (b) gain and directivity measurements [134].(c) Realized array with integrated balun, (d) gain directivity of the modified array.[135]

Alongside with the latter work, another approach to design small parasitic loaded superdirective array was proposed in IETR [136]. The technique was based on calculating the optimal excitation coefficients for maximal directivity using [129] which was briefly explained in the previous chapter. The loads at the parasitic elements is then calculated from the array's active impedance. This method was first applied on a 2 element array with inter-element separation of $0.1\lambda$. The unit element is an electrically small half loop antenna having a resonance frequency at $906MHz$, an impedance bandwidth of $2.6MHz$, 36% radiation efficiency and a quasi-omnidirectional radiation pattern. The two element array exhibits a $7dBi$ peak directivity in the end-fire direction ($\phi$ = 270°) when the parasitic element is loaded with $5.1pF$ capacitance. However, the array's radiation efficiency decreases to 7.1% in addition to a narrow impedance bandwidth (0.2%) as well as 0.19% directivity bandwidth. By integrating the array on a PCB, a maximal total directivity of $7.2dBi$ is achieved by loading the parasitic element with a $4.2nH$ inductance. Due to the increase in the overall electrical size of the array, the radiation efficiency was significantly enhanced (62%), yet, the impedance and directivity are still very narrow. Furthermore, this methodology was applied for 3 elements array and 4 element array [137], in which superdirectivity was achieved and verified in measurements.

Another design approach of superdirective parasitic arrays was reported in literature [138]. A two-element superdirective array composed of electrically small magnetic dipole elements on a ground metal plane with an inter-element distance of $0.18\lambda$ was studied (Fig.4.10). The element close to the ground plane was fed through an excitation monopole while the element on top is the parasitic element. By tuning the gap $g_2$ in the parasitic element, the relative phase and magnitude was tuned untill the directivity achieves its maximum ($11.14dBi$) value while the efficiency attains 35% (Fig.4.10). Changing the gap typically resembles tuning the

loads on the parasitic elements so that they couple electromagnetically and produce a high directivity. Other studies on superdirective parasitic arrays can be found in [140, 141, 142]

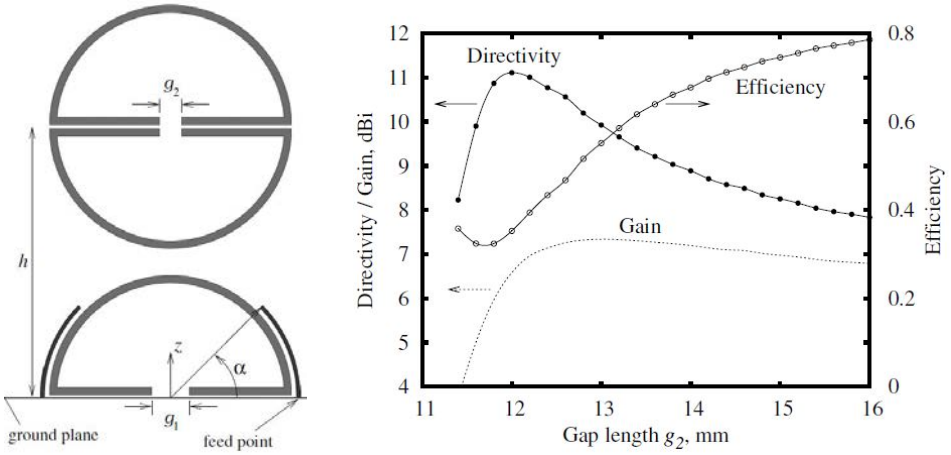


(a) (b)

Figure 4.10: (a) Array configuration, (b) direticvity, gain and efficiency as a function of $g_2$. [138]

Parasitic and fully driven superdirective directive arrays have been proven to be an effective approach in overcoming the low directivity of electrically small antennas. However, these arrays suffer from a low directivity bandwidth and low efficiency which makes it impractical for some applications. In the next chapter we present the few attempts which aimed to design wideband superdirective arrays.

### 4.3.3 Broadband Superdirective Arrays

Dawoud and Anderson were the first to suggest enhancing the bandwidth of superdirective arrays [143]. They suggested adding transistor at the feeding points of the array elements. These transistors serve in decoupling the closely spaced array elements making them less sensitive to changes in frequency. This approach was confirmed by a four element array of $\frac{\lambda}{4}$ printed circuit monopoles with transistors integrated at its input. With the proper feeding network, it was possible to maintain a stable directivity over a 5% band.

Later Newman suggested the design of wideband superdirective array by finding the optimized excitations for a reasonable directivity (not optimal directivity) considering a reasonable tolerance factor [144]. This optimization was done on various frequency points in a band $[f_0 - 3f_0]$. The method was applied on a four element circular array. However, due to the mismatch losses in the array and the losses in the feeding network, the array did not exhibit the expected performance.

Recently, a technique to enhance the bandwidth of superdirective arrays was proposed in [145]. In a 3-element parasitic dipole array with inter-element separation of $0.1\lambda_0$, it was noticed that in order to achieve a wideband directivity, the loads at the parasitic elements should be non-Foster (Fig.4.11a,b). With these active loads, it was possible to stabilize the directivity of the array over a broadband (Fig.4.11c). However, in a practical case, the inevitable resistance of the non-Foster circuit might alter the directivity behaviour over frequency and might also degrade the total efficiency.

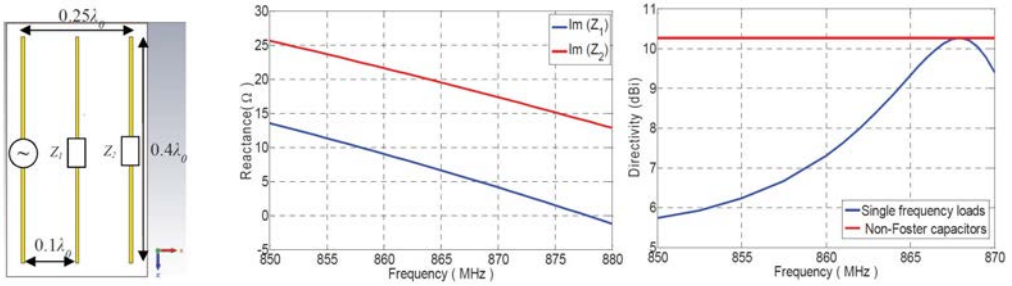


(a) (b) (c)

Figure 4.11: 3-element parasitic array(a) Array configuration, (b)reactance versus frequency of required loads at the parasitic elements, (c)peak directivity comparison between passive parasitic loads and ideal non-Foster loads. [145]

## 4.4 Superdirective Array Based on Wideband Unit Element

Most of the superdirective array designs were based on using canonical antennas such as dipoles or monopoles mounted on large ground plane. Despite the fact that with these antennas a high level of compactness can be achieved, at very close separation distances the efficiency drops significantly, in addition to a limited directivity bandwidth. Few superdirective array designs used other forms of narrowband ESAs as unit elements such as in [66, 138]. Yet the limitations in efficiency and directivity bandwidth were still visible. In this context, a question arises: *How could a compact array of wideband unit elements provide an advantage in enhancing the performance of superdirective arrays in terms of efficiency and bandwidth with respect to classical arrays which are based on narrowband unit elements?*

In this section we present the design of superdirective arrays based on a wideband unit element. This unit element is similar to the wideband S-shaped antenna presented in chapter 2. Two configurations are considered. First we consider a stacked configuration which allows a minimal separation distance between the array elements. In this case we show that for an array of wideband unit elements a high efficiency is maintained even at very close separations. In the second case, a linear configuration is considered where it is demonstrated that a superdirective array with a wide bandwidth can be achieved. However, in order to determine the optimal excitations for the designed arrays, the NCM is used. In the next section we present the optimization methodology based on NCM after which the wideband unit element and the superdirective arrays are presented.

### 4.4.1 Directivity Optimization with NCM

Directivity optimization of antenna arrays using NCM have already been used by Chen and Wang to design reactively controlled array antenna and to optimize the gain in a Yagi-Uda antenna [52, 53]. This was briefly explained in the Chapter 1. In addition to classical arrays, this method can be also applied to superdirective arrays.

In an $N$ element superdirective array (Fig.4.12), there exists $N$ network characteristic current vectors of size $N \times 1$. The $n^{th}$ network characteristic current can be expressed by (4.4).

$$I_n^{mode} = \begin{bmatrix} I_{n1} \\ I_{n2} \\ \vdots \\ I_{nN} \end{bmatrix} \tag{4.4}$$

In this chapter, the characteristic currents will be expressed as $I_n^{mode}$. Each element in the current vector represents a current excitation at a corresponding antenna port. For instance $I_{n1}$ excites port $p_1$, $I_{n2}$ excites port $p_2$ and so on. Therefore, if the array is excited by the characteristic current $I_n^{mode}$, a characteristic field $E_n^{mode}$ will be radiated. Consequently the total directivity at a specific direction $(\theta_0, \phi_0)$ can be expressed as follows (4.5):

$$D(\theta_0, \phi_0) = 4\pi \frac{\left|\sum_{n=1}^{N} a_n E_n^{mode}(\theta_0, \phi_0)\right|^2}{\int_0^{2\pi}\int_0^{\pi}\left(\left|\sum_{n=1}^{N} a_n E_n^{mode}(\theta, \phi)\right|^2\right) sin\theta d\theta d\phi} \tag{4.5}$$

Hence, in order to optimize the directivity, it is sufficient to optimize the modal weighting coefficients $a_n$. The optimization is also based on the differential evolution algorithm (explained in chapter 2), in which the population is the set of the modal excitations and the objective function is simply given by (4.6).

$$F(a) = -D(\theta_0, \phi_0) \tag{4.6}$$

Since the DE is minimizes the objective function, a weight of value $-1$ is multiplied by the objective. Therefore, the algorithm minimizes $-D$ in the direction of $(\theta_0, \phi_0)$, which hence maximizes $D(\theta_0, \phi_0)$.

After finding the optimized modal weighting coefficients $a_{nopt}$, the current excitation at the ports is given by 4.7:

$$I_{opt} = \sum_{n=1}^{N} a_{nopt} I_n^{mode} = \begin{bmatrix} I_1 \\ I_2 \\ \vdots \\ I_N \end{bmatrix} \tag{4.7}$$

By applying the current excitation $I_{opt}$ at the array port the optimized directivity $D_{opt}(\theta_0, \phi_0)$ will be obtained. However, in case of a parasitic configuration, in which

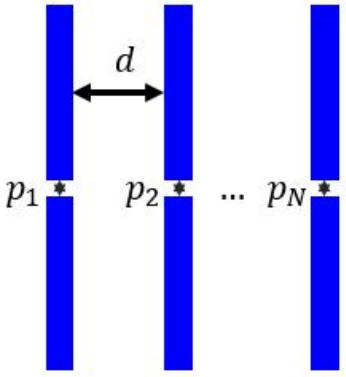


Figure 4.12: Schematic representation of an N-element Superdirective array.

only one port is driven - let's say port $p_1$, the loads at the parasitic elements should be calculated in order to guarantee the optimized excitations at the antenna ports. In this case the load $Z_{Ln}$ at port the $n^{th}$ parasitic element can be calculated as following:

$$Z_{Ln} = -\frac{([Z_A][I_{opt}])_n}{[I_{opt}]_n}, n = 2, \cdots, N \tag{4.8}$$

Yet, in this case, it is important to notice that $Z_{Ln}$ is a complex impedance whose real part will dissipate losses in the system and degrade its efficiency. In order to avoid such inconvenience, an additional constraint that minimized or eliminates the resistance of $Z_{Ln}$ must be added to the objective function:

$$F(a) = w_1 \times D(\theta_0, \phi_0) + w_2 \times real(Z_{Ln}) \tag{4.9}$$

$w_1$ and $w_2$ are the weighting coefficients that define the contribution of each element of the objective function. Similar to the fully drive case, $w_1$ should be a negative value in order to maximize the directivity in the desired direction, while $w_2$ is a positive value that minimizes the resistance of the parasitic load impedance. The methodology to optimize the directivity at an angular frequency $\omega_0$ is given in Fig.4.13. It should also be noted that only one full wave simulation is needed to extract the impedance matrix of the array. The other steps are done in MATLAB or in the post processing of HFSS [146].

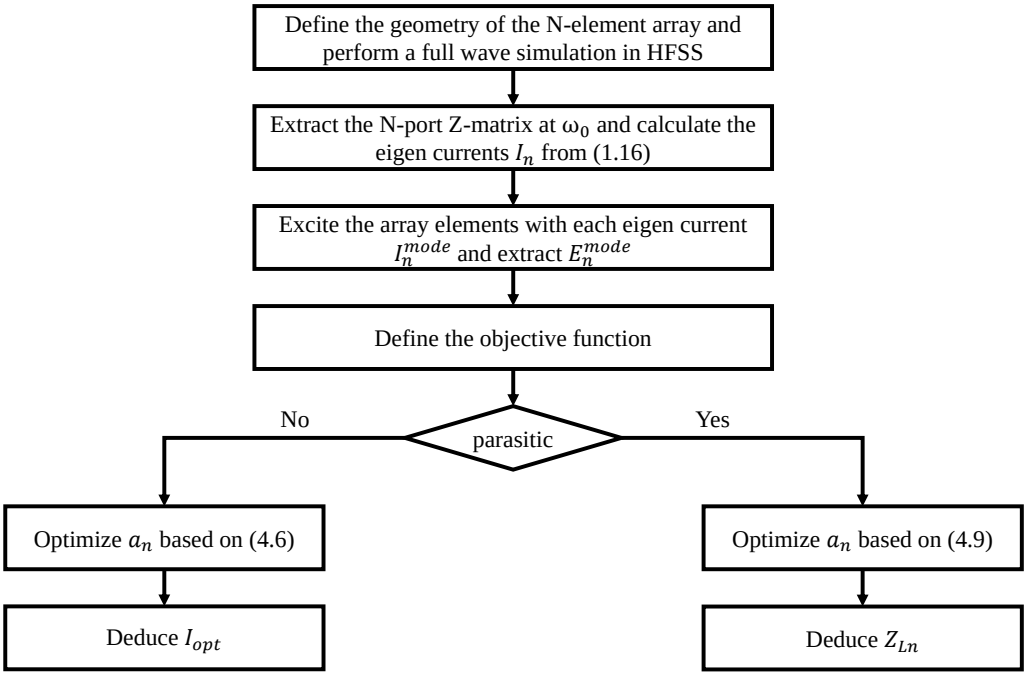


Figure 4.13: Flow diagram of the directivity optimization approach based on NCM.

### 4.4.2 Unit Element

#### 4.4.2.1 Wideband Small Unit Element

The geometry unit element of the array is presented in Fig.4.14. The antenna is exactly similar to the design presented in Chapter 2 section 2.5, however the ground plane on the bottom side is removed and the near field parasitic meander line is connected to the ground plane of the top side through a via. The ground is removed for the purpose of integrating a feed network on the array structure in the case of a linear configuration in order to achieve a wideband directivity. Nevertheless, this unit element will be used in both the stacked and linear configurations. Following the bandwidth optimization approach using the NCM, the antenna is loaded at the two positions shown in Fig.4.14. The first port is loaded by inductance $L_1 = 13nH$ while the second one is loaded by $L_2 = 28nH$.

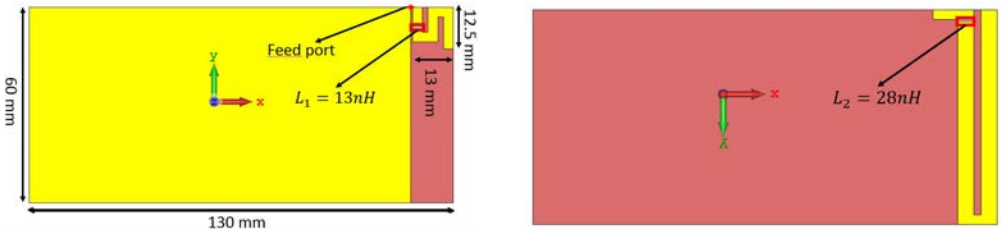


(a) (b)

Figure 4.14: Unit element. (a) Top view, (b) bottom view.

With the optimized inductive loads, the antenna is matched over a wide bandwidth [0.85-1.05 GHz] (Fig.4.15a) which represents a 20% relative bandwidth. Compared to the original unloaded S-shaped antenna, the reactive loads with the parasitic meander line miniaturize the antenna by a factor of 2.3. The loaded antenna exhibits an efficiency higher than 80% over this 20% bandwidth (Fig.4.15b) and it radiates a quasi-omnidirectional pattern with null along the x-axis (Fig.4.16).

Despite that the electrical size of the overall structure is not electrically small, the antenna (S-monopole + meander line parasitic) are limited in an electrically small volume. Achieving a wideband at this frequency with this limited antenna size is a challenging task.

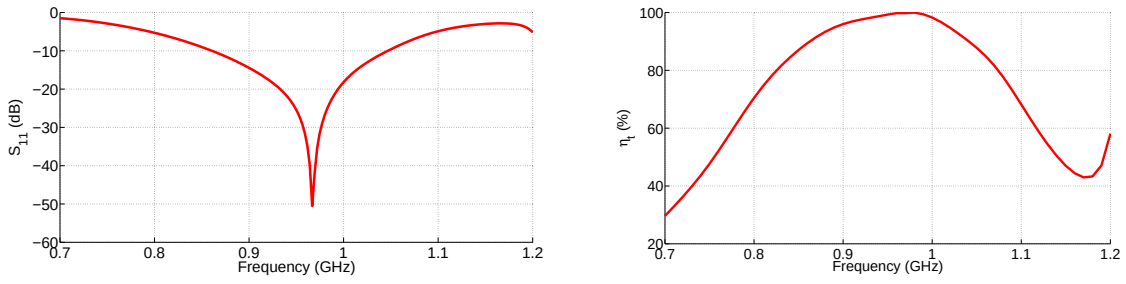


(a) (b)

Figure 4.15: Unit element. (a) Input reflection coefficient, (b) total efficiency.

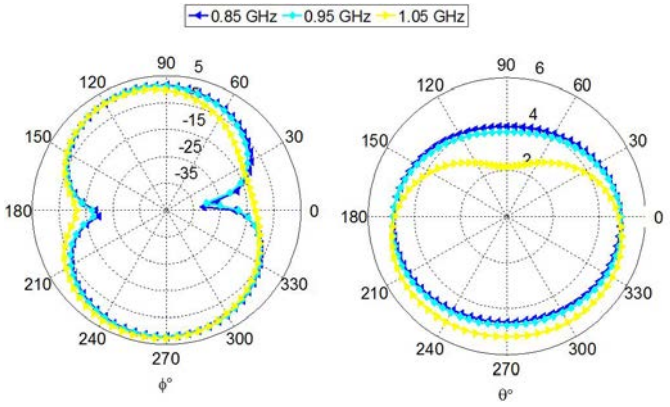


Figure 4.16: 2-D total directivity radiation pattern of the unit element at different frequency points. Horizontal plane (left), vertical plane (right).

#### 4.4.2.2 Narrowband Small Unit Element

In order to show the advantage of using a wideband small unit element in a superdirective array, an electrically small half loop antenna is considered for comparison. The antenna of dimension $(24mm \times 20mm)$ is integrated on a $(116mm \times 60mm)$ ground plane (Fig.4.17). For a fair comparison the overall structure occupies the same volume $(130mm \times 60mm \times 0.76mm)$ as the wideband antenna. The antenna exhibits a narrowband resonance at $872MHz$ with a radiation efficiency of 93% and a 47% total efficiency due to the mismatch (Fig.4.18). More over the radiation of the antenna at the resonance frequency resembles that of the wideband unit element with a null along x-axis and a quasi-uniform radiation in the yz-plane (Fig.4.19).

In the next section we present the design of a two element superdirective array in a stacked configuration. Using a wideband unit element, very close inter-element separations can be achieved while maintaining a high efficiency. The results demonstrate a significant improvement with respect to an array formed of a narrowband unit element.

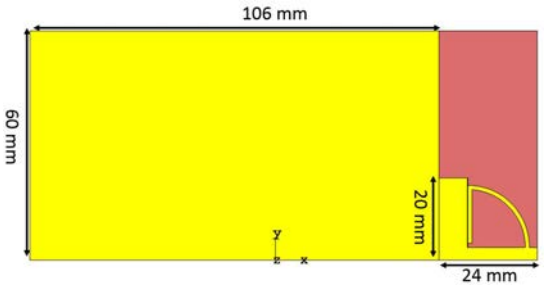


Figure 4.17: Geometry Electrically small half-loop antenna integrated on a PCB.

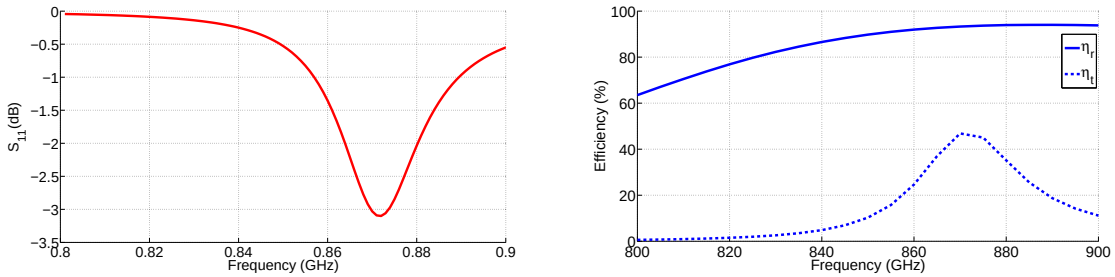


(a) (b)

Figure 4.18: Characteristic of the half-loop. (a) Input reflection coefficient, (b) efficiency

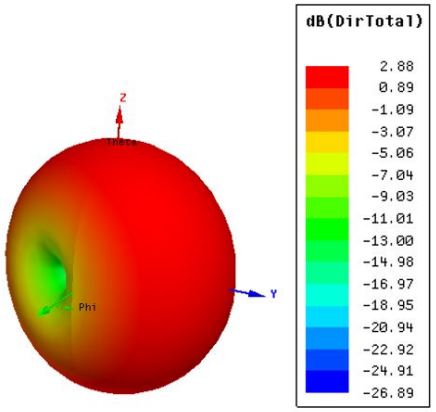


Figure 4.19: Radiation pattern of the half-loop antenna at the resonance frequency $872MHz$.

### 4.4.3 Stacked Two-Element End-fire Array

Very close separation distance for superdirective arrays can be achieved by placing the elements in a stacked configuration. This is mainly beneficial when the electrically small antenna is mounted on a finite ground planes such as the case of the proposed unit element. In this case, forming an array in a linear configuration limits the inter-element separation distance and hence its size is less compact compared to a stacked configuration.

Two element stacked end-fire arrays are studied in this section. The first array is formed of the wideband unit element which will be considered as Array 1 (Fig. 4.20a), while the second array is formed of the narrowband half loop antenna which will be considered as Array 2 (Fig. 4.20b). In both arrays the inter-element separation is $d$. The arrays are fed at ports 1 and 2 while the unit elements of Array 1 are loaded with the optimized inductive loads.

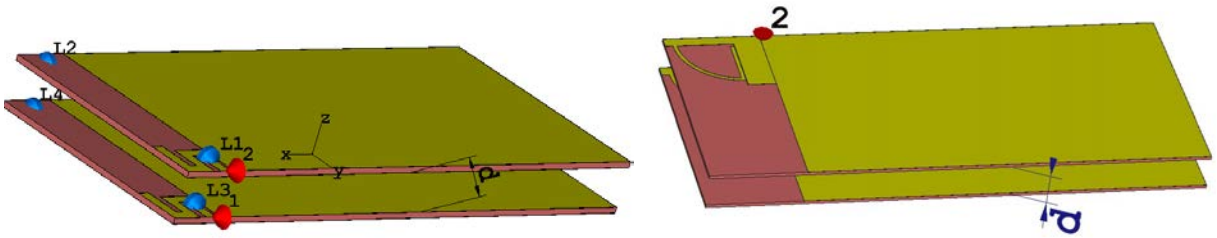


(a) (b)

Figure 4.20: Geometry of the stacked two-element arrays. (a) Wideband unit elements (Array 1), (b) narrowband unit elements (Array 2).

#### 4.4.3.1 Parametric Analysis

In order to examine the behaviour of both superdirective arrays the current excitations were optimized for different separation distances $d$ using the objective function from (4.6) at the resonance frequencies of the arrays. It should be noted that this resonance shifts slightly up or down as the inter-element distance changes. The optimized relative excitation magnitudes and phases for both arrays are given in Fig.4.21.

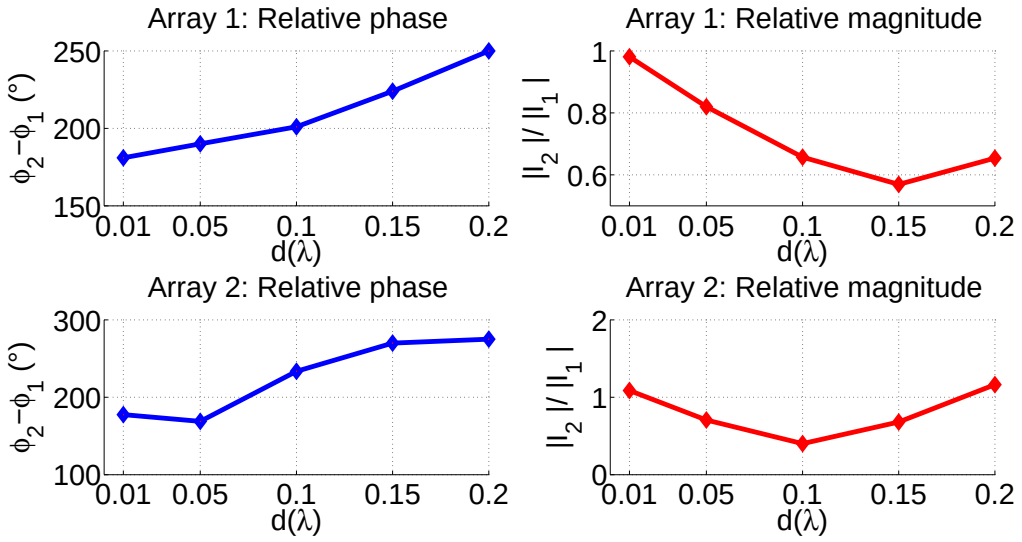


Figure 4.21: Optimized relative phase and magnitude for the arrays versus separation distance.

For Array 1, as $d$ decreases the relative phase decreases monotonically until it reaches 181° at a very close separation distance of $0.01\lambda$. On the other hand, a monotonic increase in the relative magnitude is noticed starting from $d = 0.15\lambda$ until it reaches 0.98 at $d = 0.01\lambda$. This phase opposition and magnitude equality is translated in a significant decrease in the radiation efficiency at this very close separation (Fig. 4.22). As $d$ decreases, the antenna maintains a high radiation efficiency ($\eta_r > 94\%$) and a stable peak end-fire directivity ($D_{max} \simeq 7.8dBi$) until $d = 0.01\lambda$. At this very close separation the efficiency drops to 45%.

The relative phase for Array 2 exhibits a similar behaviour to that of Array 1. As

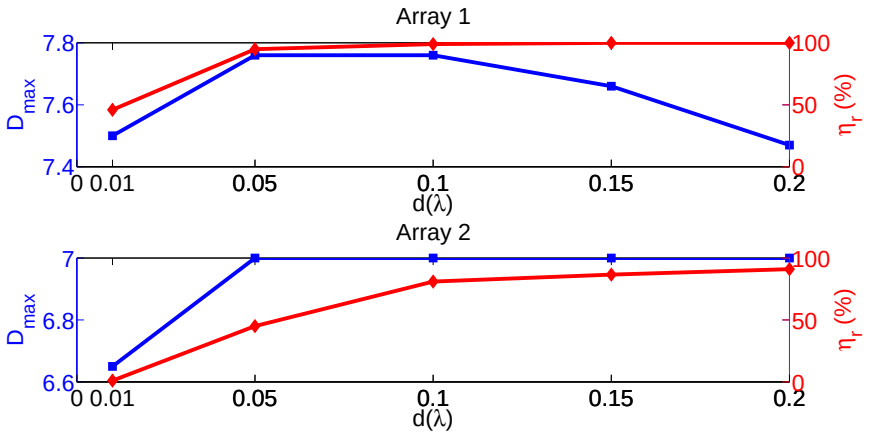


Figure 4.22: Peak end-fire directivity and radiation efficiencies of the arrays versus frequency.

$d$ decreases, the relative phase decreases until it becomes 169° at $d = 0.05\lambda$ then it increases to 178° at $0.01\lambda$ (Fig.4.21). This is associated with a relative magnitude of 0.7 at $d = 0.05\lambda$ and 1.08 at $d = 0.01\lambda$. Contrary to Array 1, the radiation efficiency slightly decays at $0.1\lambda$ after which it dramatically decreases at $d = 0.05\lambda$ where it attains a value of 45% while it becomes 1% at $d = 0.01\lambda$. Moreover, a stable peak end-fire directivity versus $d$ is noticed ($D_{max} = 7dB$) with a slight decrease at $d = 0.01\lambda$.

Comparing both results, it is noticed that for the case of Array 1 where the unit elements are wideband, a much better performance in terms of radiation efficiency and directivity is achieved especially at very close separation distances ($d < 0.05\lambda$). Despite the phase opposition in Array 1, the low Q factor of the unit element maintains a high radiation efficiency relative to Array 2. Moreover, by examining the input impedance of the elements of both Arrays, it is noticed that the input resistance of Array 2 to becomes null at $d = 0.05\lambda$ while that of Array 1 is about $40Ohm$ showing that it is insensitive to inter-element separations (Fig. 4.23). This explains the 1% efficiency of Array 2 at the aforementioned distance (Fig.4.22).

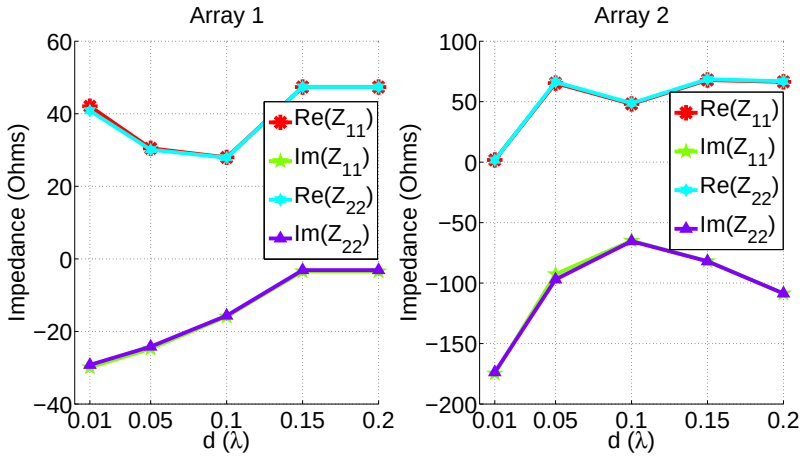


Figure 4.23: Input impedance of the array elements versus $d$.

Therefore, by forming an array of wideband unit elements, a remarkable in the performance is noticed, especially in the radiation efficiency. Contrary to classical superdirective array, with wideband unit elements, the input resistance of the array elements maintains a high value even when the inter-element separation decreases, which results in high radiation efficiencies. In order to verify the simulation, the next section presents a measurement case of the array with wideband unit elements separated by $d = 0.05\lambda$

#### 4.4.3.2 Experimental Validation

In the array formed of wideband unit elements, a separation distance of $0.05\lambda$ shows the best compromise between the radiation efficiency and the occupied volume. The simulated input reflection coefficient of the array at $d = 0.05\lambda$ ($\lambda$ corresponds to $f = 880MHz$) is given in Fig.4.24a. The array exhibits an 11.2% relative impedance bandwidth for $S_{11} < -10dB$. In order to facilitate the experimental implementation, the array excitations is reoptimized using (4.9) for a parasitic configuration. In this case, port 1 is driven while port 2 is loaded with a capacitance $C = 5pF$ resulting in a maximal end-fire directivity $D_{max} = 7.5dB$ at $880MHz$. However, the added reactive load causes a mismatch at the optimization frequency which implies the need for a matching network at port 1. A one stage ladder LC circuit is connected at the feeding port ($L = 1.3nH$, $C = 9pF$) which matches the antenna at $880MHz$ (Fig.4.24b).

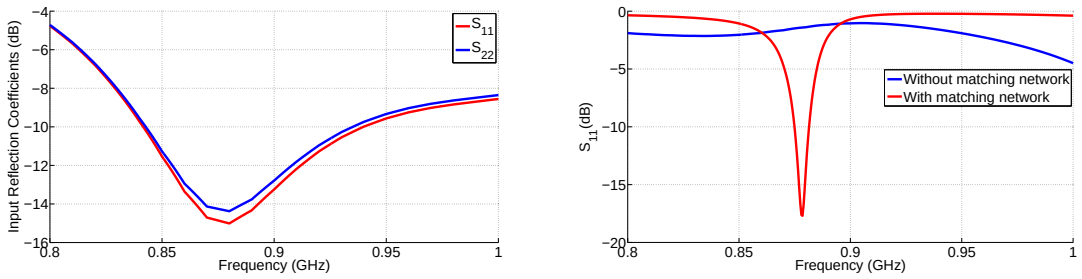


(a) (b)

Figure 4.24: (a) Input reflection coefficients of the array element in fully driven configuration, (b) Input reflection coefficienct of the array in a parasitic configuration with and without an input matching network.

It should be noted that connecting the matching network at the input port will have no effect on the antenna directivity. The prototype is shown in Fig.4.25. The measured peak end-fire directivity versus frequency plotted in Fig.4.26 exhibits a maximum of $7dB$ at $890MHz$ which is shifted $10MHz$ with respect to the simulated results. However, the $1-dB$ directivity drop is of narrow bandwidth ($25MHz$). The 2-D directivity pattern of the measured and simulated antennas is plotted in the E and H-planes (Fig.4.27). The measured results at $890MHz$ are in good agreement with the simulated ones at $880MHz$. The measured antenna is matched at $890MHz$ and exhibits a high total efficiency ($\eta_t = 87\%$) at this frequency (Fig.4.28) with however a narrow bandwidth ($6MHz$).

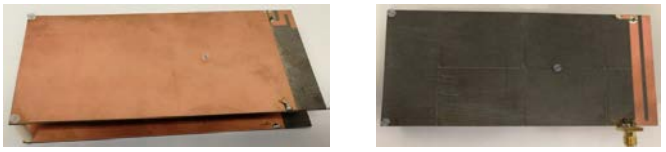

(a) (b)

Figure 4.25: Prototype of the stacked end-fire parasitic array. (a) Top view, (b) bottom view

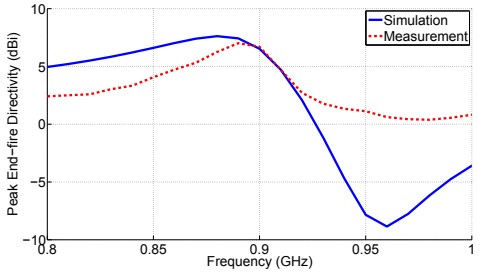


Figure 4.26: Simulated and measured peak end-fire directivity as a function of frequency.

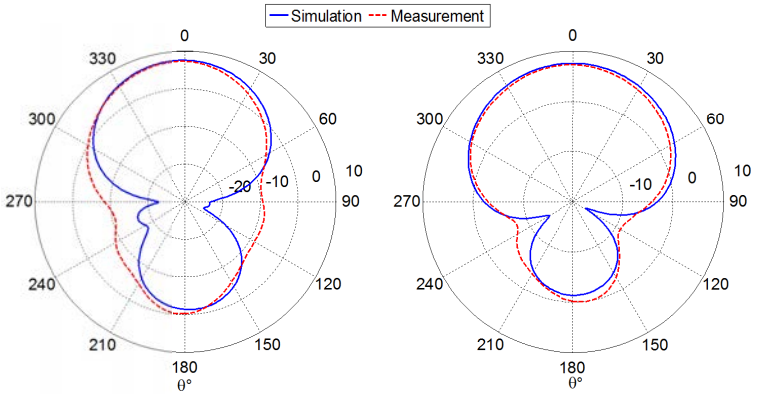


Figure 4.27: 2D radiation pattern of the simulated and measured array in the E-plane (left) and H-plane (right).

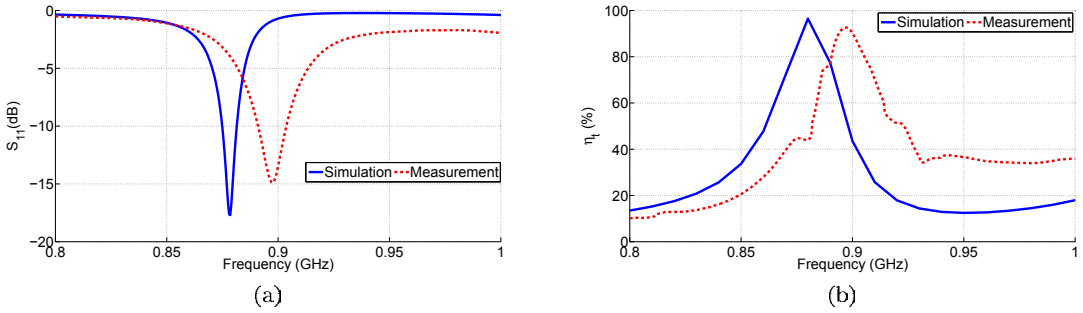


(a) (b)

Figure 4.28: Characteristics of the measured array. (a) Input reflection coefficient, (b) total efficiency.

Therefore, we demonstrated in this section the advantage of using a wideband unit element in superdirective arrays. With a wideband unit element closer inter-element separation distances can be achieved while maintaining an efficient radiation and high directivity. Contrary to narrow band unit elements whose radiation resistance drops to zero at very close separations, with a wideband unit element the radiation resistance maintains relatively high values permitting the array to radiate efficiently when the distance becomes very small. The simulated results are then verified for the case where the elements are separated by $d = 0.05\lambda$. The measured antenna in parasitic configuration exhibits a peak directivity of $7dBi$ and a high total efficiency 87%. Nevertheless, it is limited in bandwidth. Therefore, even if the elements are narrow band, the high coupling at small distances will cause a mismatch and result in a narrowband behaviour.

In the next chapter, we examine the behaviour of an end-fire array based on the wideband unit element in a linear configuration. In this configuration, due to the size of the ground plane the separation distance can not be lower than about $0.18\lambda$. By compromising the size, the bandwidth capability of this array is studied showing that it is possible to achieve a wideband directivity if the array elements are properly excited .

### 4.4.4 Linear Endfire array

A two-element linear end-fire array is formed based on the wideband unit element. The geometry of the array is shown in Fig.4.29. Due to the dimension of the ground plane, the inter-element separation is $65mm$ with $5mm$ gap. For a matching level of $S_{ii} < -10dB$, the array exhibits a wideband impedance matching $[0.83 - 1.11GHz]$ for port 1 and $[0.835 - 1.09GHz]$ for port 2 which represents 28.9% and 26.5% respectively with respect to the central frequency (Fig.4.29c). With this wideband impedance performance, this studied the directivity behaviour of this array in both parasitic and driven configuration in order to examine the possibility to design a superdirective array with a wideband directivity.

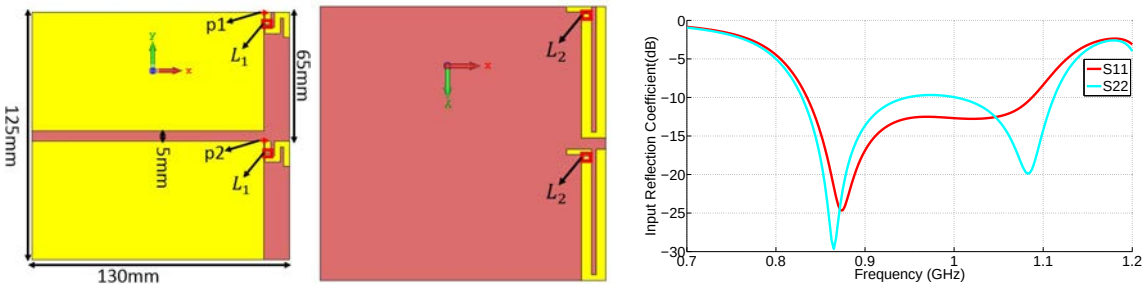


(a) (b) (c)

Figure 4.29: Geometry of the two-element linear end-fire array.(a) Top view, (b) bottom view, (c) input reflection coefficients

#### 4.4.4.1 Parasitic Configuration at Single Frequency

In order to study the possibility to achieve a wideband directivity the array is first studied in a parasitic configuration. Using the objective function of (4.9). Since the DE minimizes the objective function, $w1$ is set to $-1$ in order to maximize the

directivity in the end-fire direction, where $\phi_0 = 270°$ and $\theta_0 = 90°$. In order to minimize the resistance of the parasitic load at the second port $w_2$ is set to 0.5 and $n = 2$ referring to the impedance of the parasitic load at the second port $p_2$. The optimization is initialized at $0.83GHz$ since impedance bandwidth of the array starts at this frequency point.

To demonstrate the approach, an example of optimizing the array end-fire directivity at $0.83GHz$ is presented. The impedance matrix of the array at $0.83GHz$ is given by:

$$Z_a = \begin{bmatrix} 25.7 - 37.1i & 16.6 - 34.2i \\ 16.6 - 34.2i & 29.9 - 37.8i \end{bmatrix} \tag{4.10}$$

The two network characteristic currents are then calculated using (1):

$$I_1^{mode} = \begin{bmatrix} -0.99 \\ 1 \end{bmatrix}; I_2^{mode} = \begin{bmatrix} -1 \\ -0.65 \end{bmatrix} \tag{4.11}$$

The array ports are then excited by the characteristic currents $I_1^{mode}$ and $I_2^{mode}$ respectively using HFSS. The 2D radiation patterns of the characteristic fields $E_1^{mode}$ and $E_2^{mode}$ in the yz-plane are shown in Fig.4.30. $E_2^{mode}$ exhibits a bi-directional pattern ($D_{max} = 6.2dBi$) in the end-fire direction, while that of $E_1^{mode}$ is more quasi-omnidirectional with a null along the x-axis ($D_{max} = 3.8dBi$).

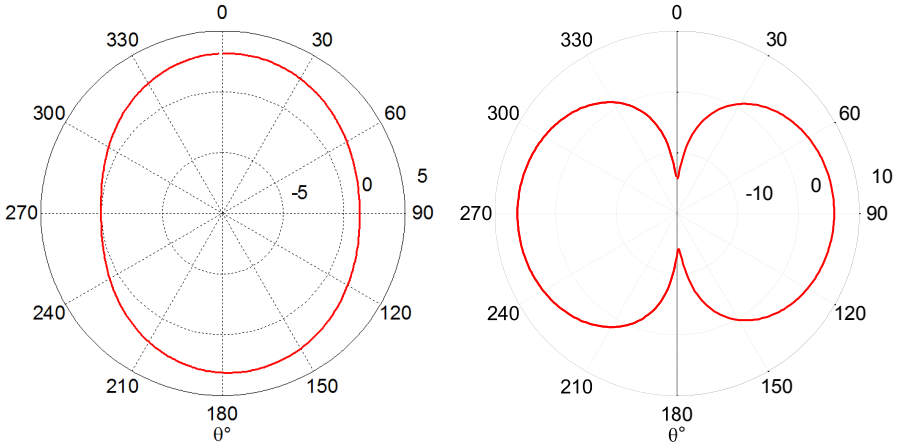


Figure 4.30: Elevational radiation pattern ($\phi = 90°$) at $830MHz$ of the characteristic fields $E_1^{mode}$ (left plot) and $E_2^{mode}$ (right plot) radiated by the current $I_1^{mode}$ and $I_2^{mode}$.

The components of the characteristic fields are then imported in the optimization algorithm, in order to optimize the modal weighting coefficients $a_1$ and $a_2$. The optimization yields a the modal weighting coefficients: $a_{opt1} = 0.35e^{-j173°}$ and $a_{opt2} = 0.85e^{j81°}$. The optimal port current excitation $I_{opt}$ is then calculated from (4.7) as follows:

$$I_{opt} = a_{opt1}I_1^{mode} + a_{opt2}I_2^{mode} = \begin{bmatrix} I_1 \\ I_2 \end{bmatrix} = \begin{bmatrix} 0.872e^{-j142°} \\ 1 \end{bmatrix} \tag{4.12}$$

The corresponding parasitic load is calculated from Eqn(4.8). The optimization yields an inductive parasitic load of value $3.6nH$ loaded at port $p2$. The simulated

and measured results of this array is given in Fig.4.31. With this load the array achieves a measured peak end-fire directivity of $6.5dBi$ ($7dBi$ in simulation) at $\phi = 270°$, a $5.5dBi$ $FBR$ and a 98% radiation efficiency at $0.83MHz$. The array is matched in a wideband $[0.82 - 1.04GHz]$ (24%) . However, the $1dB$ directivity bandwidth is just limited to 7.1% ($[0.81 - 0.87GHz]$). The degradation in the antenna directivity in the band beyond $0.87GHz$ can be explained by studying the normalized modal weighting coefficients $a_1$ and $a_2$ as a function of frequency (Fig. 4.32). In the band where the antenna is directive, the directive mode 2 contributes more in the antenna radiation compared to mode 1, which results in an overall directive antenna. Yet, there is still a significant contribution from the first characteristic fields, that reacts with the directive field ($E_2^{mode}$) resulting in maximal end-fire directivity. However,with the variation of the reactance of the passive parasitic load as a function of frequency, it becomes hard to establish a relatively stable excitation, that can maintain the dominance of the directive mode over a wideband, and hence maintaining a constant directivity.

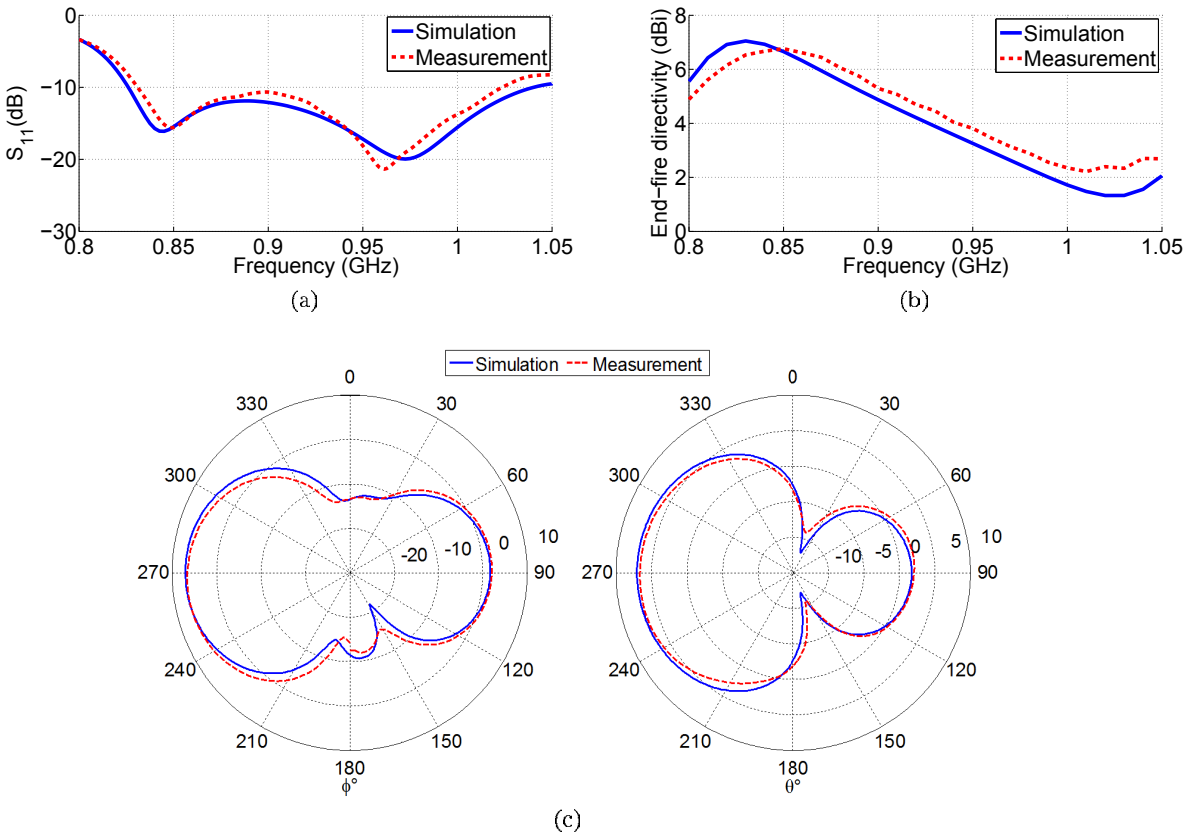


Figure 4.31: Simulated and measured results of the parasitic end-fire array optimized at $830MHz$. (a) Input reflection coefficient, (b) end-fire directivity versus frequency, (c) radiation pattern in the xy plane (left) and the yz plane (right).

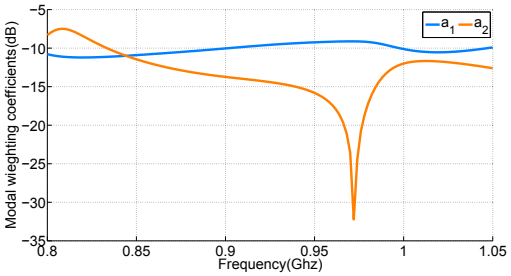


Figure 4.32: Modal weighting coefficients versus of the parasitic loaded end-fire array

#### 4.4.4.2 Parasitic Configuration in Wide Frequency Band

The same study has been done at different frequency points. The results are summarized in Table. 4.2. With the optimized parasitic loads, the array maintains a relatively constant peak directivity of $7dBi$ in the end-fire direction ($\phi$ = 270°) and a high radiation efficiency. On the other hand, the directivity bandwidth increases as the optimization frequency increases. The 2-D directivity radiation patterns of the parasitic loaded array at the optimization frequencies is given in Fig.4.33. For all the optimized parasitic loads, the arrays exhibits a relatively constant radiation pattern. Therefore, a wideband directivity can be achieved by providing the optimal reactance at the parasitic element. This reactance establishes the optimal excitation phase and magnitude to have a maximal directivity.

Table 4.2: Optimized parasitic load values at different frequency points

| $f(GHz)$ | $load$ | $D_{max}(dB)$ | $BW_{1dB}(\%)$ | $\eta_r(\%)$ | $FBR$ |
|---|---|---|---|---|---|
| 0.83 | $3.6nH$ | 7 | 7.1 | 98 | 5.5 |
| 0.88 | $10.94pF$ | 7 | 8.9 | 99 | 5.2 |
| 0.93 | $3.2pF$ | 6.9 | 10.7 | 99 | 5.3 |
| 0.98 | $1.3pF$ | 6.76 | 11.1 | 100 | 5.7 |
| 1.03 | $0.9pF$ | 6.4 | 12.3 | 100 | 7.1 |

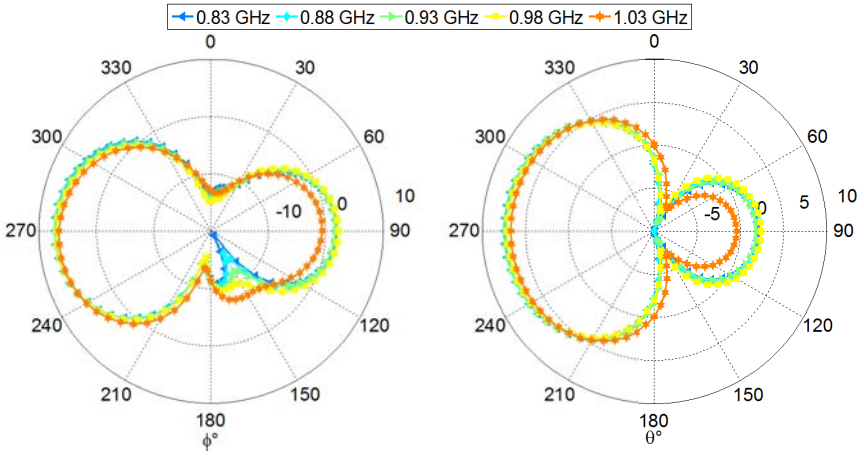


Figure 4.33: 2-D total directivity radiation pattern. Horizontal plane (left), vertical plane (right).

Fig. 4.34a shows the variation of the optimal parasitic reactance value as a

function of frequency. The reactance (blue curve) exhibits a negative slope as a function of frequency which corresponds to a non-Foster load. With such load, a relatively constant directivity is maintained over the entire bandwidth of operation (green curve). From a modal point of view, loading the parasitic element with the non-Foster load, maintains the dominance of the second mode with respect to the first one (Fig. 4.34b), which provides the proper excitation in order to achieve a wideband directivity over the whole bandwidth.

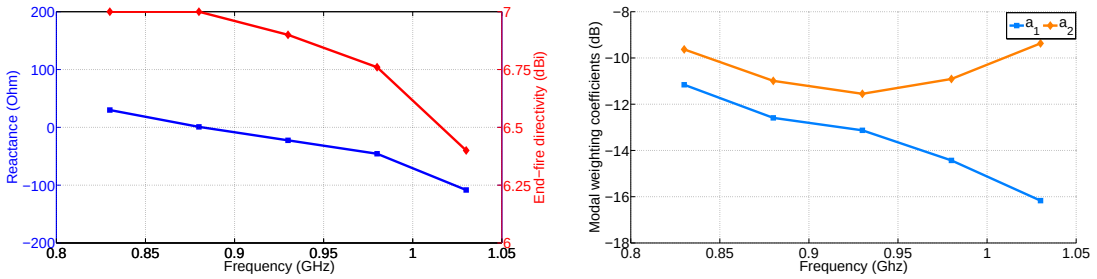


(a) (b)

Figure 4.34: (a) Optimized parasitic loads values that maximizes the end-fire directivity of the array, (b) modal weighting coefficients versus frequency of the array with the optimized parasitic loads.

Therefore, in order to maintain a wideband directivity as a function of frequency for a parasitic configuration, a non-Foster load should be added at the second port $p2$. To avoid the complexity of the non-foster circuit design, we present in the next section the design of a wideband superdirective array by integrating a feed network that provides the required excitation at the array ports to maintain a constant directivity. The current excitation are optimized at various frequency points in order to conclude a specific excitation that provides the best compromise in providing a stable and wideband directivity.

#### 4.4.4.3 Fully Driven Configuration

In the case where both antennas are driven, the objective function of (4.6) is used where $w_1$ is set to $-1$. Similar to the previous section, the directivity optimization is carried at different frequencies. At each frequency point, the modal weighting coefficients are optimized and the total current is extracted from (4.7). Fig. 4.35 shows the optimized relative current phases and magnitudes and their corresponding end-fire directivities at each frequency of optimization. With these excitation, the array attains a maximal directivity of $7.13dBi$ at $0.88GHz$ after which it slightly decreases to become $6.82dBi$ at $1.03GHz$ while the backwards radiations increases from $1.8dBi$ at $0.83GHz$ to each $3.2dBi$ at $0.98GHz$ after which it decreases to $2dBi$ at $1.03GHz$ (Fig.4.36).

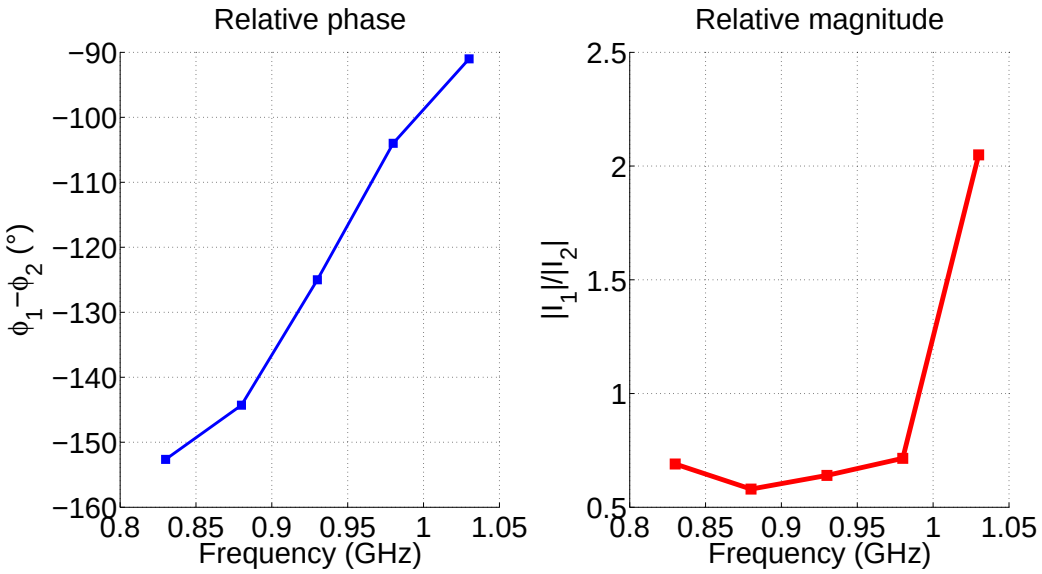


Figure 4.35: Optimized current excitation at the array ports for a fully driven configuration

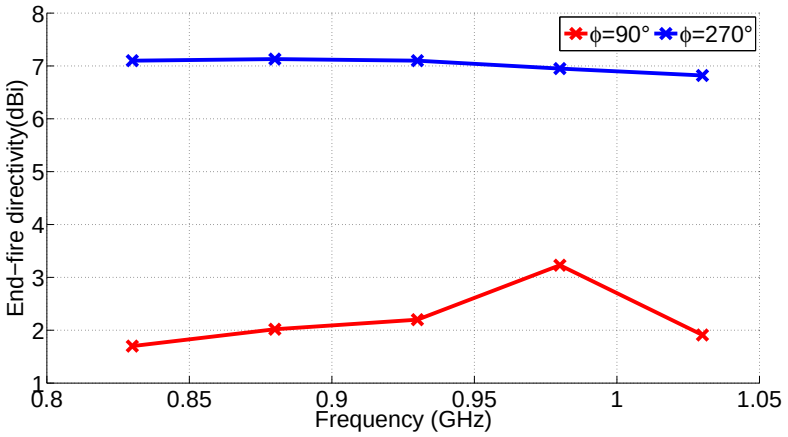


Figure 4.36: End-fire directivity as a function of frequency for optimized excitations.

Therefore, if the array ports are fed with the optimized excitation at each frequency point, it is possible to have a wideband directivity over the whole band. Although the optimized relative amplitude values are relatively constant in the band $[0.83-0.98GHz]$ having a value around 0.7, the relative phase is significantly changing in this band from $-152°$ at $0.83GHz$ up till $-91°$ at $1.05GHz$.

Another optimization is carried out by adding an additional constraint to the optimization function for optimizing the directivity and the Front-to-back ratio at the same time. The idea is to study the possibility to manipulate the modal excitation in a way to maintain a quasi-optimal directivity with a high $FBR$ and compare the optimized current values with respect to the values from the previous optimization, in order to finally conclude a constant current excitation that provides a compromise in maintaining a relatively stable directivity as a function of frequency. The new optimization function is given by:

$$F(a) = w_1 \times D(\theta_0, \phi_0) + w_3 \times |FBR - 10| U(FBR - 10) \tag{4.13}$$

where $w_1 = -1$ and $w_3 = 10$ is the weighting coefficient that determines the contribution of $FBR$ value in the optimization and $U$ is a step function which is equal to zero when $(FBR > 10)$ and equal to 1 when $FBR < 10$. In other words, the objective function optimizes the excitation coefficients in a way to obtain a maximal end-fire directivity ($\phi_0 = 270°$ and $\theta_0 = 90°$) while having an $FBR < 10dB$. In this case, due to the presence of another constraint, the obtained directivity values are not the optimal but however "near optimal". The optimization is carried out at the previously defined optimization points. Fig.4.37 shows the comparison between the optimized excitation of the original objective function denoted by $F_1(a)$ and the current objective function denoted by $F_2(a)$. The optimized relative magnitudes for both objective function have relatively similar values in the frequency band while there is a significant change in the values of the relative currents. This difference in the relative current excitations is translated by an increase in the $FBR$ which becomes higher than $10dB$ in the entire bandwidth while the peak end-fire directivity levels are slightly lower than the optimal values obtained by $F_1(a)$ (Fig.4.38a).

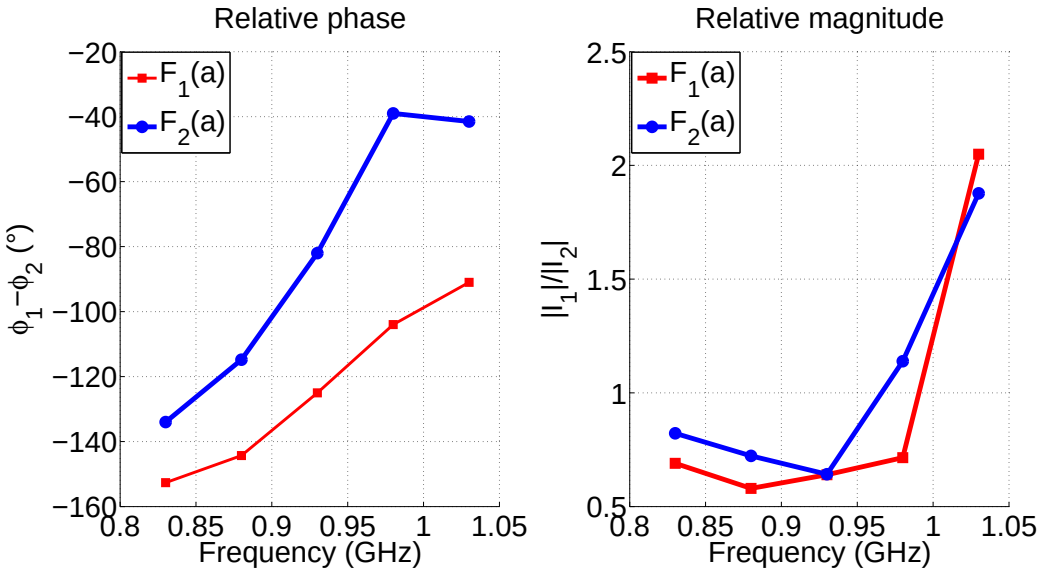


Figure 4.37: Optimized current excitation for the original optimization function and the added $FBR$ constraint.

By analyzing the relative current and phase magnitude, we find that a trade off can be made by providing a constant excitation at the ports while maintaining a relatively constant peak directivity. For the relative current magnitude it is easy to conclude that a value of $(\frac{I_1}{I_2} = 0.7)$ presents a good compromise as an excitation in the studied band. However, for the relative phase, various excitation values have been studied to find the one which provide the best compromise. The excitation values chosen are $-130°$,$-110°$ and$-70°$. These phases represent average values lying between the optimized phases of $F_1(a)$ and $F_2(a)$ given in Fig.4.37. Fig.4.38b shows the variation of the end-fire directivity for these specified phases while maintaining a constant relative magnitude of 0.7. The phase difference of $-130°$ exhibits the good

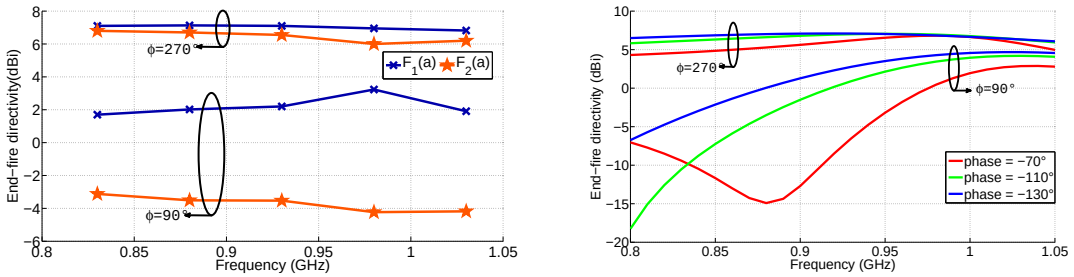


(a) (b)

Figure 4.38: End-fire directivity versus frequency of the fully driven array. (a) Optimized excitation for both objective function $F_1(a)$ and $F_2(a)$, (b) constant excitation for chosen phase differences.

compromise in terms of the stability of the directivity as a function of frequency while a phase difference of $-70°$ shows a poor directivity bandwidth. Therefore value of $-130°$ was found to be a good compromise in maintaining a relatively constant directivity. With this excitation ($\frac{I_1}{I_2} = 0.7e^{-j130°}$), the array exhibits a wideband directivity ($BW_{1dB} > 27\%$) with a peak value $D_{max} = 7.1dBi$ at $0.92GHz$. Yet, the $FBR$ decreases versus frequency which is expected since the applied excitation phase and magnitude both deviate from the optimized excitations as the frequency increases, which was mostly visible at $1.05GHz$ where the relative magnitude jumps to values higher than 1.

Hence in order to provide the suggested excitation a feed network should be designed and well integrated on the array structure in order to provide the chosen relative phase and magnitude at the ports so that the directivity remains constant, while maintaining the impedance matching of the array.

#### 4.4.4.3.1 Feeding Network: Design and Integration

Before starting the design of the feeding network, it is necessary to transform the desired current excitation into power excitations. The transformation into power excitation is given by:

$$P_n = I_n^2 Z_{active(n)} e^{-j4\pi(n-1)d} \tag{4.14}$$

$P_n$, $I_n$, and $Z_{active(n)}$ are respectively the power and current excitations, and the active impedance at the $n^{th}$ port. $d$ is the inter-element separation as a function of lambda. The relative power excitation corresponding to the chosen current excitation is $\frac{P_1}{P_2} = 0.75e^{-j130°}$, where $P_1$ is the power delivered to port 1 of the array, and $P_2$ is the power delivered to port 2. Therefore the desired feed network should be formed of an unequal power divider cascaded with a phase shifter. The schematic of the feeding network with the antenna is given in Fig. 4.39.

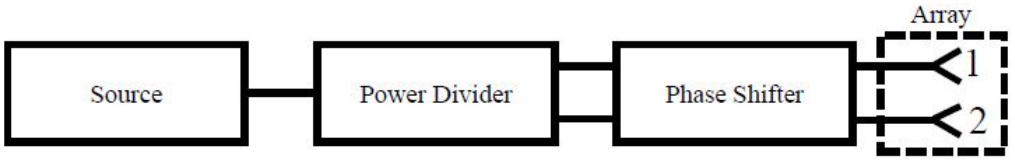


Figure 4.39: Schematic of the antenna with the feeding network.

The parameters of the feed network are optimized to provide the desired power excitation at its output.However, in the optimization procedure, the matching of the array when it is connected to the feeding network is taken into account. Therefore, an additional constraint is added to the optimization which limits the possibility to obtain exactly the desired phase shift from the feeding network.

The behaviour of the feeding network in terms of delivered power and phase shift is shown in Fig. 4.40a. The power ratio at the two ports is approximately stable over the desired bandwidth $0.7 < \frac{P_{f1}}{P_{f2}} < 0.75$ where $P_{f1}$ and $P_{f2}$ are the output powers of the feeding network delivered respectively to ports 1 and 2 of the array. The phase shift is not exactly $-130°$ in the desired band. The phase shift is changing the margin of $(-100°$ to $-127°)$ between $(0.8 - 1.05GHz)$. To investigate the effect of the deviation in the provided excitation with respect to the desired one, the end-fire directivity of the array with the excitations provided by the feeding network is compared to the previously chosen current excitation $(\frac{I_1}{I_2} = 0.7e^{-j130°})$.

Fig.4.40b shows that with the power excitation provided by the feeding network, the end-fire directivity maintains a relatively stable peak value $(D_{max} \simeq 6.5dBi)$ which is just $0.5dBi$ less than the peak end-fire directivity obtained by the chosen current excitations. Since the overall behaviour of array with the ideally connected feeding network is in good agreement with the current excitations, this feeding network is chosen to be integrated on the array structure.

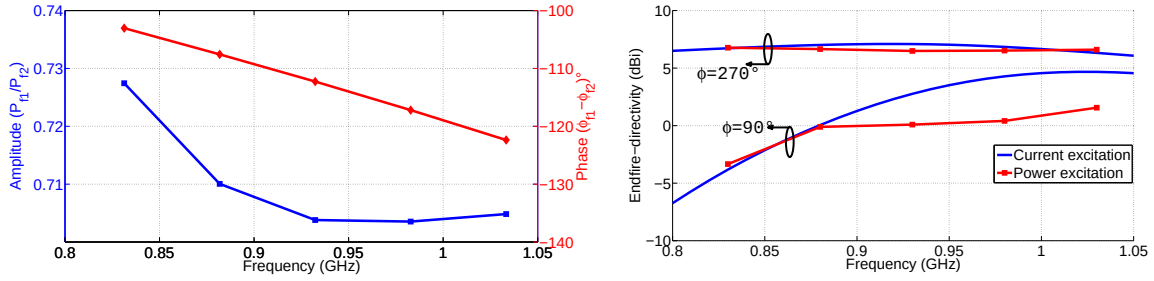


(a) (b)

Figure 4.40: Performance of the feeding network. (a) Relative amplitude and phase and the output ports, (b) end-fire directivity of the array with the power excitations of the feeding network compared to the chosen current excitations.

The topology of the feeding network is given in Fig.4.41, and the optimized parameter values are given in Table.4.3.

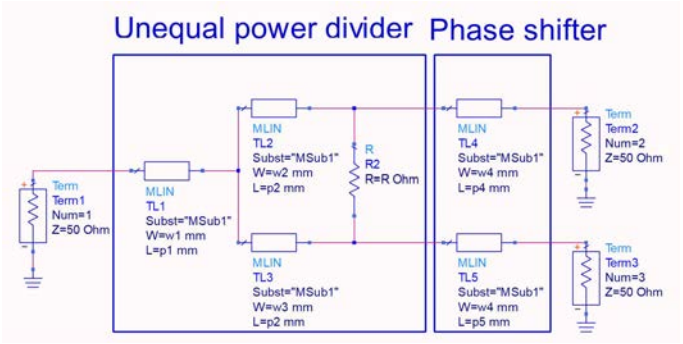


Figure 4.41: Topology of the feeding network.

Table 4.3: Parameters of the optimized feeding network.

| $w1(mm)$ | $w2(mm)$ | $w3(mm)$ | $w4(mm)$ | $R(Ohm)$ |
|---|---|---|---|---|
| 5 | 1.3 | 2.2 | 1.4 | 111 |
| $p1(mm)$ | $p2(mm)$ | $p4(mm)$ | $p5(mm)$ | |
| 60 | 48.4 | 200 | 94 | |

After verifying that the schematic design of the feeding network provides the array with excitations that can maintain its directivity constant in a wideband, the next step is to integrate this network on the bottom side of the array structure. Although it might seem a straight forward process, careful attention should be taken while integrating the feeding network in order not to perturb the currents on the array structure and deteriorate its performance. Especially that there is a gap between the ground planes of the two elements. A transmission line passing below this gap, might significantly alter the radiations of the array. Consequently, the characteristic modes analysis (CMA) is used to provide us with guidelines on defining the placement and the geometry of the feeding network.

The surface current distribution of the first two characteristic modes (dominant modes) at 950 MHz is given in Fig.4.42). By examining this current distribution we conclude that in order to minimize the effect of the feeding network on the behaviour of the modes, some constraints on its topology must be set. The feeding network topology should be as far as possible from the points where the modal current distribution is high, which are mainly the upper edges of the ground planes. In addition the transmission line passing under the gap should also be from the farthest possible from the upper edges.

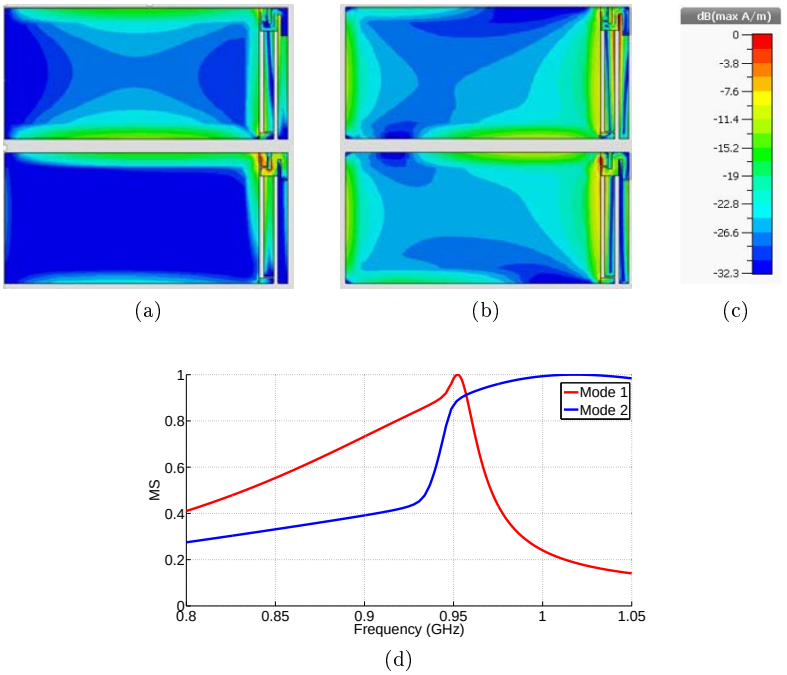


Figure 4.42: Modal surface current distribution. (a) Mode 1, (b) mode 2, (c) scale, (d) modal significance of the first two modes.

To verify this observation, three topologies of the integrated feeding network are considered for comparison (Fig.4.43). The feeding network of case 1 presents the topology that mostly agrees with the constraints that were set based on CMA where the line under the gap is as far as possible from the upper edges and it passes under the part where the current distribution is low for both modes. In addition, the transmission lines are not interfering with the upper edge current. On the other hand, in the topology of case 2 the line under the gap is closer to the upper edge and the transmission line of the phase shifter is interfering with the edge currents of the lower antenna. A more extreme case is shown in (Fig.4.43c) where the transmission lines are concentrated under the upper edge of the lower antenna. The modal significance of these three cases are compared with respect to the array without integrated feed (Fig.4.44). As expected the feeding network of case 1 presents the best modal performance, in which the effect on the first two original array modes is minimal. For case 2, the effect of is more visible in mode 1 where its resonance shifts about $40MHz$ while mode 2 remains in general unchanged, except in the upper part of the band where it becomes less significant. Case 3 presents the maximal effect in perturbing the modes especially mode 1 whose resonance is shifted from $0.95GHz$ to $0.82GHz$, in addition to its effect on mode 2 whose modal significance drops in the upper part of the band.

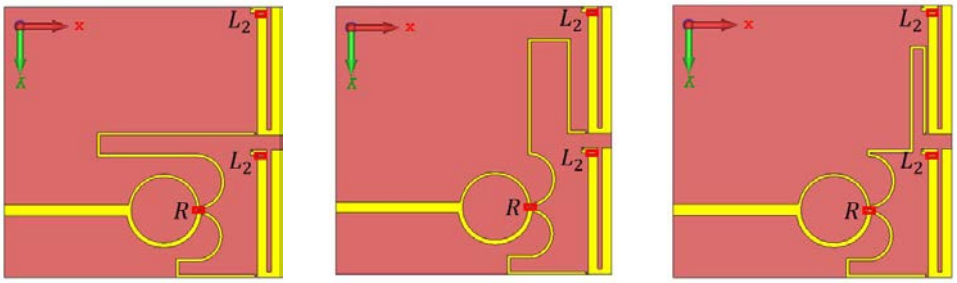


(a) (b) (c)

Figure 4.43: Different topologies of integrated feeding network. (a) Case 1, (b) case 2, (c) case 3.

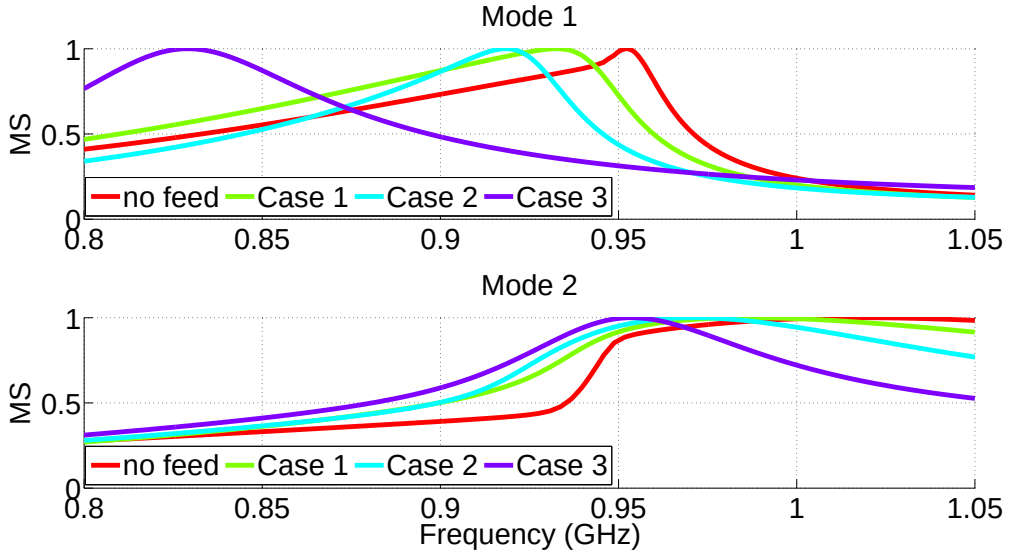


Figure 4.44: Modal Significance of the original array and the three feeding topologies.

The consequence of perturbing the modal behaviour of the array is visualized in its radiation and impedance characteristics. Fig. 4.45 shows the front and backwards end-fire directivity of the array with the three integrated feeds compared to the case where the feed and the array are schematically connected. As expected, the end-fire directivity of case 1 exhibits the best performance among the other cases. The end-fire directivity at $\phi = 270°$ is stable in the band with a 23% bandwidth, and a maximal value of $6.1dBi$ which is just $0.4dBi$ less than the ideal case. Moreover, the backwards radiations of case 1 are lower than that of the ideal case. However, for case 2, the directivity drops to $5dBi$ and the backwards radiations are high, on the other hand the maximal end-fire directivity for case 3 is switched to $\phi = 90°$ which however exhibits a narrowband.

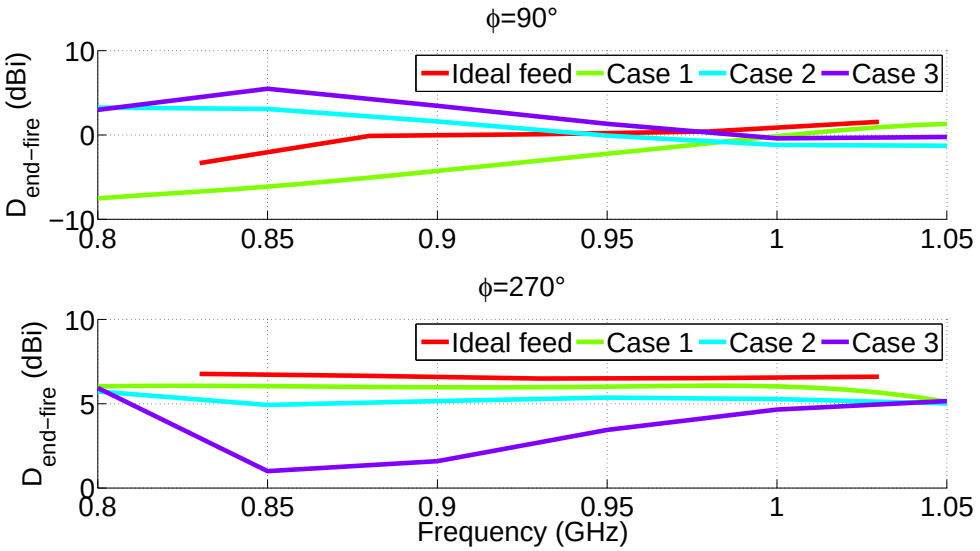


Figure 4.45: End-fire directivity versus frequency of the array with the three integrated feeding networks compared to the ideal current excitations.

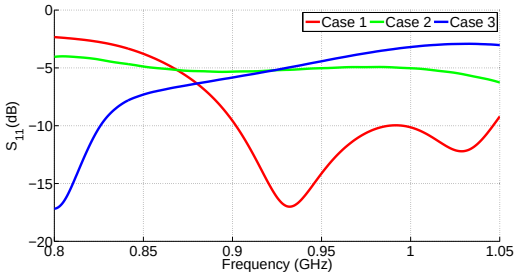


Figure 4.46: Input reflection coefficients for the cases of the integrated feeding networks.

Fig.4.46 shows the input reflection coefficient of the above three cases. Case 1 exhibits the best impedance performance where the array is matched in 15% relative bandwidth $[0.9-1.04GHz]$, while case 2 is mismatched in the whole band and case 3 is matched in the lower part of the band. Therefore, using the characteristic modes analysis it was possible to define a specified feeding network topology with the minimal effect on the original modes supported by the array structure in order to maintain a stable directivity which is similar to that provided when the ideal feeding network is connected to the array.

#### 4.4.4.3.2 Measurements

The simulation results have been validated by the prototype given in Fig.4.47. The measurement are in good agreement with the simulations. The array is matched in a 12% relative bandwidth $[0.92-1.03GHz]$ which is 3% narrower than the simulations (Fig.4.48). On the other hand, the measured end-fire directivity exhibits a relatively constant value in the principle direction ($\phi = 270°$) and a maximum of $D_{max} = 6.1dBi$ with reduced backwards radiations compared to the simulations (Fig.4.48b).

(a) (b)

Figure 4.47: Prototype of the array. (a) Top view, (b) bottom view.

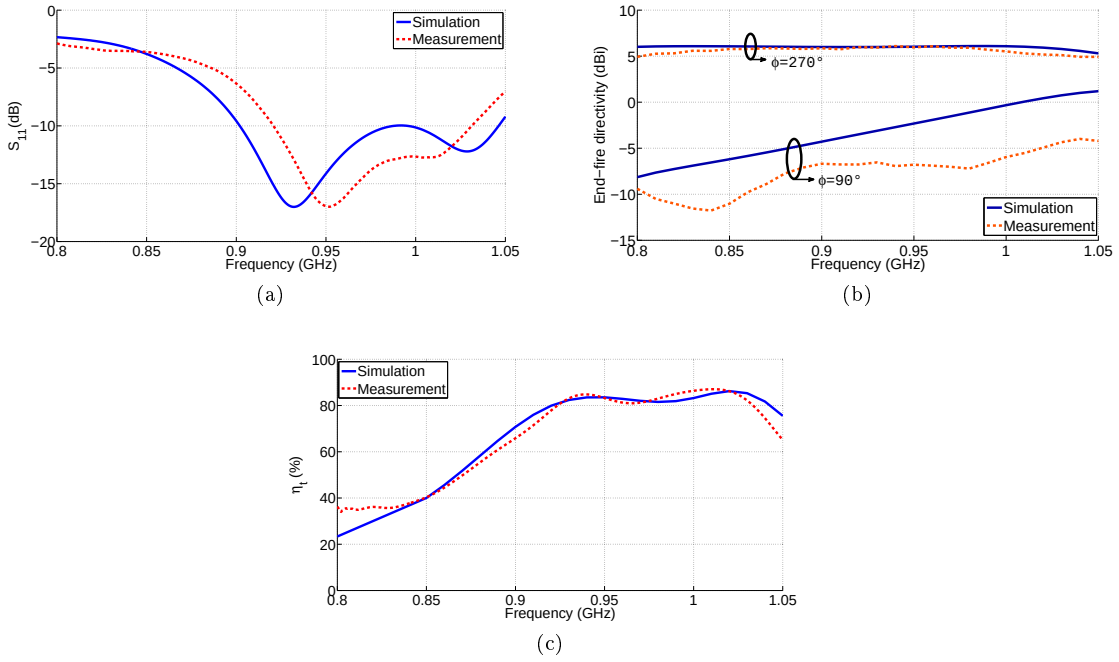


(a) (b)

(c)

Figure 4.48: Measurement results of the fabricated antenna. (a) Input reflection coefficient, (b) end-fire directivity in the front ($\phi = 270°$) and backwards ($\phi = 90°$) directions, (c) total efficiency.

The array efficiency was measured using the Wheeler cap method. The measurements are also in good agreement with the simulation (Fig.4.48c). the measured prototype is efficient in the operating bandwidth, with a peak efficiency of 87% at $1.01GHz$. Fig.4.49 shows the measured elevational and azimuthal 2D radiation patterns of the array at various frequency points in the band where it is matched. The results shows that the array exhibits a relatively stable pattern with a gradual increase in the backwards radiations as the frequency increases.

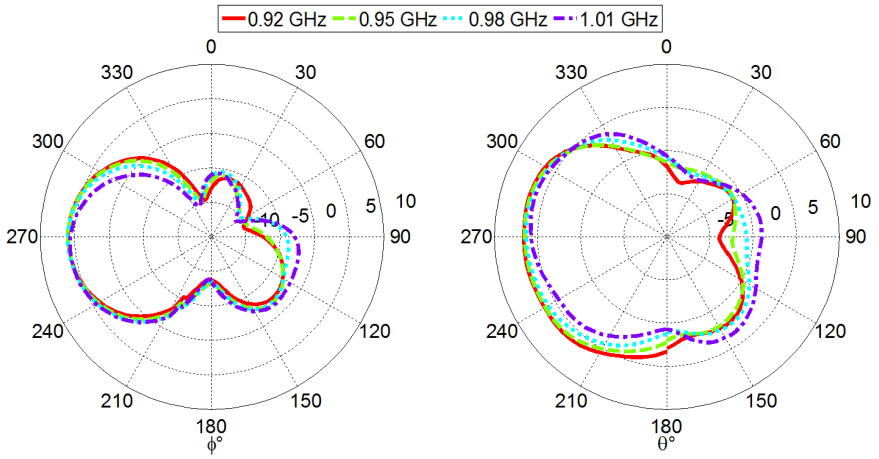


Figure 4.49: 2D radiation pattern of the array in the horizontal (left) and vertical (right) planes

#### 4.4.4.3.3 Three-element array

A two-element end-fire array with a wideband superdirectivity achieving a $D_{max}$ = $6.1dBi$ was designed. In order to go further and increase the peak end-fire directivity, more elements should be added. In this section we examine the effect of introducing an additional element on the array in terms of the achieved directivity bandwidth and impedance matching. The geometry of the array is shown in Fig.4.50. Similar to the previous configuration, the inter-element separation in $65mm$ with the unit elements internally loaded by the optimized inductive loads.

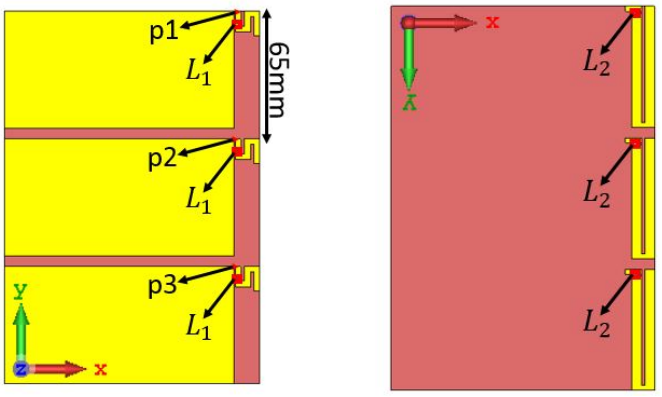


Figure 4.50: Geometry of the three-element end-fire array. (a) Top, (b) bottom.

The input reflection coefficients of the 3-port array is are given in Fig.4.51a. The elements situated at the extremity of the array are matched in a wideband $[0.83 - 1.08GHz]$ for element 1 and $[0.83 - 1.13GHz]$ for element 2. On the other hand, the second element lying in the middle is mismatched in the mentioned bands due to the high electromagnetic coupling at this position.

From a directivity point of view, an approach similar to the two element was applied to this array. After various optimization, it was noticed that with the relative excitations: $\frac{I_1}{I_2} = 0.6e^{-j174^\circ}$ and $\frac{I_3}{I_2} = 0.68e^{-j191^\circ}$ a peak end-fire directivity $D_{max}$ =

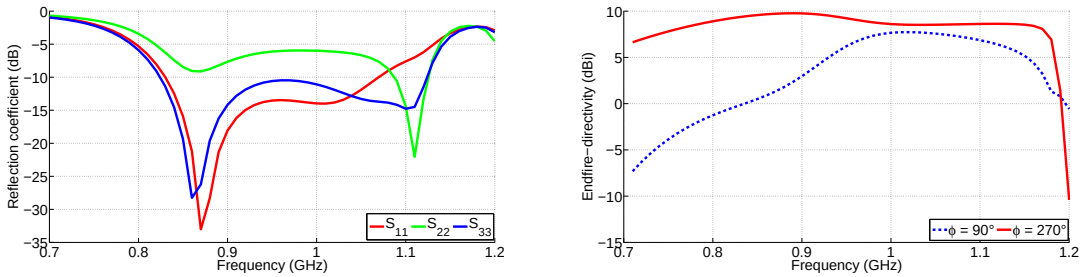


(a) (b)

Figure 4.51: Performance of the three element end-fire array. (a) Input reflection coefficient, (b) forward and backward end-fire directivity.

$9.8dBi$ can be achieved with a $1-dB$ drop bandwidth of 20% ($[0.8-0.98GHz]$) (Fig.4.51b). Compared to the simulated two-element array with the ideal current excitation $\frac{I_1}{I_2} = 0.7e^{-j130^\circ}$, this array achieves about a maximal directivity of about $3dBi$ higher, while however its directivity bandwidth is lower and one of its elements is mismatched.

Furthermore, for a parasitic case, where port $p_1$ is driven while the other ports are loaded with reactive loads $L = 2nH$ at port $p_2$ and $L = 2.4nH$ at port $p_3$, the array achieves a maximal end-fire directivity of $8.5dBi$ at $820MHz$ and a narrow 1-dB directivity bandwidth of 2% [818−840] (Fig.4.52). Besides, the array is mismatched at the frequency of maximal directivity with a matching level $S_{11} = -4.7dBi$.

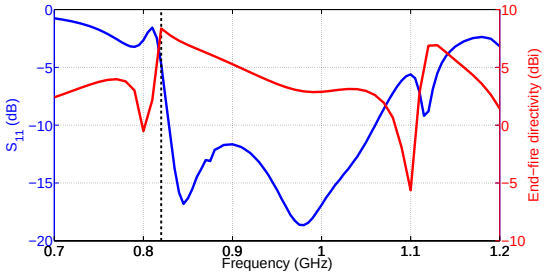


Figure 4.52: Input reflection coefficient at the active element and End-fire directivity of the parasitic array at $\phi = 270^\circ$.

Therefore, the design process becomes more complicated when dealing with more elements in the superdirective array. Although higher directivities can be achieved, the array becomes more constrained in terms of directivity bandwidth and matching level. This would therefore require a hybrid optimization that optimizes the directivity and the matching at the same time by controlling the modes through internal loads. However, such a process is not straight forward as the variation of the loads embedded inside the antenna would definitely alter the radiation characteristics of the fields corresponding to each mode. There is hence more work to be done in terms of wideband directivity optimization for multi-element superdirective arrays.

## 4.5 Conclusion

The design of superdirective arrays based on wideband unit elements was presented in this chapter. After presenting a literature review on the evolution of the design of superdirective arrays in both drive and parasitic configuration. It was noticed that in most of the designs the arrays suffered from a very narrow bandwidth and a low efficiency. In this context, the advantage of using a wideband unit element to form a superdirective array was shown. Two configurations were considered: stacked and linear. In a stacked configuration, a two-element array based on wideband unit element was compared to array based on a narrowband unit element. By optimizing the modal weighting coefficients of the characteristic fields to obtain a maximal end-fire directivity, It was shown that with wideband unit element it is possible to maintain an efficient and superdirective array even at very close separation distances ($d \leq 0.05\lambda$)) contrary to an array based on narrow band antenna whose efficiency is tends to zero as the separation distance decrease. Nevertheless, despite the high efficiency, at close separations the array exhibit a narrowband directivity and impedance. In order to enlarge the bandwidth, a compromise should be made by increasing the inter-element separation distance. Consequently, a two wideband unit element were placed in a linear configuration with a $65mm$ inter-element separation. With this separation, and with the proper excitations, the array exhibited a wideband behaviour in terms of bandwidth and superdirectivity. In order to provide the required excitations to the array, a feeding network was integrated on the bottom side of the array structure. The integration was done using the characteristic modes theory which provided guidelines to determine the geometry of the feed that can minimally perturb the currents on the array structure. A prototype was then fabricated and measured to verify the simulation results. Finally, in order to investigate the limitations, a third element was added to the linear array showing that a significant enhancement in directivity can be achieved while the directivity bandwidth is lower compared to the two-element configuration, in addition to mismatched input reflection coefficient of the middle element.

Therefore, choosing a proper unit element is a critical point to design superdirective arrays. With wideband unit element, it is possible to overcome the efficiency limitations at close separation distances that exist with classical unit elements in addition wide bandwidths can be achieved at higher distances. However, there is always a compromise to make in terms of size, bandwidth, the maximal directivity (number of elements).

Fig. 4.53 shows the comparison of the designs we presented compared to the state of the art. The plot compares the designs with respect to their Gain-Bandwidth product ($G \times B$) as a function of their electrical size $ka$. The blue curve represents the upper bound on the $G \times B$ imposed by the electrical size occupied by an antenna. For a matching level of $S_{11} = -6dB$ the upper bound is expressed as:

$$G \times B = \frac{2}{\sqrt{3}} \left( \frac{1}{ka} + \frac{1}{(ka)^3} \right)^{-1} \times \left( N^2 + 2N \right) \tag{4.15}$$

where $N = ka + 1$ as derived from the re-normalized Harrington limit [124].

The two cases of stacked and linear configurations are considered in the comparison denoted respectively "This Work Stacked" and "This Work Linear". In both

cases it is evident that our designs present a significant performance enhancement with respect to the literature where they achieve a good compromise in terms of bandwidth, directivity and efficiency. However, there is always the effect of the electrical size, where a more compact design (stacked) would have a lower $(G \times B)$ product compared to the larger design (linear).

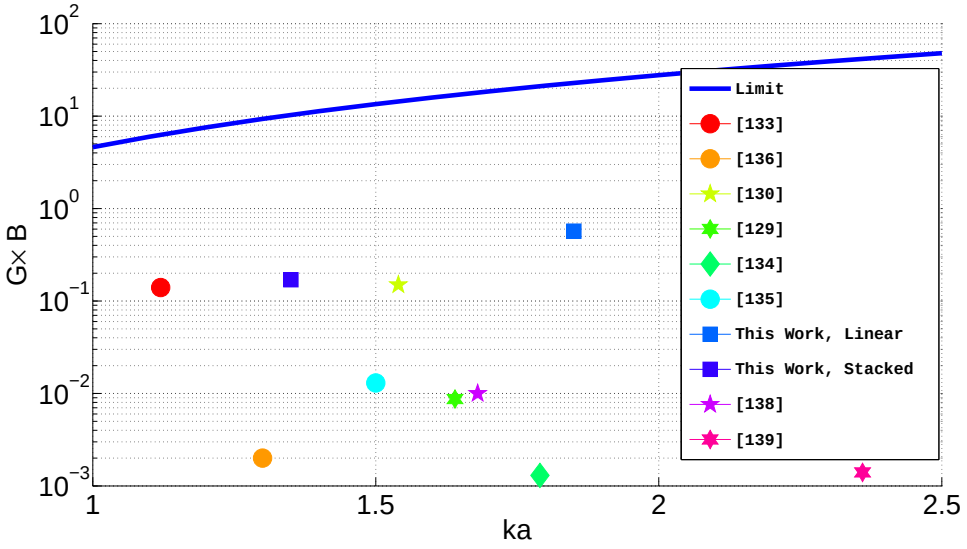


Figure 4.53: Gain-Bandwidth product comparison of our designed arrays compared to the state of the art.

After presenting and validating the approaches to design compact wideband and supredirective antennas using the NCM, in the next chapter we present the design of a broadband circularly polarized slot antenna using the characteristic modes. The characteristic modes analysis is used to manipulate the modes of a pre-selected structure through geometry modifications in order to finally achieve a broadband circular polarization and impedance matching.

# Chapter 5

# Design of Broadband Circularly Polarized Antenna Using Characteristic Modes Analysis

## 5.1 Introduction

Circularly polarized (CP) antennas are demanded in various wireless communication applications such as WLAN, RFID, radar, Global Navigation Satellite Systems (GNSS). The circular polarization is attractive due to its immunity to multipath interference, low sensitivity to polarization between the transmitter and the receiver, and higher weather penetration. Hence, a reliable signal link can be achieved using circular polarization [147]. CP antenna can be realized using either single feed or multiple feed. Although with multiple feeds it is possible to achieve wider bandwidth, yet this approach requires the integration of wideband power dividers and phase shifters and would increase the system complexity and cost [148, 149]. On the other hand, CP antenna with single feed have generally lower Axial Ratio (AR) bandwidth. Conventionally, patch antennas have been proposed to generate circular polarization using truncated edges and slots [150]. However, these designs suffer from a narrow AR bandwidth. In this context various researches have been dedicated to design compact single fed CP antennas with broadband AR. Slot antenna designs have become a popular approach in achieving broadband CP radiation.

Although the wideband single fed CP slot antennas presented in literature exhibit a satisfying performance, there is no physical insight provided towards the design of the antenna. The design is mostly based on parametric optimization of the antenna geometry. Consequently, This chapter presents a didactic approach on how to use the Characteristic Modes Analysis (CMA) in order to systematically design a compact CP antenna starting from an arbitrary geometry. By considering an arbitrarily slotted antenna, the CMs on the structure are analyzed and then it's geometry is accordingly modified and made more compact in order to permit the candidate modes to produce circular polarization. After achieving the desired modal behaviour on the slot, a feeding monopole is added to properly excited the desired modes and successfully generate circular polarization in the GPS L1 band.

The chapter is organized as follows: first, a state of the art on the low profile CP slot antenna designs will be presented, after which a detailed design procedure of a compact CP slot antenna with a broadband AR is explained. Finally, a prototype

of the designed antenna is measured to verify the approach.

## 5.2 State of the Art

Wideband CP slot antennas have been widely studied in literature. In this section we mention few of the remarkable designs that were found.

In [151], a wideband L-shaped monopole slot antenna with a C-shaped feed was designed. The antenna of size $(70mm(0.33\lambda) \times 70mm(0.33\lambda))$ achieved a CP bandwidth of 23%. With the L-shaped slot it was possible to generated E-fields which are orthogonal in the band of $[1.5 - 1.9GHz]$. A similar performance was achieved in [152] using a fractal slot geometry fed by a straight microstrip line. The fractal Iteration Order (IO) and Iteration Factor (IO) were optimized to achieve the desired performance (Fig.5.1a). The antenna of size $(65mm(0.34\lambda) \times 65mm(0.34\lambda))$ exhibited a wideband AR bandwidth of 23% $[1.47 - 1.83GHz]$ and a 26% Impedance bandwidth $[1.37 - 1.77GHz]$ (Fig.5.1b). In order to direct the radiation in the + z-axis and suppress the Right Hand Circular Polarization (RHCP), a copper plate reflector is placed parallel to the antenna at a distance of $\lambda_0/4$ (Fig.5.1c). With this configuration the antenna maintained its wideband AR and impedance bandwidth.

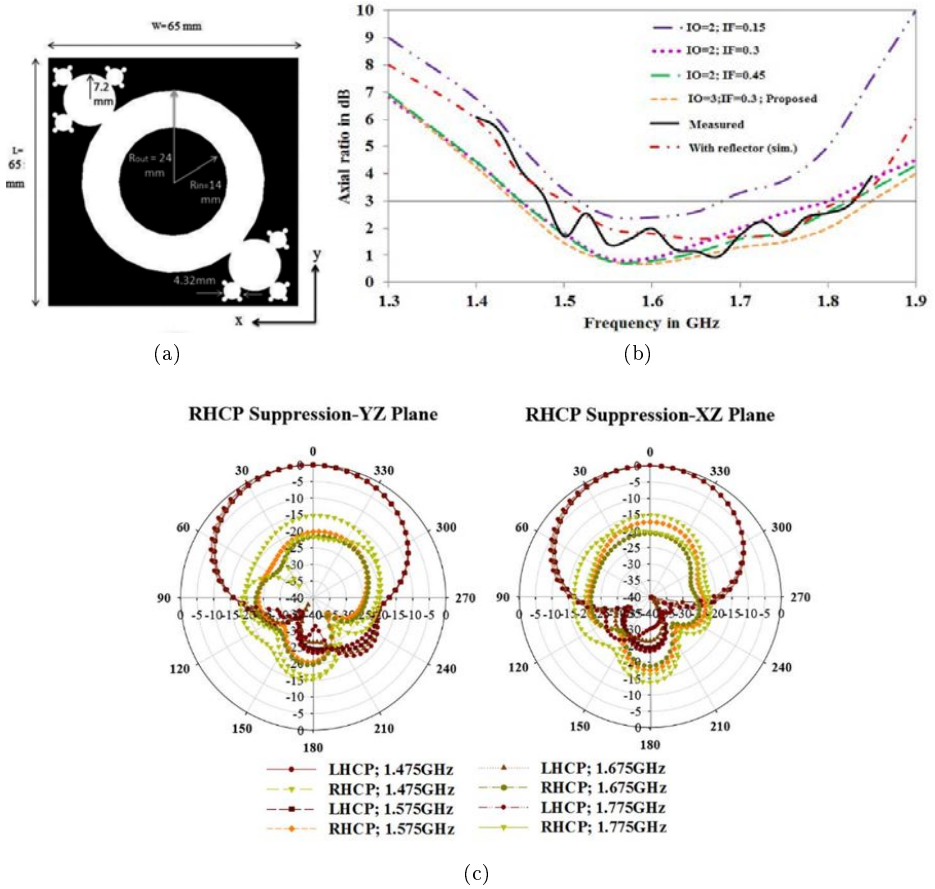


Figure 5.1: CP Fractal antenna characteristics. (a) Geometry, (b) axial ratio, (c) radiation pattern.[152]

Aly and Wang designed a wideband bidirectional CP antenna operating in the

GNSS band [153]. An L-shaped metal strip is fed to couple with the cross-slotted ground plane (Fig.5.2a). The dimensions of the L-shaped feed were optimized in order to achieve a wideband performance. Moreover, a supplementary vertical slot was added to control the AR bandwidth. A 20% AR bandwidth and 34% impedance bandwidth was achieved with this antenna occupying a size of $(75mm(0.38\lambda) \times 80mm(0.41\lambda)$ (Fig.5.2b,c).

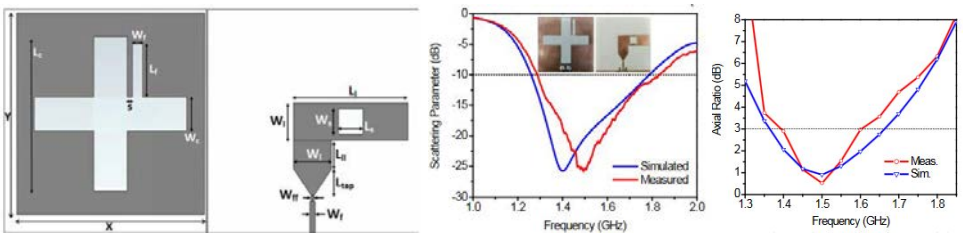


(a) (b) (c)

Figure 5.2: CP cross slotted antenna. (a) Geometry, (b) input reflection coefficient, (c) axial ratio. [153]

Another interesting wideband slot CP antenna design was proposed by the authors in [154]. The wideband circular polarization is obtained by introducing an antipodal Y-strip to square slot antenna. Furthermore, in order to achieve a wideband impedance bandwidth, the U shaped feedline is used. The antenna of having a compact size of $28mm(0.3\lambda) \times 28mm(0.3\lambda)$ exhibits an AR bandwidth of 41.3% $[4.4 - 6.67GHz]$ and an 84% impedance bandwidth $[3.25 - 8GHz]$ with a stable radiation pattern and a gain higher than $3dBi$ (Fig.5.3). Many other wideband CP antennas are found in literature [155, 156, 157].

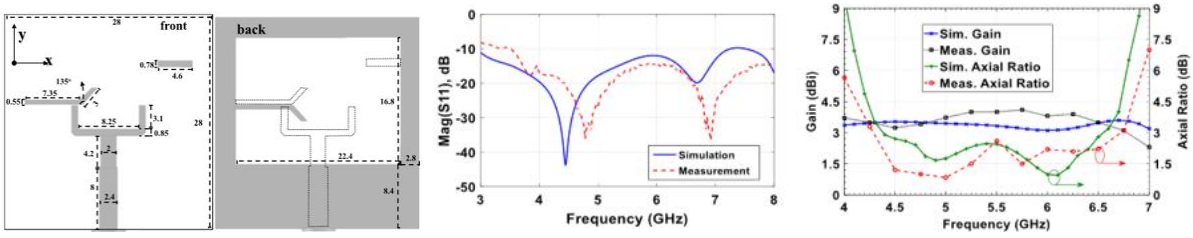


(a) (b) (c)

Figure 5.3: Square slot antenna with antipodal Y-strip and U shaped feed. (a) Geometry, (b) input reflection coefficient, (c) axial ratio. [154]

Few work on CP antennas using CMA was found in literature. The first design was already mentioned in chapter 1 which was performed by Chen and Wang to find the optimal excitation point in a U slotted patch antenna to produce circular polarization. With an offset feed, the antenna achieved a circular polarization at $2.32GHz$ with 3% bandwidth [39].

In a recent publication by Zhao and Wang, a wideband CP patch antenna consisting of H-shaped unit cells was designed [158]. With the highly coupled units a wideband impedance bandwidth of 38.8% and a $3dB$ AR bandwidth of 14.3% is achieved (Fig.5.4). However, the overall size of the antenna is large compared to the central operating frequency $75mm(1.3\lambda) \times 75mm(1.3\lambda)$. The design approach

is based on analyzing the characteristic modes currents supported by the structure and identifying the modes that can generate circular polarization, then exciting these modes using a microstrip line.

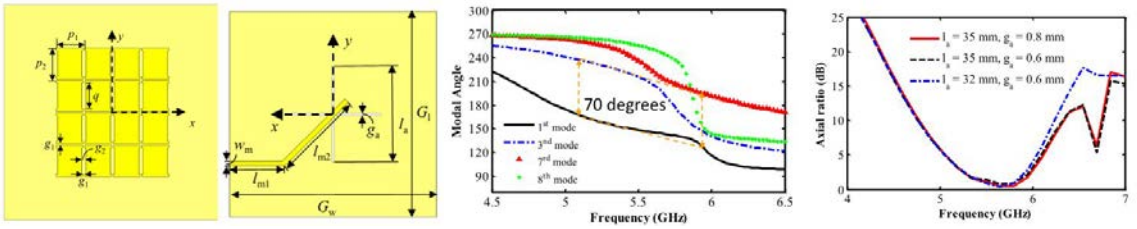


(a) (b) (c)

Figure 5.4: Performance of the patch antenna with H shaped unit cells. (a) Geometry, (b) characteristic angle (c) axial ratio. [158]

After presenting a brief literature review on some of the CP slot antenna designs presented in literature, in the next section we present the design of a broadband CP slot antenna using CMA.

## 5.3 Broadband Circularly Polarized Antenna

While designing CP antenna, two modal parameters should be taken into account. The first parameter is the Modal Significance $MS$ which shows the strength of the mode or its coupling capability with an external source. Therefore in order to excite a specific strong mode, the feeding should be carefully chosen to couple this mode with the excitation, otherwise it will not contribute in the overall antenna performance which means it would not have a high modal weighting coefficient $a_n$. The second parameter is the characteristic angle $\alpha_n$. $\alpha_n$ represents the constant phase lag between the $n^{th}$ characteristic current and its corresponding tangential characteristic field $E_n^{tan}(S)$ on surface $S$. Therefore, two modes $n_1$ and $n_2$ having a characteristic angle difference of $\Delta\alpha = \alpha_{n_2} - \alpha_{n_1} = \pm 90°$ could be candidates to realize circularly polarized radiation, on the condition that both modes are comparably excited i.e. they have comparable high $MS$ and they are well coupled with the excitation. The equations for $a_n$,$\alpha_n$ and $MS$ were given in chapter one in equation (1.9),(1.13) and (1.14).

Therefore, starting with any arbitrary structure, it can be possible to control the $MS$ and $\alpha$ by applying some modifications guided by the $CM$ analysis in order to finally produce a circularly polarized radiation. Also with CM analysis we can conclude some geometry modifications that can result in a more compact design.

### 5.3.1 Initial Geometry

The initial chosen geometry of the antenna is given in Fig.5.5. This geometry is denoted by Antenna A. Starting with the slotted ground plane of the antenna on which a triskele shape is etched. This shape consists of triple spiral exhibiting rotational symmetry. The reason of chosing this shape is due to the presence of spiral shapes that might permit the circulation of the fields. However, this shape is unconventional in designing antennas and we would like to examine its possibility to produce

circular polarization. For a central frequency of $1.57GHz$ the overall dimensions of the ground plane are: $(75mm(0.39\lambda) \times 75mm(0.39\lambda))$ and it is mounted on a Rogers RO5880 substrate of $\epsilon_r = 2.2$. As a first step, the characteristic modes that are supported by the structure should be analyzed in order to study its capability to produce a circular polarization and to apply some geometry modification in case its modes do not comply with the criteria of circular polarization. Then, after finding the acceptable geometry whose modes are good candidates to produce circular polarization, an excitation monopole will be added on the bottom side in order to equally excite the desired orthogonal modes. The flow chart of the design process is given in Fig.5.6

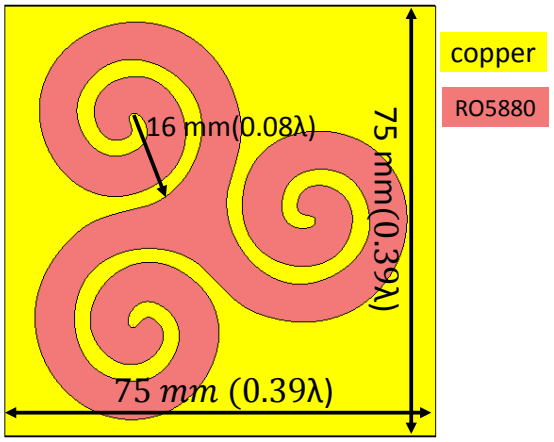


Figure 5.5: Initial geometry of the un-excited antenna (Antenna A) having a triskele etched ground plane.

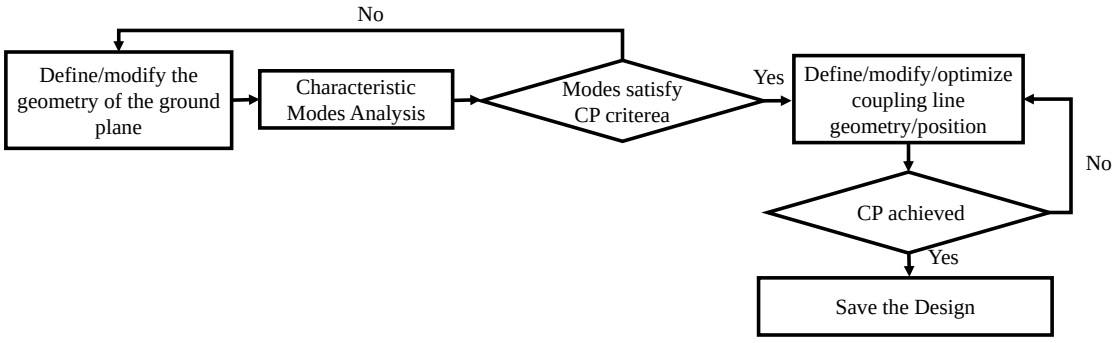


Figure 5.6: Design process of the circularly polarized antenna.

### 5.3.2 Characteristic modes Analysis

After defining the intitial geometry of the structure, its characteristic modes are then calculated and analyzed using the Multilayer solver in CST [84]. The CMA is applied in the frequency band $[1-2GHz]$. In this band we are mostly interested in generating a broadband circular polarization around the GPS L1 $[1.559-1.61GHz]$. At this frequency point $1.575GHz$, the first two modes exhibit the highest modal significance ($MS_1 = 0.81$, and $MS_2 = 0.85$) (Fig.5.7a).

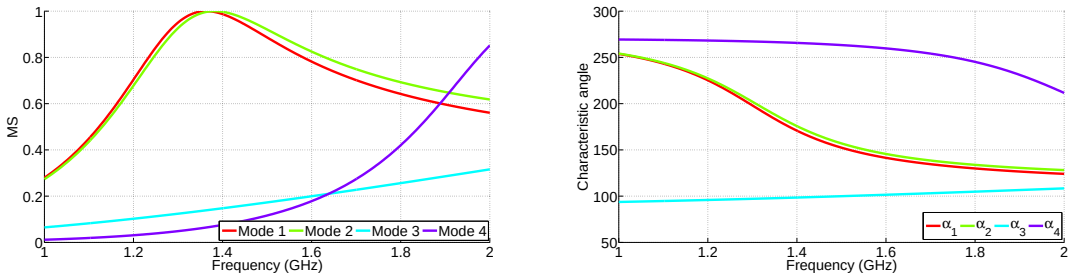


(a) (b)

Figure 5.7: Characteristic modes analysis of the defined geometry. (a) Modal significance, (b) characteristic angle.

Hence these are the modes that could eventually be coupled with the excitation. However, looking at the characteristic angle of these two modes, it is visible that they will not generate a circular polarization as they have almost similar characteristic angle $\Delta\alpha = \alpha_2 - \alpha_1 = 4°$, so the condition of $\pm 90°$ phase shift is not satisfied for this geometry. Therefore, some geometry modifications should be applied in order to increase the characteristic angle shift between the desired modes to finally be able to generate a circular polarization at this frequency.

However, the interest is to generate a circular polarization in a broadband and not just at one frequency point. In this case, the MS of the modes should be high and significant over a broad band, in addition, the characteristic angle difference should be around $\pm 90°$ inside this bandwidth.

In the next section we present the approach to modify the geometry of the structure in order to generate a circular polarization in a broadband.

### 5.3.3 Geometry modification

In order to apply geometry modification, it is important to examine the surface current distribution of the modes in order to understand their behaviour and identify the best choice of modifications in terms of modal performance and size. The surface current distribution of the first four modes at the central frequency $1.575GHz$ is given in Fig.5.8. It is evident that the currents supported by Mode 1 are horizontal, while those supported by Mode 2 are vertical ones. In general, this should results in a $\pm 90°$ shift between the modes and should be visible in their characteristic angles. However, a deeper look at the current distribution of these two modes in the spirals, we notice that both modes exhibit a maximal current in the right spiral. However, the currents corresponding to Modes 1 and 2 inside this spiral are in opposite phase. This phase opposition might be the reason why $\Delta\alpha$ is low, although the modes should naturally have an almost orthogonal phase difference. Therefore, in order to discard this inconvenience, the right spiral part is cut away from the geometry, and a copper line is added to join the two spirals as shown in Fig.5.9. The new geometry is denoted by Antenna B having a more compact dimensions than the original geometry $(75mm(0.39\lambda) \times 45mm(0.23\lambda)$.

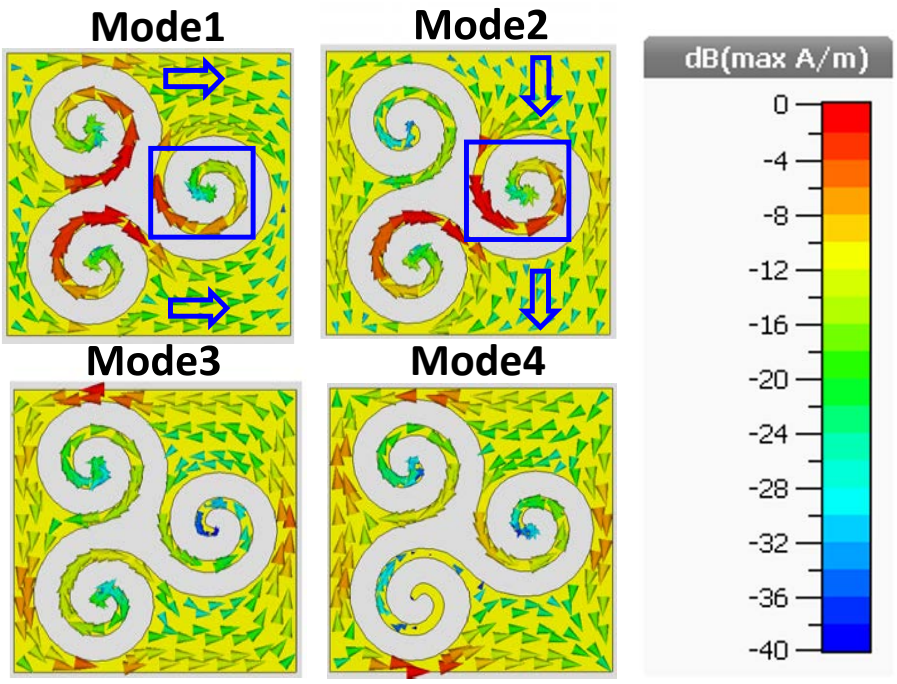


Figure 5.8: Surface current distribution of the characteristic currents at 1.575 $GHz$ of Antenna A.

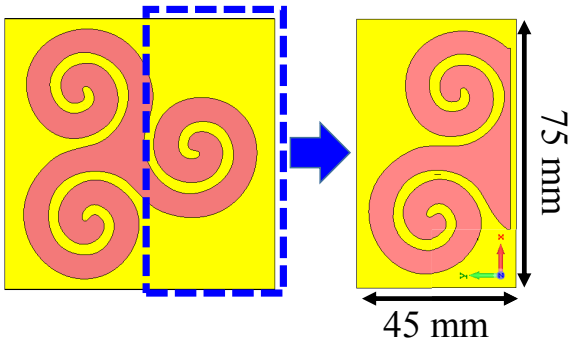


Figure 5.9: Geometry modification of the structure following the CMA, Antenna B.

In order to verify that this geometry modification was efficient in increasing the characteristic angle difference between the first two modes. CMA is applied on the new structure. A significant improvement in the characteristic angle difference is notice in the new compact geometry. $\Delta\alpha$ maintains a relatively stable value of about 120° in the bandwidth of interest (Fig.5.10b) . Although $\Delta\alpha$ did not attain the 90° value after this geometry modification, this value might be sufficient to produce circular polarization. Moreover, this value can be further optimized when adding the coupling feed. However, if we examine the modal significance of the desired modes in the bandwidth around $1.575GHz$, it is noticed that the modes do not have a comparable MS. The MS of modes 2 increases from 0.57 at $1.57GHz$ up till 0.65 at $1.61GHz$. On the contrary, mode 1 is less significant in this band where it exhibits an MS whose value varies in the range of 0.3 in this band (Fig.5.10a).

Compared to the initial configuration, the modal behaviour of the modified struc-

ture have totally changed, where the modes have no more similar behaviour in terms of MS and characteristic angle. The inductive mode 2 became capacitive after cutting the spiral shape. Moreover, the resonance behaviour have also changed. In the initial configuration, both modes were resonant at about $1.28GHz$. After the modification, the resonance of mode 1 drops to $1.19GHz$ while that of mode 2 increases up to $1.8GHz$. Although with this modification it was possible to achieve an acceptable $\Delta\alpha$, the low MS of mode 1 will prevent the production of a circular polarization since it will not be excited since it will have a low modal weighting coefficient as shown in equation (1.15).

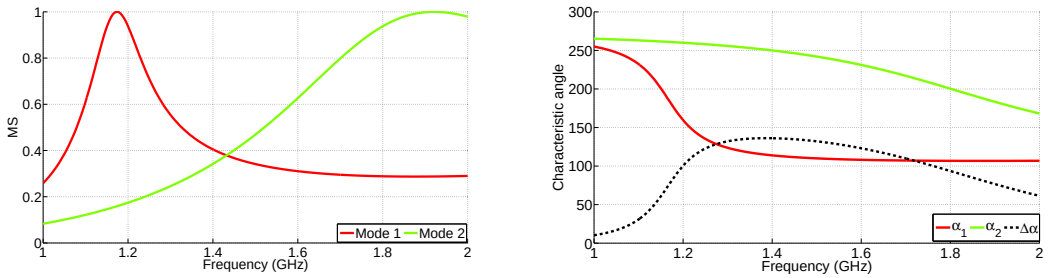


(a) (b)

Figure 5.10: Characteristic modes analysis of Antenna B. (a) Modal significance, (b) characteristic angle.

This implicates the need to apply another geometry modification in order to reduce the inductive effect of mode 1. This will serve in increasing the level of its characteristic angle in the bandwidth of interest such that $\Delta\alpha$ approaches 90°. To apply the geometry modification, it is then important to study the current distribution of the first two modes in order to identify the appropriate changes that must be done. It should be noted that only the first two modes are studied since the other higher order modes are insignificant in the bandwidth of interest.

Fig.5.11 represents the surface current distribution of the first two modes at $1.57GHz$. Mode 1 exhibits a very low current distribution in the area marked by the red square. The current at both sides of this null circulate in opposite direction which might be the reason of the high inductive behaviour of mode 1. Therefore, a gap added at the position of the current might impose the continuity of the first modal current and hence reduce its inductive effect. The new modified geometry denoted Antenna C is shown in Fig.5.12. The gap of size $(19mm \times 2.8mm)$ is added along the strip line connecting the two spirals.

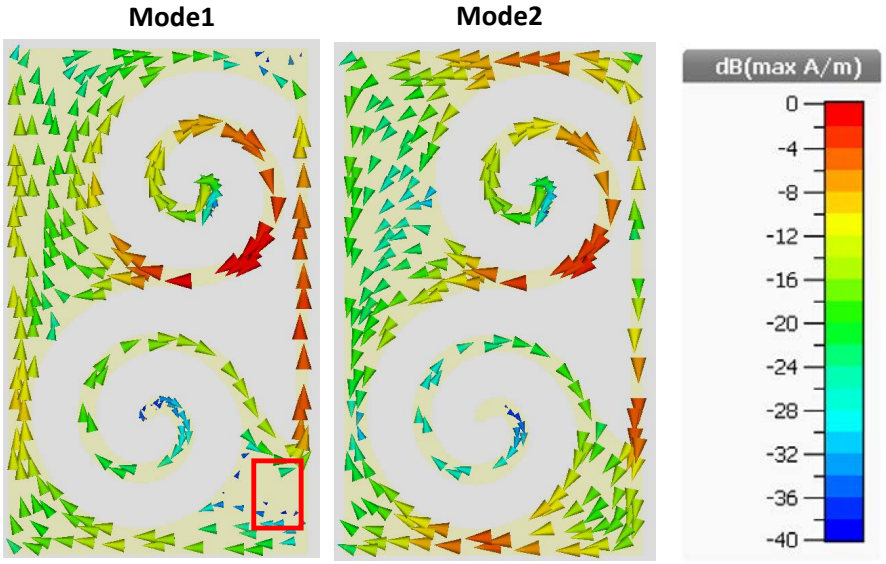


Figure 5.11: Surface current distribution of the first two modes in Antenna B.

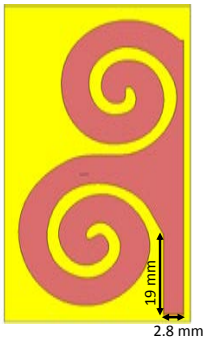


Figure 5.12: Geometry modification of the structure following the CMA, Antenna C.

To verify that this modification have effectively enhanced the potential of the structure to produce circular polarization, CMA is applied and the results are given in Fig.5.13. This modification have effectively increased the MS of mode 1 in the bandwidth of interest. Considering a mode to be significant for $MS > 0.6$, mode 1 is significant between which became significant in a wideband $[1.21 - 1.82GHz]$. However, mode 2 is significant starting from $1.6GHz$ up till beyond $2GHz$. At $1.57GHz$ mode 2 exhibits a modal significance of 0.57 which can still be considered as significant (Fig.5.13). Comparing these results to those of the previous geometry, it is noticed that the MS of mode 1 was impacted while that of mode 2 was slightly changed.

Furthermore, the inductive effect of mode 2 has been effectively increased by the addition of the gap, while that of mode 2 is still relatively unchanged with respect to the previous geometry. This increase in $\alpha_1$ has resulted in decreasing $\Delta\alpha$ which exhibits a relatively constant value of 90° in the GPS L1 band. At the frequency point $f = 1.65GHz$, $MS_1 = MS_2 = 0.7$ and $\Delta\alpha = 90°$. This presents the perfect condition for generating a circular polarization. In addition, the stable value of $\Delta\alpha$

and the comparable modal significance of the first two modes over a broadband offers the potential to realize a broadband circular polarization using this geometry.

The surface current distribution of modes 1 and 2 at $1.57GHz$ of the modified geometry is given in Fig.5.14. It is shown that mode 1 has no more a null current region in the area surrounding the gap. After adding the gap, the current of mode 1 maintains its continuity in the region where it was null. This continuity have decreased its inductive and insured a vertical surface current distribution along the structure, while on the other hand, mode 2 remained a horizontal mode after this modification.

It should be noted that even though the perfect condition to realize circular polarization exists in a frequency point which is outside the bandwidth of interest, the modal conditions presented inside this bandwidth are sufficient to realize such polarization. Besides, as stated before, adding the coupling feed might also have an impact on reducing the resonances of both modes and enhance more the circular polarization conditions in this bandwidth.

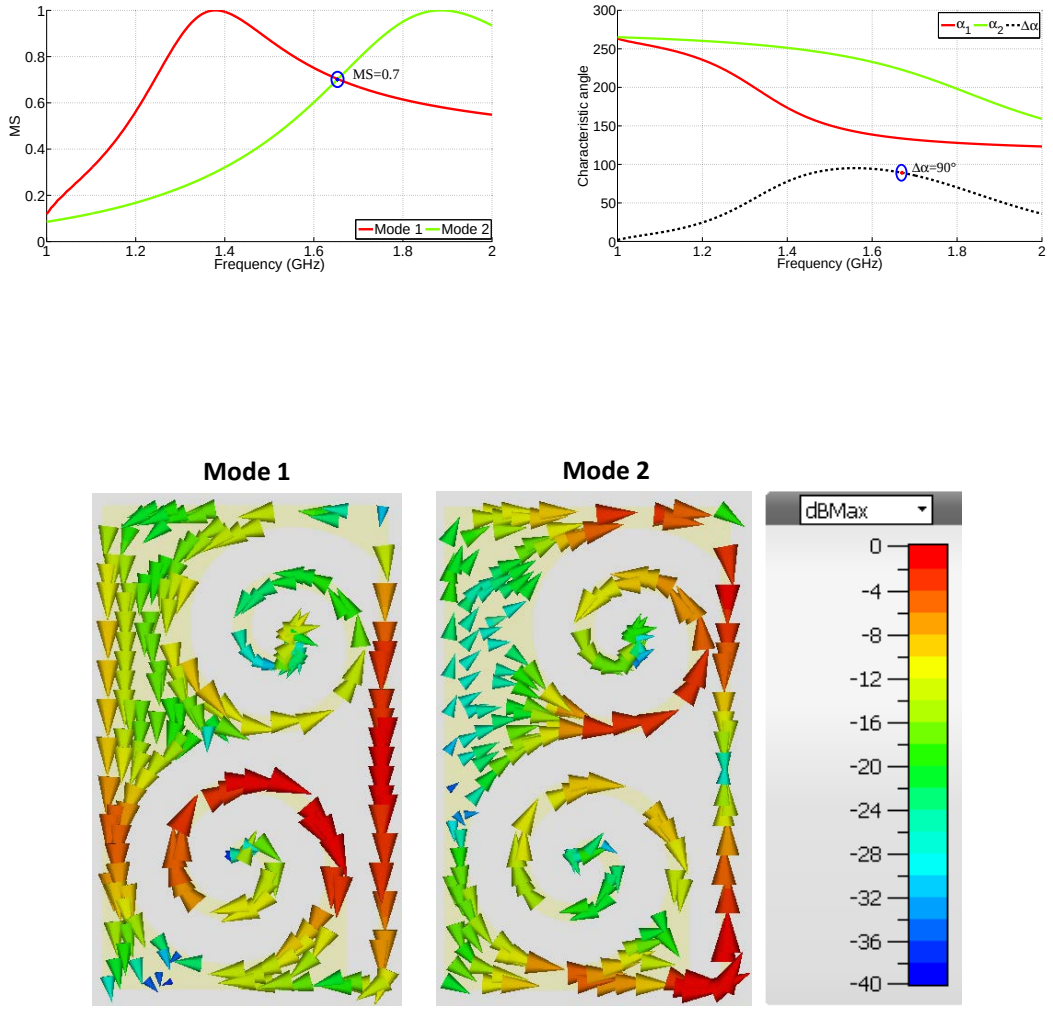


Figure 5.14: Surface current distribution of the first two modes in the geometry in Antenna C.

After applying the necessary geometry modifications required to provide a circular polarization, in the next section we present the integration of the coupling feed. This feed should couple with the desired modes (mode 1 and 2) supported by the optimized compact geometry with the excitation in order to assure the production of a circular polarization.

### 5.3.4 Modal excitation

The optimized structure supports the two modes which present good candidates to generate circular polarization in a broadband. Yet, in order to reach a final design with the desired characteristics, the aforementioned modes should be properly coupled with the excitation. As stated in the previous section, the optimized structure represent a ground plane, and in order to excite the modes supported by this ground plane, a coupling feed should be added at the bottom side of the structure. In order to study the excitation possibility of the first two modes, the surface current distribution of these modes should analyzed to identify the best position and geometry of the coupling feed.

#### Feeding Design

The surface current distribution is presented in Fig.5.15. Mode 1 exhibits a high surface current distribution in the bottom spiral shape and in the right strip line connecting the two spirals. On the other hand, mode 2 exhibits a high surface current distribution mainly in the bottom edge of the gap and the upper spiral. Therefore in order to excite these modes, the feed should couple with the regions

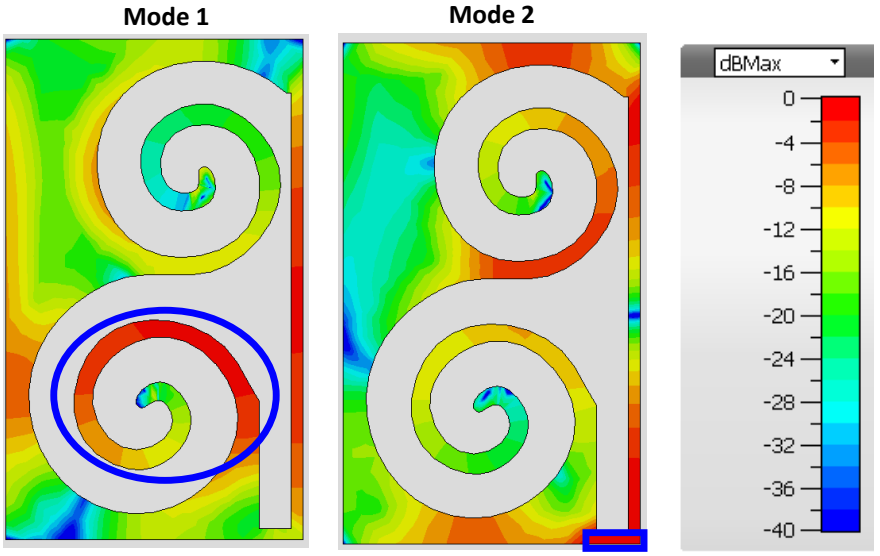


Figure 5.15: Surface current distribution of the first two modes in Antenna c, with the excitation regions marked in blue.

To excite both regions simultaneously, the feed should normally have an L-shaped

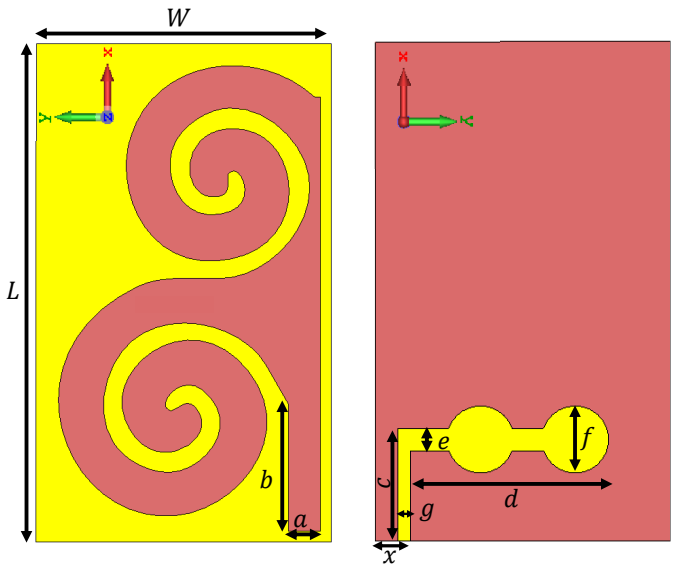


Figure 5.16: Geometry of Antenna D.

geometry which starts from the bottom edge of the gap to couple with mode 1 and then deflects in a right angle towards the bottom spiral. The geometry of the spiral structure with the L-shaped feed is given in Fig.5.16. The new geometry is denoted by Antenna D. The coupling feed is a classical monopole with two circular shapes at its extremity. The reason of choosing this structure to excite the ground plane modes rather than using a strip line of constant width is that the circular form will provide impedance variations of the feed and allow to match it in a wide impedance bandwidth in which it will be simultaneously circularly polarized. Of course, the parameters of the feed need to be optimized in order to satisfy the desired specifications.

Yet, in order to verify that the modes of Antenna D are still fit to produce circular polarization, CMA is applied to the new structure. The MS and the characteristic angles are plotted in Fig.5.17. In general the behaviour of the modes is still the same as the ones in Antenna B, with a slight shift in the frequency and a small variation in the values of $\Delta\alpha$. The MS of both modes become equal at $1.59GHz$ with a value of 0.63. At this point the value of the characteristic angle difference is $\Delta\alpha = 100°$. Moreover, similar to the previous structure, the modes maintain their dominance in a broadband around this frequency and a relatively stable $\Delta\alpha$.

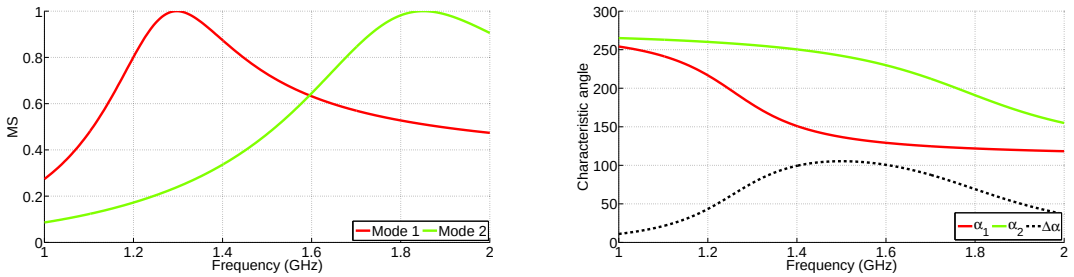


(a) (b)

Figure 5.17: Characteristic modes analysis of Antenna D. (a) Modal significance, (b) characteristic angle.

The surface current distribution of the first two modes at $1.57GHz$ is given in Fig.5.18. Both modes maintain a current distribution which is relatively similar to the Antenna C. The current distribution of mode 1 is still concentrated in the strip line connecting the two spirals and in the lower spiral, with a slightly added contribution from the feeding monopole. Mode 2 also maintains a current distribution

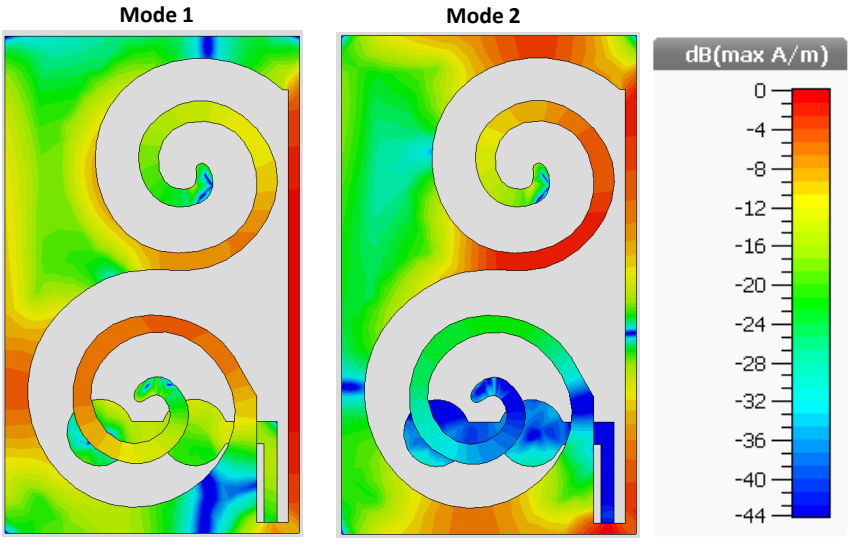


Figure 5.18: Surface current distribution of the first two modes in Antenna D.

### 5.3.5 Results Outline

The evolution in the modal behaviour throughout the geometry changes is given in Fig.5.19. The first modification from Antenna A to Antenna B was the most effective in changing the behaviour of the modes, where the resonance of Mode 1 shifts downwards and that of Mode 2 shifts upwards. Due to this change, mode 2 becomes capacitive in the desired band( $180° < \alpha_2 < 270°$), while Mode 1 becomes more inductive. This change was the key point in creating a high phase difference between the two modes as a primary step to make them compatible for circular polarization. On the other hand, the changed towards Antenna B and C mainly

targeted the first modes where its characteristic angle was increases along with its modal significance, while Mode 2 was slightly affected by these modifications.

It should be mentioned, that when changing the geometry of the structure, the modes on both structures are not totally identical. However, when analyzing the modes of the initial and modified structure, we allow approximating or associating modes of both structures in order to depict the evolution of its behaviour.

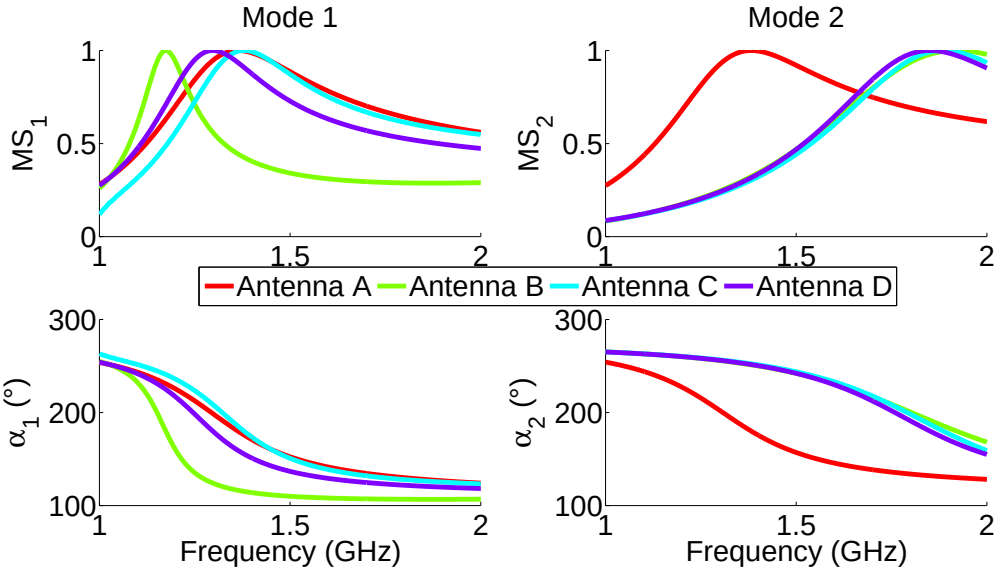


Figure 5.19: Variation of the modal characteristics as a function of geometry changes.

**Feed Excitation**

After verifying that final structure supports two dominant orthogonal modes with almost 90° phase shift. The next step is to excite the feed and to verify the capability to produce circular polarization. Antenna D is excited at the edge of the feeding monopole whose ground plane is the spiral shaped structure. The excited antenna is shown in Fig.5.20.

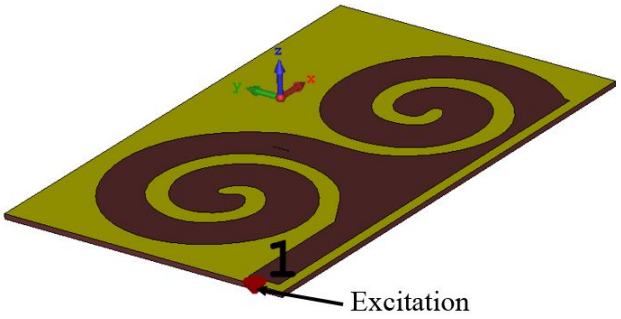


Figure 5.20: Schematic representation of the excited antenna.

Yet in order to insure that the antenna achieves the desired behaviour. The dimensions of feed and its positions should be correctly optimized. The final dimensions of the antenna geometry are given in Table.5.1. For a matching level of $S_{11}$ <

Table 5.1: Dimensions in $mm$ of the final design.

| $L$ | $W$ | $a$ | $b$ | $c$ | $d$ | $e$ | $f$ | $g$ | $x$ |
|---|---|---|---|---|---|---|---|---|---|
| 75 | 45 | 2.8 | 19 | 17 | 29 | 3.4 | 11 | 1.95 | 3.8 |

$-10dB$ the antenna is matched in a wide impedance bandwidth $[1.16 - 1.68GHz]$ (36%) in which it is circularly polarized in the frequency band $[1.55 - 1.68GHz]$ (8%) which indicated that the antenna can operate in the GPS L1 with a circularly polarized radiation (Fig.5.21). $AR < 3dB$ is considered as a criteria for circular polarization. Moreover, the antenna is efficient in its bandwidth of operation with a total efficiency of higher than 90%, while the realized gain is about $3dB$. The obtained results verify the CMA approach in exciting the first two orthogonal modes and hence generating circular polarization.

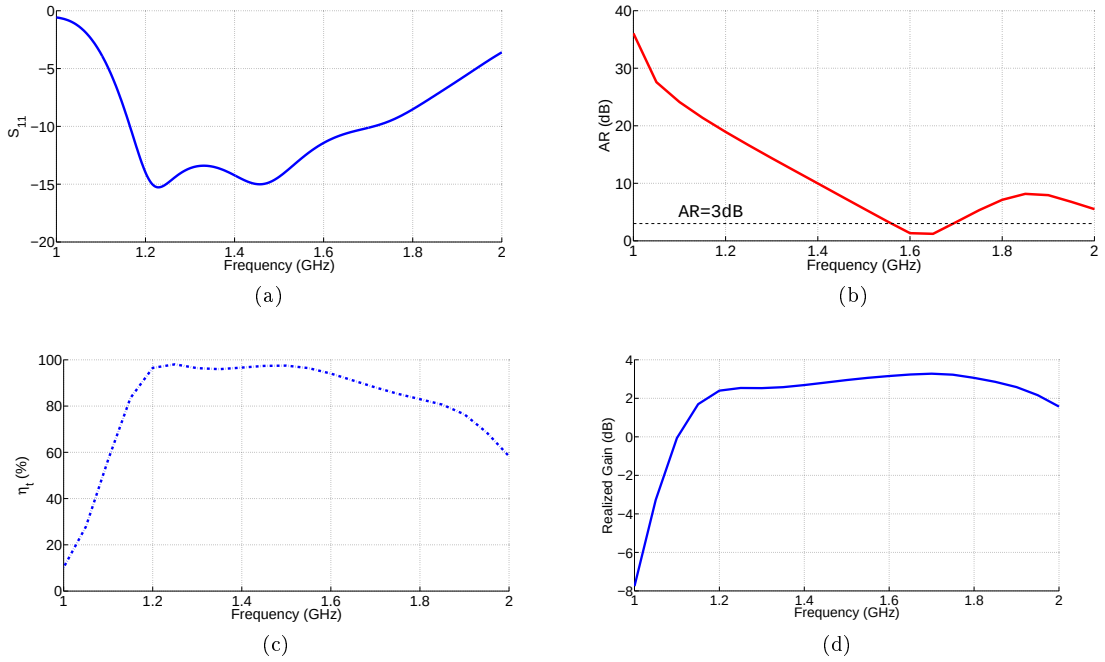


Figure 5.21: Simulated performance of the excited antenna. (a) Input reflection coefficient, (b) axial ratio, (c) total efficiency, (d) realized gain.

**Radiation Characteristic**

The simulated radiation patterns in the XZ and YZ planes of the antenna at some frequency points in the bandwidth of interest is given in Fig.5.22. It is notice that the antenna exhibits a bidirectional radiation characteristics. It radiates a Right Hand Circularly Polarized (RHCP) pattern in the direction of $\theta = 180°$ and a Left Hand Circular Polarization (LHCP) in the direction of $\theta = 0°$.

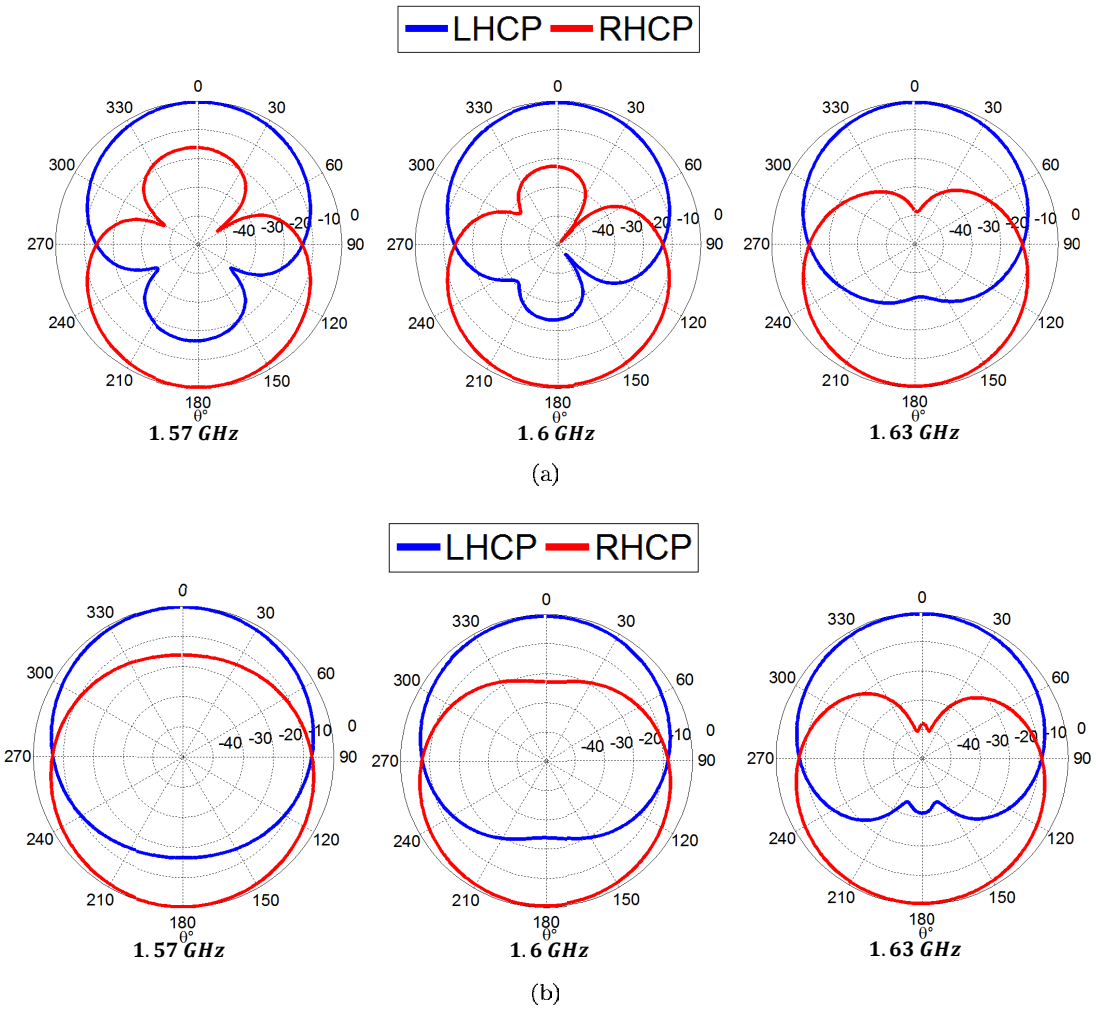


Figure 5.22: Simulated radiation pattern for different frequency points. (a) XZ plane, (b) YZ plane.

## 5.4 Measurements

Since the bidirectional radiation limits the performance of a circularly polarized antenna, the RHCP should be suppressed using a reflector. To suppress the RHCP radiation the prototype a copper plate of dimensions $(90mm \times 90mm)$ is used as a reflector. This plate placed in the xy plane at a distance of $48mm$ from the antenna in the $-$ z-axis. This distance corresponds to approximately a quarter wavelength for the frequency $1.57GHz$. The prototype and its configuration with a reflector, is given in Fig.5.23 where the green material is a foam substrate having an $\epsilon_r \approx 1$, which is used to maintain a stable separation distance between the antenna and the reflector.

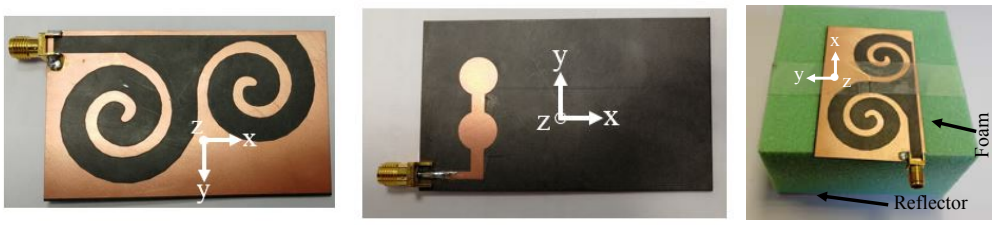


(a) (b) (c)

Figure 5.23: Prototype. (a) Top view, (b) bottom view, (c) Antenna on copper plate reflector

With this reflector, the RHCP is effectively suppressed as shown in these simulated and measured radiation pattern samples given in Fig.5.23. A cross polarization discrimination greater than $10dB$ is achieved for all frequency samples with a good agreement between the simulation and measurements.

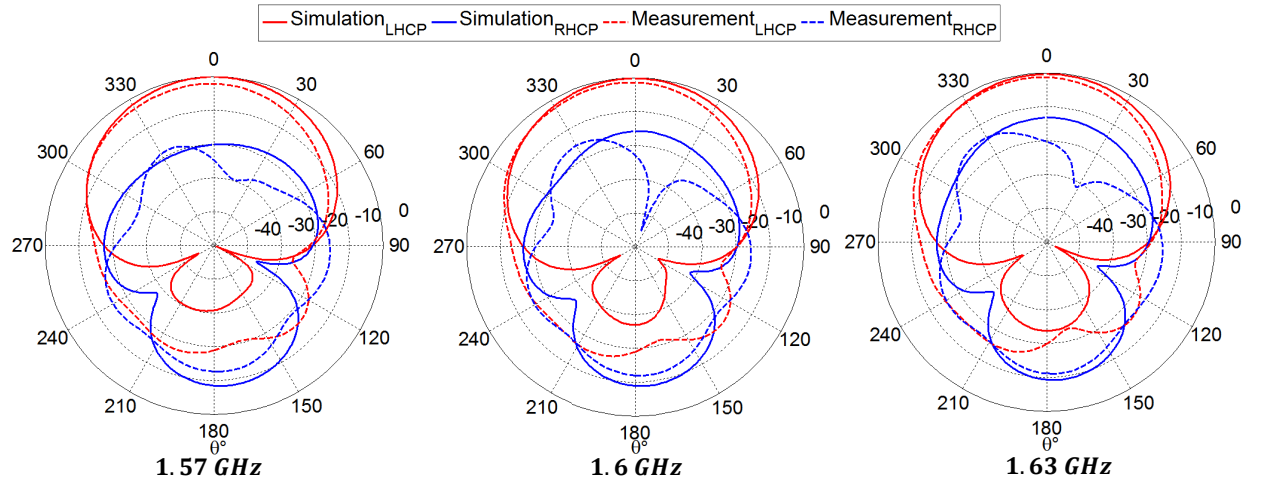


(a)

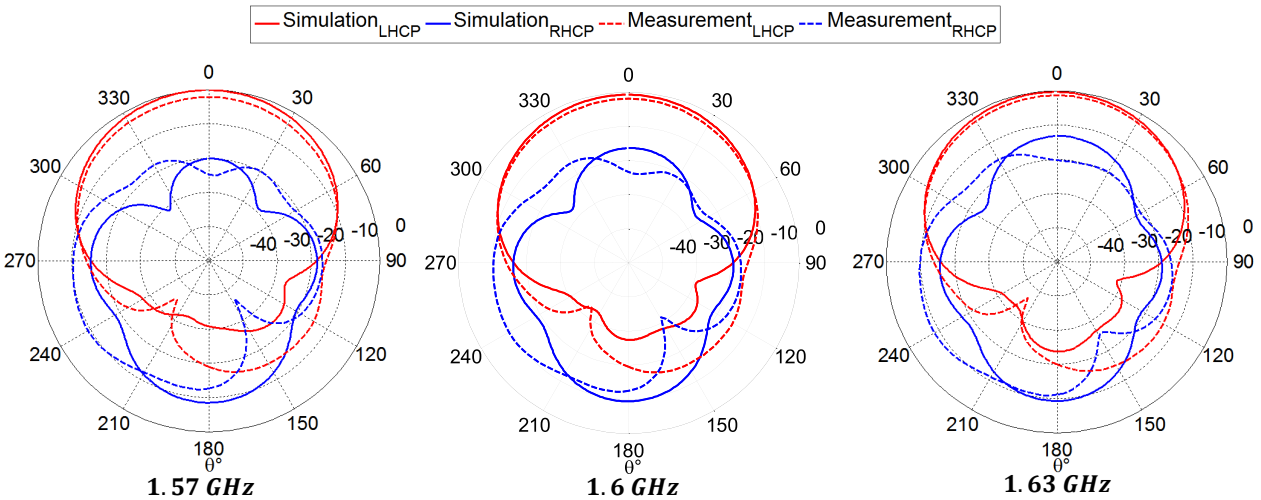


(b)

Figure 5.24: Simulated and measured radiation patterns for the antenna with suppressed RHCP. (a) XZ plane, (b) YZ plane.

On the other hand, the antenna on the ground plane maintains a matched impedance in a wideband with a slight mismatch in the measured $S_{11}$. On the other hand, the AR bandwidth after placing the reflector is still satisfactory with a measured 9.5% fractional bandwidth $[1.5-1.65GHz]$. The measured efficiency and realized gain are also in good agreement with the simulation where the measured antenna maintains an efficiency higher than 80% in the bandwidth of interest and a maximal gain higher the $5dB$.

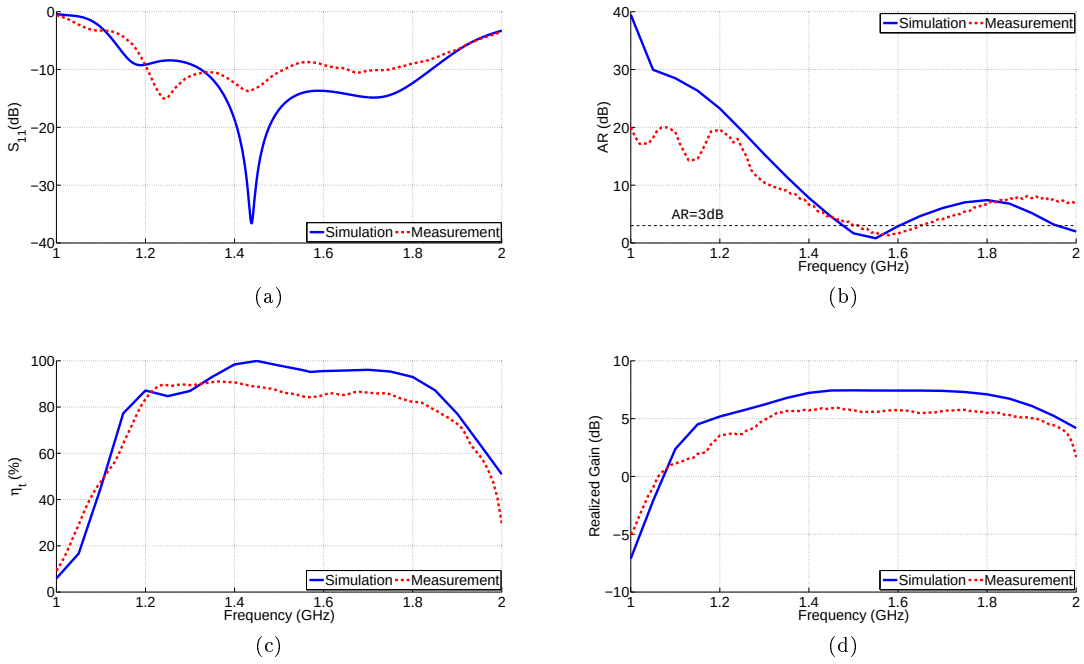


Figure 5.25: Performance of the excited antenna. (a) Input reflection coefficient, (b) axial ratio, (c) total efficiency, (d) maximum realized gain.

## 5.5 Conclusion

In this chapter, a systematic approach to design broadband circularly polarized antenna was presented. The initial geometry was chosen as a square ground plane of dimensions $(0.39\lambda \times 0.39\lambda)$ with a triskele shaped slot in the center, this shape is unconventional in the antenna designs and it was chosen to examine if it is possible to produce a broadband compact circularly polarized antenna based on it. The design procedure is simple and straight forward, it is sufficient to analyze the characteristics modes on the structure in the bandwidth of interest and identify the modes that might be possible candidates for the desired application. By examining the current distributions of the first four modes, it was noticed that modes 1 and 2 support horizontal and vertical currents respectively, yet their exhibit almost equal characteristic current values. By cutting out the third spiral part of the geometry, it was possible to significantly increase $\Delta\alpha$ while making the antenna more compact with a size of $0.39\lambda \times 0.23\lambda$. Further geometry modifications were applied to have a better modal behaviour mostly for mode 1 whose MS needed to be increased.

When the modal current on the structure became suitable to generate circular polarization, an L-Shaped monopole with internal circular loads was used to feed

the slot antenna. By exciting the monopole, the circular polarization was successfully generated in the desired GPS L1 band with an 8% AR bandwidth and 36% impedance bandwidth and an efficiency higher than 90%. Nevertheless, in order to suppress the RHCP in the -z-axis, a $90mm \times 90mm$ reflector is placed parallel and $48mm$ away from it. With this configuration, the antenna maintained a similar behaviour with 9.5% fractional bandwidth and 34% fractional bandwidth.

Although the final design is matched and circularly polarized in the band of interest, further analysis should be carried to try to apply further manipulation on the characteristic modes in order to achieve a wider CP polarization and more compactness. This can also be done by integrating reactive loads on the structure and optimizing their values using NCM in order to force the modes to posses CP characteristics. Finally, the initial geometry choice is also important in attaining a certain CP performance. Starting with a more conventional geometry which originally supports modes that produce CP, can simplify the design approach in achieving a wider AR and impedance bandwidth.

# Conclusion

When the size of the antenna becomes small with respect to the wavelength, it becomes physically limited in bandwidth, efficiency and directivity. In this thesis, we developed optimization approaches using the characteristic modes theory in order to address these limitations.

The theory of characteristic modes, provides us with deep physical insights about the modes that are naturally supported by the antenna structure independent of the excitation. By placing reactive loads at specific positions inside the antenna, it is then possible to control the characteristic modes in order to achieve a desired performance. However, when dealing with multiport ($N$ ports) structures, the Network Characteristic Modes is used instead of the classical characteristic modes. The network characteristic modes calculates the modes of the network from its $N$ port impedance matrix. Therefore the infinite number of characteristic modes will be coupled into finite $N$ modes. The approach of reactively loading the antenna was then used to miniaturize and enhance the performance of a compact antenna.

A summary of the contributions that was studied and validated in this dissertation, is as follows:

- A novel distributed reactive matching approach have been introduced to miniaturize and match a small antenna in a wideband. The approach is based on combining the NCM with an optimization algorithm (DE) in order to find the optimized reactive loads values that can match the antenna in a wideband. The reactive loads serve in manipulating the NCM's inside the antenna in a way that maximizes its bandwidth in a desired frequency range. This technique have then been applied on a meandered S-shaped monopole integrated on a ground plane. With the optimization, it was shown that with an internal negative capacitive load the small antenna can be matched in a wideband of 30% fractional bandwidth, which can also be improved up to 50% if an additional passive capacitive load is added . Another example was provided for the same S-shaped monopole, while however, a meander line parasitic was added to compensate the capacitive reactance of the antenna at low frequency. With this new geometry, it was possible to maximize the bandwidth of the antenna and achieve a wideband impedance behaviour of 20% fractional bandwidth using just two simple inductive loads, and a 32% fractional bandwidth using three embedded inductive loads. Subsequently, the multiband behaviour of this antenna was then examined showing that it is possible to achieve such behaviour where the antenna was matched in the GSM850/900 bands and the bluetooth band.

  Despite these successful designs, two cases were presented to highlight some key elements that may prevent the convergence of the method to the desired

solution. A port placed in a position where the surface current distribution is low will have a minimal effect on the modal currents and hence achieving a wideband matching would require changing the port position. On the other hand, depending on the size and the geometry of the antenna, the maximal impedance bandwidth attains a limit after which adding more ports will not help in increasing it. In this case, it is required to apply geometry changes on the structure and re-initialize the optimization.

Therefore, the proposed NCM optimization scheme is a powerful technique in designing wideband small antennas. Compared to NCM matching techniques presented in literature, this approach provides a simpler and more practical design solutions in which the optimization is set for a defined level of $S_{11}$ rather than finding the loads can that achieve a perfect matching which yields to a very complicated and impractical design. However, the initial antenna geometry and the choice of the ports are crucial in insuring a successful design.

A comparison of the obtained antenna performance with the literature was also performed. The comparison was based on the bandwidth-efficiency product with respect to the electrical size showing that the antenna which was designed based on our proposed geometry exhibits a better compromise of $B\eta$ product than similar designs present in literature.

- Since in certain cases, non-Foster loads are needed to match a small antenna. Matching of an electrically small monopole antenna using internal non-Foster circuit was studied in Chapter 3. The value of the optimal internal load was calculated using the previous approach. A floating type Linvill circuit was then used for this purpose. While taking into account the EM model of the non-Foster circuit in the presence of the antenna, it was possible to parametrically optimize the geometry of the antenna, the components of the active circuit, and its position in order to maximize the efficiency. Two cases were studied, and fabricated for different NIC topologies. For the first topology, the antenna attained an 18% efficiency with a 44% bandwidth and $-4.6dB$ realized gain, while in the second case, with the access port of the NIC brought closer to each other, it achieved a 25% efficiency and a 50% fractional bandwidth and a $-3.6dB$ of peak gain.

  Although the design approach of modeling the antenna in the presence of the NIC have provided some guidelines to optimize the performance of the antenna, and despite that the final results present an enhancement with respect to other results, it still seems that using NIC for antenna matching is quite a complicated technique which does not provide very satisfying results, as the circuit remains lossy and it significantly affect the efficiency of the antenna.

- The superdirectivity of the internally loaded wideband compact antenna was then studied. It was shown that forming a superdirective array of wideband unit element is a key element in overcoming the low efficiency of classical superdirective arrays. With a wideband unit element, very close separation distances can be achieved while maintaining a high efficiency. At higher separation distances, the benefits of using a wideband unit element was also examined. With a wideband unit element a wideband impedance and superdirective behaviour can be achieved by exciting the array elements with the proper relative phase

and magnitude. A feeding network was then integrated on the bottom side of the array to demonstrate the analytical results. For both superdirective arrays, the NCM was also used to optimize the directivity. The fields radiated by the characteristic currents are extracted and their excitation coefficients are optimized to maximize the directivity in a desired direction. On the other hand, the integration of the feeding network in the wideband array was achieved using the guidance of the characteristic modes theory. By studying the surface current distributions of the dominant modes, we identified the best feeding topology whose effect on the array currents is as low as possible, and therefore leading to a successful design.

- After studying the possibility to use the guidance of CMA and NCM to analyze and design wideband and superdirective antennas, the design of broadband CP antenna was then examined. The aim was to analyze an unconventional structure of slot antenna and study the possibility to generate CP by manipulating the modes using geometry modifications. A triskele slotted antenna of dimensions $70mm(0.39\lambda) \times 70mm(0.39\lambda)$ was chosen as an initial geometry. The modal analysis of the structure indicated that there are two dominant modes in the bandwidth of interest (GPS L1). However, these modes do not exhibit properties that allow circular polarization ($MS_1 = MS_2$,$\alpha_1 - \alpha_2 = \pm 90°$). The structure is then modified accordingly by cutting a part of the geometry in order to permit the modes to have the desired properties and making it more compact ($70mm(0.39\lambda) \times 45mm$). After various geometry modification, the feeding monopole is designed to excite these desired modes. The excited antenna exhibits an AR bandwidth of 8% and an impedance bandwidth of 36%. Yet, in order to suppress the bidirectional radiation and force an LHCP in the +z-axis, a copper plate reflector is placed parallel to the antenna at a distance of $\lambda/4$. With this configuration, the RHCP was successfully suppressed with a cross-polarization discrimination higher than $10dB$, an AR bandwidth of 9.5% and a 34% impedance bandwidth.

# Future Work

A bandwidth optimization technique using internal loads have been developed in this thesis. However, the position of the loads was chosen based on visualizing the surface current distribution of the antenna. Future work should be done on finding the optimal load positions inside the antenna by performing sensitivity tests on the port position candidates and developing a figure of merit equation that identifies the best choice. Also, further study should be done on the limitations of the method in terms of the number of loads versus the maximal achievable bandwidth. On the other hand, it would be interesting to optimize the modal behaviour of the antenna based on a criteria other than the modal admittance. For example optimizing Q factor (minimizing the Q factor of the modes) might be more effective in the convergence of the optimizer and might yield better results.

It should also be noted, that the types of antennas which were addressed in this manuscript were mainly printed planar antennas. Using initial antenna geometries occupying volumetric shapes would provide an advantage in having a lower electrical size and a lower Q factor. This kind of antennas would be interesting to study using our methodology to attempt to achieve a higher $B\eta$ product so that we can approach more the upper bounds.

Concerning the active antenna, further work needs to be done on optimizing the circuit and/or the antenna geometry in order to enhance more the efficiency of the system. This might be done by using an antenna whose resonance is originally present in the electrically small domain. This should facilitate the matching of the antenna and might help in increasing the efficiency. On the other hand, using other topologies to produce negative capacitance should be investigated. The current circuit topology does not seem to be the best choice as the overall performance of the antenna is still not totally satistfying ($\eta = 24\%$). A similar performance can be achieved by an passive antenna considering a higher matching level.

For superdirective array, due to the narrow bandwidth of the stacked configuration, it would be interested to design a stacked superdirective array which has an agility versus frequency by using a varactor as a parasitic element whose values would maximize the directivity at discrete frequency points. For the end-fire array, further work should focus on studying the performance of the array with more than two elements, in addition to decreasing the size of the ground plane. It would also be interested to investigate the effect of the internal loads in maximizing the directivity. In this thesis, the internal loads inside the antenna are of fixed values and the optimization is done on the excitation ports, adding more optimization ports might provide the possibility to maximize the directivity.

In the CP antenna, It was shown that the designed antenna does not actually present a better performance compared to the slotted antenna designs reported in

literature. However, the systematic design approach using CMA could be used to examine other structures to realize a wider AR bandwidth and a more compact geometry. In addition, the NCM could also be incorporated in the design to optimize the modal behaviour on the structure using reactive loading. On the other hand, it might also be interesting to study the designed antenna with an Artificial Magnetic Conductor (AMC). An AMC will result in a lower profile when suppressing the radiation in -z-axis, and it might also act as a polarizer which increases the AR bandwidth. Here the CMA might also be useful to identify the most suitable unit cell geometry of the AMC for achieving the desired performance. Preliminary simulation of the antenna with AMC is presented in the Appendix.

# Appendix 1: Characteristic Modes Tracking

At each angular frequency $\omega$ the characteristic modes are calculated from the generalized eigenvalue problem as follows:

$$[X_a]\bar{J}_n = \lambda_n[R_a]\bar{J}_n \tag{1}$$

Therefore to study the characteristic modes in a wide frequency band. The eigenvalues and eigenvectors should be calculated at discrete frequency points. However, it is often noticed that when calculating the modes at discrete frequencies, the modes having the same index are not actually the same physical mode. Hence, it becomes mandatory to develop some tracking algorithms to track associate the modes physically. Various mode tracking techniques have been developed in literature[159, 160, 161, 162, 163]. In [159], Capek *et al.* tracked the modes by correlating the eigen current vectors across frequency and then this modes were sorted in ascending order realtive to the eigenvalue magnitude, however the correlated values were unbounded. Later, Raines *et al.* defined a bounded correlation $[C]$ ($c_{ij} \in [0,1]$) matrix which relates the eigen vectors at two consecutive angular frequency points $\omega_1$ and $\omega_2$ [160]

$$\begin{aligned}[X_{\omega_1}][\Gamma_{\omega_1}] &= \Lambda_{\omega_1}[R_{\omega_1}][\Gamma_{\omega_1}] \\ [X_{\omega_2}][\Gamma_{\omega_2}] &= \Lambda_{\omega_2}[R_{\omega_2}][\Gamma_{\omega_2}]\end{aligned} \tag{2}$$

where $\Lambda$ is a diagonal matrix containing the eigenvalues associated to each eigen vector. $\Gamma$ is a matrix whose columns are the eigen vectors. The correlation matrix $[C]$ is then given by:

$$[\Gamma_{\omega_1}] = [C][\Gamma_{\omega_2}] \tag{3}$$

$[C]$ is then calculated from the multiplication of $[\Gamma_{\omega_2}]$ with the inverted matrix of $[\Gamma_{\omega_1}]$

$$[C] = [\Gamma_{\omega_2}][\Gamma_{\omega_1}]^{-1} \tag{4}$$

The modes at frequency $\omega_2$ are then associated with the modes at frequency $\omega_1$ based on the correlation matrix $[C]$. The association process is simple, it is sufficient to examine find the maximal element $c_{ij}$ of $[C]$, which implements that $mode_i$ at $\omega_1$ is associated with $mode_j$ at $\omega_2$ after which row $i$ and column $j$ of $[C]$ are deleted, and then another maximal value $c_{ij}$ is identified for another mode association.

A rather simpler tracking approach was introduced by the authors in [161] which uses bounded linear correlation based on the Pearson's correlation equation. The

elements of the correlation matrix $c_{ij}$ are bounded in the domain $[-1, 1]$. Given eigen vector $J_1$ at frequency $\omega_1$ and eigenvector $J_2$ at frequency $\omega_2$, the correlation coefficient $c_{12}$ of these two vectors is calculated as follows:

$$c_{ij} = \frac{N \sum_{i=1}^{N} (J_1)_i (J_2)_i - \sum_{i=1}^{N} (J_1)_i . \sum_{i=1}^{N} (J_2)_i}{\sqrt{N \sum_{i=1}^{N} (J_1^2)_i - (\sum_{i=1}^{N} (J_1)^2} . \sqrt{N \sum_{i=1}^{N} (J_2^2)_i - (\sum_{i=1}^{N} (J_2)^2}} \tag{5}$$

where $(J_n)_i$ is the $i^{th}$ element in the $n^{th}$ eigenvector and $N$ is the number of elements in the vector $J$ which represent the number of modes being tracked. The correlation coefficient is calculated for each pair of eigen vectors at $\omega_1$ and $\omega_2$ to finally form the correlation matrix $[C]$. After that, the association procedure is quite similar to the one in [160]. Other complex tracking or hybrid tracking algorithms where presented in [162, 163].

In our case, since we are studying the network characteristic modes in which the number of modes is limited to the number of ports. A simple tracking algorithm is convenient to insure a good association between the modes at different frequency. Therefore, the tracking algorithm which uses the linear correlation matrix is used. To examine the importance of using the tracking algorithm to study the modal behaviour in a wideband, we compare the modes of the 5-port unloaded antenna presented in Fig.2.25. Fig.A.1 shows the plot of the eigenvalue magnitudes of the 5 NCMs in the case where the modes are untracked and tracked. In both cases the resonances of the structure are visible at $0.53GHz$, $0.87GHz$, and $1.15GHz$. However in the case where the modes are untracked it is clear that the modes are not well associated and it gets hard to visualize the behaviour of each mode separately. On the other hand, the tracked modes are more clear to analyze and it is much easier to interpret their behaviour as a function of frequency.

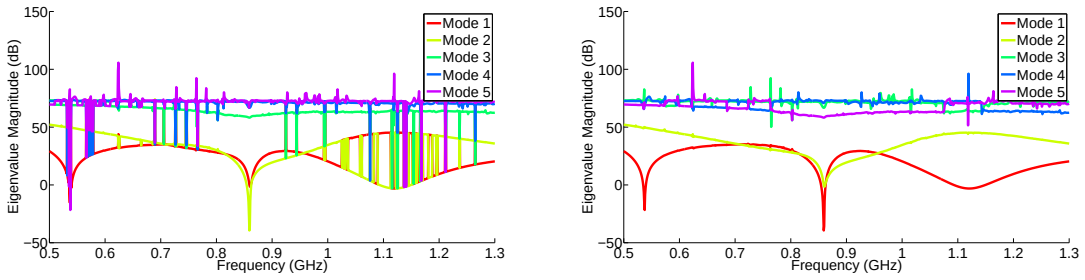


Figure A.1: Comparison of the visualization of the eigen modes. (a) Un-Tracked modes, (b) tracked modes

# Appendix 2: Circularly Polarized Antenna on Artificial Magnetic Conductor

To supress the backwards radiation and force the radiation in the +z-axis, a metallic reflector has to be placed at a specific distance with respect to the radiator. A classical metallic reflector produces a 180° phase shift and hence it should be placed on a distance of $\lambda/4$ with respect to the radiator in order to suppress the backwards radiations. On the other hand, an Artificial Magnetic Conductor (AMC) produces a 0° phase shift and hence it can be placed close to the radiator and still effectively reflect the backwards radiation [147]. Moreover, by changing the separation distance from the radiator, the AMC could also act as a polarizer to achieve a wideband circular polarization.

It was shown with the CP antenna designed in chapter 5, that it was possible to suppress the RHCP using a metallic reflector placed at $\lambda/4$. In this short section, we present some preliminary simulation results of the designed CP antenna placed on an AMC.

## Unit cell

The AMC unit cell is given in Fig.A.2. It is composed of a square patch mounted on a two layer substrate of height $h_t = h_1 + h_2$. The lower substrate layer is air of $\epsilon_r = 1$ and the upper layer is FR4 having $\epsilon_r = 4.3$. On the bottom a ground plane of dimensions $a \times a$ is placed. The dimensions of the unit cell in mm are as follows: $a = 20mm$, $b = 19mm$, $h1 = 10mm$, $h_2 = 1.5mm$. In this study, the substrate losses are not taken into account. The chosen unit cell is based on the work presented in[164].

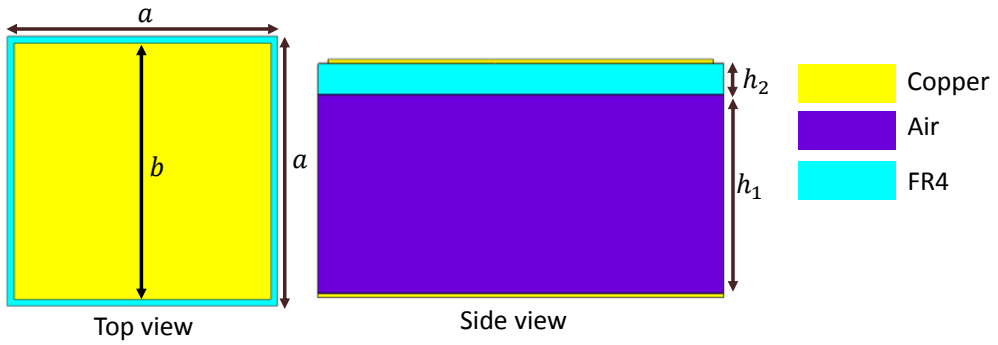


Figure A.2: Geomertry of the unit cell.

The bandwidh of an AMC is defined as the frequency range where its reflection phase varies between +90° to −90° [165]. Based on this definition, this unit cell exhibits a wide bandwidth 36% $[1.28 - 1.84GHz]$ (Fig.A.3), which is compatible with the bandwidth of operation of the antenna.

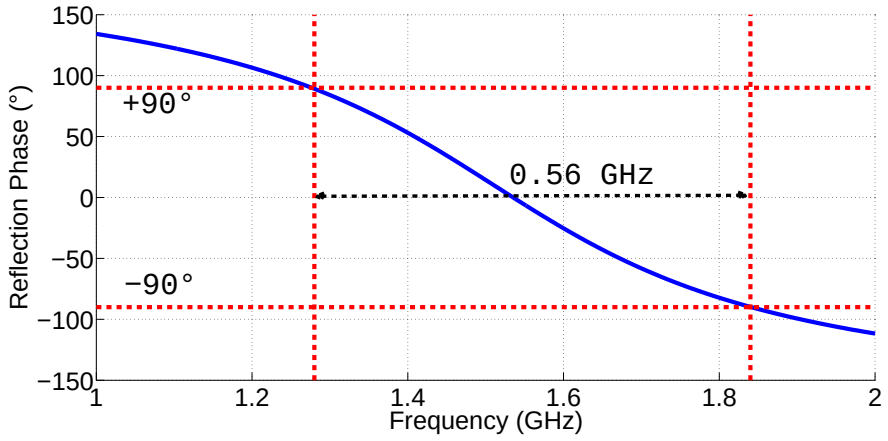


Figure A.3: Reflection phase of the unit cell.

## CP Antenna on AMC

After defining the unit cell, the AMC is formed of a $7 \times 7$ unit cells, resulting in overall reflector dimensions of $140 \times 140mm^2$. The antenna is then placed parallel to the AMC in the +z-axis. The separation distance between the ground plane of the AMC and the antenna is defined by $d$. Fig.A.4 presents the geometry of the antenna on top of the AMC.

In order to examine the behaviour of the antenna in the presence of the AMC, a parametric study has been carried out for various separation distances. The results of the parametric simulation are given in Fig.A.5. Starting with a separation distance of $14.5mm$ $(0.07\lambda)$ the antenna is matched in a wideband $[1.31–1.7GHz]$ (26%), yet it does not radiate circularly polarized fields since the AR is higher the $3dB$ in all the band. On the other hand, as the separation distance increases, the axial ratio level starts to drop with a slight decrease in the impedance bandwidth. At a separation distance of $26.5mm$ $(0.13\lambda)$, the antenna exhibits a dual band circular polarization:

the first band is $[1.44 - 1.58GHz]$ (9%) while the second band is $[1.74 - 1.83GHz]$ (5%).

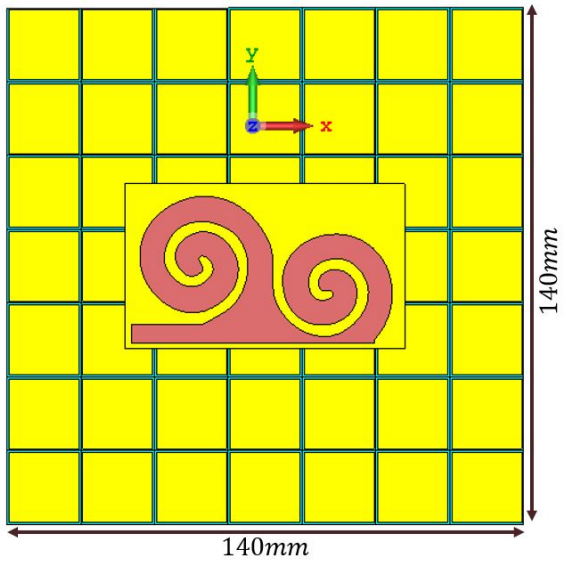


(a)

(b)

Figure A.4: Representation of the antenna on AMC. (a) Top view, (b) side view.

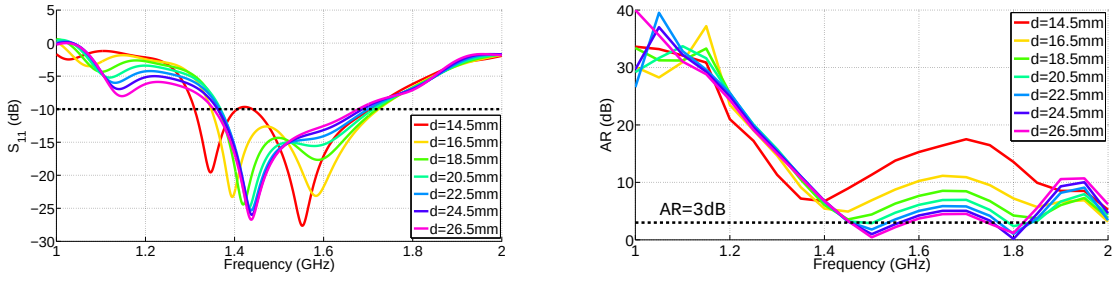


(a) (b)

Figure A.5: Characteristics of the antenna as a function of separation distance from the AMC. (a) Input reflection coefficient, (b) axial ratio.

## Antenna with Parasitic Elements

The dual band CP is separated by a $2dB$ increase in the level of the AR. In order to reduce this level so that $AR < 3dB$ and the two bands unit into one wideband, parasitic strips are added around the antenna. The strips serve in forcing the rotation of the fields and hence they would enforce a circular polarization. The geometry of the antenna with the parasitic strips is shown in Fig.A.6. The dimensions of the antenna in this case are as follows: $W = 65mm$, $L = 96mm$, $e = 38mm$,$f = 6mm$,

$g = 54mm$, $h = 1.8mm$, $i = 0.3mm$ and the separation distance between the antenna and the ground plane is $d = 30mm$. Therefore the antenna has an overall dimensions of $(140 \times 140 \times 30mm^3)$ which corresponds to $(0.73 \times 0.73 \times 0.15\lambda^3)$. These values are found after optimizing the geometry in CST to have the best AR bandwidth.

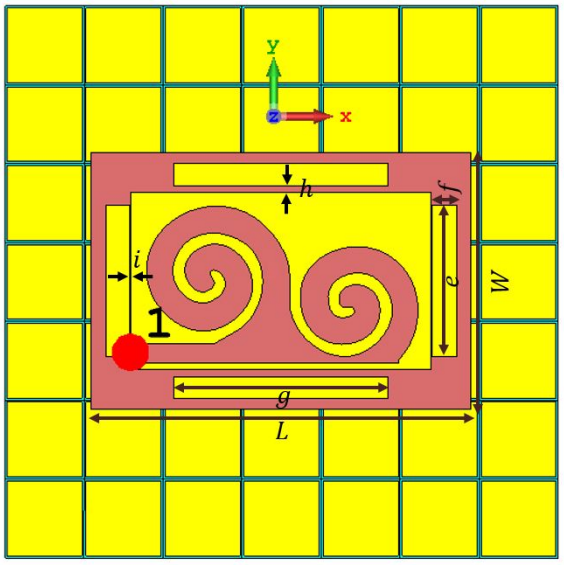


Figure A.6: Antenna with parasitic strips on top of AMC.

With this configuration the antenna is matched in a wideband $[1.33 - 1.8GHz]$ (30%) with a wideband AR bandwidth $[1.42–1.81GHz]$ (24.15%) (Fig.A.7). Besides a high cross polarization discrimination is achieved where the RHCP was successfully suppressed and the radiation is directed in the +z-axis where the LHCP achieves a realized gain of about $9dBi$ (Fig.A.8).

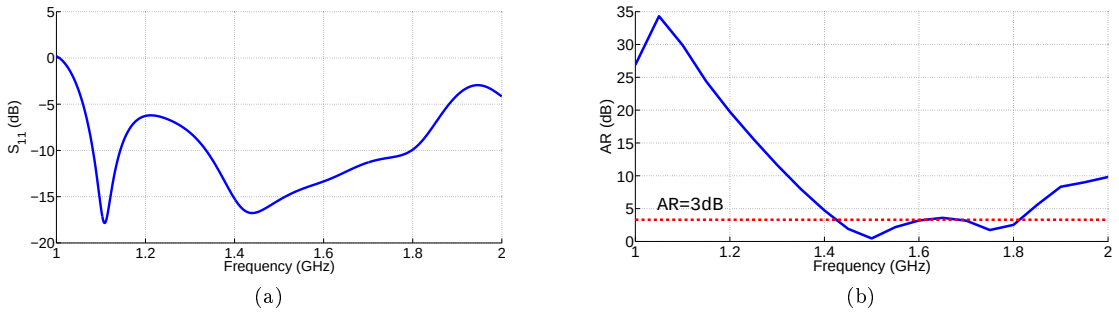


(a) (b)

Figure A.7: Characteristics of the antenna with parasitic strips on top of the AMC. (a) Input reflection coefficient, (b) axial ratio.

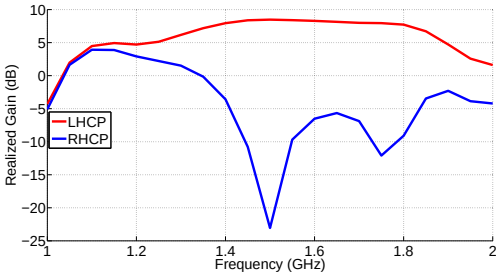


Figure A.8: Realized gain of the co and cross polarizations in the final design in the direction of $\theta = 0°$.

Therefore by adding an AMC it is possible to suppress the backwards radiation in addition to increasing the AR bandwidth. However more studies should be carried out to optimize the performance of the antenna in the presence of the antenna and obtain a design with a lower profile.

It should be noted that in this part, the design was totally based on parametric optimization and the CMA was not used to enhance the design. It might therefore be interesting to examine this in future works.

# Publications

### Refereed Journal Papers

1. H. Jaafar, S. Collardey and A. Sharaiha, "Optimized Manipulation of the Network Characteristic Modes for Wideband Small Antenna Matching," in *IEEE Transactions on Antennas and Propagation*, vol. 65, no. 11, pp. 5757-5767, Nov. 2017.

2. (Accepted for publication in IEEE Transactions on Antennas and Propagation ) H. Jaafar, S. Collardey and A. Sharaiha, " Characteristic Modes Approach to Design Compact Superdirective Array With Enhanced Banwidth".

3. (under review, IEEE Transactions on Antennas and Propagation) H. Jaafar, D. Lemur, S. Collardey and A. Sharaiha, "Efficiency Optimization of a Wideband Electrically Small Antenna Embedded With Non-Foster Circuit".

### Refereed International Conferences

1. H. Jaafar, S. Collardey, and A. Sharaiha, "Characteristic Modes Analysis to Integrate a Feeding Network in a Wideband Superdirective Array", 2018 International Symposium on Antenna and Propagation, 23-26 October, Busan, Korea.

2. H. Jaafar, D. Lemur, S. Collardey and A. Sharaiha, "Wideband Electrically Small Antenna Internally Loaded With Non-Foster Circuit", *18th International Symposium on Antenna Technology and Applied Electromagnetics*, August 19-22 2018, Waterloo Canada.

3. H. Jaafar, S. Collardey, and A. Sharaiha, "Network Characteristic Modes for Wideband and Superdirective Small Antennas", *2nd URSI AT-RASC, Gran Canaria*, 28 May-1 June 2018.

4. H. Jaafar, S. Collardey, and A. Sharaiha, "Internally Loaded Endfire Superdirective Array for Wideband Performance" 2018 11th European Conference on Antennas and Propagation (EUCAP),8-13 April 2018,London, UK.

5. H. Jaafar, S. Collardey, and A. Sharaiha,"A broadside efficient superdirective compact array with internally loaded wideband unit elements", *2018 International Workshop on Antenna Technology (iWAT)*,4-7 March, 2018.

6. H. Jaafar, S. Collardey, D. Lemur, A. Haskou and A. Sharaiha, "A Compact Multiband Antenna for Mobile Handset Using Characteristic Modes Optimization," *The Loughborough Antennas and Propagation Conference (LAPC)*, Loughborough, 12-13 Nov. 2018.

7. H. Jaafar, A. Sharaiha and S. Collardey, "Design of a wideband superdirective endfire antenna array using characteristic modes optimization," *2017 XXXI-Ind General Assembly and Scientific Symposium of the International Union of Radio Science (URSI GASS)*, Montreal, QC, 2017, pp. 1-4.

8. H. Jaafar, S. Collardey, D. Lemur, A. Haskou and A. Sharaiha, "Characteristic modes optimisation approach to design a wideband electrically small antenna,"*2017 11th European Conference on Antennas and Propagation (EUCAP)*, Paris, 2017, pp. 2184-2186.

9. H. Jaafar, S. Collardey and A. Sharaiha, "Bandwidth enhancement of a multiport double notched antenna using the Network Characteristic Modes," *2017 International Workshop on Antenna Technology: Small Antennas, Innovative Structures, and Applications (iWAT)*, Athens, 2017, pp. 359-362.

**Refereed National Conference**

1. H. Jaafar, S. Collardey, D. Lemur, A. Haskou and A. Sharaiha, "Optimisation des Modes Charactéistiques pour la Conception d'Antennes Électriquement Petites Large Bande", *XXémes Journées Nationales Microondes (JNM)* 16-19 mai 2017- Saint-Malo, France.

# Bibliography


[1] L. J. Chu, "Physical limitations of omni-directional antennas", *J. Appl.Phys.*, vol. 19, no. 12, pp. 1163-1175, Dec. 1948.

[2] H.A. Wheeler, "Fundamental Limitations of Small Antennas", *Proceedings of IRE*, vol. 35, December 1947, pp. 1479-1484.

[3] R. F. Harrington, "On the gain and beamwidth of directional antennas", *IRE Trans. Antennas Propag.*, vol. 6, no.3,pp. 219-225, Jul. 1958.

[4] H.A. Wheeler, "The Radian Sphere Around a Small Antenna", *Proceedings of IRE,* vol. 47, August 1959, pp. 1325-1331.

[5] R.E. Collin and S. Rothschild, "Evaluation of Antenna Q",*IEE Transactions on Antennas Propagation* vol. 12, 1964, pp. 23-27.

[6] R.C. Hansen, "Fundamental Limitations in Antennas", *Proceedings of IEEE*, vol. 69,1981, no. 2,pp. 170-181.

[7] J. S. McLean",A re-examination of the fundamental limits on the radiation Q of electrically small antennas", in *IEEE Transactions on Antennas and Propagation*, vol. 44, no. 5, pp. 672-, May 1996.

[8] M. Gustafsson, C. Sohl and G. Kristensson",Illustrations of New Physical Bounds on Linearly Polarized Antennas", in *IEEE Transactions on Antennas and Propagation*, vol. 57, no. 5, pp. 1319-1327, May 2009.

[9] A. D. Yaghjian and S. R. Best",Impedance, bandwidth, and Q of antennas", in *IEEE Transactions on Antennas and Propagation,* vol. 53, no. 4, pp. 1298-1324, April 2005.

[10] E. E. Altshuler, T. H. O'Donnell, A. D. Yaghjian and S. R. Best, "A monopole superdirective array", *IEEE Transactions on Antennas and Propagation*, vol. 53, no. 8, pp. 2653-2661, Aug. 2005.

[11] R. Harrington and J. Mautz, "Theory of characteristic modes for conducting bodies", *IEEE Transactions on Antennas and Propagation*, vol. 19, no. 5, pp. 622-628, Sep 1971.

[12] R. Harrington and J. Mautz, "Computation of characteristic modes for conducting bodies", *IEEE Transactions on Antennas and Propagation*, vol. 19, no. 5, pp. 629-639, Sep 1971.

[13] J. Mautz and R. Harrington, "Modal analysis of loaded N-port scatterers", *IEEE Transactions on Antennas and Propagation*, vol. 21, no. 2, pp. 188-199, Mar 1973.

[14] R. J. Garbacz, "Modal expansions for resonance scattering phenomena", in Proceedings of the IEEE, vol. 53, no. 8, pp. 856-864, Aug. 1965.

[15] R. Garbacz and R. Turpin, "A generalized expansion for radiated and scattered fields", in IEEE Transactions on Antennas and Propagation, vol. 19, no. 3, pp. 348-358, May 1971.

[16] A. Yee and R. Garbacz, "Self- and mutual-admittances of wire antennas in terms of characteristic modes", *IEEE Transactions on Antennas and Propagation*, vol. 21, no. 6, pp. 868-871, Nov 1973.

[17] E. Newman, "Small antenna location synthesis using characteristic modes", in IEEE Transactions on Antennas and Propagation, vol. 27, no. 4, pp. 530-531, Jul 1979.

[18] M. Cabedo Fabres",Systematic design of antenna using the theory of characteristic modes", Ph. D. Dissertation,Universidad Politecnica De Valencia, February 2007.

[19] R. Harrington and J. Mautz, "Control of radar scattering by reactive loading", in IEEE Transactions on Antennas and Propagation, vol. 20, no. 4, pp. 446-454, July 1972.

[20] J. J. Adams and J. T. Bernhard, "A Modal Approach to Tuning and Bandwidth Enhancement of an Electrically Small Antenna", in IEEE Transactions on Antennas and Propagation, vol. 59, no. 4, pp. 1085-1092, April 2011.

[21] Y. Chen and C. F. Wang, "Electrically Small UAV Antenna Design Using Characteristic Modes", in IEEE Transactions on Antennas and Propagation, vol. 62, no. 2, pp. 535-545, Feb. 2014.

[22] M. Li and N. Behdad, "Dual-band platform-mounted HF/VHF antenna design using the characteristic mode theory", in IET Microwaves, Antennas & Propagation, vol. 12, no. 4, pp. 452-458, 3 28 2018.

[23] K. Obeidat, R. G. Rojas and B. Raines, "Design of antenna conformal to V-shaped tail of UAV based on the method of Characteristic Modes", 2009 3rd European Conference on Antennas and Propagation, Berlin, 2009, pp. 2493-2496.

[24] S. M. Sow, L. Guo, S. G. Zhou and T. H. Chio, "Electrically small structural antenna design for small UAV based on characteristics modes", 2017 11th European Conference on Antennas and Propagation (EUCAP), Paris, 2017, pp. 2134-2138.

[25] Y. Chen and C. F. Wang, "Shipboard NVIS radiation system design using the theory of characteristic modes", 2014 IEEE Antennas and Propagation Society International Symposium (APSURSI), Memphis, TN, 2014, pp. 852-853.

[26] R. Martens, E. Safin and D. Manteuffel, "Selective excitation of characteristic modes on small terminals", Proceedings of the 5th European Conference on Antennas and Propagation (EUCAP), Rome, 2011, pp. 2492-2496.

[27] D. Manteuffel, R. Martens, "A Concept for MIMO Antennas on Small Terminals Based on Characteristic Modes", *IWAT2011,* Hong Kong,March 2011.

[28] R. Martens and D. Manteuffel, "A feed network for the selective excitation of specific characteristic modes on small terminals", 2012 6th European Conference on Antennas and Propagation (EUCAP), Prague, 2012, pp. 1842-1846.

[29] R. Martens and D. Manteuffel, "2-port antenna based on the selective excitation of Characteristic Modes", Proceedings of the 2012 IEEE International Symposium on Antennas and Propagation, Chicago, IL, 2012, pp. 1-2.

[30] R. Martens, E. Safin and D. Manteuffel, "Inductive and capacitive excitation of the characteristic modes of small terminals", 2011 Loughborough Antennas and Propagation Conference, Loughborough, 2011, pp. 1-4.

[31] A. E. Rodriguez, E. Elghannai, R. G. Rojas and R. Bustamante, "Design and evaluation of an antenna array for MIMO systems and handset wireless applications", *2015 38th International Conference on Telecommunications and Signal Processing (TSP)*, Prague, 2015, pp. 182-186.

[32] D. W. Kim and S. Nam, "Systematic Design of a Multiport MIMO Antenna With Bilateral Symmetry Based on Characteristic Mode Analysis", in*IEEE Transactions on Antennas and Propagation*, vol. 66, no. 3, pp. 1076-1085, March 2018.

[33] D. Manteuffel and R. Martens, "Compact Multimode Multielement Antenna for Indoor UWB Massive MIMO", in IEEE Transactions on Antennas and Propagation, vol. 64, no. 7, pp. 2689-2697, July 2016.

[34] Z. Miers, H. Li and B. K. Lau, "Design of Bandwidth-Enhanced and Multiband MIMO Antennas Using Characteristic Modes", in *IEEE Antennas and Wireless Propagation Letters*, vol. 12, pp. 1696-1699, 2013.

[35] H. Li, Z. T. Miers and B. K. Lau, "Design of Orthogonal MIMO Handset Antennas Based on Characteristic Mode Manipulation at Frequency Bands Below 1 GHz", in IEEE Transactions on Antennas and Propagation, vol. 62, no. 5, pp. 2756-2766, May 2014.

[36] H. Li, Z. Miers and B. K. Lau, "Generating multiple characteristic modes below 1GHz in small terminals for MIMO antenna design", 2013 IEEE Antennas and Propagation Society International Symposium (APS-URSI), Orlando, FL, 2013, pp. 180-181.

[37] Z. Miers, H. Li and B. K. Lau, "Design of bezel antennas for multiband MIMO terminals using Characteristic Modes", The 8th European Conference on Antennas and Propagation (EuCAP 2014), The Hague, 2014, pp. 2556-2560.

[38] D. W. Kim and S. Nam, "Systematic Design of a Multiport MIMO Antenna With Bilateral Symmetry Based on Characteristic Mode Analysis", in IEEE Transactions on Antennas and Propagation, vol. 66, no. 3, pp. 1076-1085, March 2018.

[39] Y. Chen and C. F. Wang, "Characteristic-Mode-Based Improvement of Circularly Polarized U-Slot and E-Shaped Patch Antennas", in IEEE Antennas and Wireless Propagation Letters, vol. 11, pp. 1474-1477, 2012.

[40] K. Saraswat, AR. Harish "Analysis of wideband circularly polarized ring slot antenna using characteristic mode for bandwidth enhancement",*Int J RF Microw Comput Aid Eng.*, 2017;12:e21186.

[41] M. Cabedo-Fabres, A. Valero-Nogueira and M. Ferrando-Bataller, "Systematic study of elliptical loop antennas using characteristic modes", *IEEE Antennas and Propagation Society International Symposium*, 2002, pp. 156-159 vol.1.

[42] Q. Wu, W. Su, Z. Li and D. Su, "Reduction in Out-of-Band Antenna Coupling Using Characteristic Mode Analysis", in IEEE Transactions on Antennas and Propagation, vol. 64, no. 7, pp. 2732-2742, July 2016.

[43] E. A. Elghannai and R. G. Rojas, "Study of the total Q of antennas in terms of modal Qn provided by Characteristic Modes Theory", *2014 IEEE Antennas and Propagation Society International Symposium (APSURSI)*, Memphis, TN, 2014, pp. 49-50.

[44] M. H. Rabah and D. Seetharamdoo, "Calculation of the total Q-factor for electrically small antennas with metamaterials using characteristic modes", *2016 10th European Conference on Antennas and Propagation (EuCAP),* Davos, 2016, pp. 1-5.

[45] M. Capek, P. Hazdra and J. Eichler, "A Method for the Evaluation of Radiation Q Based on Modal Approach", in*IEEE Transactions on Antennas and Propagation,* vol. 60, no. 10, pp. 4556-4567, Oct. 2012.

[46] M. Capek and L. Jelinek, "Optimal Composition of Modal Currents for Minimal Quality Factor $Q$", in *IEEE Transactions on Antennas and Propagation,* vol. 64, no. 12, pp. 5230-5242, Dec. 2016.

[47] F. H. Lin and Z. N. Chen, "Low-Profile Wideband Metasurface Antennas Using Characteristic Mode Analysis", in *IEEE Transactions on Antennas and Propagation*, vol. 65, no. 4, pp. 1706-1713, April 2017.

[48] F. H. Lin and Z. N. Chen, "A Method of Suppressing Higher-Order Modes for Improving Radiation Performance of Metasurface Multiport Antennas Using Characteristic Mode Analysis", in *IEEE Transactions on Antennas and Propagation*, vol. PP, no. 99, pp. 1-1.

[49] A. Adam Salih, Z. N. Chen and K. Mouthaan, "Characteristic Mode Analysis and Metasurface- Based Suppression of Higher Order Modes of a $2 \times 2$ Closely Spaced Phased Array", in '*IEEE Transactions on Antennas and Propagation*, vol. 65, no. 3, pp. 1141-1150, March 2017.

[50] R. Harrington, "Reactively controlled directive arrays", in *IEEE Transactions on Antennas and Propagation*, vol. 26, no. 3, pp. 390-395, May 1978.

[51] R. Harrington and J. Mautz, "Pattern synthesis for loaded N-port scatterers", in *IEEE Transactions on Antennas and Propagation,* vol. 22, no. 2, pp. 184-190, March 1974.

[52] Y. Chen and C. F. Wang, "Synthesis of Reactively Controlled Antenna Arrays Using Characteristic Modes and DE Algorithm", *in IEEE Antennas and Wireless Propagation Letters*,vol. 11, no. , pp. 385-388, 2012.

[53] Y. Chen and C. F. Wang, "Electrically loaded Yagi-Uda antenna optimizations using characteristic modes and differential evolution" *J. Electromagn. Waves Appl.*,vol. 26, pp. 1018-1028, 2012.

[54] J. Ethier and D. A. McNamara, "An Interpretation of Mode-Decoupled MIMO Antennas in Terms of Characteristic Port Modes", in *IEEE Transactions on Magnetics,* vol. 45, no. 3, pp. 1128-1131, March 2009.

[55] I. Tzanidis, K. Sertel and J. L. Volakis, "Characteristic Excitation Taper for Ultrawideband Tightly Coupled Antenna Arrays", in *IEEE Transactions on Antennas and Propagation*, vol. 60, no. 4, pp. 1777-1784, April 2012.

[56] E. Safin and D. Manteuffel, "Manipulation of Characteristic Wave Modes by Impedance Loading", *in IEEE Transactions on Antennas and Propagation*, vol. 63, no. 4, pp. 1756-1764, April 2015.

[57] K. A. Obeidat, B. D. Raines and R. G. Rojas, "Application of Characteristic Modes and Non-Foster Multiport Loading to the Design of Broadband Antennas", *IEEE Transactions on Antennas and Propagation*, vol. 58, no. 1, pp. 203-207, Jan. 2010.

[58] K. A. Obeidat, B. D. Raines, R. G. Rojas and B. T. Strojny, "Design of Frequency Reconfigurable Antennas Using the Theory of Network Characteristic Modes", *IEEE Transactions on Antennas and Propagation*, vol. 58, no. 10, pp.

[59] E. A. Elghannai, B. D. Raines and R. G. Rojas, "Multiport Reactive Loading Matching Technique for Wide Band Antenna Applications Using the Theory of Characteristic Modes", *IEEE Transactions on Antennas and Propagation*, vol. 63, no. 1, pp. 261-268, Jan. 2015

[60] E. A. Elghannai and R. G. Rojas, "Antenna design via current control of antenna currents using theory of Characteristic Modes", *2015 9th European Conference on Antennas and Propagation (EuCAP)*, Lisbon, 2015, pp. 1-5.

[61] S. R. Best, "The radiation properties of electrically small folded spherical helix antennas", *IEEE Transactions on Antennas and Propagation*, vol. 52, no. 4, pp. 953-960, April 2004.

[62] S. R. Best, "Low Q electrically small linear and elliptical polarized spherical dipole antennas", *IEEE Transactions on Antennas and Propagation*, vol. 53, no. 3, pp. 1047-1053, March 2005.

[63] H. W. Bode, "Network Analysis and Feedback Amplifier Design", New York, NY, USA: Van Nostrand, 1945.

[64] R. M. Fano, "Theoretical limitations on the broadband matching of arbitrary impedances", *J. Franklin Inst.*, vol. 249, pp. 139-154, 1950.

[65] J. T. Aberle; R. Loepsinger-Romak, "Antennas with Non-Foster Matching Networks", *Antennas with Non-Foster Matching Networks*, 1, Morgan & Claypool, 2007.

[66] A. Haskou, D. Lemur, S. Collardey and A. Sharaiha, "Miniature and wide-Band ILA Antenna with non-Foster matching", *2016 10th European Conference on Antennas and Propagation (EuCAP)*, Davos, 2016, pp. 1-3.

[67] G. Bit-Babik, C. Di Nallo, J. Svigelj and A. Faraone, "Small Wideband Antenna with non-Foster Loading Elements", *2007 International Conference on Electromagnetics in Advanced Applications*, Torino, 2007, pp. 105-107.

[68] A. Erentok and R. W. Ziolkowski, "Metamaterial-Inspired Efficient Electrically Small Antennas", *IEEE Transactions on Antennas and Propagation*, vol. 56, no. 3, pp. 691-707, March 2008.

[69] C. Zhu et al., "Electrically Small Metamaterial-Inspired Tri-Band Antenna With Meta-Mode", in *IEEE Antennas and Wireless Propagation Letters*, vol. 14, pp. 1738-1741, 2015.

[70] E. Ramanandraibe, M. Latrach and A. Sharaiha, "Multiband metamaterial-inspired antenna", '*The 8th European Conference on Antennas and Propagation (EuCAP 2014)*, The Hague, 2014, pp. 2876-2879.

[71] M. S. Majedi and A. R. Attari, "A Compact and Broadband Metamaterial-Inspired Antenna", in *IEEE Antennas and Wireless Propagation Letters*, vol. 12, pp. 345-348, 2013.

[72] P. Jin and R. W. Ziolkowski, "Broadband, efficient, electrically small metamaterial-inspired antennas facilitated by active near-field resonant parasitic elements", *IEEE Transactions on Antennas and Propagation*, vol. 58, pp. 318-327, Feb. 2010.

[73] N. Zhu and R. W. Ziolkowski, "Broad-Bandwidth, Electrically Small Antenna Augmented With an Internal Non-Foster Element", in *IEEE Antennas and Wireless Propagation Letters*, vol. 11, pp. 1116-1120, 2012.

[74] A. R. Raslan and A. M. E. Safwat, "N-Internal Port Design for Wide Band Electrically Small Antennas With Application for UHF Band", in *IEEE Transactions on Antennas and Propagation*, vol. 61, no. 9, pp. 4431-4437, Sept. 2013.

[75] M. A. Othman, T. M. Abuelfadl and A. M. E. Safwat, "Dual and Wide-Band Inductively-Loaded Dipole-Based Antennas for WLAN/UMTS Applications", in *IEEE Transactions on Antennas and Propagation*, vol. 61, no. 3, pp. 1430-1435, March 2013.

[76] Y. Kabiri, P. Gardner and C. Constantinou, "Injection matched approach for wideband tunable electrically small antennas", in *IET Microwaves, Antennas and Propagation*, vol. 8, no. 11, pp. 878-886, August 19 2014.

[77] R. Storn and K. Price, "Minimizing the real functions of the ICEC 96 contest by differential evolution", *Proc. IEEE Conf. Evol. Computat.*, Nagoya, 1996, pp. 842-844.

[78] T. Wu and R. King, "The cylindrical antenna with nonreflecting resistive loading", in *IEEE Transactions on Antennas and Propagation*, vol. 13, no. 3, pp. 369-373, May 1965.

[79] Liang-Chi Shen, "An experimental study of the antenna with nonreflecting resistive loading", in *IEEE Transactions on Antennas and Propagation*, vol. 15, no. 5, pp. 606-611, September 1967.

[80] B. D. Popovic, M. B. Dragovic, and D. S. Paunovic, "Broadband cylindrical antenna with continuous resistive and concentrated capacitive loadings", in *Electronics Letters*, vol. 11, no. 25, pp. 611-613, December 11 1975.

[81] J. G. Maloney and G. S. Smith, "A study of transient radiation from the Wu-King resistive monopole-FDTD analysis and experimental measurements", in *IEEE Transactions on Antennas and Propagation*, vol. 41, no. 5, pp. 668-676, May 1993.

[82] P. Rocca, G. Oliveri and A. Massa, "Differential Evolution as Applied to Electromagnetics", *IEEE Antennas and Propagation Magazine*, vol. 53, no. 1, pp. 38-49, Feb. 2011

[83] J. L. Guo and J. Y. Li, "Pattern Synthesis of Conformal Array Antenna in the Presence of Platform Using Differential Evolution Algorithm", *IEEE Transactions on Antennas and Propagation*, vol. 57, no. 9, pp. 2615-2621, Sept. 2009.

[84] CST STUDIO SUITE, CST AG, Germany, www.cst.com.

[85] Online.Available: http://psearch.en.murata.com/inductor/spec

[86] W.i. Kwak, et al, "A Folded Planar Inverted-F Antenna for GSM/DCS/Bluetooth Triple-Band Application", *IEEE Antennas and Wireless Propagation Letters,*, vol. 5, no. 1, pp. 18-21, Dec. 2006.

[87] K. L. Wong and C. Y. Tsai, "Small-Size Stacked Inverted-F Antenna With Two Hybrid Shorting Strips for the LTE/WWAN Tablet Device", *IEEE Transactions on Antennas and Propagation,*, vol. 62, no. 8, pp. 3962-3969, Aug. 2014.

[88] Y. Chi and K. Wong, "Compact Multiband Folded Loop Chip Antenna for Small-Size Mobile Phone," in *IEEE Transactions on Antennas and Propagation*, vol. 56, no. 12, pp. 3797-3803, Dec. 2008.

[89] M. A. C. Niamien, L. Dussopt and C. Delaveaud, "A Compact Dual-Band Notch Antenna for Wireless Multistandard Terminals," in *IEEE Antennas and Wireless Propagation Letters*, vol. 11, pp. 877-880, 2012.

[90] Y. Liu, P. Liu, Z. Meng, L. Wang and Y. Li, "A Planar Printed Nona-Band Loop-Monopole Reconfigurable Antenna for Mobile Handsets," in *IEEE Antennas and Wireless Propagation Letters*, vol. 17, no. 8, pp. 1575-1579, Aug. 2018.

[91] C. Hsu and S. Chung, "Compact Antenna With U-Shaped Open-End Slot Structure for Multi-Band Handset Applications," in *IEEE Transactions on Antennas and Propagation*, vol. 62, no. 2, pp. 929-932, Feb. 2014.

[92] Y. Ban, C. Liu, J. L. Li, J. Guo and Y. Kang, "Small-Size Coupled-Fed Antenna With Two Printed Distributed Inductors for Seven-Band WWAN/LTE Mobile Handset," in *IEEE Transactions on Antennas and Propagation*, vol. 61, no. 11, pp. 5780-5784, Nov. 2013.

[93] Z.Chen et al. "Bandwidth Enhancement of LTE/WWAN Printed Mobile Phone Antenna Using Slotted Ground Structure", *PIERS*, vol. 129, pp. 469-483, 2012.

[94] C. Lee and K. Wong, "Planar Monopole With a Coupling Feed and an Inductive Shorting Strip for LTE/GSM/UMTS Operation in the Mobile Phone," in *IEEE Transactions on Antennas and Propagation*, vol. 58, no. 7, pp. 2479-2483, July 2010.

[95] G. Kim and T. Yun, "Small Wideband Monopole Antenna With a Distributed Inductive Strip for LTE/GSM/UMTS," in *IEEE Antennas and Wireless Propagation Letters,* vol. 14, pp. 1677-1680, 2015.

[96] K. Wong, C. Chang and Y. Lin, "Printed PIFA EM Compatible With Nearby Conducting Elements," in IEEE Transactions on Antennas and Propagation, vol. 55, no. 10, pp. 2919-2922, Oct. 2007.

[97] Chih-Ming Su, Kin-Lu Wong, Chia-Lun Tang and Shih-Huang Yeh, "EMC internal patch antenna for UMTS operation in a mobile device," in *IEEE Transactions on Antennas and Propagation*, vol. 53, no. 11, pp. 3836-3839, Nov. 2005.

[98] C. Lee and K. Wong, "Internal WWAN clamshell mobile phone antenna with reduced groundplane effects using a current trap," 2009 Asia Pacific Microwave Conference, Singapore, 2009, pp. 1781-1784.

[99] S. J. Jeong and K. C. Hwang, "Compact loop-coupled spiral antenna for multiband wireless USB dongles," in *Electronics Letters*, vol. 46, no. 6, pp. 388-390, 18 March 2010.

[100] D. F. Sievenpiper et al., "Experimental Validation of Performance Limits and Design Guidelines for Small Antennas," in *IEEE Transactions on Antennas and Propagation*, vol. 60, no. 1, pp. 8-19, Jan. 2012.

[101] R.M. Foster, "A reactance theorem". *Bell System Technical Journal*,3(2):259-267, 1924.

[102] J.G. Linvill, "Transistor negative impedance converters "Proc IRE 41 pages 725-729,1953.

[103] S. S. Hakim, "Some new negative-impedance convertors", *Electron. Lett.*, vol. 1, no. 1, pp. 9-10,Mar. 1965.

[104] B. R. Myers",New subclass of negative-impedance convertors with improved gain-product sensitivities", *Electron. Lett.*, vol. 1, no. 3, pp. 68-70, May 1965.

[105] A. I. Larky, "Negative-impedance converters", *'IRE Trans. Circuit Theory,* vol. 4, no. 3, pp. 124-131, Sep. 1957.

[106] T. Yanagisawa, "Rc active networks using current inversion type negative impedance converters", *IRE Trans. Circuit Theory,* vol. 4, no. 3, pp. 140-144, Sep. 1957.

[107] I. W. Sandberg, "Synthesis of driving-point impedances with active rc networks", *Bell Syst. Tech.J.*, vol. 39, no. 4, pp. 947-962, July 1960.

[108] H. Mirzaei and G. V. Eleftheriades, "Realizing Non-Foster Reactive Elements Using Negative-Group-Delay Networks", in *IEEE Transactions on Microwave Theory and Techniques*, vol. 61, no. 12, pp. 4322-4332, Dec. 2013.

[109] D. S. Nagarkoti, Y. Hao, D. P. Steenson, L. Li, E. H. Linfield and K. Z. Rajab, "Design of Broadband Non-Foster Circuits Based on Resonant Tunneling Diodes", in*IEEE Antennas and Wireless Propagation Letters*, vol. 15, pp. 1398-1401, 2016.

[110] A. D. Harris and G. A. Myers, " An investigation of broadband miniature antennas" Tech. Rep., Naval Postgraduate School. Monterey, CA, Sep.1968.

[111] G. Skahill, R. M. Rudish, and J. A. Pierro, "Apparatus and method for broadband matching of electrically small antennas", US Patent 6 121 940, Sep., 2000.

[112] J. T. Aberle, "Two-Port Representation of an Antenna With Application to Non-Foster Matching Networks", in *IEEE Transactions on Antennas and Propagation*, vol. 56, no. 5, pp. 1218-1222, May 2008.

[113] Y. Fan, K. Z. Rajab, M. Munoz and Y. Hao, "Electrically small half-loop antenna design with non-foster matching networks", *2012 6th European Conference on Antennas and Propagation (EUCAP)*, Prague, 2012, pp. 126-129.

[114] S. E. Sussman-Fort and R. M. Rudish, "Non-Foster Impedance Matching of Electrically-Small Antennas", in *IEEE Transactions on Antennas and Propagation*, vol. 57, no. 8, pp. 2230-2241, Aug. 2009.

[115] C. Di Nallo, G. Bit-Babik and A. Faraone, "Wideband antenna using non-foster loading elements", *2007 IEEE Antennas and Propagation Society International Symposium*, Honolulu, HI, 2007, pp. 4501-4504.

[116] M. C. Tang and R. W. Ziolkowski, "Electrically small metamaterial-inspired antennas with active near field resonant parasitic elements: From theory to practice", *2017 11th European Conference on Antennas and Propagation (EUCAP)*, Paris, 2017, pp. 1559-1563.

[117] M. C. Tang, T. Shi and R. W. Ziolkowski, "Electrically Small, Broadside Radiating Huygens Source Antenna Augmented With Internal Non-Foster Elements to Increase Its Bandwidth", in *IEEE Antennas and Wireless Propagation Letters*, vol. 16, pp. 712-715, 2017.

[118] H. Mirzaei and G. V. Eleftheriades, "A Resonant Printed Monopole Antenna With an Embedded Non-Foster Matching Network",*IEEE Transactions on Antennas and Propagation,* vol. 61, no. 11, pp. 5363-5371, Nov. 2013.

[119] F. Albarracin-Vargas, V. Gonzalez-Posadas, F. J. Herraiz-Martinez and D. Segovia-Vargas, "Design Method for Actively Matched Antennas With Non-Foster Elements", in *IEEE Transactions on Antennas and Propagation*, vol. 64, no. 9, pp. 4118-4123, Sept. 2016.

[120] A. M. Elfrgani and R. G. Rojas, "Non-Foster circuit embedded within electrically small antenna",*2014 IEEE Antennas and Propagation Society International Symposium (APS-URSI),* Memphis, TN, 2014, pp. 466-467.

[121] Abdullah Haskou, Dominique Lemur, Sylvain Collardey, Ala Sharaiha, "Small Wide-Band Printed Inverted-L Antenna with Non-Foster Matching",*IEICE Transactions on Communications* vol E101.B, no. 2, pp. 309-315.

[122] L. Batel, L. Rudant, J. F. Pintos and K. Mahdjoubi",Sensitivity of negative impedance converter circuit with respect to PCB design effects",*2015 International Workshop on Antenna Technology (IWAT),* Seoul, 2015, pp. 221-224.

[123] I. Uzkov, "An approach to the problem of optimum directive antennae design", *C. R. (Dokladey) Acad. Sci. URSS,*,vol. 53, no. 1, pp. 35-38,1946.

[124] M. Pigeon, A. Clemente, C. Delaveaud and L. Rudant, "Analysis of Harrington limit for electrically small antenna directivity", *The 8th European Conference on Antennas and Propagation (EuCAP 2014), The Hague*, 2014, pp. 2921-2925.

[125] A. Bloch, R. G. Medhurst and S. D. Pool, "A new approach to the design of super-directive aerial arrays", in *Electrical Engineers, Journal of the Institution of*, vol. 1953, no. 10, pp. 324-326, October 1953.

[126] N. Yaru, "A Note on Super-Gain Antenna Arrays", in *Proceedings of the IRE*, vol. 39, no. 9, pp. 1081-1085, Sept. 1951.

[127] E. Newman, J. Richmond and C. Walter, "Superdirective receiving arrays", in *IEEE Transactions on Antennas and Propagation*, vol. 26, no. 5, pp. 629-635, Sep 1978.

[128] M. Dawoud and A. Anderson, "Design of superdirective arrays with high radiation efficiency", in *IEEE Transactions on Antennas and Propagation*, vol. 26, no. 6, pp. 819-823, Nov 1978.

[129] E. E. Altshuler, T. H. O'Donnell, A. D. Yaghjian and S. R. Best, "A monopole superdirective array", *IEEE Transactions on Antennas and Propagation*, vol. 53, no. 8, pp. 2653-2661, Aug. 2005.

[130] S. R. Best, E. E. Altshuler, A. D. Yaghjian, J. M. McGinthy and T. H. O'Donnell, "An Impedance-Matched 2-Element Superdirective Array", *IEEE Antennas and Wireless Propagation Letters,* , vol. 7, pp. 302-305, 2008.

[131] T. H. O'Donnell and A. D. Yaghjian, "Electrically small superdirective arrays using parasitic elements", *2006 IEEE Antennas and Propagation Society International Symposium,* Albuquerque, NM, 2006, pp. 3111-3114.

[132] T. H. O'Donnell, A. D. Yaghjian and E. E. Altshuler",Frequency optimization of parasitic superdirective two element arrays", *2007 IEEE Antennas and Propagation Society International Symposium,* ,Honolulu, HI, 2007, pp. 3932-3935.

[133] A. D. Yaghjian, T. H. O'Donnell, E. E. Altshuler and S. R. Best, "Electrically Small Supergain end-fire arrays", *Radio Science*, Vol. 43, RS3002, 2008.

[134] A. Clemente, M. Pigeon, L. Rudant and C. Delaveaud, "Design of a Super Directive Four-Element Compact Antenna Array Using Spherical Wave Expansion", in *IEEE Transactions on Antennas and Propagation*, vol. 63, no. 11, pp. 4715-4722, Nov. 2015.

[135] A. Clemente, C. Jouanlanne and C. Delaveaud, "Analysis and design of a four-element superdirective compact dipole antenna array," *2017 11th European Conference on Antennas and Propagation (EUCAP), Paris, 2017, pp. 2700-2704.*

[136] A. Haskou, A. Sharaiha and S. Collardey",Design of Small Parasitic Loaded Superdirective End-Fire Antenna Arrays", *IEEE Transactions on Antennas and Propagation*, vol. 63, no.12, pp. 5456-5464, Dec,2015.

[137] A.Haskou",Contribution á l'Etude des Antennes Miniatures Directives ou Large Bande avec des Circuits Non-Foster", Université de Rennes 1, Rennes, France, 2016.

[138] O. S. Kim, S. Pivnenko and O. Breinbjerg, "Superdirective Magnetic Dipole Array as a First-Order Probe for Spherical Near-Field Antenna Measurements", in *IEEE Transactions on Antennas and Propagation*, vol. 60, no. 10, pp. 4670-4676, Oct. 2012.

[139] T. Kokkinos and A. P. Feresidis, "Electrically Small Superdirective Endfire Arrays of Metamaterial-Inspired Low-Profile Monopoles," in *IEEE Antennas and Wireless Propagation Letters*, vol. 11, pp. 568-571, 2012.

[140] S. Lim and H. Ling, "Design of a Closely Spaced, Folded Yagi Antenna", in *IEEE Antennas and Wireless Propagation Letters*, vol. 5, pp. 302-305, 2006.

[141] Z. Bayraktar, P. L. Werner and D. H. Werner, "The design of miniature three-element stochastic Yagi-Uda arrays using particle swarm optimization", in IEEE Antennas and Wireless Propagation Letters, vol. 5, pp. 22-26, 2006.

[142] B. Sentucq, A. Sharaiha and S. Collardey, "Superdirective compact parasitic array of metamaterial-inspired electrically small antenna", *2013 International Workshop on Antenna Technology (IWAT)*, Karlsruhe, 2013, pp. 269-272.

[143] M. M. Dawoud and A. P. Anderson, "Superdirectivity with Appreciable Bandwidth in Arrays of Radiating Elements FED by Microwave Transistors", *1974 4th European Microwave Conference, Montreux, Switzerland*, 1974, pp. 278-282.

[144] E. Newman and M. Schrote, "A wide-band electrically small superdirective array", in *IEEE Transactions on Antennas and Propagation*, vol. 30, no. 6, pp. 1172-1176, Nov 1982.

[145] L. Batel, L. Rudant, J. F. Pintos, A. Clemente, C. Delaveaud and K. Mahdjoubi, "High directive compact antenna with non-foster elements", *2015 International Workshop on Antenna Technology (IWAT),*,Seoul, 2015, pp. 381-384.

[146] ANSYS HFSS, Pittsburg, PA, USA.

[147] C. A. Balanis, "Antenna Theory and Design", *3rd ed. New York, NY, USA,:* Wiley Int., 2005.

[148] M. He, X. Ye, P. Zhou, G. Zhao, C. Zhang and H. Sun, "A Small-Size Dual-Feed Broadband Circularly Polarized U-Slot Patch Antenna", in *IEEE Antennas and Wireless Propagation Letters*, vol. 14, pp. 898-901, 2015.

[149] C. Sun, Z. Wu and B. Bai, "A Novel Compact Wideband Patch Antenna for GNSS Application", in *IEEE Transactions on Antennas and Propagation*, vol. 65, no. 12, pp. 7334-7339, Dec. 2017.

[150] K. F. Lee, S. L. Steven Yang, A. A. Kishk and K. M. Luk, "The Versatile U-Slot Patch Antenna", in *IEEE Antennas and Propagation Magazine, vol. 52, no. 1, pp. 71-88, Feb. 2010.*

[151] P. Mousavi, B. Miners and O. Basir, "Wideband L-Shaped Circular Polarized Monopole Slot Antenna", in *IEEE Antennas and Wireless Propagation Letters*, vol. 9, pp. 822-825, 2010.

[152] J. Kizhekke Pakkathillam and M. Kanagasabai, "Circularly Polarized Broadband Antenna Deploying Fractal Slot Geometry", in *IEEE Antennas and Wireless Propagation Letters*, vol. 14, pp. 1286-1289, 2015.

[153] M. G. Aly and Y. Wang, "A wideband circularly polarised cross-slot antenna with an L-shaped feed-line", *Loughborough Antennas and Propagation Conference (LAPC 2017)*, Loughborough, 2017, pp. 1-4.

[154] M. Nosrati and N. Tavassolian, "Miniaturized Circularly Polarized Square Slot Antenna With Enhanced Axial-Ratio Bandwidth Using an Antipodal Y-strip", in *IEEE Antennas and Wireless Propagation Letters*, vol. 16, pp. 817-820, 2017.

[155] S. Ahdi Rezaeieh, A. Abbosh and M. A. Antoniades, "Compact CPW-Fed Planar Monopole Antenna With Wide Circular Polarization Bandwidth", in *IEEE Antennas and Wireless Propagation Letters*, vol. 12, pp. 1295-1298, 2013.

[156] T. Kumar and A. R. Harish, "Broadband Circularly Polarized Printed Slot-Monopole Antenna", in *IEEE Antennas and Wireless Propagation Letters*, vol. 12, pp. 1531-1534, 2013.

[157] H. Liu, Y. Liu and S. Gong, "Broadband microstrip-CPW fed circularly polarised slot antenna with inverted configuration for L-band applications", in *IET Microwaves, Antennas and Propagation*, vol. 11, no. 6, pp. 880-885, 5 12 2017.

[158] C. Zhao and C. F. Wang, "Characteristic Mode Design of Wide Band Circularly Polarized Patch Antenna Consisting of H-Shaped Unit Cells",in *IEEE Access*, vol. 6, pp. 25292-25299, 2018.

[159] M. Capek, P. Hazdra, P. Hamouz, and J. Eichler, "A method for tracking characteristic numbers and vectors", *Prog. Electromagn. Res.B, vol. 33, pp. 115-134, 2011.*

[160] B. Raines and R. Rojas, "Wideband characteristic mode tracking", *IEEE Trans. Antennas Propag., vol. 60, no. 7, pp. 3537-3541, Jul. 2012.*

[161] D. J. Ludick et al., "A tracking algorithm for eigenvectors calculated with characteristic mode analysis", in *8th European Conference on Antennas and Propagation (EuCAP),pp. 629-632, 2014.*

[162] D. J. Ludick et al., "A hybrid tracking algorithm for characteristic mode analysis", in *Proc. ICEAA, Aug. 3˜8, 2014, pp. 455-458.*

[163] Z. Miers and B. K. Lau, "Wideband Characteristic Mode Tracking Utilizing Far-Field Patterns", in *IEEE Antennas and Wireless Propagation Letters*, vol. 14, pp. 1658-1661, 2015.

[164] Wasim Alshrafi, Vladimir Ekaterinichev, Dirk Heberling, "Wideband Crossed Dipoles Antenna for All GNSS Bands Using Wideband AMC", *2018 11th European Conference on Antennas and Propagation (EuCAP), London, UK, 8-13 April. 2018.*

[165] S. A. Tretyakov, "Analytical Modeling in Applied Electromagnetics". Norwood, MA: Artech House, 2003.